Development of Highly Efficient and Stable Lead-Free Perovskite Solar Cells Through Composition and Interface Engineering

Gabriella A. Tosado

A dissertation

submitted in partial fulfilment of the

requirements for the degree of

Doctor of Philosophy

University of Washington

2020

Reading Committee:

Qiuming Yu, Chair

Vincent Holmberg

Samson A. Jenekhe

Program Authorized to Offer Degree:

Chemical Engineering

University of Washington

ABSTRACT

Development of Highly Efficient and Stable Lead-Free Perovskite Solar Cells Through Composition and Interface Engineering

Gabriella A. Tosado

Chair of the Supervisory Committee:
Professor Qiuming Yu

Solar energy has the highest capacity to power our energy needs sustainably without emitting greenhouse gases. Hybrid organic-inorganic lead halide perovskite solar cells (PVSCs) have emerged in the past decade as a promising low-cost, low energy intensity, thin film solar cell with lab efficiencies reaching 25.2%. The toxicity of Pb perovskites and performance and stability issues with Sn lead-free alternatives remains a major roadblock to commercialization. In this work, novel perovskite compositions are designed and used to study the transition from Pb to Sn perovskites, cations are tuning to implement stabilizing components for pure Sn perovskites, and Sn perovskites performance and stability issues are tackled.

The triple cation methylammonium (MA), formamidinium (FA) and Cs, with double halide composition $Cs_x(MA_{0.17}FA_{0.83})_{1-x}Pb_{1-y}Sn_y(I_{0.83}Br_{0.17})_3$ films with x = 0.05, 0.10, and 0.20 and y = 0, 0.25, 0.50, 0.75, and 1.0 was used to create a library of new perovskites and study novel band gap trends near the maximum Schockley Quiesser limit. The simple inverted device structure of indium tin oxide (ITO)/poly (3,4, -ethylenedioxythiphene): polystyrene sulfonate (PEDOT:PSS)/Perovskite/[6,6]-phenyl-C_{60}-butyric acid methyl ester ($PC_{60}BM$)/fullerene (C_{60})/2,9-dimethyl-7,7-diphenyl-1,10-phenanthroline (BCP)/Ag eliminated dopant instabilities. Due to a high-quality film morphology and optimal Band gap,

$Cs_{0.05}(MA_{0.17}FA_{0.83})_{0.95}Pb_{0.25}Sn_{0.75}(I_{0.83}Br_{0.17})_3$ (band gap = 1.30 eV), achieved a record maximum efficiency of 11.05% for any 75% Sn composition. Moreover, the 75% Sn PVSCs retained 80% of initial PCE after 30 days storage in inert conditions and 100 hours in ambient conditions.

After optimizing antisolvent choice, solvent annealing, and hot casting conditions for pure Sn perovskite films, the novel composition with Cs, FA, and guanidinium (GA), $(CsGA)_xFA_{100-2x}SnI_3$ was implemented. This cation mixture combines the benefits of a guanidinium cation, such as increased hydrogen bonding and no dipole moment, with Cs to fill point defects and relax the crystal lattice to better integrate a large stabilizing agent, ethylenediammonium diiodide ($EDAI_2$). The $EDAI_2$ additive not only yielded pinhole-free cubic phase $(CsGA)_xFA_{100-2x}SnI_3$ perovskite films but also decreased both shallow and deep trap states in the perovskite films. The devices with $(CsGA)_{15}FA_{70}SnI_3$ and 0-2% $EDAI_2$ all achieved a maximum PCE higher than 5% with the highest of 5.72% for a fresh device with $(CsGA)_{15}FA_{70}SnI_3$ and 1% $EDAI_2$. After storage, the maximum PCE was increased from 5.69% to 6.39% for the $(CsGA)_{15}FA_{70}SnI_3$ and 1.5% $EDAI_2$ devices.

Finally, to tackle energy loss issues that have plagued pure Sn perovskites (loss = 0.6-0.9 V), the misalignment between the PEDOT:PSS hole transport layer and the Sn perovskite valence band was studied due to the energy misalignment between the hole transport layer and pure Sn perovskite valence band. Cosolvent methods, solvent wash methods, and solvent immersion methods with DMSO, EG, and CH_3OH were implemented to alter the PSS content and work function of the HTL to improve alignment. Utilizing the $(CsGA)_{15}FA_{70}SnI_3$+1.0% $EDAI_2$ perovskite film we demonstrated a higher performance of 6.29% and 6.16% with a 5% DMSO cosolvent and methanol solvent wash, respectively. This work is a comprehensive push to improve the performance and stability of non-toxic Sn perovskite devices, bringing this technology one step closer to commercialization.

TABLE OF CONTENT

LIST OF FIGURES

LIST OF TABLES

ABBREVIATIONS

ABX_3 or AMX_3- Formula for 3D halide perovskites where A = +1 organic or inorganic cation (MA, FA, GA, Cs, Rb), B/M = +2 transition metal (Pb,Sn), and X = -1 halide anion (Cl, Br, I)

BS- Backward scan

CBM – Conduction band minimum

CIGS – Copper indium gallium selenide

DMF- *N*,*N*-dimethylformamide

DMSO - Dimethyl sulfoxide

DOS - Density of states

$EDAI_2$ – Ethylenediammonium diiodide

EDA^{2+} - Ethylenediammonium

E_{CBM} – Energy of conduction band minimum

E_{VBM} – Energy of valence band maximum

E_g – Energy of Band gap

EQE – External quantum efficiency

ETL – Electron-transport layer

FA^+ - Formamidinium, $[H_2N\text{-}CH{=}NH_2]^+$

FS – Forward scan

FF – Fill Factor

FWHM – Full width at half maximum

GA – Guanidinium, $[(H_2N)_2\text{-}C{=}NH_2]^+$

GBL - ɣ-butyrolacetone

HOMO – Highest occupied molecular orbital

HTL – Hole-transport layer

IPA – Isopropyl alcohol

ITO-Indium tin oxide

J – Current density

J_{ph} – Photocurrent

J_{sc} – Short-circuit current density

LUMO – Lowest unoccupied molecular orbital

MA – Methylammonium, $[CH_3NH_3]^+$

MPP- Maximum power point

OC- Open-circuit

$PC_{60}BM$ – Phenyl-C_{61}-butyric acid methyl ester

PCE- Power conversion efficiency

PEDOT:PSS – poly (3,4-ethylenedioxythiophene)-poly(styrenesulfonate)

PL -Photoluminescence

PV- Photovoltaic

PVSCs- Perovskite solar cells

SC-Short-Circuit

SQ- Shockley-Queisser

UV-Vis – Ultraviolet-visible

V_{oc} – Open-circuit voltage

WF – Work function

XRD – X-ray diffraction

ACHKNOWLEDGEMENTS

I must first thank my wonderful advisor, Professor Qiuming Yu, for her guidance and support over the past five years. I feel extremely lucky to have been a part of her lab and grateful to have had her as a mentor during my PhD. Her creative way of seeing research problems and solutions, technical knowledge, and broad expertise has helped evolve my research and contributions to the scientific community. Professor Yu's support towards my research, my professional development and aspirations, and scientific curiosity have been essential to my successes throughout my graduate degree. Her mentorship has helped me to discover how I can use my knowledge to contribute to society and has allowed me to grow as an engineer, a science communicator, an advocate, a researcher, and a person.

My committee members deserve a special thanks for dedicating their time to my research. To Professors Vincent C. Holmberg, Samson A. Jenekhe, and Lih Y. Lin, thank you for sharing your expertise, training through my coursework, and taking the time to be a part of my dissertation committee. Their valuable insights and suggestions helped shape my research and my thinking as a scientist and I am grateful for their mentorship. I would also like to thank Professor Hugh W. Hillhouse and Alex K-Y Jen and their research group members for access to several pieces of equipment, expertise, and discussion that were critical to my research.

I want to acknowledge the financial support from the UW Department of Engineering, the UW Clean Energy Institute through the Education Fellowship and Outreach Fellowship, and the National Science Foundation through the Graduate Research Fellowship Program. A special thanks to the Clean Energy Institute for training me in science communication and allowing me to thrive in the world of outreach and science education. These programs supported my research and person financially and their voice of confidence in my work pushed me forward through moments of doubt. I would like to acknowledge the facilities at UW campus, including the Photonics Research Center, and Molecular Analysis Facility, as well as the Sandia National Laboratory that provided access to and training on essential fabrication and characterization equipment.

I would like to thank both past and present members of the Qiuming Yu Research Group. I was able to join a research family that helped train me, helped me strive, and grow both technology and personally. I consider myself lucky to have completed my PhD alongside Dr. Beau

Richardson, Dr. Ping Wu, Dr. David Galvin, Dr. Monica Esopi, Emerson Chen, Julie Blachfield, Vidit Parehk, Yi-Yu Lin, Xiaoyu Zhang, Beiying Zhou, Hao Dong, Zhiyin Niu, Jacob Albrikan, Shukun Zhong, Zizhao Xu, Zonglun Li, E-lin Liu, Chen Cai, and Kaiqiang Wang. A special thanks to Erjin Zheng for the invaluable perovskite discussions and experiment troubleshooting. Perovskite buddies have to stick together. I would also like to thank the undergraduate students who have shaped me as a teacher and aided in my research, including Kevin Garcia, Dat Nguyen, Rebecca Zhao, and Smriti Somasundaram. I am grateful to the Department of Chemical Engineering for creating a welcoming environment and always striving to include the voices of graduate students. Thanks to Professor Elizabeth Nance who has been an advocate, mentor, and teacher, not only to me, but many other through her founding of Women in Chemical Engineering, creating a space where students can better and grow themselves. Thanks to Professor Lilo Pozzo for the opportunity to use my research and expertise to help people through the Puerto Rico project and making Seattle feel a little more like home.

Finally, to my friends and family, who have supported me to new heights. Thank you to Mami, Papa, and Nana, who showed me there was more than my backyard at a young age, allowed me to be myself and follow my passions, and gave me the courage to tackle what seem like impossible challenges. I would not have made it this far without your constant support. You all inspire me and I hope I continue to make you proud. Thank you to the family I have created here in Seattle, Brittany Bishop, Robyn Veraa, and Jon Witt. I could not have imagined the experiences I would have had when I started this journey from conquering mountains to joining a dance troupe to being involved in multiple political efforts. You guys have been through all the joy and all the terrors of graduate school and I appreciate you being a part of my life. I am immensely grateful to all my friends, from my Charter School days, University of Miami, and Seattle, from creating a supportive and fun community around me and rolling with random Gaby adventures. Thank you Thomas Musselwhite for being a part of the last leg of my PhD, bringing new joy, laughter, adventures, and fulfillment along the way. Finally, I would like to thank the amazing ladies of science that have supported me through the different phases of my life, and those who came before me, paving the way for me to succeed in this field.

DEDICATION

To Mami, Papa, and Nana

You made me the person I am today

CHAPTER ONE: INTRODUCTION

1.1 The Focus on Solar Energy

World energy consumption is predicted to increase by 28% between 2015 and 2040.[1] Although there has been significant growth in alternative fuel sources, generation from fossil fuels still accounts for 80% of power, dominating the energy landscape. These unsustainable energy sources emit greenhouse gases, such as CO_2 and CH_4, that have led to anthropogenic climate change which has been linked to, among other consequences, rising sea levels, increased strength of super storms, droughts and wildfires. Other pollutants emitted by unregulated burning fossil fuels have also been linked to several health issues such as asthma and a variety of cancers. Additionally, the exhaustible and finite supply of fossil fuels has led to national energy security concerns as well as rising costs to consumers. Renewable and sustainable energy sources have thus been pursued to decouple economic growth with fossil fuels, allowing us to avoid the worst consequences of global warming, as well as encourage energy independence. Of the renewable resources available, electricity generated through solar energy has the highest capacity to fuel our energy economy. The amount of the sun's energy hitting the Earth every hour is enough to power human civilization for a year.[2] When paired with storage and an optimized grid, harnessing 0.03% of the constant 120,000 terawatts of solar energy potential could fulfill energy needs worldwide without emitting greenhouse gases or other pollutants.

Although solar energy can be harnessed through several indirect ways, such as by thermal collectors that receive solar radiation and convert it to thermal energy, photovoltaic (PV) cells can convert incident light directly into electricity. PV cells are semiconductor devices that work under a variety of lighting conditions, can be imbedded, and used in several applications, and offer scalable installation making them advantageous over sources of renewable energy. Using

current, commercialized solar cells, PVs covering a square area of 133 miles x 133 miles would satisfy all the US's energy needs. Despite the enormous potential for harnessing energy and incredible technological progress over the last few decades, PV contributes to < 2% of the global energy consumption. The cost of PV technologies currently prohibits them from competing with cheaper fossil fuels, preventing the transition of a clean energy economy. Further research and development is imperative to improve current PV technology efficiencies and consumer costs to reach the U.S. Department of Energy's cost target of $0.06 per kilowatt-hour (kWh) for utility scale PV, allowing for further integration into renewable grid systems.[3]

1.2 Basic Principles of Photovoltaic Cells

A photovoltaic cell is a device that directly converts light energy to electrical energy. When photons are absorbed by matter, the photovoltaic effect occurs, meaning their energy is absorbed by electrons, which are then excited to higher energy states. In other materials, the excited electrons relax back to their ground state and give off heat energy. In a PV cell, a two-terminal electrical diode takes advantage of the electric potential created by the separation of charges and the built-in asymmetric conductance pulls the excited electrons away before relaxing. A photovoltage, or potential difference, is generated by the excited electrons driving the charges through an external circuit to perform electrical work.[4] In order for excited electrons to be separated from their oppositely charged holes, they must absorb enough energy to cross a band gap. A band gap (E_g) is the energy difference between the valence band maxima, also known as highest occupied molecular orbital (HOMO), and the conduction band minima, also known as the lowest unoccupied molecular orbital (LUMO), of a solid material. Insulators have a very large band gap meaning they require a lot of energy to excite electrons, giving them heat and electrical resistant properties. PV cells use semiconductors as the photoactive layers and whose specific

band gap can be crossed by electrons when they absorb photons of light with an energy larger than their band gap. This separation of the electron-hole pairs, or exciton, created by electrons crossing a band gap, is necessary to make the potential energy available as electrical energy. The operation of a PV cell, therefore, requires three basic steps. First, the absorption of light by the electrons in an active layer to an exciton. Second, the separation of positive and negative charge carriers. Third, the separation of the free charge carriers to an external circuit to perform work.

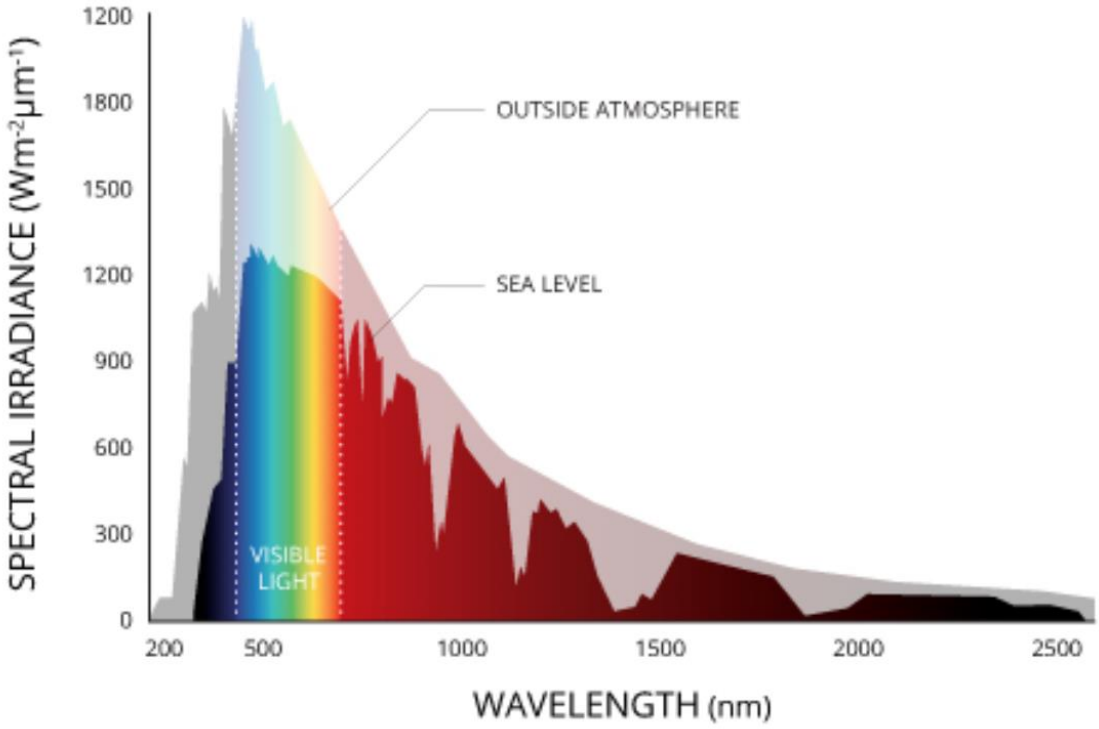

Figure 1-1. Standard solar spectral irradiance data for AM0 (light grey line) and AM1.5 G (black line) emphasizing the visible spectra.[5]

To eliminate changes in the solar spectrum as a factor when analyzing device performance, standard reference spectra are used to compare devices. PV cells are tested under a solar simulator at standard conditions. Standard conditions include a cell temperature of 25˚C, an incident light intensity of 100 mW/cm^2 perpendicular to the device surface, and the air mass 1.5 global (AM 1.5G) spectrum considering the path length of sunlight through the atmosphere. Figure 1-1 shows

the AM0, also known as airmass zero (black), spectrum outside the earth's atmosphere where there is no air between the sun and the receiver.[5] Figure 1-1 also shows the standard AM 1.5G spectrum (black line) which is the standard solar spectrum that hits the earth's surface at a zenith angle of 48˚ at sea level. The main differences in the AM0 and AM 1.5G spectra are due to atmospheric absorption and scattering from molecules and aerosols, with water droplets and dust having the greatest impact.

Figure 1-2 shows the basic equivalent circuit model for a single diode and is governed by the following equation using Kirchoff's law for current (I)[6]:

$$I = I_L - I_D - I_{sh} \quad 1.1$$

Where I_L is the light-generated current in the PV cell, I_D represents the voltage-dependent current lost due to recombination, and I_{sh} is the shunt resistance dependent current loss. The shunt current (I_{sh}) is written as the following equation:

$$I_{sh} = \frac{(V+IR_s)}{R_{sh}} \quad 1.2$$

with V representing the voltage, R_{sh} representing the shunt resistance and R_s representing the series resistance. I_D is modeled using the Shockley equation for an ideal diode and is illustrated in the following equation:

$$I_D = I_0 \left[\exp\left(\frac{V+IR_s}{nV_T}\right) - 1\right] \quad 1.3$$

Where n is the unitless ideality factor, I_0 is the current at saturation, and V_T is the thermal voltage dependent on Boltzmann's constant, the elementary change, and temperature:

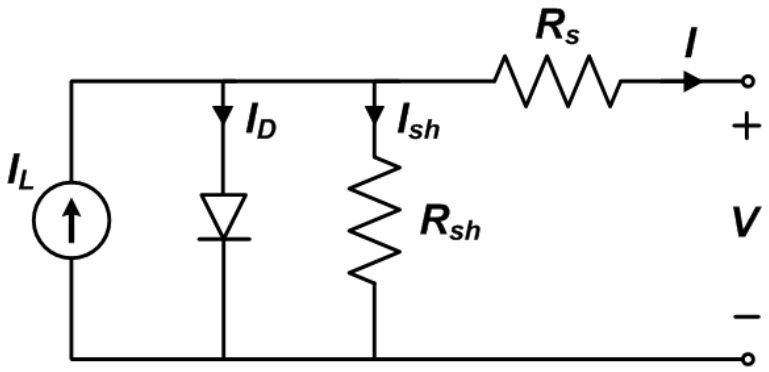

Figure 1-2. Basic equivalent circuit model for a single solar cell where I_L is the light-generated current in the PV cell, I_D represents the voltage-dependence current lost due to recombination, and I_{sh} is the shunt resistance dependent current loss, R_s is the series resistance and R_{sh} is the shunt resistance with I representing current and V representing voltage.[6]

$$V_T = \frac{kT_c}{q} \quad 1.4$$

Combining equations 1, 2, and 3 creates the complete governing equation for a single diode model:

$$I = I_L - I_0 \left[\exp\left(\frac{V+IR_s}{nV_T}\right) - 1\right] - \frac{(V+IR_s)}{R_{sh}} \quad 1.5$$

PV cells can be characterized by a few different device performance parameters including the open-circuit voltage (V_{oc}), the short-circuit current (I_{sc}), which can be converted to the short-circuit current density (J_{sc}), the fill factor (FF), and the power conversion efficiency (PCE). When under standard conditions, these curves are generated to measure I_{sc}, V_{oc}, and FF which can then be used to calculate the PCE. Figure 1-3 shows a typical device J-V curve. The PCE is the ratio of the maximum output power ($P_{m,out}$) of the device divided by the input power (P_{in}) from Figure 1-1. The output power of the device and PCE are calculated using the following equation:

$$P_{m,out} = FF \times V_{oc} \times I_{sc} = V_{MPP} \times I_{MPP} \quad 1.6$$

$$\eta_{PCE} = \frac{P_{m,out}}{P_{in}} = \frac{FF \times V_{oc} \times I_{sc}}{P_{in}} \quad 1.7$$

The $P_{m,out}$ is equal to the product of voltage at the maximum power point (V_{MPP}) and the current at the maximum power point (I_{MPP}) while P_{in} is the power shining on the cell and is calibrated to the AM 1.5G spectrum or 100 mW/cm^2. The V_{oc} is the maximum voltage available from a solar cell with infinite load resistance, or open circuit, and occurs at zero current. On the other hand, the I_{sc} is the maximum current measured at zero resistance, or short circuit, that occurs when the voltage reaches zero. Although V_{oc} and I_{sc} are the maximum voltage and current respectively, the power at both operating points is zero. FF is a ratio of parameters at the PV actual max power point compared to the theoretical maximum parameters and is represented through the following equation.

$$FF = \frac{V_{MPP} \times I_{MPP}}{V_{oc} \times I_{sc}} \qquad 1.8$$

The FF, therefore, describes the "squareness" of the current density-voltage (J-V) curve and is used to describe how close to ideal is the curve.

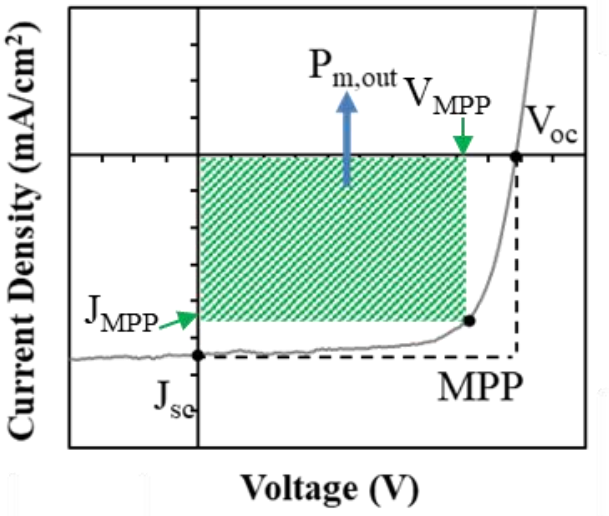

Figure 1-3. J-V curve and the PV parameters of a typical PV device showing the open-circuit voltage (V_{oc}), the short-circuit current density (J_{sc}), the current density at the max power point (J_{MMP}), the max power point (MPP), the voltage at the max power point (V_{MPP}), and the power at max power ($P_{m,out}$).

1.3 Perovskite Solar Cells in the Context of the Photovoltaic World

The development of solar energy conversion devices began with the first-generation solar cell made of polycrystalline silicon which now dominates the PV industry with a 90% share. Although commercialized silicon solar cells have the benefit of a long lifetime (20+ year lifetime warranty) and high efficiency (15-20% typical module efficiency), its cost has been kept uncompetitive by an energy intensive manufacturing process and required expensive protection.[7] Even though silicon PV is modeled to become more affordable based on predictions, it still has inherent technological limitations such as an indirect band gap (E_g), material requirements such as high temperature processing and purity, and protection requirements that constrain its system costs and module efficiency. To decrease fabrication costs, research has been done on alternative second-generation thin film active layer materials that do not require high energy intensive synthesis or high costs to manufacture. There are a few low temperature solution processed alternative that can easily be scaled up such as dye-sensitized solar cells and organic solar cells. Unfortunately, both of these alternatives have much lower efficiency of less than 10% and are unstable over long periods of time with dye sensitized solar cells degrading at varying temperatures and organic solar cells degrading in ambient conditions. Cadmium telluride (CdTe) is one such thin film material that uses continuous, low cost manufacturing processes such as chemical vapor deposition, spin coating and electrodeposition. CdTe photovoltaic cells have the smallest carbon footprint, lowest water use, and shortest energy payback time. Unfortunately, the average CdTe module reaches a lower efficiency of 11% and uses rare materials, such as telluride, that act as a limiting factor to large, industrial scalability and already limit the base costs. Copper indium gallium selenide (CIGS) is another thin film solar active layer material that can be deposited on flexible materials due to its low temperature deposition, allowing for the implementation of inexpensive roll-to-roll

solar printing mass manufacturing, which would greatly decrease costs. Unfortunately, the CIGS large modules also have a lowered efficiency commercially (7-11%) compared to silicon, have a shorter lifetime, and use a scarce element indium.[7,8]

Hybrid organic-inorganic lead halide perovskite solar cells (PVSCs) have emerged in the past decade as a promising low-cost thin film solar cell with PCE increasing from 3.8% to 25.2% in less than a decade.[9] PVSCs combine several merits of the previous PV technologies such as a high efficiency (comparable to silicon PV), low temperature solution processing, scalability and color tuning ability (dye-sensitized, organic), flexibility and lightweight (CIGS, CdTe, GaAs inorganic thin film PVs).[10] Because of the enormous potential of perovskite material as a PV active layer, extensive research efforts have enabled unprecedented efficiency growth in the lab scale. The key roadblocks towards commercialization remain PVSC toxicity and long-term stability which are being research extensively in multiple labs worldwide. [11–13] In tandem, solving challenges involving large scale modules, roll-to-roll printing, and other large scale up models have begun in both industrial and academia fields.[14–16] Currently, PVSC have already emerged in the start-up companies for tandem solar materials and will continue to enter the PV market in off-grid niche applications such as portable and wearing devices.[17] In the long term with toxicity, stability, and scalability issues tackled, PVSCs will join on-grid PV technologies and become an affordable source of solar energy on the terawatt scale. Figure 1-4 illustrates important materials properties such as absorption coefficients,[18] energy loss on lab and large scale module,[19]and electronic properties as well as commercializing potential illustrating power-per-weight,[20] performance with growing size modules,[19] and energy pay back periods[21] for PVSCs and other thin film PV technology.

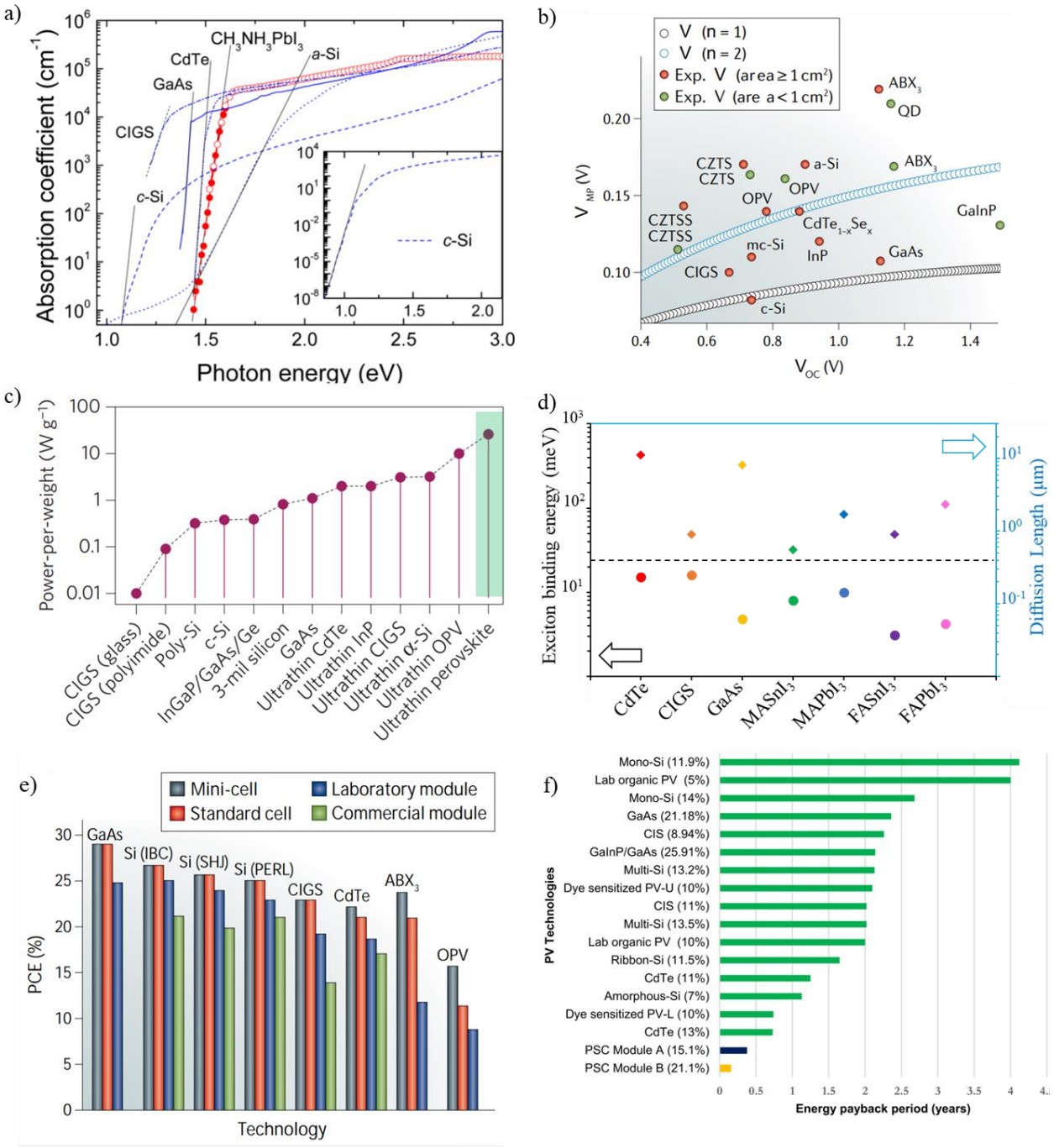

Figure 1-4. Optoelectronic and commercialization aspects PVSCs compared to other thin film PV. (a) Absorption coefficient of different PV materials. (b) Experimental and theoretical voltage losses for operation at maximum power. The expected ΔV for a given VOC has been calculated for ideal contacts and only radiative recombination with a diode ideality factor (n) of 1 and for ideal contacts with n = 2. The experimental values of ΔV have been determined for both small-area and large area. (c) Power-per-weight of various lightweight solar cells. (d) Binding energy and diffusion length for PV materials and PVSCs with various active layer compositions. (e) The PCE of different solar technology at the mini-cell, standard cell, lab module, and commercial module level. (f) Energy payback period for different PV technologies.[18-21]

1.4 Hybrid Organic-Inorganic Perovskite Materials and Solar Cells

1.4.1 Structure and Composition Tuning

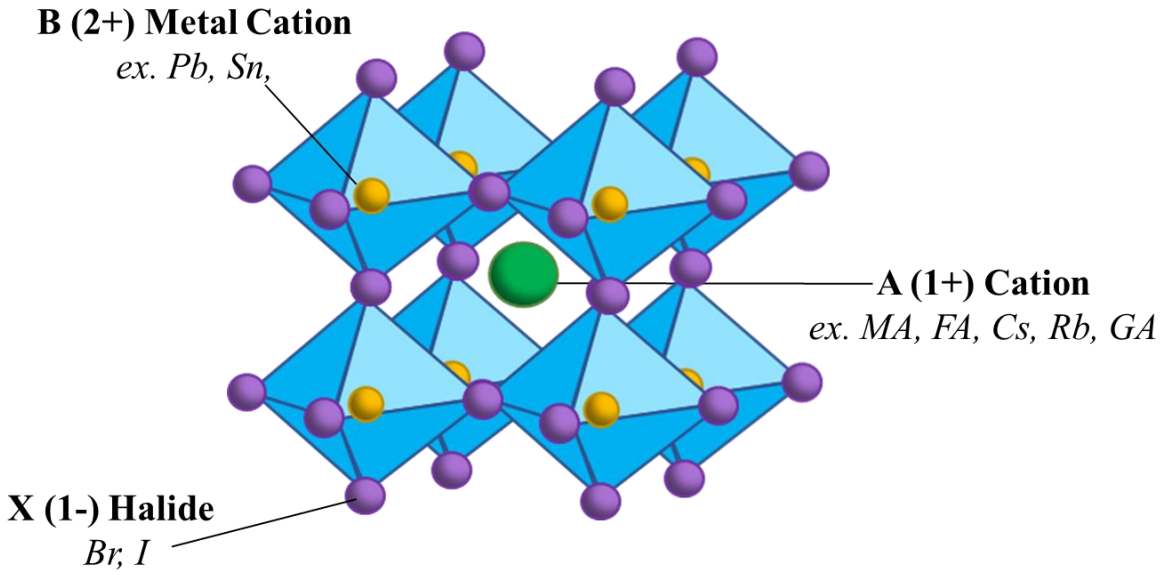

Figure 1-5. Perovskite cubic structure with chemical formula ABX_3. For the hybrid perovskite solar cell, A is typically an organic cation, B is a transition metal, and X is a halide.

Perovskites were named after a mineralogist L.A. Perovski and followed the specific crystal structure AMX_3 (also noted as ABX_3) shown in Figure 1-5 where the larger A cation occupied a cubo-octahedral site with X anions. The smaller M cation is in a stabilized octahedral site shared with six X anions. Oxide perovskites were the most studied due to their electrical properties of ferroelectricity or superconductivity until it was found that halide perovskites had changes in electrical properties and a decreased band gap with increased dimensionality from 2D to 3D.[13] In organic-inorganic perovskites found in photovoltaic cell follow the formula where A can be a wide range of monovalent cation such as methylammonium (MA^+, $[CH_3NH_3]^+$), formamidinium (FA^+, $[H_2N\text{-}CH{=}NH_2]^+$), rubidium ($Rb^+$), guanidinium ($GA^+$, $[(H_2N)_2\text{-}C{=}NH_2]^+$) and/or cesium ($Cs^+$)),[22] B (or M) is a divalent transition metal cation such as lead (Pb^{2+}), germanium (Ge^{2+}), and/or tin (Sn^{2+}),[23] and X is a halide anion such as iodide (I^-), bromide (Br^-),

and/or chloride (Cl^-).[24,25] The inorganic components (M and X) are in-plane covalently bonded, while the cation component (A) interacts with the metal-halide cage through van der Waals forces. The crystal structure of the perovskite can be estimated by the tolerance factor. The Goldschmidt Tolerance Factor (GTF) was first used for metal-oxide perovskites and has been applied to metal-halide perovskites as a way to quasi-quantify the stability of various composition perovskites.[26,27] The GTF of a 3D cubic ABX_3 perovskite is represented by:

$$\text{GTF} = \frac{(r_A + r_X)}{\sqrt{2}(r_B + r_X)} \qquad 1.9$$

where r_A, r_B and r_X are the ionic radii of the monovalent cation, divalent transition metal cation, and halide anion, respectively. The octahedral factor (μ) is another quantifying ratio of divalent transitional metal cation radium to halide anion radium (r_B/r_x). Stable cubic α–phase perovskites are expected to exhibit a GTF between 0.813 to 1.107 and an octahedral factor, μ, between 0.442 and 0.895.[28] Experimentally, perovskites are more cubic stable when GTF is between 0.9 and 1 as GTF > 1 enters the hexagonal/tetragonal phase and GTF < 0.8 enters the orthorhombic phase. The effects on octahedral tilting for each crystal structure can be seen in Figure 1-6 which shows the

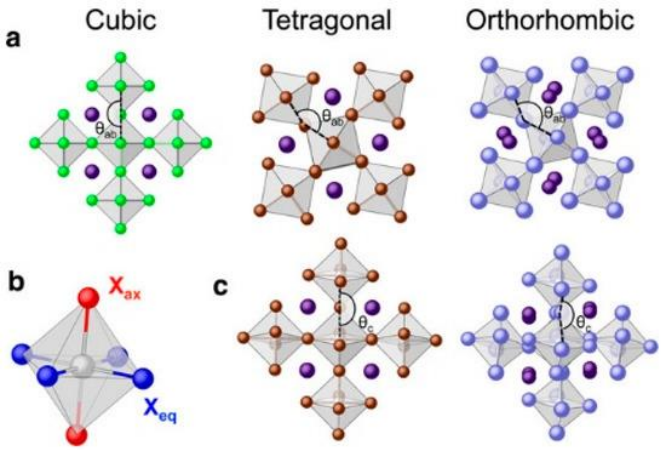

Figure 1-6. The cubic, tetragonal, and orthorhombic crystal structure of a perovskite. (a) Illustration of the cubic structure that is characterized by 90° angles and equal lattice parameters, (b) An octahedral cage. c) Illustration of the tetragonal structure that is still characterized by certain 90° angles and lattice parameters a = b ≠ c.[29]

cubic structure having near 180° θ bond angles.[29] The tetragonal and orthorhombic structure are affected by more severe octahedral tilting, pushing the bond angles to be less linear.

1.4.2 Material Properties Tuning

The intrinsic properties of perovskites have contributed to high device performance, such as a direct band gap[30] with a high absorption coefficient and sharp onset with low Urbach energy over the visible spectrum,[31] excellent emission, direct generation of free charge carrier under photo-excitation due to a low exciton binding energy,[32] high point-defect tolerance, and excellent charge carrier transport properties (carrier mobility[33], long carrier diffusion length, and long carrier lifetime[34]). These excellent material properties make them a desirable candidate as solar cell absorber. Due to the intrinsic nature of these properties, they can be tuned by altering the composition of the perovskite. For example, the $MAPbI_3$ perovskite material possess an exciton binding energy between 37-50 meV [35] while mixed halide perovskites such as $MAPbI_xCl_{1-x}$ exhibit an exciton binding energy of 35-75 meV at room temperature, enabling the decoupling of excitons at room temperature.[8] Figure 1-7 illustrates the fundamental efficiency limits for solar materials.[10]

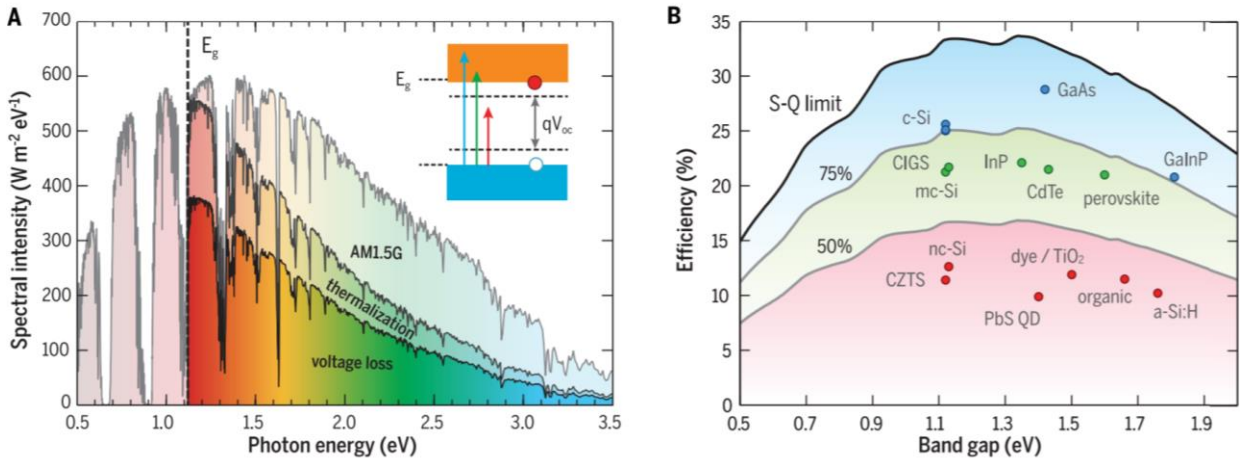

Figure 1-7. (a) AM1.5G solar spectrum with fundamental solar cell efficiency limits. (b) Theoretical Shockley-Queisser detailed-balance efficiency limit as a function of band gap (black line) and 75% and 50% of the limit (grey lines) with corresponding record photovoltaic efficiencies for different materials.[10]

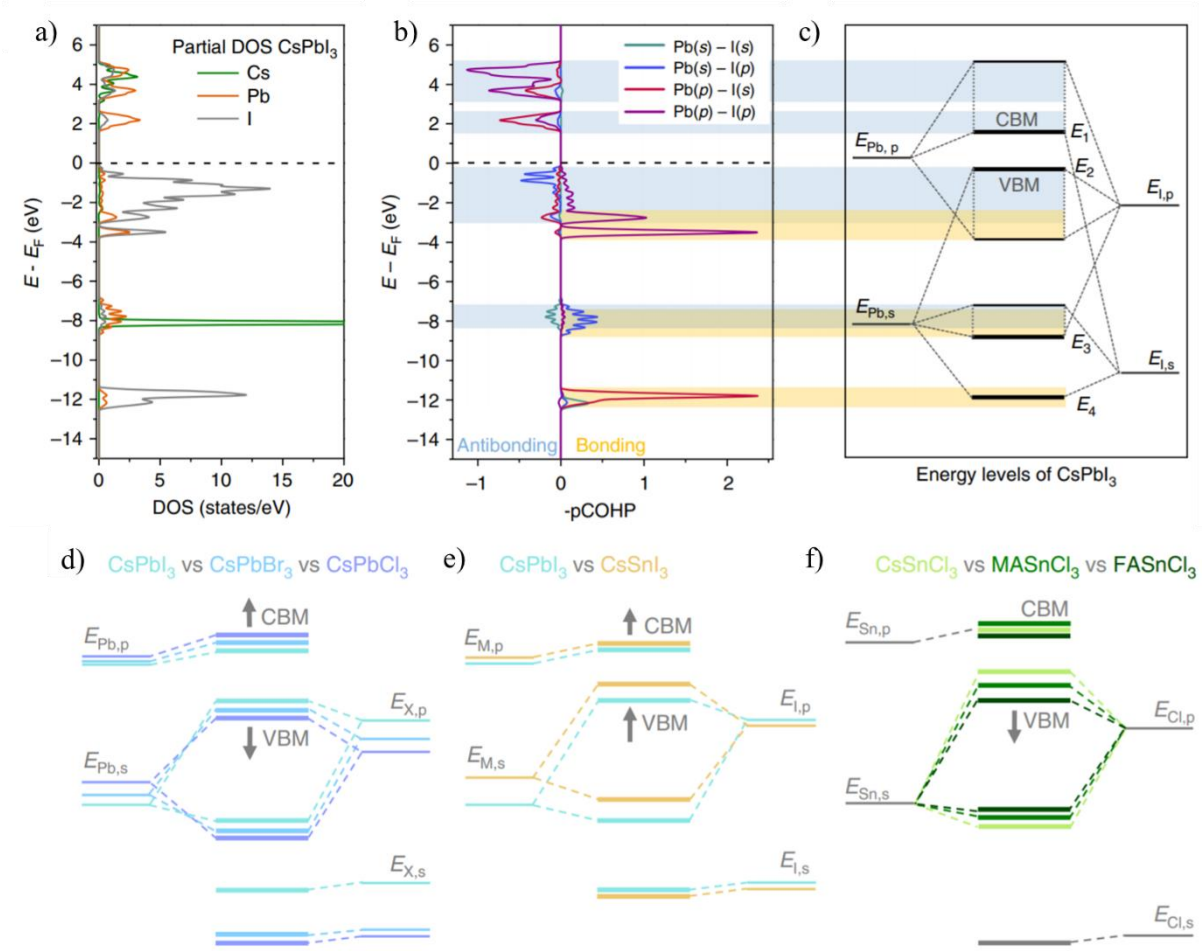

Figure 1-8. Orbital contributions to the energy bands of $CsPbI_3$. (a) Density of states (DOS) projected from Cs, Pb, and I atoms in $CsPbI_3$. (b) Orbital-resolved COHP color coordinated indicates which atomic orbitals are involved in the bonds (anti-bonds). (c) Schematic energy level diagram extracted from the COHP analysis; Bonding interactions are shaded in yellow, and anti-bonding interactions in blue. Energy level schematics for AMX_3 perovskites showing trends with changing (d) halide anions, (e) transition metal choice and (f) organic cation choice with arrows indicating shifts in energy levels.[36]

The inset in Figure 1-7a shows how photons with energies not above the band gap are not converted into electrical energy because of the thermalization of charge carriers or the recombination of excitons releasing heat energy. Taking this into account, 45% of the incident solar spectrum could still be converted for band gaps of 1.1-1.4 eV. This assumes that the cell operated at a voltage corresponding to the band gap energy and all active layer is able to fully capture all photons with an energy about the band gap, followed by full collection of generated carriers. This is an unrealistic maximum limit because the open-circuit voltage V_{oc} is always lower

than the band gap because the PV cell must be in equilibrium with its environment. This radiative carrier recombination represents a dark current that causes V_{oc} to be smaller than the band gap voltage V_g. The V_{mp} is also lower than the V_{oc} and the J_{mp} is lower than the J_{sc}. All these factors were accounted for by Shockley and Queisser for their Shockley-Queisser efficiency limit outlined in Figure 1-7b showing the limiting efficiency for a single-junction solar cell under one-sun. The maximum efficiency possible with this limit is 33.7% and corresponds to an E_g of 1.34 eV.

Relentless efforts have been made to narrow the band gap and broaden the light absorption coverage through compositional tuning. Due to the flexible nature of the crystallinity, a number of elements can serve in perovskite light absorbing materials while tuning the band gap. The perovskite band structure is primarily dependent on the transition metal and halide components. Figure 1-8 shows the valence and conduction band of $CsPbI_3$ with orbital contributions from Cs, Pb, and I atoms. The valence band maximum is primarily composed of Pb,s and I,p π antibonding orbitals while the conduction band minimum consists of Pb,p and I,s π antibonding orbitals.[36] The band gap, therefore, is directly determined by the $[MX_6]^{4-}$ structure. Although the A cation site does not contribute to the band-edge density of states, there are indirect influences that allow tailoring of the A site to change the crystal structure and band gap. Generally, larger cations in pure Pb perovskites push against the $[MX_6]^{4-}$ cage, increasing the X-M-X bond angle and affecting M-X bond length, increasing more orbital overlap and decreasing the band gap. This trend is flipped for pure Sn perovskites with larger cations increasing the band gap which is further discussed in Chapter 3.The M site has a direct impact on band gap and the smaller Sn cation has been shown to decrease the band gap when compared to pure Pb. Although the Sn-X-Sn bond increases the orbital overlap compared to the Pb-X-Pb bond resulting in a lower band gap, the mixed Pb-X-Sn bonds allow for spin-orbital coupling and the least distorted, more linear Pb-X-Sn

bond angles, result in the minimum band gap at 75% Sn.[37] The choice of X component also directly impacts the band gap with smaller halides increasing the band gap. The huge potential compositional range and structural versatility of hybrid perovskite allows for an exceptional range of functional properties such as optical, electrical, dielectric, magnetic, and charge storage.[28] These versatile material attributes of perovskites have not only been utilized in the PV field, but have been translated to numerous other applications such as batteries,[38] transistors,[39] photodetectors,[40] piezoelectrics,[41] light-emitting diodes,[42] and lasers.[43]

1.4.3 Device Fabrication Methods and Performance

During film synthesis, the hybrid perovskite maintains a low formation of energy, allowing for self-assembly from the molecular components in both solution and vapor state without complicated processing. Even the form of the perovskite layer is versatile and can be tuned from nanocrystals, polycrystalline thin films, and macroscopic single crystals by controlling the precursor composition and solution chemistry.[44] Numerous processing routes have evolved to produce high quality perovskite thin films for efficient solar devices and range from one-step solution deposition, which can employ additive incorporation, precursor engineering and an anti-solvent wash, two-step film deposition, which utilizes a first step metal halide complex following by an organic halide treatment, and vapor deposition, which can uses evaporation or chemical vapor deposition.[12]

Miyasaka et al. was the first to use 3D perovskite $CH_3NH_3PbX_3$ (X = Br, I) in dye-sensitized solar cells in 2009 with a max PCE of 3.8%.[45] These undesirable efficiencies were attributed to the ionic crystal and high solubility in polar solvents of the organolead halide perovskite affecting the stability in a liquid electrolyte-based sensitized cell. Park et al. showed how the $CH_3NH_3PbI_3$ perovskite had an absorption coefficient 10 times greater than that other comparable molecular

dyes and reported the first long-term stable PVSC with a PCE of 9.7%.[46] Snaith et al. fabricated the first non-sensitized PVSC with a mixed halide perovskite $CH_3NH_3PbI_{3-x}Cl_x$ coated Al_2O_3 with a PCE of 10.9%, demonstrating its viability as an active layer.[23] Over the course of a year, organolead halide perovskites achieved PCEs exceeding 15% and perovskite solar cell technology was named one of the biggest scientific breakthroughs of 2013 by the editors of *Science* and *Nature*.[47] There are still many ongoing investigations on the PVSC performance trying to surpass the record PCE of 25.2% as well as improve the stability of devices.

1.5 Instabilities of Hybrid Organic-Inorganic Perovskite Materials

PVSCs have a huge roadblock to overcome before large scale commercialization: instability. External factors such as temperature, pressure, light, humidity and the chemical environmental can strongly influence the functionality of the perovskite absorber layer as well as its material characteristics.

1.5.1 Perovskite Material Degradation

Due to its soft nature and structural flexibility, perovskites are sensitive to many compounds, but its reactivity with H_2O rends permanently hinders the perovskite material as an absorber layer. Pure lead perovskites come with instabilities that have hindered PVSCs commercialization. Due to the positive enthalpy of formation of $MAPbI_3$, it easily undergoes chemical reactions in ambient conditions and is degraded by water, oxygen, and light radiation, reverting the perovskite back to its precursors.[48,49] The mechanism for decomposition of the $MAPbI_3$ perovskite film when exposed to water is shown in Figure 1-9.[50] Walsh et al. proposed a

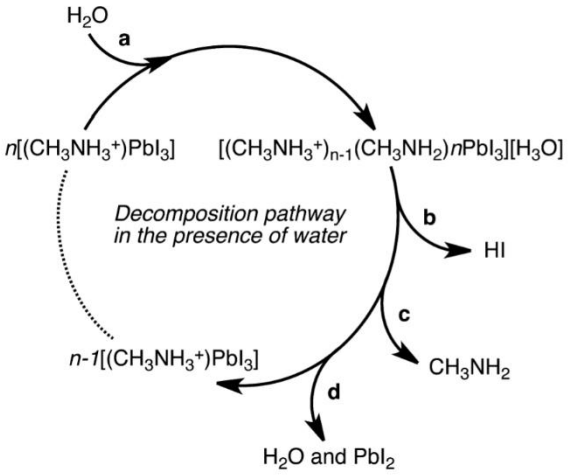

Figure 1-9. Possible decomposition pathway of hybrid halide perovskites with the presence of water with (a) the addition of H_2O, (b) the release of hydrogen iodide, and (c) the release of CH_3NH_2. (d) the removal of water-soluble lead.[50]

simple acid-base reaction deprotonating the organic cation allowing for a single water molecule to degrade the material with an excess required to dissolve the soluble byproducts HI and CH_3NH_2. In the presence of sufficient water, this pathway results in the formation of yellow, PbI_2 which has been previously experimentally observed.[50] This deprotonation reaction has also been shown to occur in air with the $MAPbI_3$ composition. Although this reaction and instability is less severe with other organic cations, it can still hinder a device's long term stability.[51]

A combination of O_2 and UV light has been shown to also initiate a severe degradation reaction with the formation of superoxide (O_2^-) and reaction of this component with organics in the perovskite material.[52] The O_2^- species result from photoexcited electrons interacting with molecular O_2. Efficient interfacial charge extraction is therefore crucial to mitigating these UV light and oxygen degradation pathways by eliminating the photoexcited electrons from interacting with oxygen for extended periods. Charges trapped at either the grain boundaries or interfaces also can induce a local electric field which can also result in deprotonation of the organic cations and permanently decompose the perovsite.[53] Carefully choosing or engineering ETL and HTL that facilitate charge carrier extraction can help prevent these instabilities. Interfaces between the

perovskite and both HTL and ETL also play a crucial role in PVSC device long-term stability and durability.

1.5.2 Device Instabilities

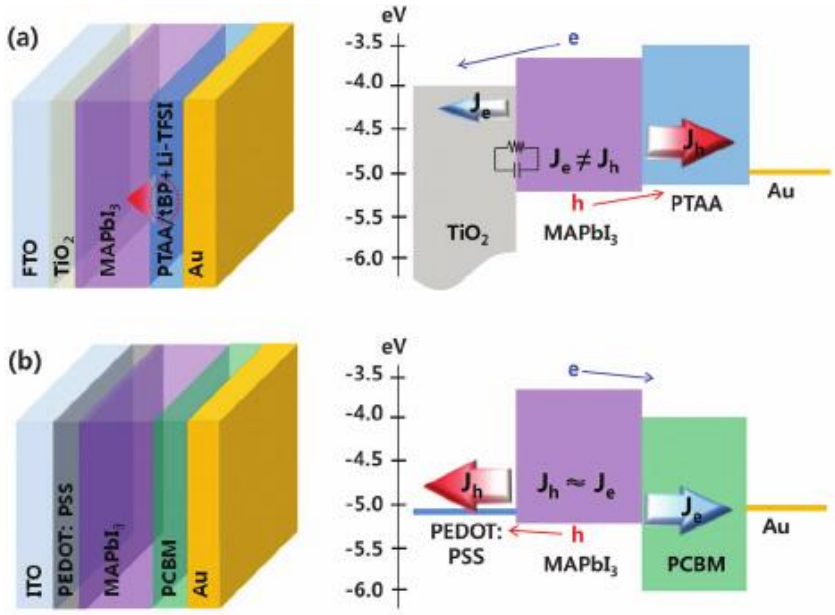

Figure 1-10. Schematic device architecture and band energy diagram of planar $MAPbI_3$ perovskite hybrid solar cells with (a) a conventional structure utilizing a PTAA hole transport layer and a TiO_2 electron transport layer and (b) an inverted structure utilizing a PEDOT:PSS hole transport layer an a $PC_{60}BM$ electron transport layer.[54]

Depending on the choice of interlayers and electrodes, reactivity with the perovskite active layer can result in PVSC instability. PVSCs typically utilize a glass substrate to hold the device stack consisting of the chosen perovskite absorber, sandwiched between the charge transport layers and a transparent and reflective electrode. Figure 1-10 illustrates the main conventional and inverted architectures for PVSCs.[54] The conventional architecture has been shown to increase efficiencies and is the architecture of the record breaking efficiency for PVSCs. This is the most common device architecture for PVSCs and has the configuration of mesoporous TiO_2/Perovskite/spiro-OMeTAD or PTAA/Au, the spiro-OMeTAD One potential instability occurs in the normal device structure when ETL TiO_2 is employed such as in Figure 1-10a. When

exposed to UV light, unoccupied deep surface trap states in the TiO_2 that are generated by a reaction between oxygen radicals and photo-generated holes induce oxidation in the perovskite layer. In lead perovskites, this results in the formation of PbI_2, resulting in increased recombination losses.[55] In tin based perovskites, this reaction directly oxidizes the Sn^{2+} to Sn^{4+}, resulting in recombination and eventually a photo-inactive material.[31] The use of mesoporous TiO_2 as an ETL also requires a high sintering temperature, which is unideal for mass manufacturing. Replacing TiO_2 with a ZnO ETL removes this photo-instability, but at high temperatures, such as those needed to anneal the perovskite layer, the basicity of ZnO results in a deprotonation reaction of the organic cation, similar to that of water, decomposing the perovskites to PbI_2.[56] The HTL in the conventional architecture also uses dopants such as lithium bis(trifluoromethylsulfonyl)imide salt and 4-tert-butylpyridine to better align the spiro-OMeTAD work function with the active layer, facilitating hole extraction. These dopants have been shown to be reactive and introduce further instability to lead-free Sn-based perovskites in inert conditions.[31]

The low temperature fabrication of the inverted structural PVSCs allows for adaptation to roll-to-roll processing, lowering manufacturing costs, improving intrinsic device stability, and lowering current density-voltage (J-V) hysteresis.[57] The inverted architecture (Figure 1-10b) alternatively has a HTL of Poly(3,4-ethylenedioxythiophene):poly(styrenesulfonate) (PEDOT:PSS) and ETL of $PC_{60}BM$. PEDOT:PSS (chemical structure shown in Figure 1-11) is a polymer electrolyte that contains a saturated, negatively charged PSS and a conjugated positively charged PEDOT component. The PSS polymer surfactant helps disperse and stabilize PEDOT in solvents, making PEDOT:PSS highly conductive and it has been previously employed in organic photovoltaics, organic light-emitting diodes, and organic field transistors.[58]

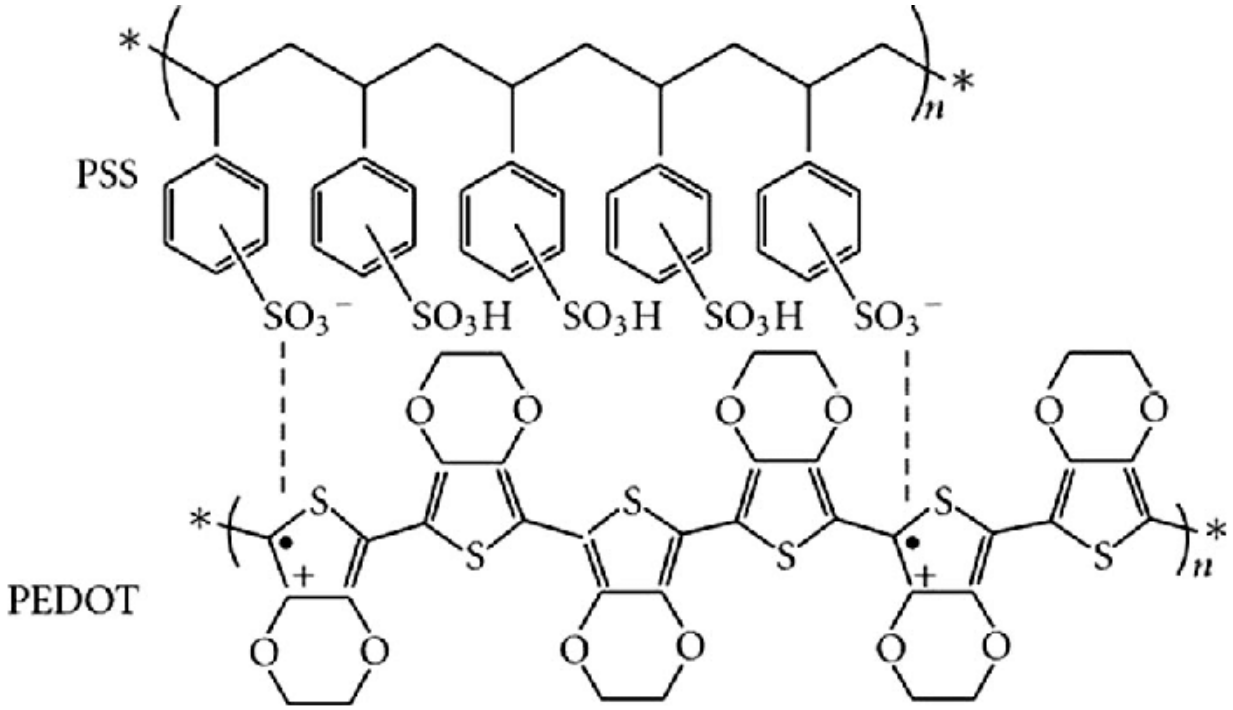

Figure 1-11. Chemical structure of PEDOT:PSS.[58]

1.5.3 Efforts to Reduce Pb-Perovskite Toxicity with Sn Replacement and Sn Oxidation

The lead in the high performing PVSCs is water soluble and can lead to ecotoxicity and human toxicity increases. Figure 1-12 illustrates how both the conventional and inverted architectures lead to these environmental impacts mainly during the fabrication of the lead-based perovskite layer.[59] To reduce environmental toxicity of lead based PVSCs, tin was investigated as a replacement due to its similar electronic configuration as a group 14 metal and the ability to form a MX_6 octahedron necessary for the cubic structure.[60] The comparable ionic radius, Sn^{2+} (1.15 Å) and Pb^{2+} (1.19 Å), allows for minimized tolerance factor differences, optimizing cubic α-phase stability.[12] Sn-based perovskites also have the benefit of lower band gaps by forming Pb-Sn binary alloyed perovskites, such as $MAPb_{0.3}Sn_{0.7}I_3$ that reaches the minimum band gap of 1.17 eV.[61–63] Combining the transition metal tuning with the halide tuning has recently created an ideal band

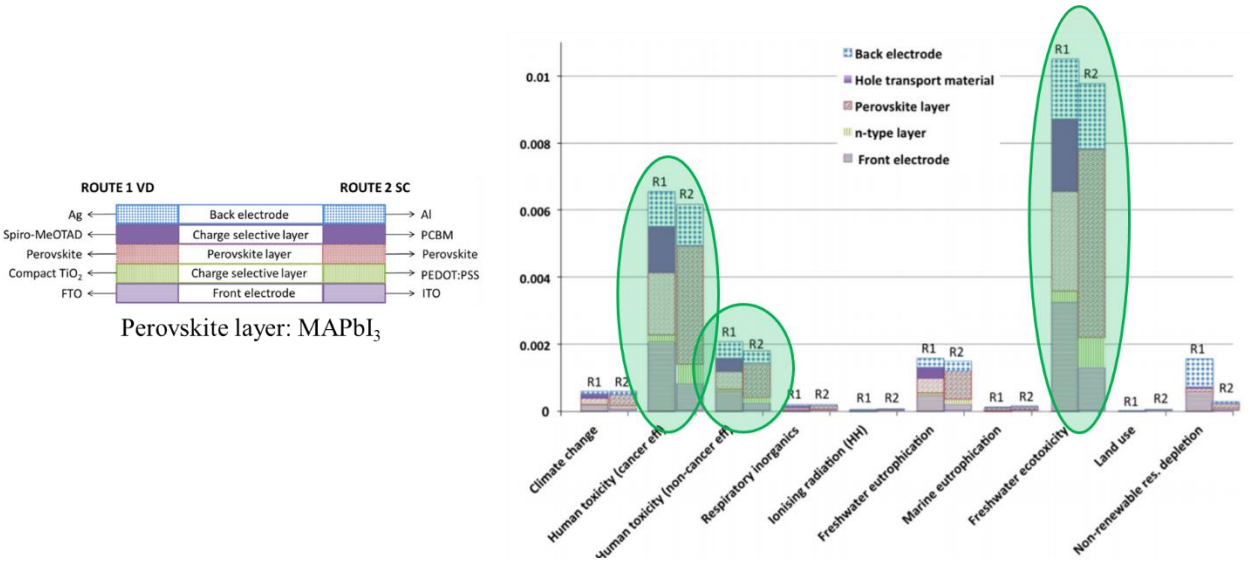

Figure 1-12. Normalized environmental impacts of production of both the inverted and conventional solar architectures.[59]

gap of 1.35 eV for $MAPb_{0.5}Sn_{0.5}(I_{0.8}Br_{0.2})_3$) perovskites that can lead to a theoretical Shockley Queisser efficiency of 33%.[64] Unfortunately, crystallization and stability of high Sn-containing perovskites have impeded the progress of Sn-based PVSCs. The reaction between MAI and SnI_2 is recognized to be faster than PbI_2 due to the greater Lewis acidity of Sn^{2+} versus Pb^{2+}, resulting in uncontrollable crystallization during solution processing.[65] $MASnI_3$ perovskites are, therefore, prone to poor film coverage with micron sized pinholes limiting device performance without solvent or deposition engineering. Solvent engineering has been used to improve the morphology of pure Sn perovskites such as perovskite films using N,N-dimethyl sulfoxide (DMSO) solvent to form $SnI_2{\cdot}3DMSO$ complex intermediate phase which resulted in pinhole free $MASnI_3$. This intermediate phase allows the MA^+ ions to react with SnI_2 in a controlled manner where the rate-limiting step is the removal of DMSO through thermal annealing.[66] Co-solvents have also been used in a one-step solution thin film formation method using γ-butyrolactone (GBL):DMSO co-solvents to dissolve precursors combined with an anti-solvent toluene wash step to further control crystallization rates, which resulted in pinhole-free perovskite films and allowed for high

performance for $MA_{0.5}FA_{0.5}Pb_{0.75}Sn_{0.25}I_3$ PVSCs[67] Sn-containing PVSCs also have been shown to degrade from the oxidation of Sn^{2+} to the more thermodynamically favored Sn^{4+}, even in inert atmospheres, due to the small formation energy and relatively weak inert pair effects.[65] McGehee et al. were propose the following mechanism for the degradation of Sn-based perovskites in air:[68]

$$2FASnI_3 + O_2 \Rightarrow 2FAI(s) + SnO_2 + SnI_4\ (g)$$

$$\Rightarrow\ 2FAI(g) + SnO_2 + SnI_4\ (g)$$

The high levels of self-p-doping caused by Sn^{4+} limit the diffusion length for charge carriers. To reduce the oxidation of Sn^{2+}, SnF_2 was first added in making $CsSnI_3$ perovskite thin films to fill Sn vacancies with extra Sn^{2+} ions, suppressing Sn^{4+} centers as well as reducing Sn^{4+} back to a divalent metal. [16,69,70] Attempts have since been made to utilize SnF_2 as a reducing agent to improve the performance of high Sn materials, but even with this additive, pure Sn perovskites begin to degrade after less than a month in ambient conditions.[11] Also, excess SnF_2 has been shown to form separated phases and phase segregation on perovskite film surfaces over time. Excess SnI_2 has been shown to be effective in preventing Sn oxidation by both compensating and suppressing Sn^{2+} vacancies without having any adverse side effects on phase stability and phase segregation. Previous research has argued that excess SnI_2 may even be more effective than SnF_2 as a reducing agent since the latter does not dissociate easily in film because of low solubility and stability.[11]

1.6 Objectives and Goals

The encompassing goal of this work is to explore new perovskite materials, additives, and devices designs that add to the collective knowledge of the perovskite material and photovoltaic community. Improving Sn based perovskite film, device performance, and stability has been a focal point of this work. Further exploring established compositional tuning effects and film

morphology engineering while extending them to high Sn perovskite films has allowed us to transition our expertise to lead-free films. Taking advantage of known lattice defects to better integrate additives in pure Sn perovskite films opens new avenues for highly stable films with minimal recombination. Finally, investigating the surrounding transport layers, focusing on improved band alignment, and decreasing energy loss in pure Sn devices has the potential to bring lead-free perovskite performance to new heights. This work is a comprehensible exploration of Sn based PVSCs and provides insight, new routes, and ideas to record breaking performances and stabilities in the future. The objectives of this research include:

1. Create a compositional library of $Cs_x(MA_{0.17}FA_{0.83})_{1-x}Pb_{1-y}Sn_y(I_{0.83}Br_{0.17})_3$ perovskite thin films mapping the various effects of cation and transition metal tuning on film morphology, crystallinity, band gap, photovoltaic parameters, and stability.
2. Explore lattice defect and relaxation through cation tuning to integrate stabilizing additives to pure Sn perovskites, further improving performance and stability.
3. Design and develop transport layers tuned for pure Sn perovskite devices while understand their effect on V_{OC} and energy losses before finally incorporating with the tailored Sn films for high efficiency and stability lead-free perovskite devices.

CHAPTER TWO: EXPERIMENTAL PROCEDURES AND FUNDAMENTALS

In this chapter, the methods for fabricating the perovskite films and the devices are described. The fundamentals behind the analysis, equations used, and instrumentation will also be discussed

2.1 Materials

For perovskite synthesis, the following materials were purchased. Lead (II) iodide (PbI_2, 99%), tin (II) iodide (SnI_2, 99.99%) , lead (II) bromide ($PbBr_2$, 99.999%), cesium iodide (CsI, 99.999%), rubidium iodide (RbI, 99.9%), guanidinium iodide (GAI, >99%) tin (II) fluoride (SnF_2 99%), toluene (anhydrous, 99.8%), chloroform (≥ 99.99%), ɣ-butyrolactone (GBL, ≥ 99%), N,N-dimethyl sulfoxide (DMSO, anhydrous, ≥ 99.9%), chlorobenzene (anhydrous, 99.8%), N,N-dimethylformamide (DMF, anhydrous, 99.8%) and bathocuproine (BCP, 96%) were purchased from Sigma-Aldrich (St. Louis, Missouri) without further purification. Methylammonium iodide (MAI), formamidinium iodide (FAI), guanidinium iodide (GAI) and formamidinium bromide (FABr) were purchased from Greatcell Solar (Queanbeyan, Australia) while ethylenediammonium diiodide ($EDAI_2$) was purchased from Millipore and used without further purification. The [6,6]-phenyl-C61-butyric acid methyl ester $PC_{60}BM$ (> 99.5%) and C_{60} (> 99.5%) were purchased from American Dye Solar (Quebec, Canada).

2.2 Perovskite Thin Film Synthesis

Plain glass was cut into 15 mm x 15 mm substrates, then were cleaned via ultrasonication for 15 min in detergent in Millipore deionized water, Millipore deionized water, acetone, and isopropanol in sequence. The substrates were treated with oxygen plasma under 100 W for 10 min.

2.2.1 Implementing the Triple Cation Double Halide in Perovskite Thin Film

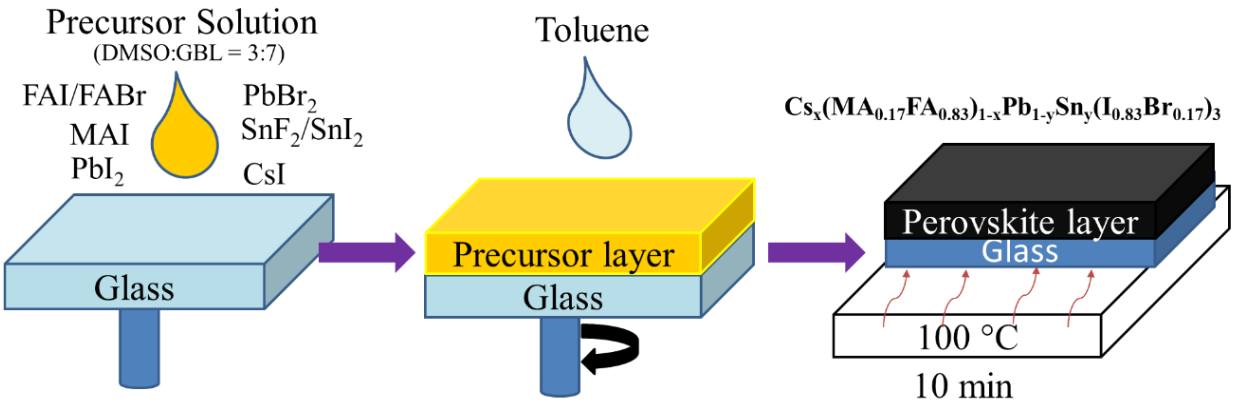

Figure 2-1. General perovskite thin film synthesis for $Cs_x(MA_{0.17}FA_{0.83})_{1-x}Pb_{1-y}Sn_y(I_{0.83}Br_{0.17})_3$ to be discussed in Chapter 3 with precursors mixture, using FAI, FABr, $PbBr_2$, MAI, PbI_2, SnF_2, SnI_2, CsI in DMSO and GBL at a volume ratio of 3:7, an anti-solvent wash using toluene, and annealing at 100°C for 10 min.

In order to fabricate $Cs_x(MA_{0.17}FA_{0.83})_{1-x}Pb_{1-y}Sn_y(I_{0.83}Br_{0.17})_3$ perovskites, the perovskite precursor solutions were made by dissolving MAI, FAI, PbI_2, $PbBr_2$, SnI_2, and FABr, at the corresponding molar ratios in GBL and DMSO (volume ratio 7:3) with a total concentration of 2.5 M. A 10 mol% SnF_2 per molar weight of SnI_2 was added in the precursor solution as a reducing agent. CsI and RbI was dissolved in DMSO at a concentration of 1.5 M and added to the precursor to achieve the correct triple cation composition. Figure 2-1 illustrates the general thin film synthesis procedure. The precursors were mixed at 60 °C for 1 h and were filtered through a 0.2 µm PTFE filter before use. A 70 µL drop of precursor solution was spin-coated on a cleaned glass substrate at 500 rpm for 5 s, 1000 rpm for 15 s, and 4000 rpm for 40 s in a nitrogen glove box. A toluene anti-solvent was *in situ* dripped onto the substrate during the last 15 s of the third spin-coating step. The volume of the anti-solvent was decreased from 800 to 700, 600, and 500, µL for $Cs_x(MA_{0.17}FA_{0.83})_{1-x}Pb_{1-y}Sn_y(I_{0.83}Br_{0.17})_3$ perovskites with x = 0.05, 0.10, 0.15, and 0.20, and y = 0, 0.25, 0.5, 0.75 and 1.0, respectively. The perovskite films were then thermally annealed at 100 °C for 10 min except for

$Cs_{0.1}(MA_{0.17}FA_{0.83})_{0.9}Sn(I_{0.83}Br_{0.17})_3$ and $Cs_{0.2}(MA_{0.17}FA_{0.83})_{0.8}Sn(I_{0.83}Br_{0.17})_3$ which were thermally annealing at 110 °C for 10 min.

To improve the pure Sn, $Cs_x(MA_{0.17}FA_{0.83})_{1-x}Sn(I_{0.83}Br_{0.17})_3$, perovskite morphology, concentration, solvent mixtures and ratios, annealing temperatures and times were optimized. The perovskite precursor solutions were made by dissolving MAI, FAI, FABr, and SnI_2 at the corresponding molar ratios in DMF and DMSO (volume ratio between 5:5 to 4:1) with a total concentration of 1 M and 2.5 M. A 10-20 mol% SnF_2 per molar weight of SnI_2 was added in the precursor solution as a reducing agent. The precursors were mixed at 60 °C for 1 h. CsI was dissolved in DMSO at a concentration of 1.5 M and added to the precursor to achieve the correct triple cation composition. A 70 µL drop of precursor solution was spin-coated on a cleaned glass substrate at 500 rpm for 5 s, 1000 rpm for 15 s, and 4000 rpm for 40 s in a nitrogen glove box. A 300-700 µL toluene anti-solvent was *in situ* dripped onto the substrate during the last 15 s of the second spin-coating step. The perovskite films were then thermally annealed at 70-120 °C for 10-20 min.

2.2.2 Introduction of Guanidinium, Cesium, and Ethylenediammonium in $FASnI_3$

In order to fabricate $(CsGA)_xFA_{100-2x}SnI_3$ perovskites, the perovskite precursor solutions were made in N_2 glove box by dissolving FAI and SnI_2, at the corresponding molar ratios in pure DMSO with a total concentration of 2.0 M. A 10 mol% excess SnI_2 was added in the precursor solution to reduce vacancies. CsI, GAI, and $EDAI_2$ were dissolved in separate vials of DMSO at a concentration of 1.5 M and added to the precursor to achieve the correct triple cation composition. For the $(CsGA)_{15}FA_{70}SnI_3$ composition with 1% $EDAI_2$ example, 0.1204 g of FAI and 0.4098 g SnI_2 were dissolved in 850 µl of DSMO and stirred at 60 °C for 0.5 h. 100 µl of the 1.5 M solution of CsI and 100 µl of the 1.5 M solution of GAI was added to the precursor and continued to stir at

60°C for 0.5 h. 14 µl of the 1.5 M solution of $EDAI_2$ was finally added to the precursor solution and stirred overnight at room temperature. The precursor solution was then filtered through a 0.2 µm PTFE filter before use. A 70 µL drop of precursor solution was spin-coated on a cleaned glass substrate at 500 rpm for 5 s, 1000 rpm for 15 s, and 4000 rpm for 40 s in a nitrogen glove box. A chlorobenzene anti-solvent of volume 500 µL was *in situ* dripped onto the substrate during the last 15 s of the third spin-coating step. The perovskite films were then thermally annealed at 110°C for 10 min.

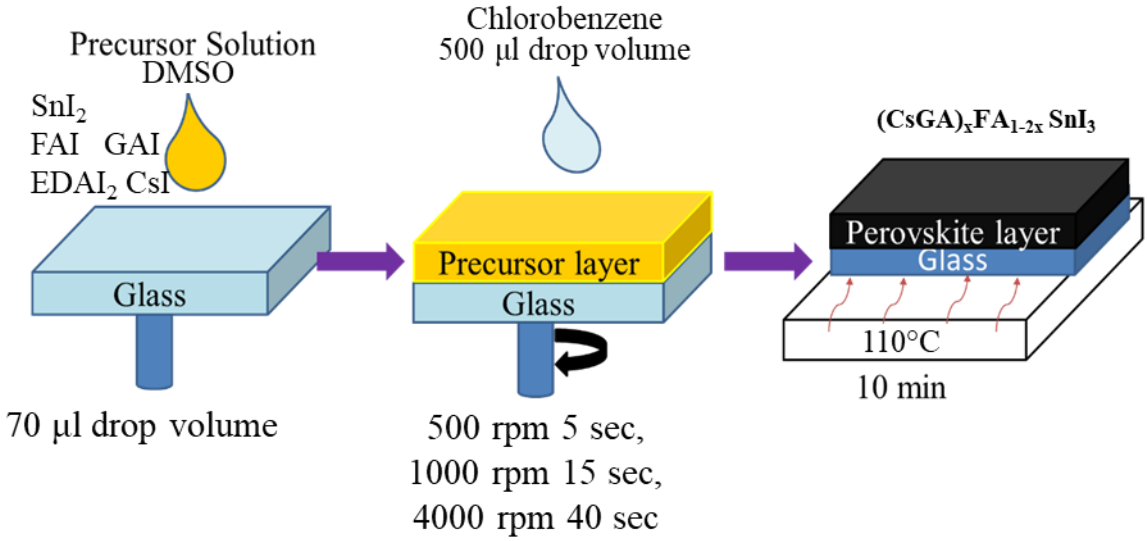

Figure 2-2. General perovskite thin film synthesis for $(CsGA)_xFA_{1-2x}SnI_3$ in Chapter 4 project with precursors mixture, using FAI, SnF_2, SnI_2, GAI, $EDAI_2$, CsI in DMSO, an antisolvent wash using chlorobenzene, and anneal conditions at 110°C for 10 min.

2.3 Characterization of Perovskite Thin Films

2.3.1 Probing the Morphology of Perovskite Films

Formation of the perovskite thin film is a pivotal fabrication step for PVSCs and a major determinant of the morphology. Controlling nucleation and crystal growth can be done on the macroscopic and microscopic level through interfacial engineering. In our case, nucleation is determined by the interfacial free energy and the wetting contact angle of the HTL surface or substrate below. Thus, nucleation increases with increased wettability which can be achieved

through increased hydrophobicity of the bottom layer since the perovskite precursor utilizes polar solvents. Keeping this in mind while treating the PEDOT:PSS layer in Chapter 5 will help the formation of uniform, crystalline perovskite films. Wettability issues can also be alleviated with the deposition of a hot precursor solution which is applied in Chapter 4, allowing for more uniform coverage.[71] At the macroscopic level, dense, smooth perovskite films with large coverage is crucial to prevent device performance by minimizing electrode shorting. Scanning electron microscopy (SEM) can be utilized to study the macroscopic level of the perovskite film and morphology. SEM images were acquired using FEI Sirion SEM operated at 5 kV to observed surface morphology and extract grain size information and the definition and width of grain boundaries. Figure 2.3 shows a schematic with the principle of the SEM.[72] The microscope column and specimen chamber are placed under vacuum to evacuate atmosphere with both prevacuum and high-vacuum pumps

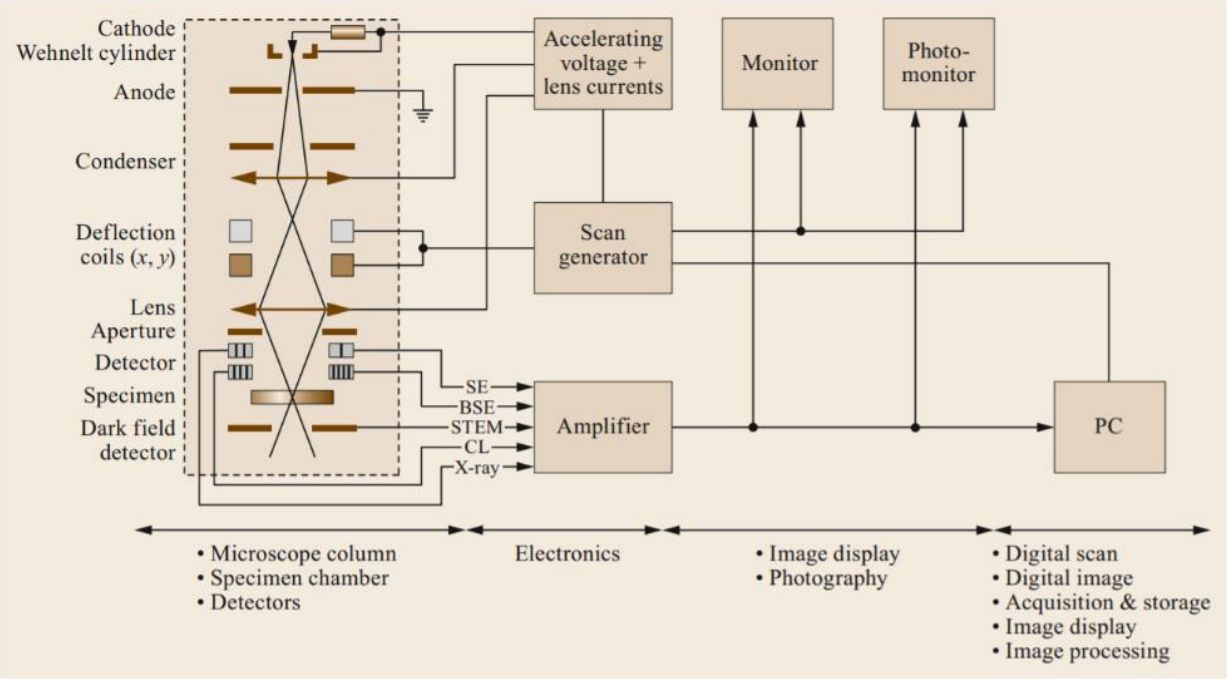

Figure 2-3. Schematic drawing of conventional SEM showing the specimen chamber and detectors, electronics to amplify and interpret the signal, and the final digital image product.[72]

until 10^{-4} PA is reached, which allows the beam electrons to travel from the cathode to the specimen with minimal interactions with gas molecules.

During characterization, the cathode emits beam electrons that are accelerated by a voltage between the cathode and anode, creating a beam cross section. The beam cross section occurs near the anode and has a diameter between 10-50 μm, which is too large of a spot size to result in a sharp image. The cross over is demagnified by the lenses, allowing a smaller spot size of 5-10 nm and ensuring the signals generated by impinging beam electrons are collected by the detectors. Because microstructures of perovskite films and solar devices can have dimensions from micron to nanoscale, the SEM's tremendous focus and range is essential for characterization. Figure 2.4 shows the types of signals generated by the impinging high energy electron beam with electrons marked by solid arrows and photons marked with dashed arrows.[73] The most common signals used for imaging in SEM are secondary electrons (SE) and backscattered electrons (BSE). The SE result from fast incoming electrons that supply energy to atomic electrons until they are released. Only surface SE escape into vacuum for collection making SE useful for topography of the sample. BSE signal is dependent on the atomic number of the material allowing it to be utilized for elemental

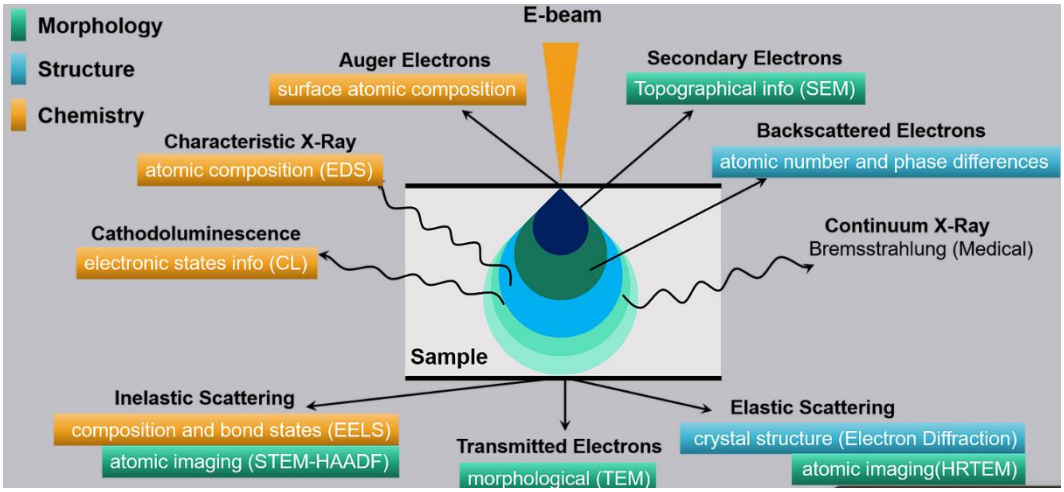

Figure 2-4. Schematic drawing of signals for a thin sample generated by impinging electrons.[73]

distribution. SE and BSE detectors have been widely used in perovskite surface morphology and cross section analysis, helping to optimize fabrication methods for both film and devices.[74]

The characteristic x-rays signals result in energy dispersion spectroscopy (EDS) testing. EDS was acquired using FEI Sirion SEM operated at 15 kV to gain elemental compositions of perovskite thin films over time to observe the composition of segregation impurities. The incident electron beam in the SEM can further excite individual electrons to quantum states of higher energy and the detected X-rays result from energy changes that is atomic species specific. EDS can thus be used to determine the chemical composition of certain spots on the perovskite film.

Tapping-mode atomic force microscope (TM-AFM) measurements were used to study the morphology of PEDOT:PSS and determine segregation of PEDOT and PSS segments. TM-AFM utilizes a probe in resonant mode so the tip and sample are only intermittently in contact. AFM was performed on a Digital Multimode AFM equipped with a Nanoscope IVa controller to study the film morphologies under ambient conditions

2.3.2 Crystal Structure Characterization

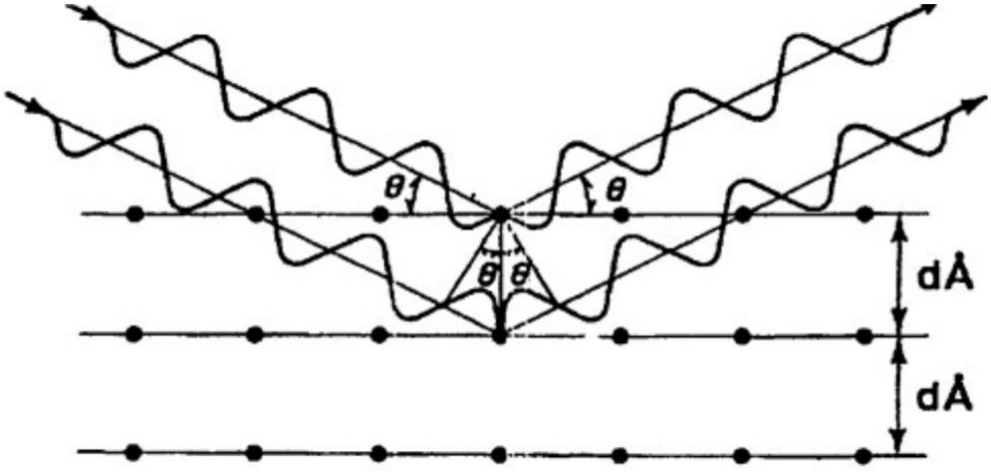

Figure 2-5. Illustration of how diffraction of x-rays by crystal plans allows derivation of lattice spacings using Bragg's Law.[75]

Looking at the microscopic scale, orientation of grains and crystal structure impact the trap state density, charge carrier mobilities, and lifetimes of the perovskite film and influence the ability to act as an absorber layer. Different crystal states and facets have a correlation with various trap states, directly impacting the PV efficiency in PVSCs.[75] Two-dimensional X-Ray diffraction (XRD) can be used to study the microscopic layer through orientation of grains and crystal structure. XRD utilizes the elastic scattering of x-ray photons by atoms in a periodic lattice. When the x-rays are a smaller size then the crystalline lattice parameter, it reflects off into a thumbprint spectrum which can be matched to a crystalline phase. Figure 2.5 illustrates how diffraction of x-rays can be used to derive lattice spacing.[76] Bragg's law is as follows:

$$n\lambda = 2d\sin\theta \qquad 2.1$$

where n in the order of reflection, λ is the wavelength of the x-rays, d is the spacing between the crystal planes of the sample, and θ is the angle between the incident beam to the normal to the reflecting lattice plane. The interplanar spacing, d, of the crystallographic phase can be determined

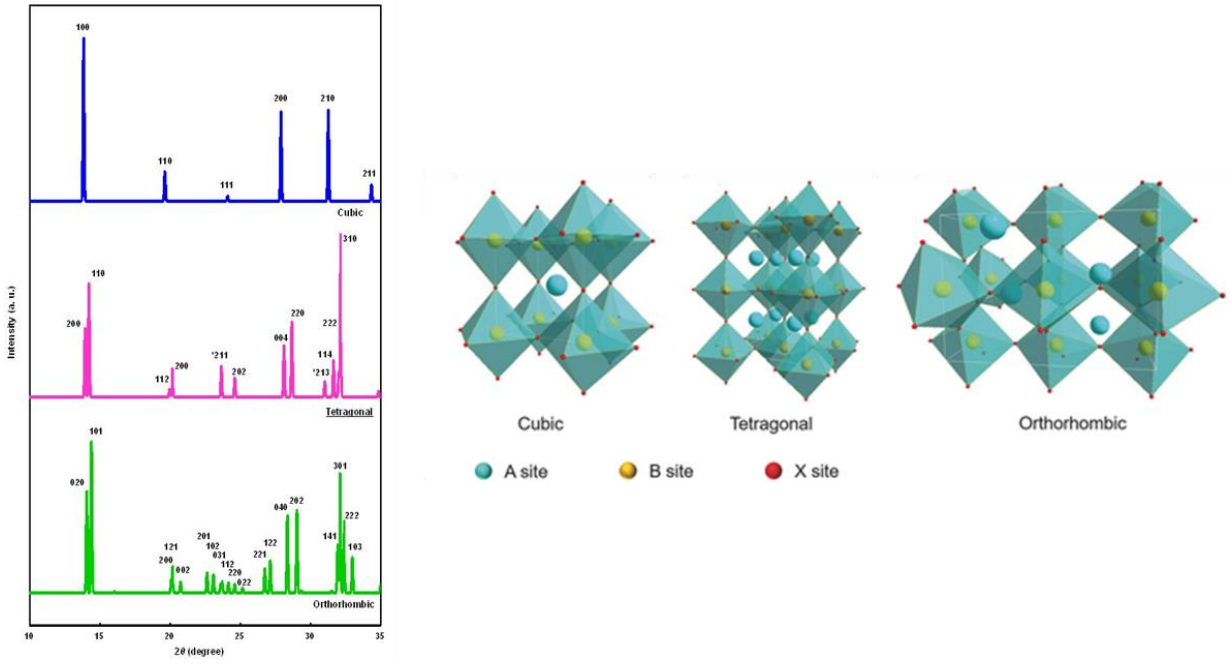

Figure 2-6. Simulated XRD patterns showing peak indices for the cubic phase, tetragonal phase, and orthorhombic phase of AMX_3 perovskite along with the corresponding crystal structure.[76,77]

by measuring the angles where the x-rays leave the crystal. The x-rays therefore can only be used for crystalline structures and will not bounce off of amorphous phases, allowing the crystallinity of the perovskite samples to be analyzed. For perovskite compositions, the phases can be the preferred cubic crystalline structure, tetragonal or orthorhombic. Although perovskite phases can be predicted through tolerance factor calculations, the soft nature of the perovskite can result in temperature related phase changes such as $MASnI_3$ transitioning from a α-cubic black phase to a tetragonal phase at 330 K and again to a nonperovskite yellow δ orthorhombic phase at 161 K which does not allow for efficient carrier generation or transport.[77] Figure 2-6 shows the AMX_3 simulated peak indices for the cubic phase, tetragonal phase, and orthorhombic phase along with the corresponding crystal structure.[78,77]

XRD patterns were collected with Bruker GADDS D8 Focus Powder Discover diffractometer using Cu Kα radiation (λ = 1.5419 Å) and the data was processed using the EVA package provided by Bruker Axs to investigate crystalline structures, impure phases, and lattice parameter size shifts of perovskite thin films. The lattice parameters can then be calculated for the cubic perovskites that are in Chapter 3 and Chapter 4 using the cubic d spacing equations and peak indexes and Bragg's Law on the (100) diffraction peak:

$$\frac{1}{d_{hkl}^2} = (h^2 + k^2 + l^2)\frac{1}{a^2} \quad 2.2$$

$$n\lambda = 2dsin(\theta) \quad 2.3$$

At the (100) peak, the d spacing is equal to the lattice parameter. The d spacing and lattice parameter trends can be used to determine whether dopants, organic cations, and halides have been successfully integrated into the crystal lattice. With the integration of a larger organic cation, there

would be a left shifted XRD peak, resulting in a larger d spacing and lattice parameter, helping probe the composition of the perovskite.

2.3.3 Chemical Composition Characterization

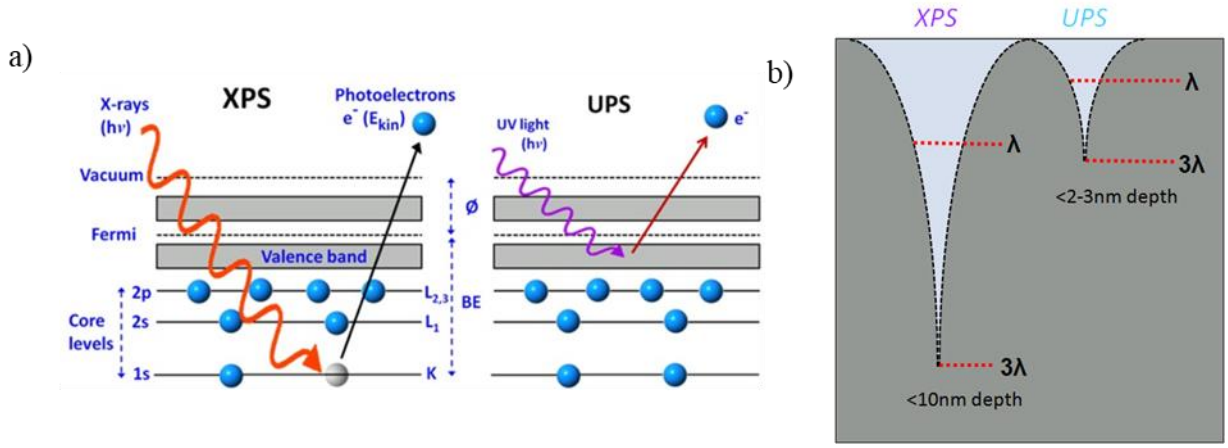

Figure 2-7. (a) Comparison of XPS and UPS source and what information can be explored in each method (b) depth of analysis comparison.[78]

X-ray photoelectron spectroscopy (XPS) was used to determine real chemical compositions of the perovskite surface as well as oxygen increased affinity for high Sn perovskites. Figure 2-7a compares the XPS and ultraviolet photoelectron spectroscopy (UPS) source vs what information can be explored in each method while Figure 2-7b illustrates the depth of analysis. For XPS, the x-rays are able to dislodge core electrons to provide chemical environment information about the composition, such as oxidation states, and surrounding atoms. The depth of the XPS is also larger than the UPS, reaching 10 nm rather than 2-3 nm, giving information about the relative deeper surface composition of perovskites.[79]

XPS was performed on the Kratos AXIS Ultra DLD. The incident x-rays were monochromatized Al Kα radiation and the source was operated at 15 mA at 15 kV. The lens mode was set to hybrid, the aperture to slot, and the spectrometer pass energy was 80 eV. Data point spacing was 1.0 eV/step.

Raman Spectroscopy measurements were used to specifically used to study the chemical structure of the PEDOT:PSS hole transport layers in Appendix 1. The Raman scattering spectroscopy relies on inelastic scattering of photons (Raman scattering). The monochromatic radiation interacts with the sample and can be reflected, absorbed, or scattered. This scattered light from a molecular can have several components: Rayleigh scatter, Stokes scatter, and Anti-Stokes Raman scatter. The change in wavelength of the scattered photon can provide a chemical finger print that can determine changes in benzoid and quinoid structure of PEDOT polymer chains. Raman measurements were carried out on a Thermo Scientific DXR2 Raman Microscope to investigate the chemical structure of PEDOT:PSS. A 532 nm green laser with the laser power between 1-5 mW was illuminated and focused through a 50x objective lens onto the polymer thin films. Raman spectra were fitted using PeakFit with assumption of 50% Gaussian and 50% Lorentzian component peaks.

2.3.4 Electronic Structure Characterization

Ultraviolet-visible (UV-Vis) absorption spectra were collected using a Varian Cary 5000 UV-Vis-NIR spectrophotometer to collected electronic information about the material optical band gap. With UV-Vis spectroscopy, UV-Vis light passes through the sample and the transmitted light is measured. When the photon is absorbed by the sample that is a semiconductor consisting of a band gap, electrons are promoted from the valence band to the conduction band when they contain enough energy. When the semiconductor sample begins absorbing, the photons at least have the energy to cross the band gap, allowing analysis to determine band gap energy. UV-Vis spectra can also be used to determine the existence of trap states.[80] In terms of perovskite research, shallow trap states can occur closer to the valence band and conduction band, creating a less sharp cutoff for absorption. Some photons absorbed would thus not be the band gap.

Static photoluminescence (PL) spectra were obtained with a modified Horiba LabRAM HR-800 with 532 nm laser excitation and a Czerny−Turner monochromator blazed at 1200 nm and the PL results were used to confirm band gap trends. Measurements were conducted at 1 Sun above band gap equivalent photon flux with a 532 nm cw laser. The PL experiments were conducted in a N_2-filled KF flange with a borosilicate glass window. The exploration of band gap though PL is similar to UV-Vis, except instead of absorbing, the exciton relaxes back to the valence releasing a photon with the energy of the band gap. PL can also be impacted by trap states resulting in a broadening of peak since the released photon may be smaller due to an initial relaxation into a trap state. The intensity can also be impacted by non-radiative recombination due to defects and trap states.

UPS was implemented to explore the valence electrons and map the valence band maximum,and Fermi level, of the perovskite filmUPS uses low ionizing radiations to induce photoelectric effect and is limited to valence band region because most core level photoemissions are not accessible at these low energies. Figure 2-8b shows a typical UPS scan with the low kinetic energy cutoff, Fermi Level cutoff, and valence band area with the calculation for work function[81],

$$\Phi = h\mu - (E_{cutoff} - E_F) \qquad 2.4$$

where Φ is the work function, h is Planck's constant, μ is the frequency of the photon, E_{cutoff} represents the low kinetic energy cutoff, and E_F is the Fermi Level. Figure 2-8a shows how the UPS data is translated into different components for density of states. The electronic work function can be calculated by measuring the difference between the cutoff of the low kinetic energy and the Fermi Level. The Fermi Level's position of the material can be calculated through the valence

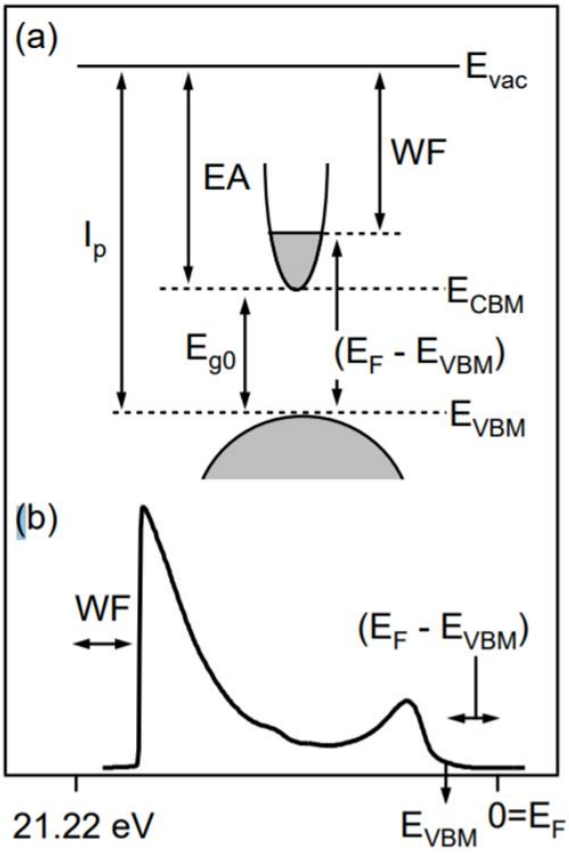

Figure 2-8. (a) Schematics of a band structure and (b) UPS spectrum with the ionization potential (I_p), electron affinity (E_A),. work function (WF), intrinsic band gap (E_{g0}), vacuum level (E_{vac}), conduction band minimum (E_{CBM}), valence band maximum (E_{VBM}), and Fermi level (E_F).[80]

band offset or (E_F – E_{VBM}). The valence band cutoff is utilized to determine the valence band maximum (E_{VBM}). UPS allows this calculation from a single spectrum. The fundamental band gap (E_{g0}) can be combined with the E_{VBM} to determine the conduction band level (E_{CBM}). For the following chapters, the band gaps observed through UV-vis and PL were used in combination with the determined valence band maximum to calculate the conduction band minimum to graph changes in energy bands with composition changes.

UPS was performed on the Kratos AXIS Ultra DLD X-ray photoelectron spectrometer to determine the valence band maximum. The incident radiation was the He I line 21.22 eV energy produced by a Kratos UV lamp. The lamp was operated at 10 W of power. The spectrometer was operated in UPS mode, pass energy 5 eV, aperture 100 um. Data point spacing was 0.01 eV/step.

Calibration was performed using a clean gold film. Data analysis was performed using CasaXPS software version 2.3.15.

2.4 Device Fabrication

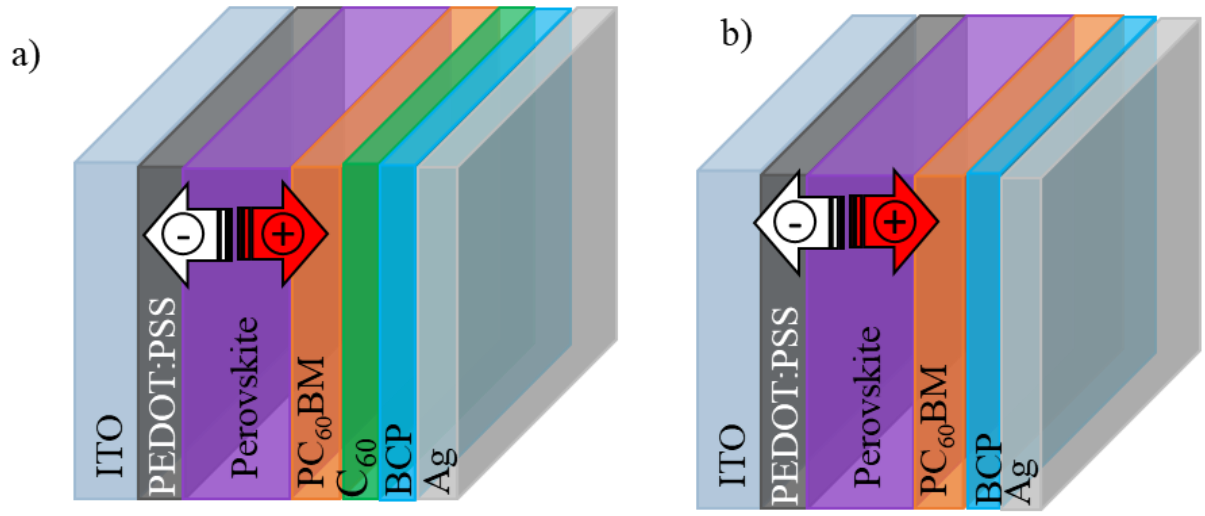

Figure 2-9. Device architectures that are adopted for studies in (a) Chapter 3 and (b) Chapter 4.

The interlayers for photovoltaic action establish a built-in electric field that acts as a driving force necessary for charge separation. Selection and fabrication of each layer in the device structure can help the competition between interfacial charge transfer and recombination processes, maximizing charge generation, separation, and transfer to create highly efficient devices. The fabrication method in the thesis works is as follows: ITO coated glass substrates (10 ohm/sq ITO, Colorado Concept Coatings LLC) were cut and cleaned with the methodology found in section 2.2. The PEDOT:PSS (Al 4083, Heraeus Clevios^{TM}) solution was filtered with a 0.45 µm nylon filter. A 70 µL drop of PEDOT:PSS was spin-coated on a cleaned ITO coated glass substrate at 5000 rpm for 60 s and annealed at 150^{o} C for 10 min in air. The substrates were transferred to a glove box and the perovskite thin films were fabricated through the process in section 2.2.1 or 2.2.2. A $PC_{60}BM$ solution (15 mg ml^{-1} in chloroform) was then spin coated on the

perovskite films at 4000 rpm for 60 s and dried without annealing in the glove box. For Chapter 3, the substrates were loaded into a thermal evaporation chamber to thermally deposit 20 nm of C_{60} and 8 nm of BCP. For Chapter 4, the C_{60} layer was not included and the BCP was instead dissolved in 2-propanol at a concentration of 0.5 mg/ml and spun onto the film at 4000 rpm for 60 s without annealing. Finally, a mask with 3.14 x 10^{-6} m^2 area holes was placed on the devices to evaporate 100-150 nm of silver for electrodes in a high vacuum evaporator (< 1 x 10^{-6} Torr). The resulting device structure is ITO/PEDOT:PSS/Perovskite/$PC_{60}BM$/C_{60}/BCP/Ag for Chapter 3 and ITO/PEDOT:PSS/Perovskite/$PC_{60}BM$/C_{60}/BCP/Ag for Chapter 4, which is illustrated in Figure 2-9.

2.5 Device Characterization

Photoinduced charge generation and extraction need to be analyzed to determine the health of the operation for PV devices. The priority of film and device fabrication and engineering is to minimize carrier losses and recombination while facilitating favorable charge dynamics. These potential carrier losses and charge dynamics in both the perovskite film and the interfacial contacts are illustrated in Figure 2-10. After photon absorption creates the exciton, the dissociation into electrons and holes and carrier transport is dictated by the hole and electron transport layers, assisting the collection of carriers to their respective electrodes. The transport layers should preferably have energy levels to best align with the absorber layer, high carrier mobility, and a wide band gap to minimize parasitic absorption as well as minimal defects to reduce non-radiative recombination and interfacial coupling to minimize accumulation losses. Interfacial optimization can help reduce trap-assisted non-radiative monomolecular recombination (e), back charge transfer recombination (h), recombination due to contact between transport layers (i), and interfacial trap state recombination (j). The photocurrent density-voltage (J-V) can help explore carrier transport

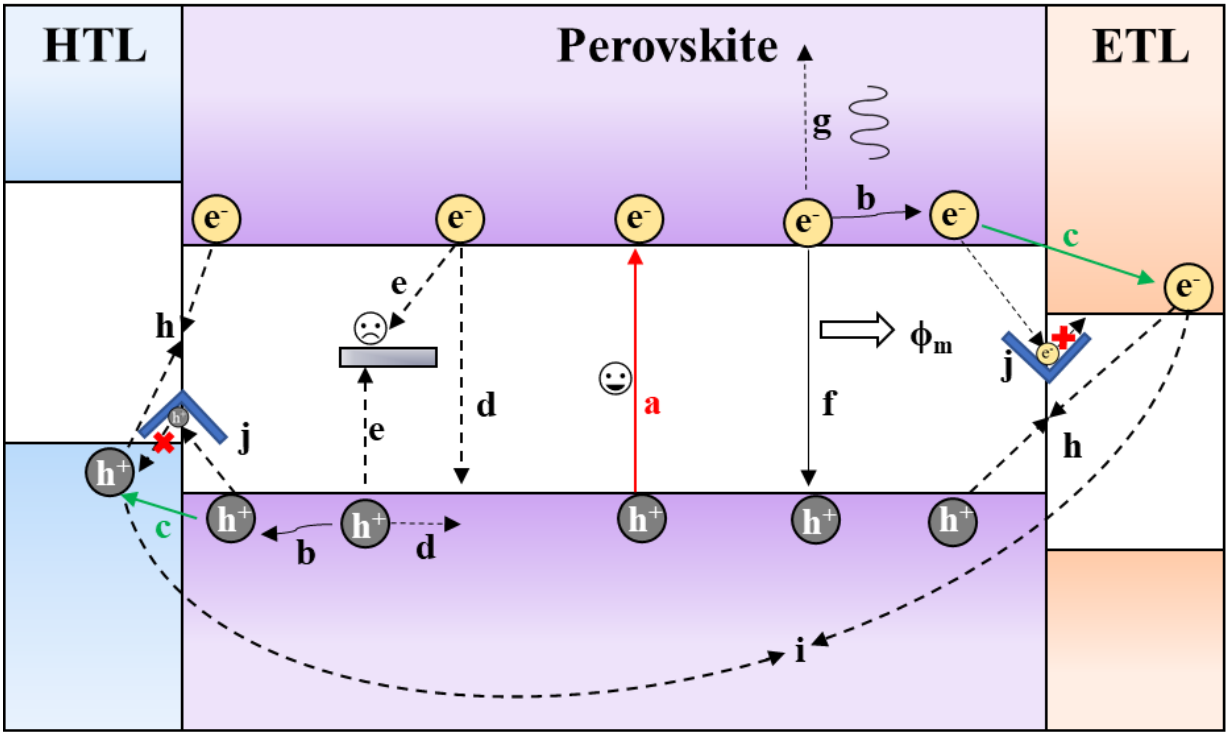

Figure 2-10. Recombination and charge transfer processes in a perovskite architecture. (a) Exciton generation which dissociates into free carrier holes and electrons. (b) Charge diffusion of carriers. (c) Injection of holes into HTL and electrons into ETL (d) Bimolecular recombination. (e) Trap-assisted monomolecular recombination (fostered by intrinsic defects and impurities.) (f) Radiative decay resulting in photoluminescence (ϕ_m = quantum yield for emission). (g) Auger recombination. (h) Back charge transfer at the interfaces. (i) Non-radiative charge recombination. (j) Surface recombination assisted by trap states at the interfaces and grain boundaries.

and recombination efficiencies. For PVSCs, V_{oc} is dependent on the band gap and charge carrier densities under illumination that influences quasi-fermi level splitting. Pure Sn perovskites are plagued by a low V_{oc} is that due to dominate non-radiative recombination processes, back charges at interfaces and interface recombination. At 100% radiative recombination, the thermodynamic limit for the V_{oc} is as follows:

$$V_{oc,rad} = \frac{k_B T}{e} In\left(\frac{J_{sc}}{e\phi_{em,0}} + 1\right) ; \phi_{em,o} = \int a(E)\phi_{BB}(E)dE \qquad 2.5$$

Where the radiative limit for V_{oc} is represented by V_{oc},rad, a(E) is the material absorption as a function of photon energy (E), and ϕ_{BB}(E) is the black body spectrum. The total V_{oc} can therefore be represented as:

$$V_{oc} = V_{oc,rad} - \Delta V_{oc,non\text{-}rad} \quad 2.6$$

$$\Delta V_{oc,non\text{-}rad} = \frac{k_B T}{e} InEQE_{EL}^{-1} \quad 2.7$$

Where non-radiative recombination losses are represented by $\Delta V_{oc,non\text{-}rad,}$ and the external voltage source (EQE_{EL}).[82] To maximize the V_{oc}, minimizing non-radiative recombination that occur from perovskite defects and interfacial contacts is crucial and can be done through transport layer tuning, defect passivation, and proper charge extraction. Transport energy level alignment specifically is key to minimize back charge carrier transfer recombination.

The J-V curve measurements were conducted in a N_2 glovebox with a Keithley 2400 Source Meter and a Solar Light Co. Xenon lamp (16S-300W) and AM 1.5G filter. Before measurements, the light intensity was calibrated to 100 mW cm^{-2} using a standardized National Renewable Energy Laboratory calibrated silicon solar cell. EQE measurements were performed in ambient conditions without encapsulation using a xenon lamp (Oriel, 450W) light source, a monochromator (Newport Cornerstone 130), optical chopper, lock-amplifier (Stanford Research Corp SR830), and finally a NIST-certified Si-photodiode (Thorlabs FDS 100-CAL) for calibration.

Series resistance (R_s) and shunt resistance R_{sh} were calculated with PV parameters by J-V curves This method utilizes the fact that the J-V curve at J_{sc} and V_{oc} are free from resistance effects. We can calculate series resistance using the equation outlined in 1963 by Wolf [4]:

$$R_s = \frac{(V_{oc} - V_{mpp})}{J_{mpp}} \quad 2.8$$

The shunt resistance uses the following:

$$R_{sh} = \frac{(J_{sc} - J_{mpp})}{V_{mpp}} \quad 2.9$$

2.6 Device and Film Stability Characterization

Due to the structural flexibility and soft nature of the perovskite films, material and device stability has hampered the promising commercialization potential of perovskite devices. In Chapter 3, perovskite thin films with the composition $Cs_x(MA_{0.17}FA_{0.83})_{1-x}Pb_{1-y}Sn_y(I_{0.83}Br_{0.17})_3$ were left in ambient condition for 10 days after initial analysis. For ambient condition studies, films were left outside of the glove box in darkness at humidity levels reaching 40%. Perovskites with bromide halides have previously shown segregation issues, so SEM images were acquired to gain surface morphologies and determine if there was segregation over time. EDS measurements were also conducted to determine composition of impurities that arose from air exposure. Because environmental degradation results in a lower crystallinity and potential phase changes, XRD patterns were collected to investigate crystalline structures of air exposed perovskite thin films. Transport layers can offer some protection to the perovskite degradation. For both Chapter 3 and Chapter 4, devices were studied in long term glove box stability tests. These studies had perovskite devices in the nitrogen glove box over the course of 30- 45 days with repeating J-V curve measurements to compare performance. Chapter 3 also had devices exposed to ambient conditions for 5 days after an initial 30 days of glove box storage with repeating JV curve to determine protection of device to the perovskite films and to compare device performance.

2.7 Conclusion

This chapter summarized the methodology, analysis techniques, and logic behind applied methods that will be used on the study of perovskite, and PEDOT:PSS films and devices in

Chapters 3, 4, and 5. For the perovskite films, morphology will be engineered to have minimal pinholes, dense coverage, and no segregation to minimize trap recombination. The crystallinity will be tested to ensure a cubic structure as well as confirming integration of the organic cation, transition metal, and halide choice. Energy band edges and band gap trends will be evaluated to better match transport layers for efficient carrier transport and minimize back charge and interface recombination. Devices will be fabricated and studied to show the effects of implemented changes on device performance and possible charge carrier recombination. Finally, stability in a nitrogen atmosphere and ambient conditions will be studied to determine if changes help not only the device performance, but intrinsic stability of the material, and ultimately, device short-term and long-term stability.

CHAPTER THREE: INORGANIC CATIONS AND COMPOSITION TUNING IN PHASE AND DEVICE STABILITY OF TRIPLE CATION PB-SN DOUBLE HALIDE PEROVSKITE FILMS AND SOLAR CELLS

3.1 Introduction

Significant scientific effort has been invested in creating a high efficiency solar material with a low-cost manufacturing process and hybrid organic-inorganic perovskites are an emerging material. The power conversion efficiencies of perovskite solar cells (PVSCs) have increased from 3% to 25.2% within the last decade and the unique properties have garnered much attention in an effort to reach record breaking PCEs.[9] Perovskite materials also can be synthesized with low energy intensive methods creating the potential for prices comparable to fossil fuels. However, many of the instabilities regarding phase changes and degradation have limited this materials potential towards commercialization. The most efficient perovskites also contain a toxic Pb element as the metal cation making them less desirable for mass-manufacturing due to the potential environmental and health hazards.

Pure cation perovskites such as $CsPbI_3$, $FAPbI_3$, $MAPbI_3$ have been shown to phase change from a favorable cubic phase to a less favorable phase, resulting in lower PCEs, and instability in ambient conditions.[26,83,84] Snaith and coworkers were first able to show how to introduction of Cs in a mixed cation, halide system could stabilize phase instabilities and maintain high PCEs with their $FA_{0.83}Cs_{0.17}Pb(I_{0.6}Br_{0.4})_3$ single junction solar cell reaching a maximum PCE of 17.1%.[85] Grätzel's group further introduced Cs to the A-site and demonstrated a device performance of 21.1% PCE with improved stability in ambient conditions for the $Cs_{0.05}(MA_{0.17}FA_{0.83})_{0.95}Pb(I_{0.83}Br_{0.17})_3$ PVSCs, which was attributed to the smaller Cs^+ (1.67 Å) and MA^+ (2.16 Å) ions "pushing" the larger FA^+ (2.53 Å) ion into the black cubic α-phase.[22] Although the influence of these mixed cation systems on pure Pb perovskites have been studied extensively, the stabilizing effects of tolerance on Pb/Sn mixed systems and pure Sn perovskite solar cells have been

unexplored. This gives rise to our strategy of using triple Cs/MA/FA cation with mixed Br/I halide to stabilize 25-75% Sn PVSCs.

Although Sn perovskites can achieve a theoretical PCE limit of 30-31%, calculated using the Shockley-Queisser limit, the inevitable optical and electrical losses further lower experimental PCEs and these high-performance devices with this band gap region are already approaching this upper limit.[86] To obtain higher PCEs over this efficiency limit, certain groups have focused on tailoring small and large band gap perovskite active layers for multijunction tandem solar cells. Unfortunately, the performance of these monolithic perovskite tandem solar cells (PCEs < 19%) have not even surpassed record single junction PCEs.[87,88] An alternative method for increasing perovskite efficiency limits is to focus on tuning perovskite composition to obtain the ideal band gap of 1.3-1.4 eV with the Shockley-Queisser PCE limit of 33% and optimal single junction band gap of 1.34 eV with the Shockley-Queisser PCE limit of 33.7%.[86] Previous research has demonstrated the feasibility of shifting single junction band gaps from 1.5-1.6 to 1.3-1.4 eV by either partial or complete substitution of Pb by Sn. Perovskites with a complete substitution of Sn have been able to reach this ideal band gap range by further tuning of the A-site cations, but are hindered by a lower V_{oc} and FF.[89] Other labs have found greater success with PCEs from Pb/Sn alloyed compositions and ideal band gap tuning. Jen *et al.* optimized process, interfacial, and compositional engineering, improving their PCE and stability of the $MAPb_{0.75}Sn_{0.25}I_3$ perovskites (E_g = 1.35 eV, PCE = 14.35%).[67] Padture *et al*. used further A-site tuning to achieve the ideal band gap with their $(FAPbI_3)_{0.7}(CsSnI_3)_{0.3}$ composition (E_g = 1.30 eV) and achieved a PCE of 14.6%.[90] Jen and coworkers also showed improvements in their Pb/Sn performance through further halide tuning of their absorber composition $MAPb_{0.5}Sn_{0.5}(I_{0.8}Br_{0.2})_3$ (E_g = 1.35 eV, PCE = 17.63%).[67] These works have reasonable device performances involving Pb/Sn hybrids with over 50% Pb.

Due to the nature of the Pb/Sn hybrid orbitals, it has been found that the minimum band gap for Pb/Sn hybrid perovskites occurs at close to 75% Sn. $MAPb_{0.3}Sn_{0.7}I_3$ was found to have a minimum of 1.17 eV before increasing for $MASnI_3$.[63] There is no work exploring the region of 75%-100% Sn where another Sn-based composition would have the optimal single junction band gap of 1.34 eV but contain much less of the Pb heavy metal. It is therefore desirable to explore this region to understand the true band gap minimum of Pb/Sn hybrids and identify the composition for the ideal single junction band gap.

The 75%-100% Sn perovskite region is particularly vulnerable to instabilities such as oxidation of Sn^{2+} to Sn^{4+} and degradation due to humidity.[50,68] Other cations have recently been explored to stabilize Pb-based perovskites from environmental degradation and to improve long-term stability. Grätzel *et al.*, the first group to introduce the triple cation system, now have introduced Rb (radius 1.52 Å) for new triple cation and quadruple cation perovskites. Their $Rb_5(Cs_5MAFA)_{95}PbI_3$ PVSC was able to reach a PCE_{max} of 21.6% due to minimizing non-radiative recombination loses and showed increased carrier transport compared to their triple cation PVSCs. The Grätzel lab also aged devices for 500 hours at 85°C under continuous illumination with full solar intensity and maximum power point tracking, which exceeds the industrial standard stress test, and found devices retained 95% of its initial performance. Hu *et al.* also explored the fundamental effects of incorporation of Cs and Rb on trap states, charge transportation, and recombination in the control $FA_{0.83}MA_{0.17}Pb(I_{0.83}Br_{0.17})_3$ system. Their research shows that 5% doped Rb prone to phase separation of the non-perovskite $RbPb(I_{1-x}Br_x)_3$, impeding performance with increased recombination. Before phase segregation occurs, Rb doped perovskites show

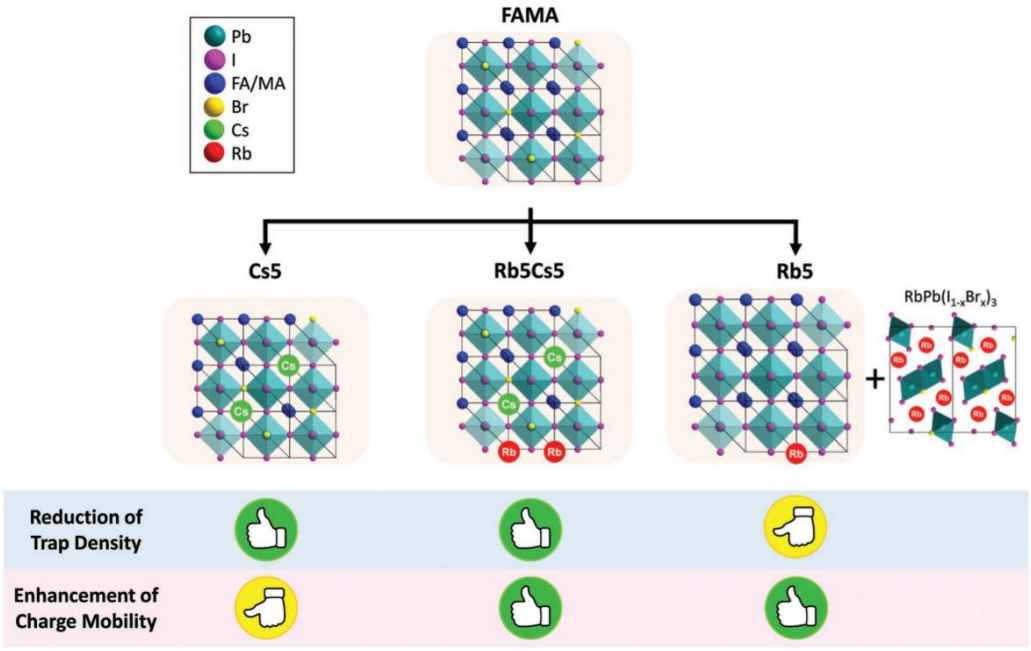

Figure 3-1. Summary of Cs and Rb effects on trap density reduction, phase stability, and charge mobility in mixed cation perovskite films.[90]

charge carrier mobilities. The quadruple cation mixture was able to remain phase stable while maintaining the enhanced charge mobility and had the highest stabilized power output under constant illumination of the compositions tested,[91] showing the value of the cation tuning. Figure 3-1 shows the summary of the benefits and drawbacks from Rb, Cs, and mixed cation perovskites.[91]

In this work, we combined compositional tolerance factor tuning and solvent-washing methodology to create the first reproduction of cubic α-phase, homogeneous and densely packed polycrystalline $Cs_x(MA_{0.17}FA_{0.83})_{1-x}Pb_{1-y}Sn_y(I_{0.83}Br_{0.17})_3$ films with x = 0.05, 0.10, and 0.20 and y = 0, 0.25, 0.50, 0.75, and 1.0. To improve general device stability, we used a simple inverted device structure of indium tin oxide (ITO)/poly (3,4, -ethylenedioxythiphene): polystyrene sulfonate (PEDOT:PSS)/Perovskite/[6,6]-phenyl-C_{60}-butyric acid methyl ester ($PC_{60}BM$)/fullerene (C_{60})/2,9-dimethyl-7,7-diphenyl-1,10-phenanthroline (BCP)/Ag. This solar cell architecture

eliminated the need for dopants that introduce instabilities and decreased hysteresis, allowing stable maximum powers. Due to the high-quality film morphology and ideal single junction band gap (1.36 eV) of $Cs_{0.10}(MA_{0.17}FA_{0.83})_{0.9}Pb_{0.75}Sn_{0.25}(I_{0.83}Br_{0.17})_3$, the derived PVSCs reached a maximum PCE of 15.78%. The triple cation mixture and SnF_2 additive alleviated Sn oxidation for $Cs_{0.05}(MA_{0.17}FA_{0.83})_{0.95}Pb_{0.25}Sn_{0.75}(I_{0.83}Br_{0.17})_3$ (band gap = 1.30 eV), resulting in a record maximum PCE of 11.05% for the corresponding PVSC. Moreover, the 75% Sn PVSCs can retain 80% of initial PCE after 30 days storage in inert conditions followed by over 100 hours in ambient conditions. We also systematically explore the unknown exploring 75-100% Sn region of the $Cs_x(MA_{0.17}FA_{0.83})_{1-x}Pb_{1-y}Sn_y(I_{0.83}Br_{0.17})_3$ and $Rb_x(MA_{0.17}FA_{0.83})_{1-x}Pb_{1-y}Sn_y(I_{0.83}Br_{0.17})_3$, studying the impacts of a variety of cations on morphology, crystallinity, and band gap for the our triple cation systems. The triple cation Pb-Sn double halide perovskites not only offer a wide tunability on band gap to achieve ideal band gaps for single-junction or tandem PVSCs but also greatly improve the performance and stability of high Sn PVSCs, leading to our research of more stable and efficient lead-free devices.

3.2 Results and Discussion

3.2.1 Compositional Tuning on Morphology, Crystallinity, and Lattice Parameter

To achieve good film morphology, we used the one-step solution process and optimized anti-solvent engineering to synthesize dense, pinhole-free perovskite thin films. All precursors (MAI, FAI, PbI_2, $PbBr_2$, and FABr) were dissolved in a DMSO:GBL (3:7, v/v) co-solvent to a total concentration of 2.5 M. 10% mol SnF_2 with respect to Sn content was added to suppress the formation of Sn^{4+}. During spin coating, the anti-solvent wash with toluene was performed to remove excess DMSO from the complexes $PbI_2 \cdot 2DMSO$ and $SnI_2 \cdot 3DMSO$ to create the rapid

formation of A-PbI_2-DMSO and A-SnI_2-2DMSO intermediates. One SnI_2 forms a complex with 3 DMSO in the precursor solution due to the high bond energy of Sn-O (528 kJ mol^{-1}) compared to that of Pb-O (374 kJ mol^{-1}) supporting the preferential attachment of DMSO to Sn.[66,92] In our previous work, we demonstrated the role of DMSO in enhancing $MAPb_{1-x}Sn_xI_3$ and $MAPbCl_3$ film

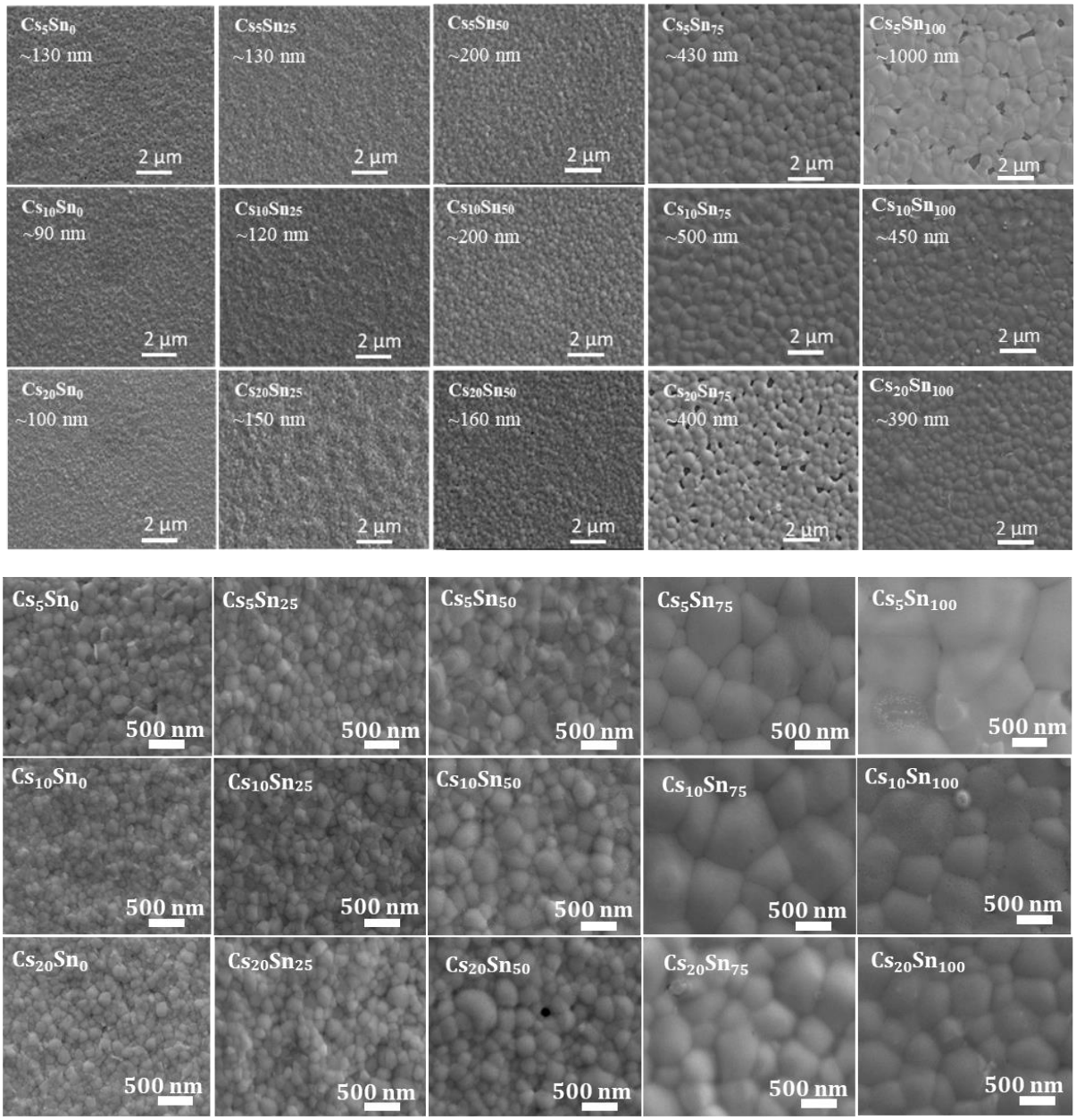

Figure 3-2. SEM images of $Cs_x(MA_{0.17}FA_{0.83})_{1-x}Pb_{1-y}Sn_y(I_{0.83}Br_{0.17})_3$ perovskite thin films with x = 0.05, 0.1 and 0.2 and y = 0, 0.25, 0.50, 0.75 and 1 at 10,000x (top panel) and 40,000x (bottom panel) magnification. The average grain size of each film is shown in the top panel images.

morphology and crystallinity.[40,93] The volume of toluene was decreased with increased Sn percentage and amount of complexed $SnI_2 \cdot 3DMSO$ to minimize multiple DMSO removal before annealing. Multiple DMSO removal would create A-SnI_2-DMSO instead of A-SnI_2-2DMSO intermediates, hindering the slower controlled removal of DMSO and reaction upon annealing, resulting in pinholes. All the films, except those of 100% Sn, were annealed at 100°C for 10 min to remove complexed DMSO under a controlled reaction of metal and cation during the annealing step, creating homogeneous, densely packed Pb-Sn perovskite films with clear grain boundaries. Films with 10 and 20 % Cs and pure Sn were found to have better morphology when annealed at 110°C, most likely due to the stronger bond in the A-SnI_2-2DMSO complex, which would require a higher temperature to break.

Figure 3-2 shows SEM images of the perovskite thin films with the compositions of $Cs_x(MA_{0.17}FA_{0.83})_{1-x}Pb_{1-y}Sn_y(I_{0.83}Br_{0.17})_3$, where x = 0.05, 0.1, and 0.2 and y = 0, 0.25, 0.50, 0.75, and 1.0. The low magnification SEM images are shown in Figure 3-2 to demonstrate the film quality and quantify the average grain sizes. To make description simple, we will use the notation Cs_xSn_y to represent the thin films. For example, Cs_5Sn_{25} represents the thin films with the composition of $Cs_{0.05}(MA_{0.17}FA_{0.83})_{0.95}Pb_{0.75}Sn_{0.25}(I_{0.83}Br_{0.17})_3$. As shown in Figure 3-2, for each Cs composition, the grain size increased slightly with the addition of Sn to 50%. A notable grain size increase was observed when the Sn composition was greater than 50%.

This could be due to the higher coordination of DMSO to Sn (A-SnI_2-2DMSO) compared to Pb (A-PbI_2-DMSO) formed for high Sn composition intermediates, allowing for even slower crystallization upon annealing as one mole of DMSO is first removed (A-SnI_2-DMSO) followed by the second, thus leading to larger grains. Sn addition has been shown to increase grain size with large grains for high Sn perovskites.[70 55] For each Sn composition, Cs addition had no notable

changes in grain size. The large area SEM images shows that pinhole-free films were formed for all Cs compositions with 50% Sn or lower. Smooth, dense, pinhole-free morphologies were also formed for the Cs_5Sn_{75} and $Cs_{10}Sn_{75}$ films while obvious pinholes were formed in the $Cs_{20}Sn_{75}$ film. The Cs_5Sn_{100} film has the largest, most prominent pinholes as well as an amorphous phase around the grain boundaries with a poor morphology apparent while both $Cs_{10}Sn_{100}$ and $Cs_{20}Sn_{100}$ films have a few, small pinholes and more even coverage. A few smaller, lighter grains appeared in the $Cs_{10}Sn_{100}$ and $Cs_{20}Sn_{100}$ films, which could be due to a slight phase segregation.

The thin films were further characterized with XRD to determine the phase and crystallinity. As shown in Figure 3-3a, all thin films have a cubic α-phase with the $Pm\bar{3}m$ space group. The absence of additional peaks, such as the photoinactive hexagonal δ-phase $FAPbI_3$ at 11.63°, the orthorhombic δ-phase $CsPbI_3$ at 9.80° and 13.00°, the unreacted, cubic PbI_2 at 12.85°, and the tetragonal perovskite peaks indicated by the asterisk symbol, confirms the pure crystalline phase of the synthesized perovskite films.[94,95,96] The strong diffraction from the (100) and (200) planes indicates a favorable orientation with the glass substrate. The shifts of the (100) diffraction peak for all synthesized perovskite films are clearly shown in Figure 3-3. For increasing Cs with a fixed Sn, the (100) peak right shifts (Figure 3-3a), resulting in a reduced lattice parameter (Figure 3-3b) because of the incorporation of the smaller Cs ion (r = 1.67 Å), supporting the successful incorporation of Cs.[97,98] Figure 3-3d illustrates that the incorporation of the smaller Cs ion pushes the Goldschmidt tolerance factor into a more cubic region for all Sn compositions and further from the hexagonal region, which stabilizes the perovskites against unwanted phase changes. The addition of Cs was also used to further optimize the Goldschmidt tolerance factor (GTF) of the perovskite compositions The radii of MA^+ (2.16 Å), FA^+ (2.53 Å), Cs^+ (1.67 Å), Pb^{2+} (1.19 Å), Sn^{2+} (1.15 Å), I^- (2.20 Å), and Br (1.96 Å) were used to calculate the GTFs of all perovskites.[99]

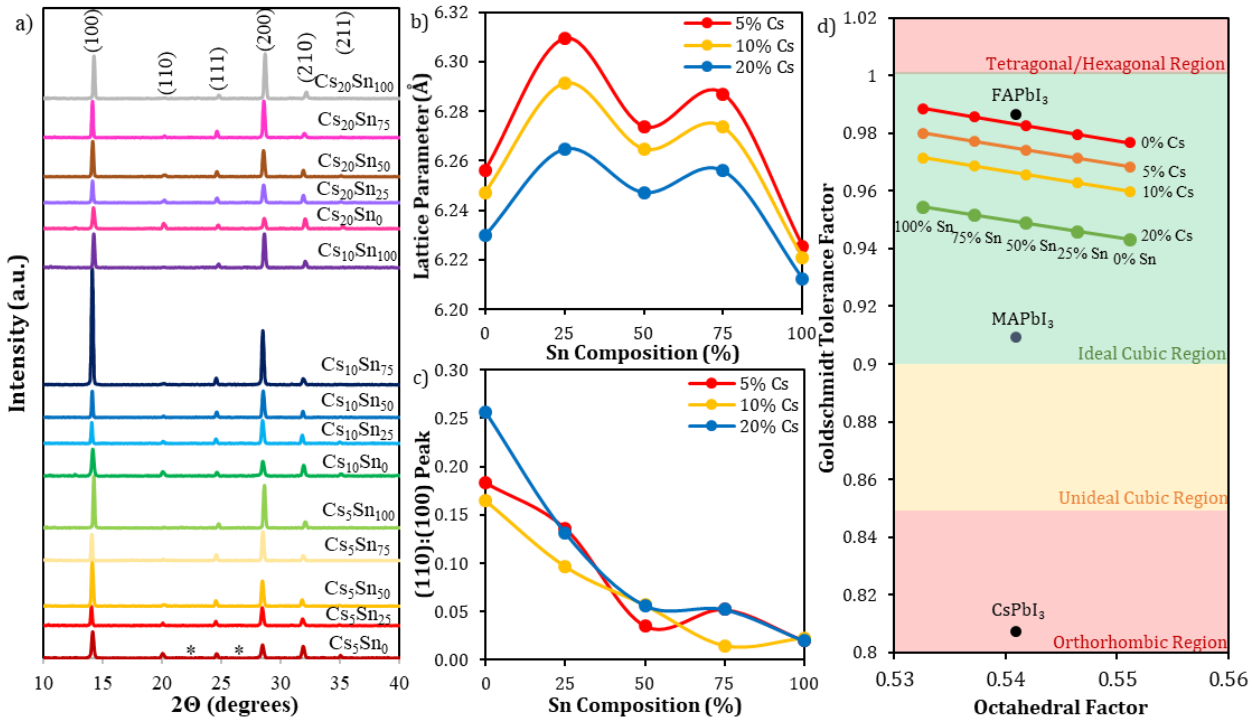

Figure 3-3. (a) X-ray diffraction (XRD) patterns of $Cs_x(MA_{0.17}FA_{0.83})_{1-x}Pb_{1-y}Sn_y(I_{0.83}Br_{0.17})_3$ perovskite thin films with x = 0.05, 0.1 and 0.2 and y = 0, 0.25, 0.50, 0.75 and 1.0. (b) The cubic lattice parameters as a function of Sn composition for each Cs composition of all perovskites. (c) The intensity ratio of the (110) and (100) peaks ($I_{(110)}/I_{(100)}$) as a function of Sn composition for each Cs composition of all perovskites. (d) The Goldschmidt tolerance and octahedral factor calculations for corresponding compositions with phase change regions.

The GTFs and octahedral factors of $Cs_x(MA_{0.17}FA_{0.83})_{1-x}Pb_{1-y}Sn_y(I_{0.83}Br_{0.17})_3$ perovskites with x = 0, 0.05, 0.1 and 0.2 and y = 0, 0.25, 0.5, 0.75 and 1 are graphed in Figure 3-3d. In addition, these factors of $CsPbI_3$, $MAPbI_3$ and $FAPbI_3$ are also marked in the graph. As shown in Figure 3-3d, all perovskites tested fall in the cubic phase range of octahedral factor. GTF is shown to increase with the increasing of Sn composition and decreases with the increasing of Cs composition. $MAPbI_3$ and $FAPbI_3$ are at the lower and higher boundary of the GTF region for ideal cubic phase, respectively. Even though the tolerance factor of α-$FAPbI_3$ is 0.986 calculated based on the radium of FA^+ (2.53 Å), the non-sphericity of FA^+ complicates the calculation, making an actual tolerance factor around 1.03.[100] This tolerance factor borders on the hexagonal region (GTF > 1) at room temperature, explaining the instabilities of α-$FAPbI_3$. adding MA and Br to form

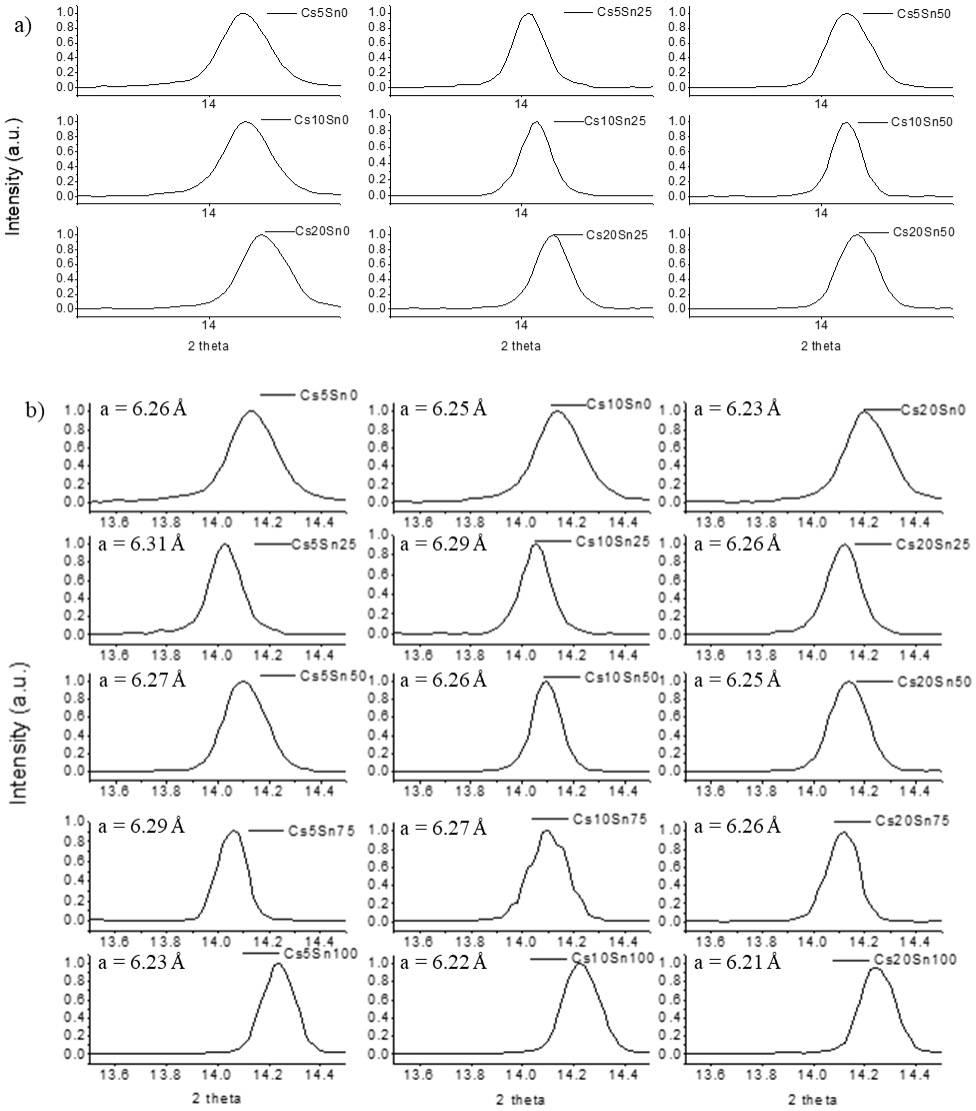

Figure 3-4. Shift of the (100) diffraction peak of perovskite thin films with the composition formula of $Cs_x(MA_{0.17}FA_{0.83})_{1-x}Pb_{1-y}Sn_y(I_{0.83}Br_{0.17})_3$ for (a) columns with constant Sn and increasing Cs, and (b) columns with constant Cs and increasing Sn.

$(MA_{0.17}FA_{0.83})Pb(I_{0.83}Br_{0.17})_3$ (i.e., Cs_0Sn_0) allows for a smaller tolerance factor (0.977) moving more into the cubic phase region. However, forming Pb-Sn alloy perovskites based on this mixed MA/FA and I/Br formula lead to increased GTFs with increasing Sn contents. Cs_0Sn_{100} reaches a GTF of 0.989, exceeding than that of $FAPbI_3$. Introducing Cs can decrease GTFs, allowing for even pure Sn perovskites to have a more cubic tolerance. For example, adding 5, 10 and 20 % Cs, i.e., Cs_5Sn_{100}, $Cs_{10}Sn_{100}$ and $Cs_{20}Sn_{100}$, decrease the GTFs to 0.980, 0.972 and 0.954, respectively.

The lower GTFs indicate that introducing Cs can entropically stabilize the perovskites at room temperature, likely leading to higher stabilities. This is in good agreement with previous reports of triple cation mixture for tolerance tuning.[26,97,101] Using the three-cation mixture also alleviates the size mismatch of Cs and FA, decreasing the chance for entropic phase separation.

Figure 3-4 shows the (100) diffraction peak for all compositions, illustrating peak shifts. While the lattice parameters decreased slightly from pure Pb to pure Sn for all fixed Cs compositions, all Pb-Sn alloys exhibited larger lattice parameters than the pure Pb or Sn perovskites with dips at the 50% Sn (Figure 3-4, 3-3b). This nonlinear deviation is consistent for all Cs compositions. McGehee and co-workers reported slight nonlinear deviations of lattice parameters for $Cs_yFA_{1-y}Pb_xSn_{1-x}I_3$ perovskites. This could be due to the nonlinear Pb-X-Sn bond resulted from octahedral tilting which creates a nonlinear lattice effect for Pb-Sn alloyed perovskites during the incorporation of more Sn. However, the trends are different. For example, our Cs_xSn_{25} perovskites have larger lattice parameters than those of Cs_xSn_0 perovskites while the lattice parameter of $FAPb_{0.75}Sn_{0.25}I_3$ perovskite is smaller than that of $FAPbI_3$ perovskite.[37] The opposite trend could be attributed to the smaller lattice parameters of Cs_xSn_0 in the range of 6.26-6.23 Å compared to $Cs_yFA_{1-y}Pb_{0.75}Sn_{0.25}I_3$ in the range of 6.39-6.33 Å due to the introduction of the smaller MA^+ and Br^-. The smaller overall lattice parameter in our perovskites could make the octahedral tilting resulted nonlinearity of mixed Pb-X-Sn bond more prominent, allowing certain Pb-Sn alloyed perovskites to have a larger lattice parameter than pure Pb or Sn perovskites.

In addition, it was noticed that the full width at half max (FWHM) of the (100) peak becomes narrower with Sn addition when compared to the pure Pb perovskites (Figure 3-4), indicating the high crystallinity of the 25-75% Sn perovskites, which is consistent with the grain growth shown in the SEM images in Figure 3-2. Figure 3-3c shows the intensity ratio of (110) and (100) peaks

for all composition perovskites, illustrating the decrease in (110) peak intensity with addition Sn. For 75% and 100% Sn compositions, there is a significant decrease in the (110) and (111) peaks showing a more preferred orientation of the (100) plane.

3.2.2 Compositional Tuning on Band Gaps

The UV-Vis absorption spectra of the $Cs_x(MA_{0.17}FA_{0.83})_{1-x}Pb_{1-y}Sn_y(I_{0.83}Br_{0.17})_3$ perovskite thin films are shown in Figure 3-5a-c. As the incorporation of Sn was increased to 100%, the absorption spectra showed a softened band edge due to sub-band gap states and scattering, making it difficult

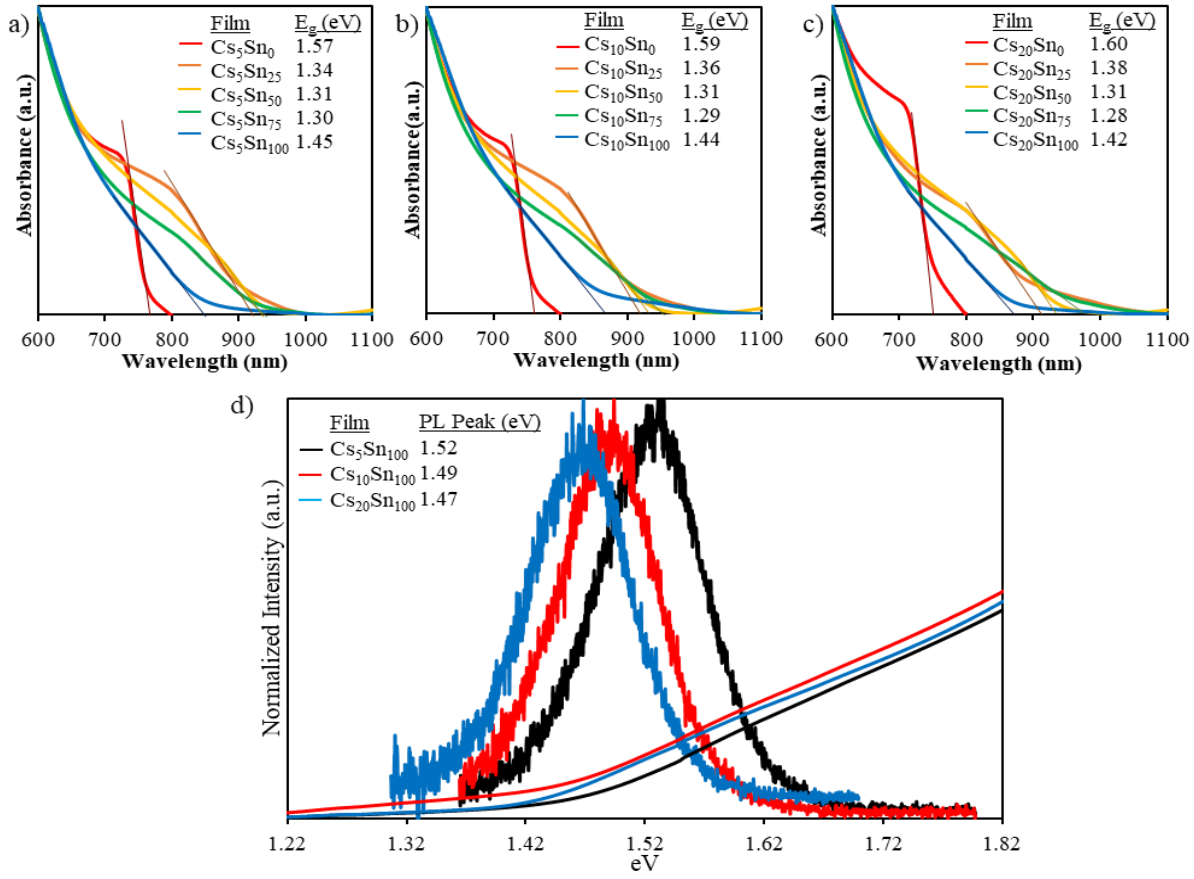

Figure 3-5. UV-vis absorption spectra of $Cs_x(MA_{0.17}FA_{0.83})_{1-x}Pb_{1-y}Sn_y(I_{0.83}Br_{0.17})_3$ perovskite thin films for (a) x = 0.05, (b) x = 0.10, and (c) x = 0.20 with y = 0, 0.25, 0.50, 0.75, and 1.0 for each x. The optical band gaps derived from the absorption onsets are also shown. (d) Normalized PL spectra overlapped with UV-Vis spectra for 100% Sn perovskites with different Cs contents. The band gaps were derived from the peaks of PL spectra.

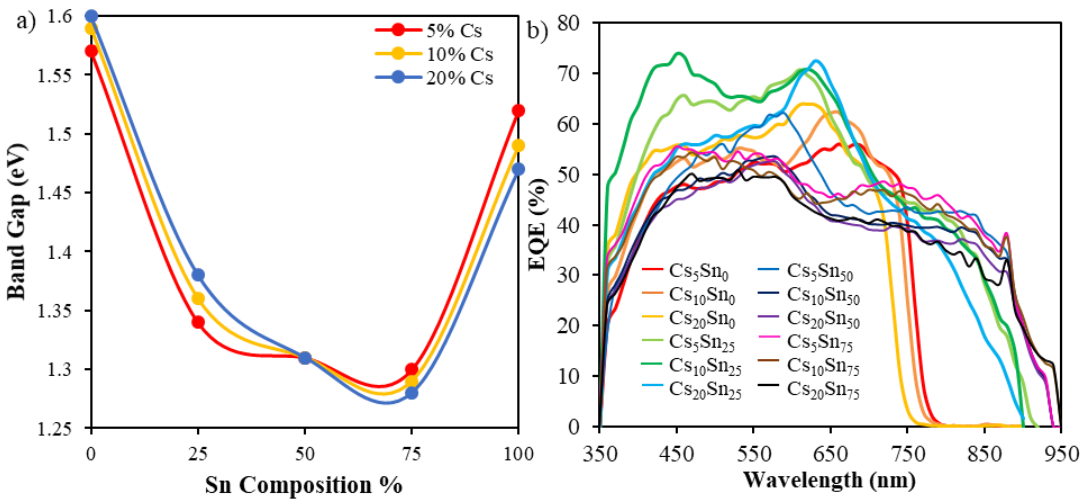

Figure 3-6. (a) The band gap of $Cs_x(MA_{0.17}FA_{0.83})_{1-x}Pb_{1-y}Sn_y(I_{0.83}Br_{0.17})_3$ perovskite thin films as a function of Sn composition for different Cs contents. (b) The EQE spectra of PVSCs with the $Cs_x(MA_{0.17}FA_{0.83})_{1-x}Pb_{1-y}Sn_y(I_{0.83}Br_{0.17})_3$ active layers.

to determine the band gap. Photoluminescence (PL) measurements were, therefore, performed with samples sealed in vacuum to better define the band gap trend (Figure 3-5d). The band gaps estimated from the onsets of the absorption spectra (0-75% Sn compositions) and PL spectra (100% Sn composition) are graphed as a function of Sn composition for different Cs contents (Figure 3-6a). For each fixed Cs composition, the band gaps decrease from the maxima around 1.57-1.61 eV of the pure Pb perovskites to the minima around 1.28 – 1.30 eV of the perovskites with 75% Sn and then increase to 1.47-1.52 eV for 100% Sn. The addition of Cs, however, causes two trends in band gap depending on Sn composition and the cross-over occurs at 50% Sn. The band gaps increase with the increase of Cs for Pb-rich perovskites while they decrease with the increase of Cs for Sn-rich perovskites. All these trends are mainly due to the influence of the M-X overlap and the A-site induced MX_6 octahedral tilting on the conduction and valence band edges of perovskites. First-principle electronic structure calculations have determined the conduction band minimum of metal halide perovskites is a hybrid of metal p and halide p orbitals with nonbonding character and the valence band maximum is an antibonding hybrid of metal s and

halide p orbitals.[101] Changes in the M-X overlap, therefore, raise the energy of the valence band more directly while the conduction band, having less orbital overlap, responds less strongly to lattice distortions, allowing the band gap to decrease with increased M-X overlap. The minimum band gaps at 75% Sn observed in this work for triple cation, double halide Pb-Sn perovskites follow the same trend for single cation, single halide $MAPb_xSn_{1-x}I_3$ perovskites.[63] The opposite trend of band gap change on Sn composition was also observed in $FA_{1-x}Cs_xPb_{1-y}Sn_yI_3$ perovskites, where x ranged from 0 to 30% and y ranged from 0 to 100%. A smaller A-site cation could increases the MX_6 octahedra tilting, which would increase the band gap, or contract the crystal lattice isotropically, which would decrease the band gap.[37] The pure Pb and Pb-rich perovskites follow a blue shift in band gap with increased Cs in the A-site, which is predominantly due to the MX_6 tilting decreasing M-X overlap, lowering the valence band. The pure Sn and Sn-rich perovskites follow the opposite, red shift in band gap with increased Cs in the A-site, which is mainly due to the isotropical lattice constrictions, resulting in an increasing M-X overlap.[37,102] Our results support these two mechanisms for A-site induced band gap changes in previous literature while also showing the shift in predominant mechanisms occurring at 50% Sn even for triple cation, double halide Pb-Sn perovskites.

The band gap trends of $Cs_x(MA_{0.17}FA_{0.83})_{1-x}Pb_{1-y}Sn_y(I_{0.83}Br_{0.17})_3$ perovskites determined from UV-Vis and PL were also shown in the external quantum efficiency (EQE) spectra of PVSCs made with these films. As shown in Figure 3-6b, fixed Cs with increasing Sn results in a red shift in EQE edges from 0% - 75% Sn. With fixed Sn and increasing Cs, there is a blue shift in EQE edge for Sn_0 and Sn_{25} and no change for Sn_{50}, while a red shift for Sn_{75}.

3.2.3 J-V Characteristics and Photovoltaic Device Performance

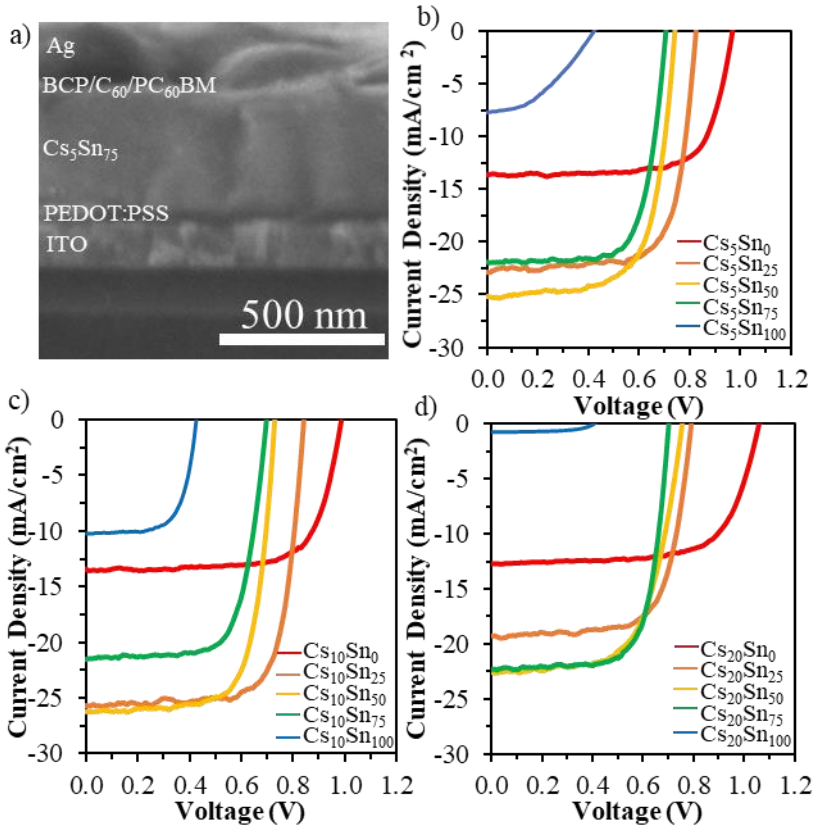

Figure 3-7. (a) Cross-section SEM image showing the $Cs_{0.05}(MA_{0.17}FA_{0.83})_{0.95}Pb_{0.25}Sn_{0.75}(I_{0.83}Br_{0.17})_3$ PVSC with the following layers: ITO (~200 nm)/PEDOT:PSS (~50 nm)/perovskite (~450 nm)/$PC_{60}BM/C_{60}$ (20 nm)/BCP (8 nm)/Ag (150 nm). The current density-voltage (J-V) characteristics of $Cs_x(MA_{0.17}FA_{0.83})_{1-x}Pb_{1-y}Sn_y(I_{0.83}Br_{0.17})_3$ PVSCs with (b) x = 0.05, (c) x = 0.10, and (d) x = 0.20 with y = 0, 0.25, 0.50, 0.75, and 1.0 for each x under AM 1.5 illumination at a scan rate of 0.01V s^{-1} from 0 to 1.2 V.

To determine the viability of these films as solar cell active layers, PVSCs were fabricated using $Cs_x(MA_{0.17}FA_{0.83})_{1-x}Pb_{1-y}Sn_y(I_{0.83}Br_{0.17})_3$ as the active layer with the inverted perovskite architecture of ITO/PEDOT:PSS/Perovskite/$PC_{60}BM/C_{60}$/BCP/ Ag as shown in the cross-section SEM image in Figure 3-7a. PEDOT:PSS acts as the solution processable hole transport layer (HTL) sandwiching the perovskite layer with the spin-coated electron transport layer (ETL) $PC_{60}BM$, which is commonly used to fill gaps in the perovskite layer, reducing surface roughness and passivating possible traps.[103] The thermally deposited C_{60} layer acts as a second ETL to

improve band energy alignment and the BCP layer acts as a hole blocking layer (HBL) to increase charge separation and minimize recombination. The photocurrent density-voltage (J-V) characteristics of fabricated PVSCs are shown in Figure 3-7b-d with detailed photovoltaic parameters summarized in Table 3-1. To determine the effects of Sn additives, pure Pb PVSCs were fabricated as a control for the three Cs compositions.

Table 3-1. Photovoltaic parameters of $Cs_x(MA_{0.17}FA_{0.83})_{1-x}Pb_{1-y}Sn_y(I_{0.83}Br_{0.17})_3$ PVSCs measured under AM 1.5 illumination obtained from forward J-V measurements.

Device	V_{oc} (V)	J_{sc} (mA cm^{-2})	FF	PCE (%)	PCE_{max}
Cs_5Sn_0	0.98 ± 0.01	12.55 ± 1.03	0.70 ± 0.03	8.61 ± 0.75	9.54
Cs_5Sn_{25}	0.82 ± 0	20.98 ± 1.35	0.71 ± 0.01	12.29 ± 0.52	13.45
Cs_5Sn_{50}	0.73 ± 0.01	21.60 ± 2.09	0.67 ± 0.01	10.66 ± 1.19	12.71
Cs_5Sn_{75}	0.71 ± 0.01	21.46 ± 0.57	0.71 ± 0.01	10.81 ± 0.15	11.05
Cs_5Sn_{100}	0.43±0.01	5.67±2.97	0.52±0.07	1.30±0.80	1.87
$Cs_{10}Sn_0$	0.98 ± 0.01	12.37 ± 0.76	0.69 ± 0.03	8.46 ± 0.79	9.56
$Cs_{10}Sn_{25}$	0.83 ± 0.01	22.39 ± 2.62	0.73 ± 0.01	13.54 ± 1.74	15.78
$Cs_{10}Sn_{50}$	0.72 ± 0.01	23.14 ± 2.69	0.65 ± 0.08	10.91 ± 2.60	13.52
$Cs_{10}Sn_{75}$	0.68 ± 0.02	20.19 ± 1.92	0.66 ± 0.04	9.01 ± 1.01	10.45
$Cs_{10}Sn_{100}$	0.41 ±0.00	8.98 ±1.39	0.65 ±0.02	2.43 ±0.45	2.81
$Cs_{20}Sn_0$	1.04 ± 0.03	11.85 ± 0.92	0.64 ± 0.04	7.92 ± 1.29	9.23
$Cs_{20}Sn_{25}$	0.78 ± 0.01	17.50 ± 1.16	0.69 ± 0.01	9.36 ± 0.60	10.56
$Cs_{20}Sn_{50}$	0.75 ± 0.01	22.07 ± 1.50	0.61 ± 0.04	9.99 ± 0.66	10.81
$Cs_{20}Sn_{75}$	0.70 ± 0.01	20.74 ± 1.19	0.67 ± 0.07	9.77± 1.31	11.01
$Cs_{20}Sn_{100}$	0.39±0.03	1.34±0.04	0.41±0.05	0.21±0.04	0.25

The open-circuit voltage (V_{oc}), short-circuit current density (J_{sc}), fill factor (FF) and PCE as a function of Sn composition for different Cs contents were plotted in Figure 3-8a-d, respectively. The average V_{oc}'s decrease from ~ 1.0 V to ~ 0.4 V with increased Sn from 0 to 100% for all three Cs contents, which has been previously attributed to mismatched energy levels from valence decrease in band gaps from 1.57-1.61 to ~1.32 eV. The smaller band gaps allow for an increased photo-response in the near infrared region as demonstrated in EQE spectra in Figure 3-6b. Further increasing Sn to 75 and 100%, different Cs contents PVSCs exhibited different trends. The J_{sc} of

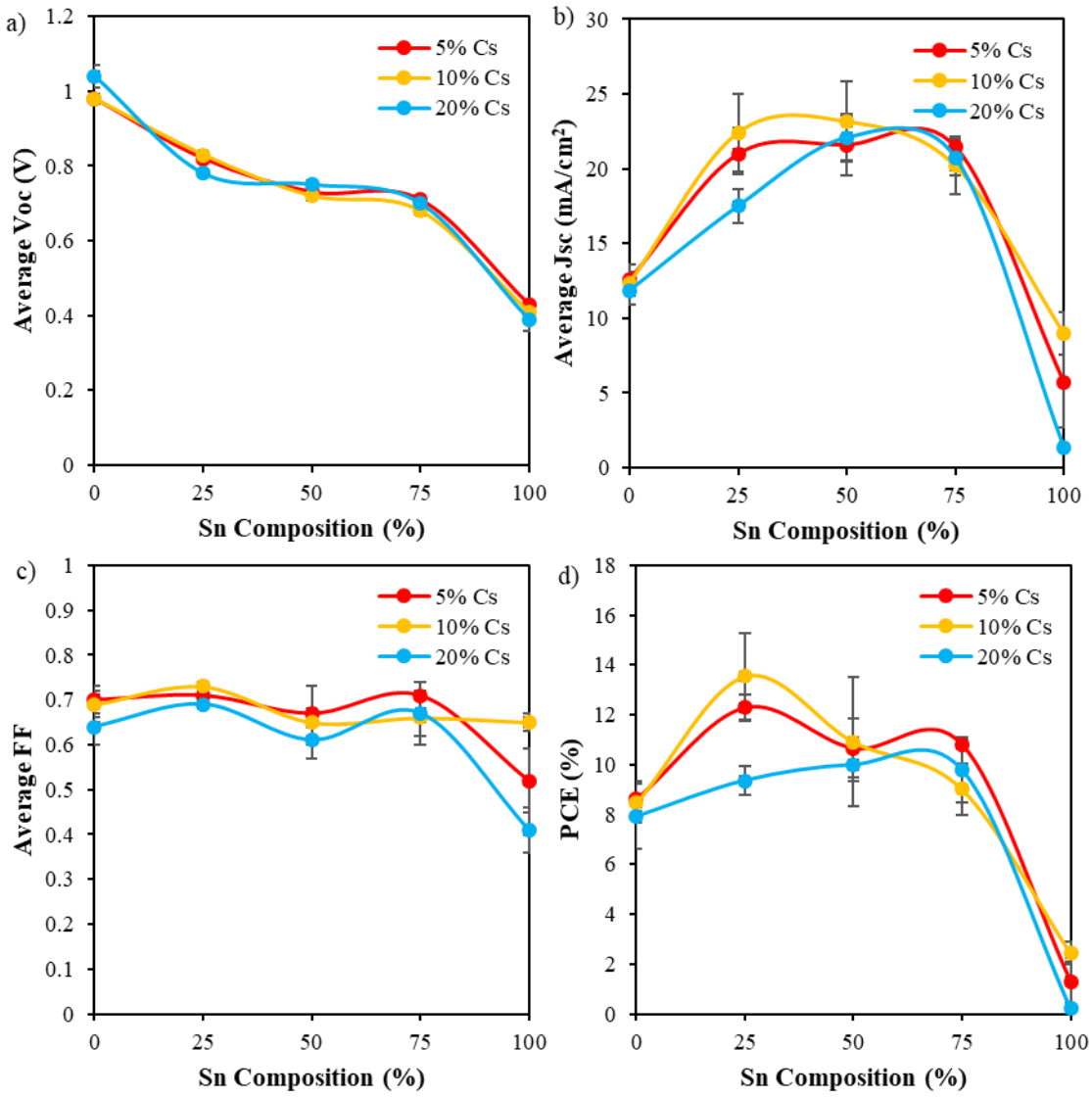

Figure 3-8. The averages of (a) V_{oc}, (b) J_{sc}, (c) FF, and (d) PCE of PVSCs as a function of Sn composition for different Cs contents with $Cs_x(MA_{0.17}FA_{0.83})_{1-x}Pb_{1-y}Sn_y(I_{0.83}Br_{0.17})_3$ perovskite thin films as the active layers.

Cs_5Sn_{75} was maintained around 21 mA cm^{-2} because of both low band gap (~1.3 eV) and high-quality film. For Cs_5Sn_{100}, the J_{sc} decreased to 5.67 mA cm^{-2} due to the introduction of large pinholes plus decreased crystallinity of the Cs_5Sn_{100} perovskite film shown. For $Cs_{20}Sn_{75}$, the J_{sc} was decreased slightly to the still reasonable level of 20 mA cm^{-2} most likely due to the introduction of small numbers of pinholes. A significant decrease of J_{sc} to 8.98 mA cm^{-2} was observed for $Cs_{10}Sn_{100}$, which could be due to the band gap increasing (~1.44 eV) and the small

particles around grain boundaries resulted from phase segregations (Figure 3-2). The overall improvement in J_{sc} demonstrates the beneficial role of Cs in improving crystallinity and film formation. The $C_{20}Sn_{100}$ PVSCs exhibited the lowest J_{sc} of 1.34 mA cm^{-2}, indicating the necessity for specified Cs tuning to optimize film formation and J_{sc}. Regardless of Cs content, FFs showed minimal variations for different Sn compositions. Combined with all parameters, the $Cs_{10}Sn_y$ PVSCs have the highest maximum PCE for each Sn composition. The $Cs_{10}Sn_{25}$ and Cs_5Sn_{75} PVSCs currently hold the record high maximum PCE, 15.78 and 11.05%, respectively, for all reported PVSCs with 25 and 75% Sn compositions and architectures. The PVSCs with 75% Sn and all three Cs contents (Cs_5Sn_{75}, $Cs_{10}Sn_{75}$ and $Cs_{20}Sn_{75}$) exhibited the maximum PCE of 11.05, 10.45, 11.01%, respectively, all surpassing the PCE record holder for 75% Sn (7.8% with $FA_{0.8}Cs_{0.2}Sn_{0.75}Pb_{0.25}I_3$)[104] and nearby 80% Sn (7.07% with $MAPb_{0.2}Sn_{0.8}I_3$).[105] This could be due to the higher V_{oc} with the V_{oc} averages of 0.71, 0.68 and 0.70 V for Cs_5Sn_{75}, $Cs_{10}Sn_{75}$ and $Cs_{20}Sn_{75}$, respectively, demonstrating that composition tuning through triple cation and double halide mixtures might improve band energy alignment in the inverted architecture. Although *Grätzel* and co-workers demonstrated a higher PCE for the respective $Cs_{0.05}(MA_{0.17}FA_{0.83})_{0.95}Pb(I_{0.83}Br_{0.17})_3$ (Cs_5Sn_0) and $Cs_{0.1}(MA_{0.17}FA_{0.83})_{0.9}Pb(I_{0.83}Br_{0.17})_3$ ($Cs_{10}Sn_0$) devices, the TiO_2 solar architecture allows for a higher average V_{oc} of 1.13 V as well as improved FF and J_{sc}.[22] Liang and co-workers reported a similar inverted PEDOT:PSS architecture and toluene anti-solvent wash method resulting in photovoltaic parameters for the maximum forward scan of $Cs_{10}(MA_{0.17}FA_{0.83})_{90}Pb(I_{0.83}Br_{0.17})_3$ devices (PCE = 9.51%, V_{oc} = 0.94 V, FF = 0.53, J_{sc} =16.95 mA cm^{-2}), which are comparable to our best performance $Cs_{10}Sn_0$ device (PCE = 9.56%, V_{oc} = 0.99 V, FF = 0.72, J_{sc} = 13.42 mA cm^{-2}), demonstrating the reproducibility of the anti-solvent wash method for our controls as we fabricated new compositions with Sn. It is worth noting that further PCE

improvements of all high and pure Sn PVSCs can be achieved with further film optimization to remove pinholes and increase phase purity and crystallinity.

3.2.4 Device and Material Stability in Long Term Inert and Ambient Conditions

The hysteresis in J-V characteristics has been previously observed in PVSCs and has been attributed to a number of factors such as slow dynamic processing from trapping and detrapping of charge carriers, ferroelectric properties of perovskites, and ion migration.[106,107] To determine the intrinsic hysteresis and device stability, the forward/backward J-V scans and the measurements of photocurrent stability at the maximum power were performed. As shown in Figure 3-9a-c, forward and backward scans exhibited negligible hysteresis for almost all Sn and Cs composition

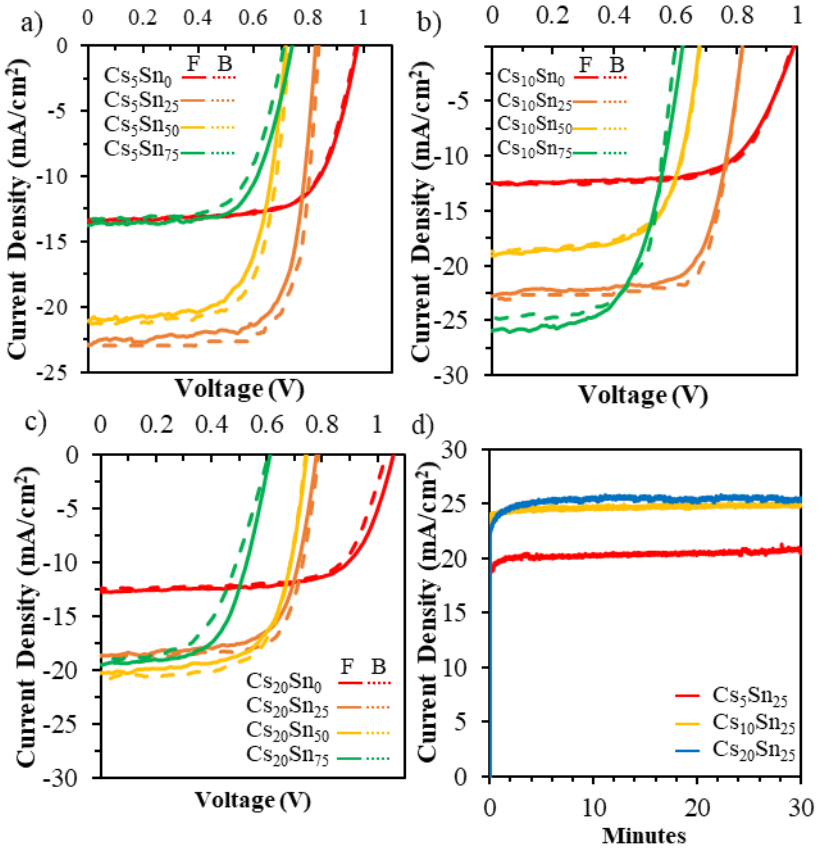

Figure 3-9. Forward and backward scans of the J-V characteristics of $Cs_x(MA_{0.17}FA_{0.83})_{1-x}Pb_{1-y}Sn_y(I_{0.83}Br_{0.17})_3$ PVSCs at a scan rate of 0.01V s-1 under AM 1.5 illumination: (a) x = 0.05, (b) x = 0.10, and (c) x = 0.20 with y = 0, 0.25, 0.50, 0.75, and 1.0.

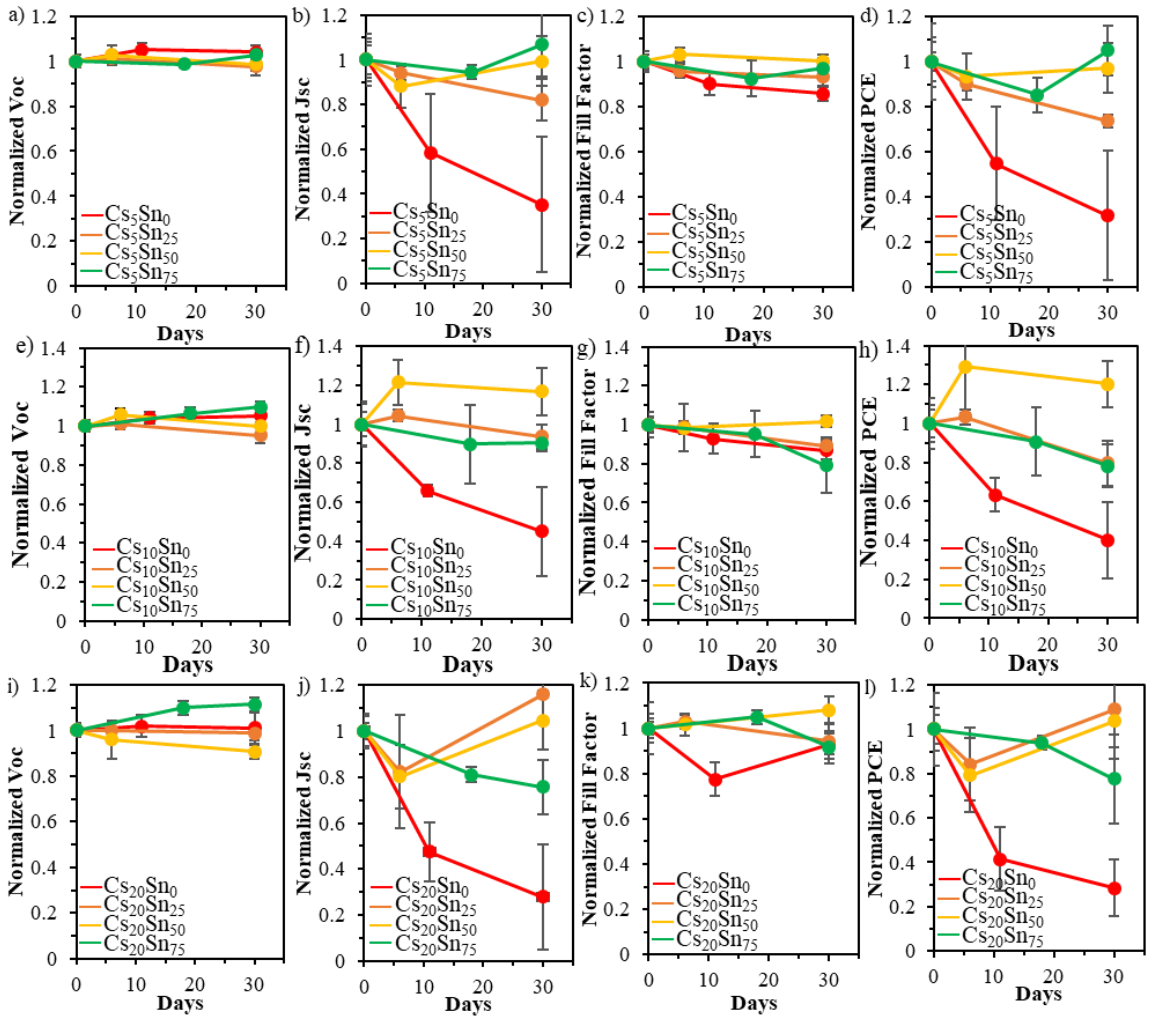

Figure 3-10. Normalized (a, e and i) Voc, (b, f and j) Jsc, (c, g and k) FF, and (d, h and l) PCE of $Cs_x(MA_{0.17}FA_{0.83})_{1-x}Pb_{1-y}Sn_y(I_{0.83}Br_{0.17})_3$ PVSCs for 5, 10 and 20% Cs, respectively, with Sn from 0 to 75% for each Cs composition, over time in the glovebox.

PVSCs. The noticeable hysteresis in $Cs_{20}Sn_{75}$ could be attributed to the small pinholes introduced to the film morphology, which could increase trapping charge carriers. As shown in Figure 3-9d of the photocurrent versus time at the maximum power, the Cs_XSn_{25} PVSCs remained stable under illumination in an inert atmosphere within the 30 min test period.

A critical issue for Sn-based PVSCs is the ambient environment instability caused by the oxidation of Sn^{2+} to Sn^{4+} and degradation in humidity. To understand the effects of the various Cs compositions on the stability of Pb-Sn PVSCs, the long-term device stability in inert and ambient

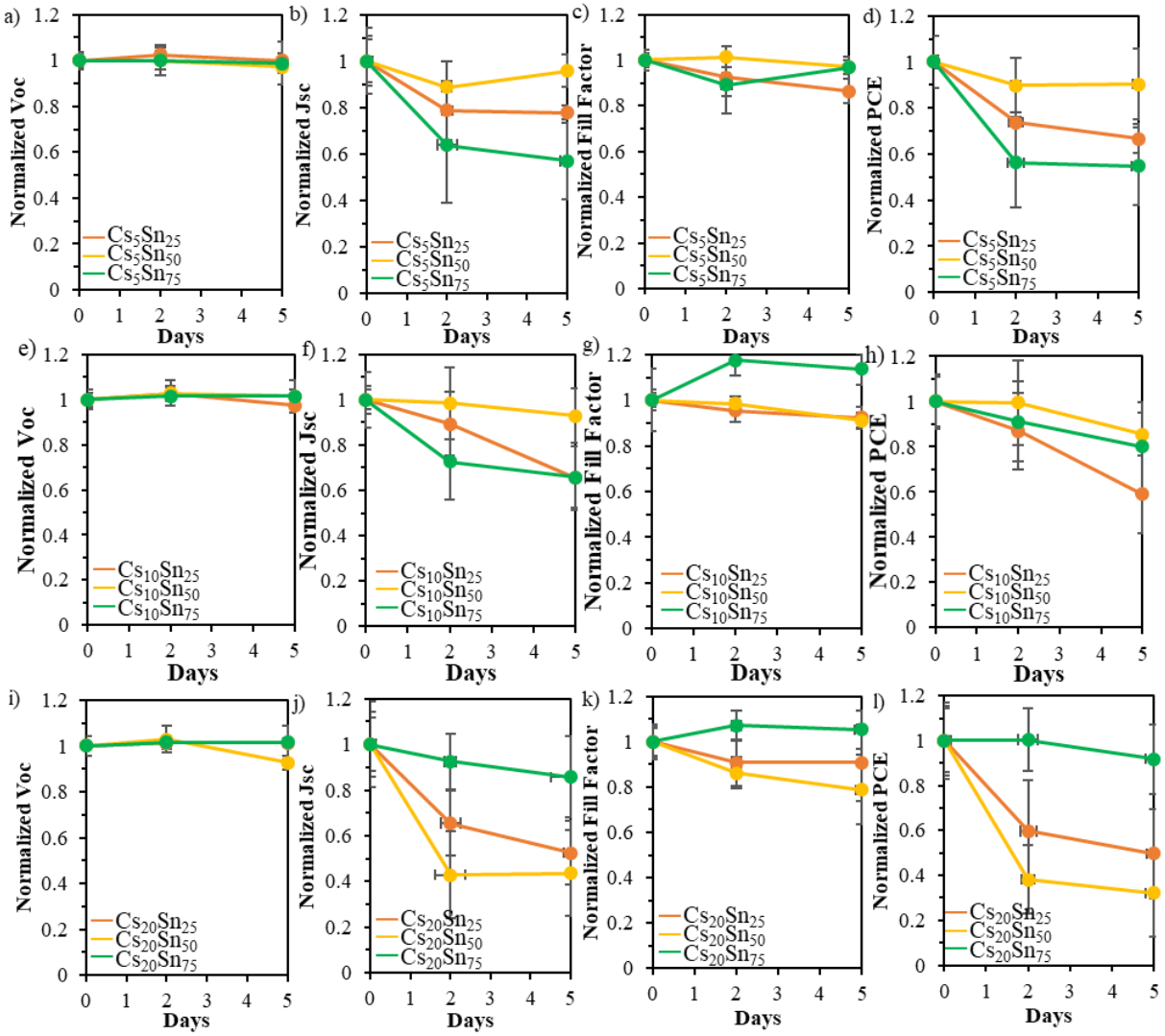

Figure 3-11. Normalized (a, e and i) Voc, (b, f and j) Jsc, (c, g and k) FF, and (d, h and l) PCE of $Cs_x(MA_{0.17}FA_{0.83})_{1-x}Pb_{1-y}Sn_y(I_{0.83}Br_{0.17})_3$ PVSCs for 5, 10 and 20% Cs, respectively, with Sn from 25 to 75% for each Cs composition, over time in ambient conditions.

conditions were evaluated. Figure 3-10 and 3-11 show the device performance of PVSCs over 30 days under the inert condition (glove box, O_2 < 10 ppm, H_2O < 10 ppm) and after an additional 5 days in ambient condition, respectively. Figure 3-12 characterizes the normalized V_{oc}, J_{sc}, FF and PCE for PVSCs as a function of Sn composition for each Cs content at the 30th day in inert and the 5th day in ambient conditions following the storage in the glove box for 30 days, comparing them to pristine devices. The 100% Sn PVSCs were omitted from stability tests due to their low performance in pristine conditions while the pure Pb PVSCs were omitted from the air exposure

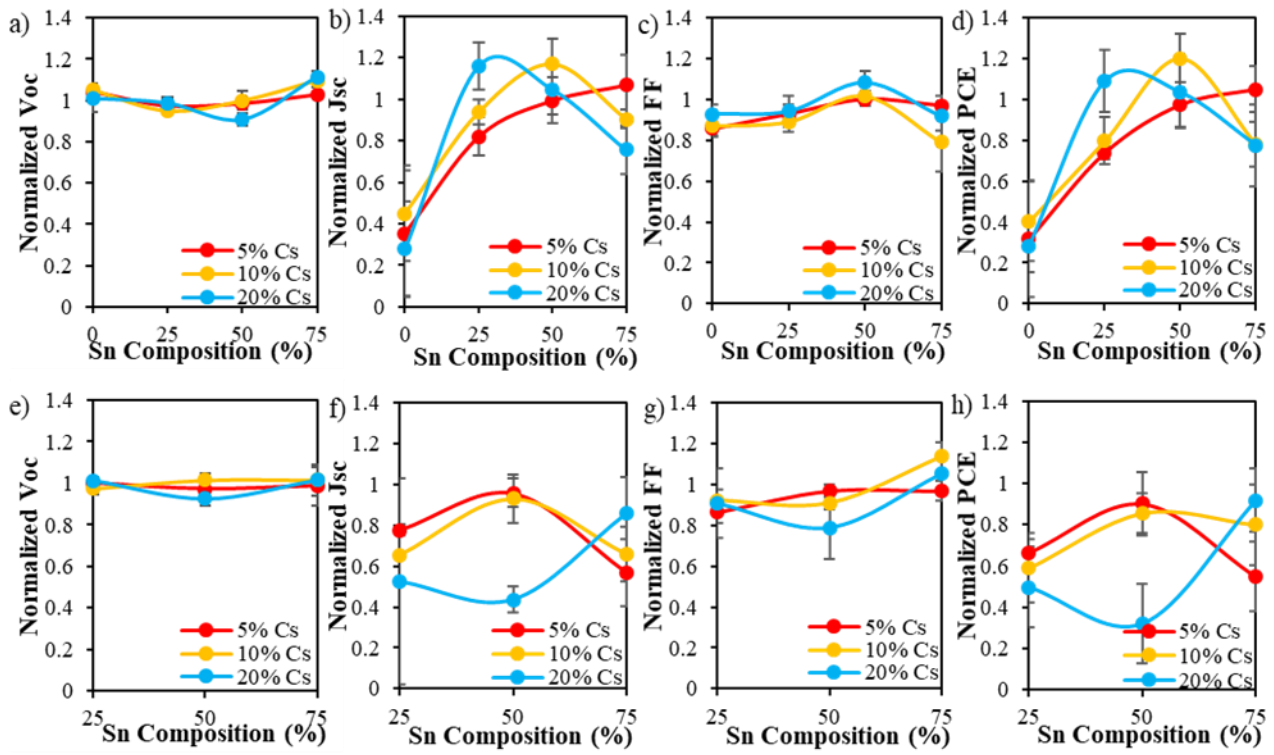

Figure 3-12. Normalized (a, e) V_{oc}, (b, f) J_{sc}, (c, g) FF, and (d, h) PCE for unencapsulated PVSCs as a function of Sn composition for each Cs under inert conditions after 30 days (a, b, c and d) and after additional 5 days under ambient conditions (e, f, g and h).

measurements due to its already degraded state after 30 days in the glove box. The V_{oc} of all PVSCs tested retained at least 87% of their original values in inert and ambient conditions demonstrating the stability of band energy alignments. Although there is fluctuation in FF values with air exposure, the biggest contributor to PCE degradation is the J_{sc}, which can be attributed to the SnF_2 segregation. Although the XRD (Figure 3-13) and SEM images (Figure 3-14) were taken from the perovskite films that were air exposed for 10 days, which may have exacerbated the segregation/degradation process, there could still be some ion migration in the active layers of the PVSCs in the inert condition that affected the J_{sc} over 30 days. Sn containing PVSCs stored in the inert condition all maintained 80% of the original PCE.

The Cs_5Sn_{75}, Cs_5Sn_{50}, $Cs_{10}Sn_{50}$, $Cs_{20}Sn_{25}$, and $Cs_{20}Sn_{50}$ all had an increase in PCE overtime and finished the 30-day period with a normalized PCE at 1 or higher. We proposed that the SnF_2

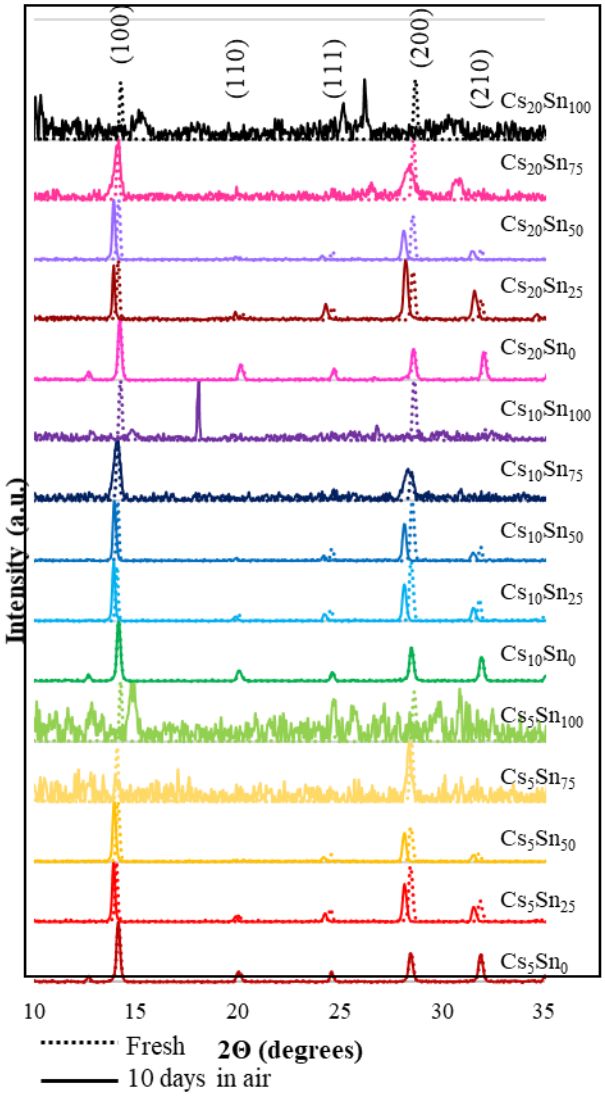

Figure 3-13. XRD patterns of pristine (dashed lines) and after 10 days of air exposure (solid lines) of the $Cs_x(MA_{0.17}FA_{0.83})_{1-x}Pb_{1-y}Sn_y(I_{0.83}Br_{0.17})_3$ perovskite thin films.

enhanced phase segregation created highly conductive Sn, F, Br rich particles as shown in the energy dispersion spectroscopy (EDS) measurements (Figure 3-15 and Table 3-2), temporarily increasing the J_{sc} before further segregation resulting in more recombination centers. Figure 3-13 shows XRD spectra of perovskite films pristine and after 10 days exposure to air. Previous reports indicate a new peak corresponding to MA_2SnI_6 at 14.9^{o} from Sn oxidation just after 1 day in ambient conditions. For all spectra, no such peak was observed even after 10 days, supporting the

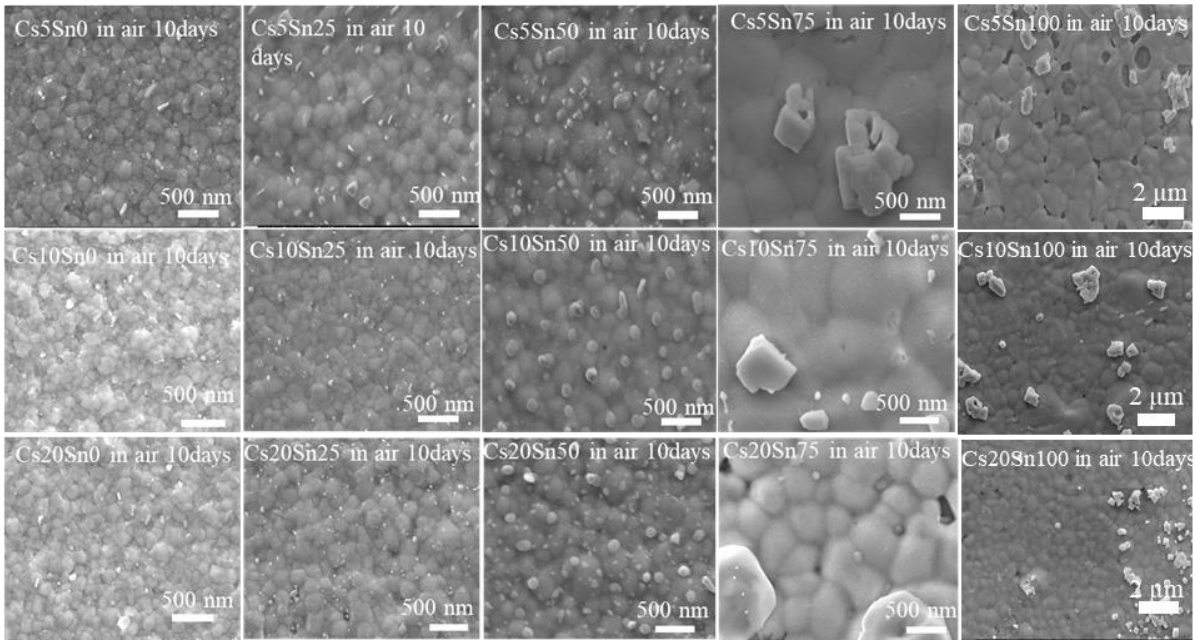

Figure 3-14. SEM images of $Cs_x(MA_{0.17}FA_{0.83})_{1-x}Pb_{1-y}Sn_y(I_{0.83}Br_{0.17})_3$ perovskite films after 10 days of air exposure.

previous literature that showed an identical suppression of an oxidation peak with the addition of Cs into the crystal lattice. The Pb-Sn alloyed perovskites exposed to air all have a right shift in peaks signaling an increase in d-spacing. This could be attributed to the phase segregation that occurs with air exposure as shown in the SEM images of air exposed perovskites in Figure 3-14. Although the air exposed perovskites have intact grains, some large particles ~500 nm appeared on the surfaces of 75 and 100% Sn perovskite thin films. EDS spot measurements on the new white rods and background on $Cs_{20}Sn_{25}$ thin film (Figure 3-15) showed that the white rods had a higher percentage of Sn, Br and F than those from the background (Table 3-2), indicating a slow segregation of these components from the perovskite thin film, resulting in an increased d-spacing of the crystal lattice. Previous reports have indicated ion migration of perovskites causing reversible Br and I rich segregation near grain boundaries under illumination and with current bias due to excess charge carriers.[108,109] We propose that the SnF_2 reducing agent, which for 75 and 100% Sn have a 7.5 and 10% mole excess SnF_2, respectively, create Br and F rich particles through

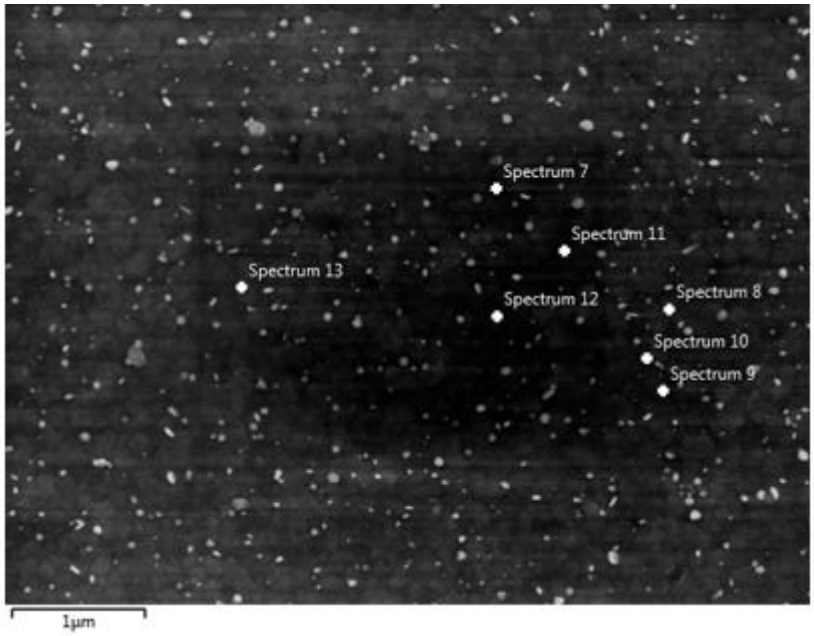

Figure 3-15. SEM image with the spots where EDS measurements were taken for $Cs_{20}Sn_{25}$ thin film after 10 days of air exposure.

Table 3-2. The EDS measured average atomic percentage of elements on rods and background from the $Cs_{20}Sn_{25}$ thin film after 10 days of air exposure.

	Cs	Pb	Sn	I	Br	F
Rods (%)	4.20±0.78	28.14±9.14	5.82±1.92	44.33±12.47	16.13±4.80	1.38±1.13
Background (%)	5.34±0.62	35.73±10.85	4.66±1.11	44.69±16.84	9.35±4.30	0.23±0.41

ion migration. This is supported by the lack of lattice shifting in the pure Pb perovskites due to the lack of SnF_2 reducing agent, avoiding the segregation effects. The air exposed XRD spectra for 75% Sn may not have the Sn^{4+} oxidation peak, but the cubic peaks are more broad, lower in intensity, and show splitting, indicating a possible degradation of the crystallinity due to this phase segregation. Unfortunately, after 10 days the pure Sn perovskites had a substantial decrease in the intensities of all cubic perovskite peaks, showing the instability of pure Sn perovskites. All the devices were moved out of the glove box after 30 days and stored in ambient condition and tested.

After leaving in ambient condition with 35 ± 5% humidity for 5 days, the Cs_5Sn_{50}, $Cs_{10}Sn_{50}$, $Cs_{10}Sn_{75}$ and $Cs_{20}Sn_{75}$ PVSCs can retain over 80% of the original PCE. The Cs_5Sn_{50} and $Cs_{20}Sn_{75}$ PVSC retained 90 and 92% of the original PCEs, respectively, demonstrating that Cs can be used to improve the stability of high Sn PVSCs in ambient conditions.

3.2.5 A-Site Cation Impacts on 75-100% Sn Region on Morphology, Crystallinity, and Band Gap

The Goldschmidt Tolerance (GT) factors and Octahedral Factors of the $XX_x(MA_{0.17}FA_{0.83})_{1-x}Pb_{1-y}Sn_y(I_{0.83}Br_{0.17})_3$ perovskites films in the 75-100% Sn region are illustrated in Figure 3-16, where XX stands for the cations Cs and Rb. The blue line indicates the GT of $FAPbI_3$ but because its octahedral factor is greater than the axis permits, it does not appear on the chart. The Rb and Rb/Cs doped perovskites have a decreased tolerance factor, pushing the perovskite more solidly into the cubic region. This could better support the cubic structure and crystallinity of these unexplored high Sn regions, allowing for further stabilization.

The one-step solution process and optimized solvent engineering was reused for all

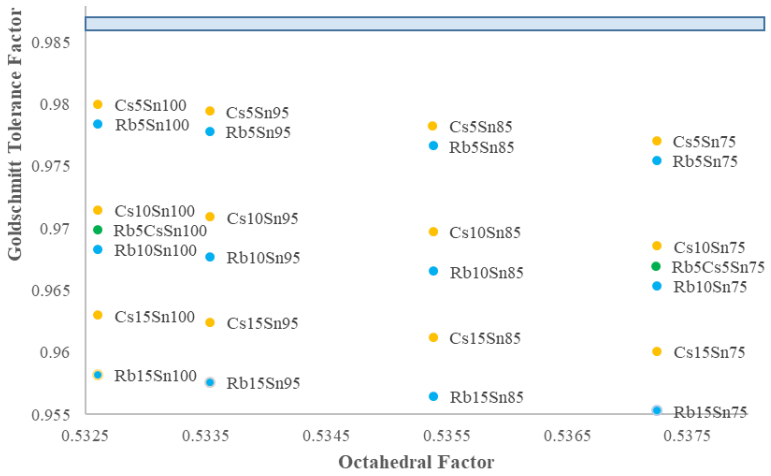

Figure 3-16. Goldschmidt Tolerance factors and Octahedral Factors of the $XX_x(MA_{0.17}FA_{0.83})_{1-x}Pb_{1-y}Sn_y(I_{0.83}Br_{0.17})_3$ perovskites films in the 75%-100% Sn region where XX stands for cations Rb and Cs.

preliminary films to better compare direct effects on cation choice. All precursors (MAI, FAI, PbI_2, CsI, RbI, GAI, and FABr) were dissolved in a DMSO:GBL (3:7, v/v) co-solvent to a total concentration of 2.5 M. 10% mol SnF_2 with respect to Sn content was added to suppress the formation of Sn^{4+}. All Sn compositions in that region were treated with the same 500 µl addition of toluene as well as annealed at 110°C for 10 min. Figure 3-17 shows the SEM images of the perovskite thin films with the compositions of $Cs_x(MA_{0.17}FA_{0.83})_{1-x}Pb_{1-y}Sn_y(I_{0.83}Br_{0.17})_3$, where x = 0.05, 0.1 and 0.15 and y = 0.75, 0.85, 0.95, 1. Cs_5 and Cs_{10} show the best film morphology with minimal pin holes in the 75%-95% region. The average grain size seems to still be maximum at 100% Sn. For Cs_5 and Cs_{10}, the grain size decreases from 75% Sn to 85% Sn and slightly increases to 95% Sn and finally reaches the maximum at 100% Sn. $Cs_{10}Sn_{85}$ is shown to have less pinholes and better grain boundary definition than Cs_5Sn_{85}, but $Cs_{10}Sn_{95}$ has grains that show poor boundary definition and poorer crystallinity. Cs_{15} shows poor morphology with an abundant of pinholes and some amorphous phase segregation. $Cs_{15}Sn_{95}$ shows arguably the poorest morphology with poor grain boundary definition, pin-holes, phase segregation, and poor crystallinity.

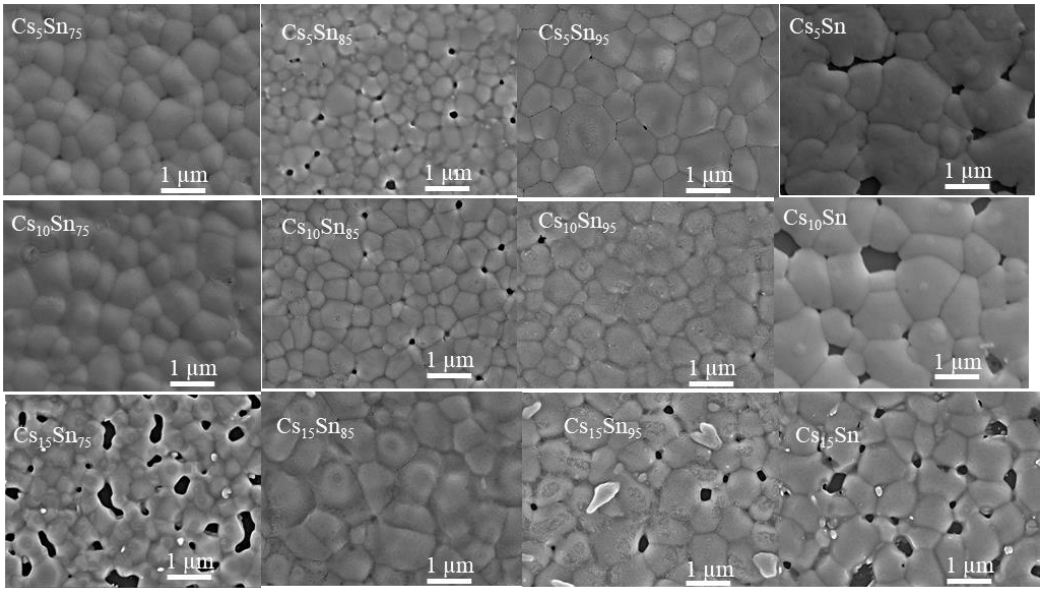

Figure 3-17. SEM images of $Cs_x(MA_{0.17}FA_{0.83})_{1-x}Pb_{1-y}Sn_y(I_{0.83}Br_{0.17})_3$ perovskite thin films with x = 0.05, 0.1 and 0.15 and y = 0.75, 0.85, 0.95, 1 at 20,000x magnification.

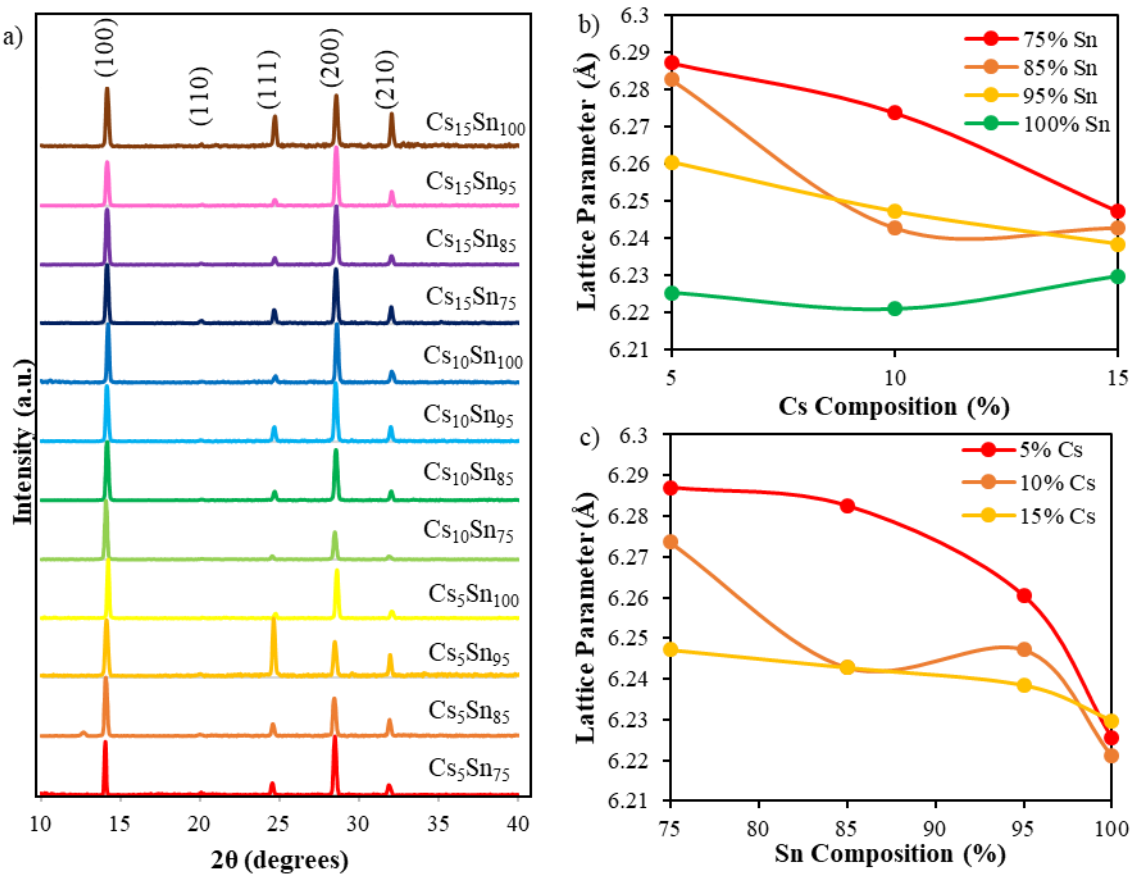

Figure 3-18. (a) X-ray diffraction (XRD) patterns of $Cs_x(MA_{0.17}FA_{0.83})_{1-x}Pb_{1-y}Sn_y(I_{0.83}Br_{0.17})_3$ perovskite thin films with x = 0.05, 0.1 and 0.15 and y = 0.75, 0.85, 0.95, and 1.0. (b) The cubic lattice parameters as a function of Cs composition for each Sn composition of all perovskites. (c) The cubic lattice parameters as a function of Sn composition for each Cs composition of all perovskites.

Figure 3-18 shows the normalized XRD spectra for each composition and the calculated lattice parameters. All perovskite compositions show a cubic structure with no additional peaks of photoinactive hexagonal δ-phase $FAPbI_3$ at 11.63°, and orthorhombic δ-phase $CsPbI_3$ at 9.80° and 13.00°. Cs_5Sn_{85} does have a small peak at 12.85° corresponding to unreacted PbI_2.[94,95,96] The (110) is almost eliminated in the 75%-100% region showing preferred orientation of the perovskite crystals. The (100) and (200) peaks have the strongest intensity indicating a preferred orientation with the glass substrates for all compositions except Cs_5Sn_{95} which has a strong (111) peak orientation. Figure 3-18b and c show a decrease lattice parameter size with increased amounts of

Sn due to the smaller ionic radius with 5% Cs decreasing from 6.287 Å for Cs_5Sn_{75}, to 6.283 Å for Cs_5Sn_{85}, to 6.260 Å for Cs_5Sn_{95} to 6.225 Å for Cs_5Sn_{100}. There is also a general decrease in lattice parameter with increased Cs, again because of the decrease in lattice parameter. For example, with 95% Sn, Cs_5Sn_{95} decreases from 6.260 Å to 6.247 Å for $Cs_{10}Sn_{95}$ to 6.238 Å for $Cs_{15}Sn_{95}$. $Cs_{15}Sn_{100}$ slightly deviates from this trend but this could be due to the amorphous phase segregation affecting the true amount of Cs in the perovskite films. The trend of decreased lattice parameter with decreased Sn is more linear than in chapter three signifying the decreased effect of octahedral tilting in this smaller region.

The UV-Vis absorption spectra of the $Cs_x(MA_{0.17}FA_{0.83})_{1-x}Pb_{1-y}Sn_y(I_{0.83}Br_{0.17})_3$ perovskite thin films and trends of cutoff are shown in Figures 3-19 a-d. Due to the sub-band gap states and scattering, the absorption spectra have a softened band edge. The band gaps estimated from the onsets of the absorption spectra are graphed as a function of Sn for each Cs composition as well as outlined in the table above. For 5% Cs, the band gap decreases from 1.30 eV to an approximate minimum of 1.21 eV at 85% Sn then increased again to 1.44 eV at 95% Sn and increased slightly to the maximum band gap of 1.46 eV at 100% Sn. For 10% C, the band gap increases slightly from 1.26 eV to 1.28 eV at 85% Sn then decreased to the approximate minimum of 1.21 eV at 95% Sn and increased to the maximum band gap of 1.43 eV at 100% Sn. Because the soft band edge, the deviation at $Cs_{10}Sn_{85}$ could be false since it is close to the band gap value for $Cs_{10}Sn_{75}$. Interestingly, it seems that the minima for the Pb/Sn hybrids can be shifts towards a higher Sn composition with an increased amount of Cs. The 15% Cs films has the band gap minimum at 1.16 eV for the 100% Sn film which is a deviation from literature that supports Pb/Sn hybrids can have

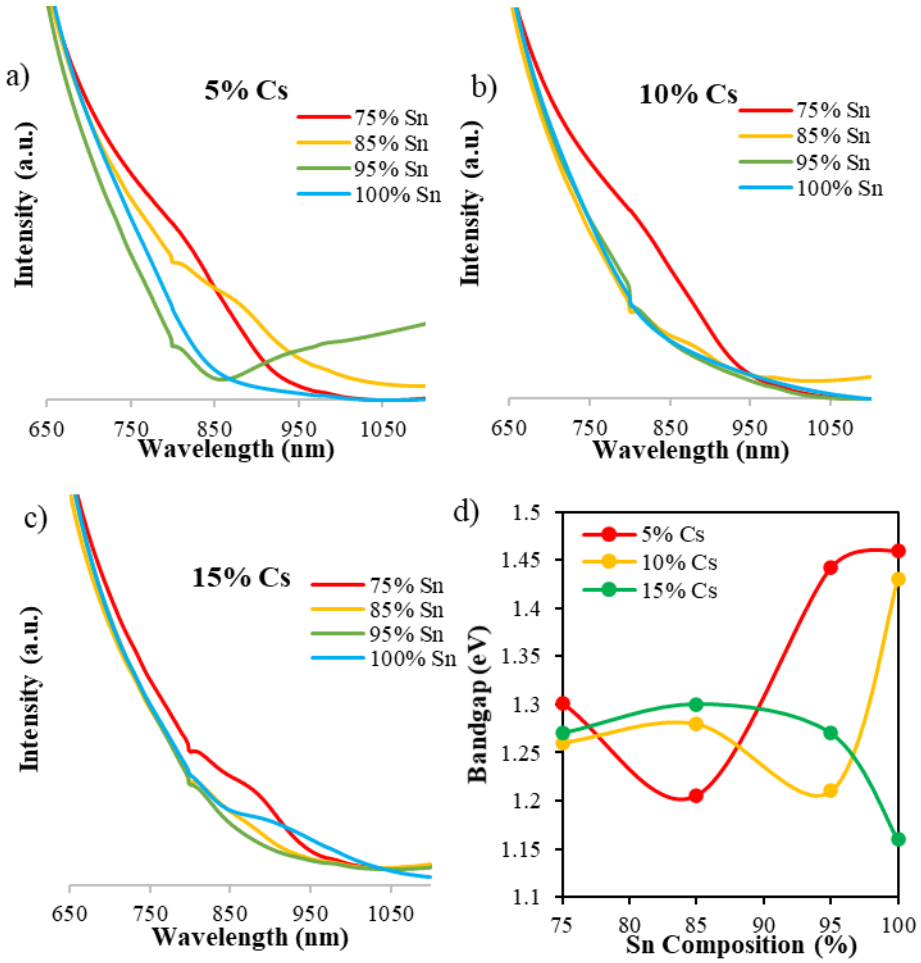

Figure 3-19. UV-vis absorption spectra of $Cs_x(MA_{0.17}FA_{0.83})_{1-x}Pb_{1-y}Sn_y(I_{0.83}Br_{0.17})_3$ perovskite thin films for (a) 5% Cs, (b) 10% Cs, and (c) 15% with y = 0.75, 0.85, 0.95, 1.0. The optical band gaps derived from the absorption onsets are also shown. (d) The band gap of $Cs_x(MA_{0.17}FA_{0.83})_{1-x}Pb_{1-y}Sn_y(I_{0.83}Br_{0.17})_3$ perovskite thin films as a function of Sn composition for different Cs contents.

a smaller minimum than either pure Pb or pure Sn perovskites. The band gaps of the 15% Cs perovskite could have been affected by the phase segregation seen in the films, affecting the true perovskite composition and thus the location of the band edges. Although the goal was to find a high Sn perovskite composition that has the ideal band gap of 1.34 eV, we were not able to locate the composition. For 5% Cs, if the upward trend is generally linear, the 1.34 eV band gap should be found at 90% Sn. For 10% Cs, the 1.34 eV band gap would correspond to 98% Sn.

3.2.6 Exploring Band Alignment in Triple Cation Perovskites

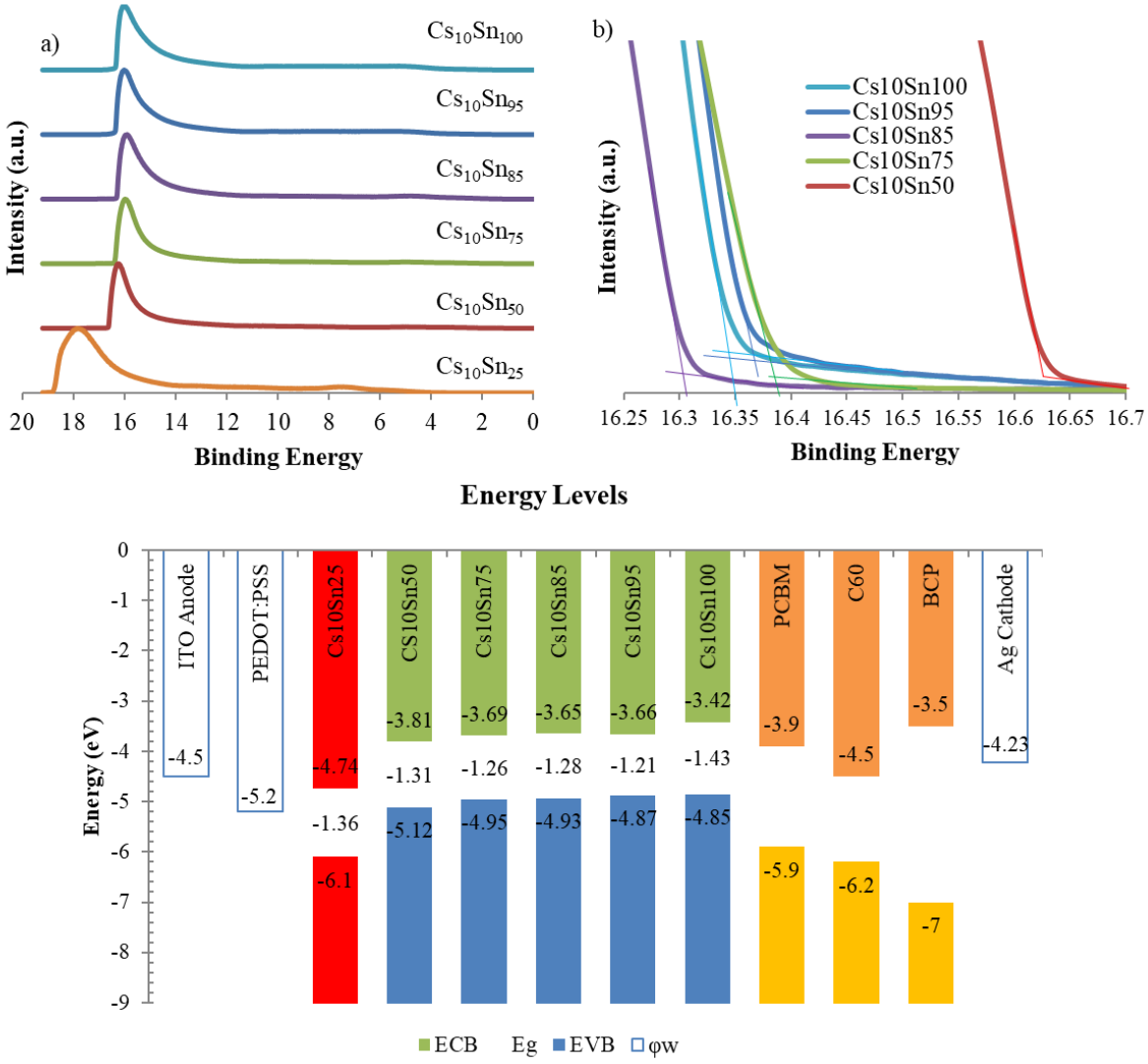

Figure 3-20. UPS spectra of six perovskite thin films: $Cs_{10}Sn_{25}$, $Cs_{10}Sn_{50}$, $Cs_{10}Sn_{75}$, $Cs_{10}Sn_{85}$, $Cs_{10}Sn_{95}$, $Cs_{10}Sn_{100}$ with (a) total UPS spectrum of as prepared film., (b) photoemission cut-off, and band energy diagram of materials deployed in the PVSCs with an inverted architecture.

To determine the valence band (VB) of the Pb/Sn hybrid perovskites, we performed UPS scans on $Cs_{10}Sn_{25}$, $Cs_{10}Sn_{50}$, $Cs_{10}Sn_{75}$, $Cs_{10}Sn_{85}$, $Cs_{10}Sn_{95}$, $Cs_{10}Sn_{100}$. The UPS spectra in Figure 3-20b show a distinct left shift with the VB lowering in binding energy with increased amounts of Sn. We normalized all the spectra in Figure 3-20 a for visual clarity.The VBM onset and photoemission cutoff were calculated with a linear extrapolation analysis and used to calculate the

valence band of the varying perovskite composition which are illustrated in Figure 3-20c. The the photoemission cutoff (Figure 3-20b) decreases from 18.74 eV to 16.35 eV for for $Cs_{10}Sn_{25}$ to $Cs_{10}Sn$, respectively. The band energy diagram in Figure 3-20c illustrate the valence band, conduction band, and band gap of each perovskite material and electron transport layer as well as the workfunction for the electrodes and hole transport layer. The valence band was calculated by substrating the VBM onset from the photoemission cutoff demonstrated in chapter 2. The conduction band was calculated using the band gaps observed from the UV-Vis spectra, which were added to the calculated valence band. The electronic structure show that with increased Sn additive, there is an upward shift of both valence and conduction band. When increasing Sn from 25%- to 50%, the valence band shifts upward at a higher level than the workfunction of PEDOT:PSS, changing this hole transport layer to a hole blocking layer. When increasing from 50% to 75% Sn, the valence band shifts increases from -5.12 eV to -4.95 eV shifting above the PEDOT:PSS workfunction by 0.25 eV. When Sn is increased to 100% Sn, the valence band of the perovskite is above the PEDOT:PSS workfunction by 0.35 eV. This further shift to a hole blocking layer would decrease the V_{oc} of devices made with high Sn, decreasing the maxmimum possible PCE. Because there is an upward shift in, even though $PC_{60}BM$ would still act as an electron transport layer, there is now a mismatch of 0.48 eV because the conduction band of $Cs_{10}Sn$ and $PC_{60}BM$, which would also be contributing to the lower V_{oc} and opens doors for an alternative electron transport layer as well.

Figure 3-21 shows the XPS survey for the $Cs_{10}Sn_{25}$, $Cs_{10}Sn_{50}$, $Cs_{10}Sn_{75}$, $Cs_{10}Sn_{85}$, $Cs_{10}Sn_{95}$, $Cs_{10}Sn_{100}$ compositions with corresponding C 1s, N 1s, O 1s, Cs 3d, Sn 3d, I 3d, Pb 4f, F 1s, and Br 3d peak positions. At approximately 486 eV, the Sn $3d_{5/2}$ peak position is shown to increase in relatively intensity from $Cs_{10}Sn_{25}$ to $Cs_{10}Sn$ showing in increase in Sn concentration. The Pb 4f

peak at 139 eV decreases in intensity until there is no visible peak for the pure Sn perovskite film showing a steady decrease in Pb concentration. Because the Pb doublets were unresolved, the Pb $4f_{7/2}$ and $4f_{5/2}$ peaks were measured for the composition area but this doublet measurement was taken to account when calculating percentage content of each atom. Unfortunately, at approximately 532 eV, there is a peak that begins to grow in intensity with increased Sn concentration that is attributed to O 1s. Because the films are briefly exposed to air when staging the substrates in the instrument, the oxygen can bind with the surface. Sn has a higher affinity for O than Pb, which is reflected in the increased oxygen concentration with higher Sn

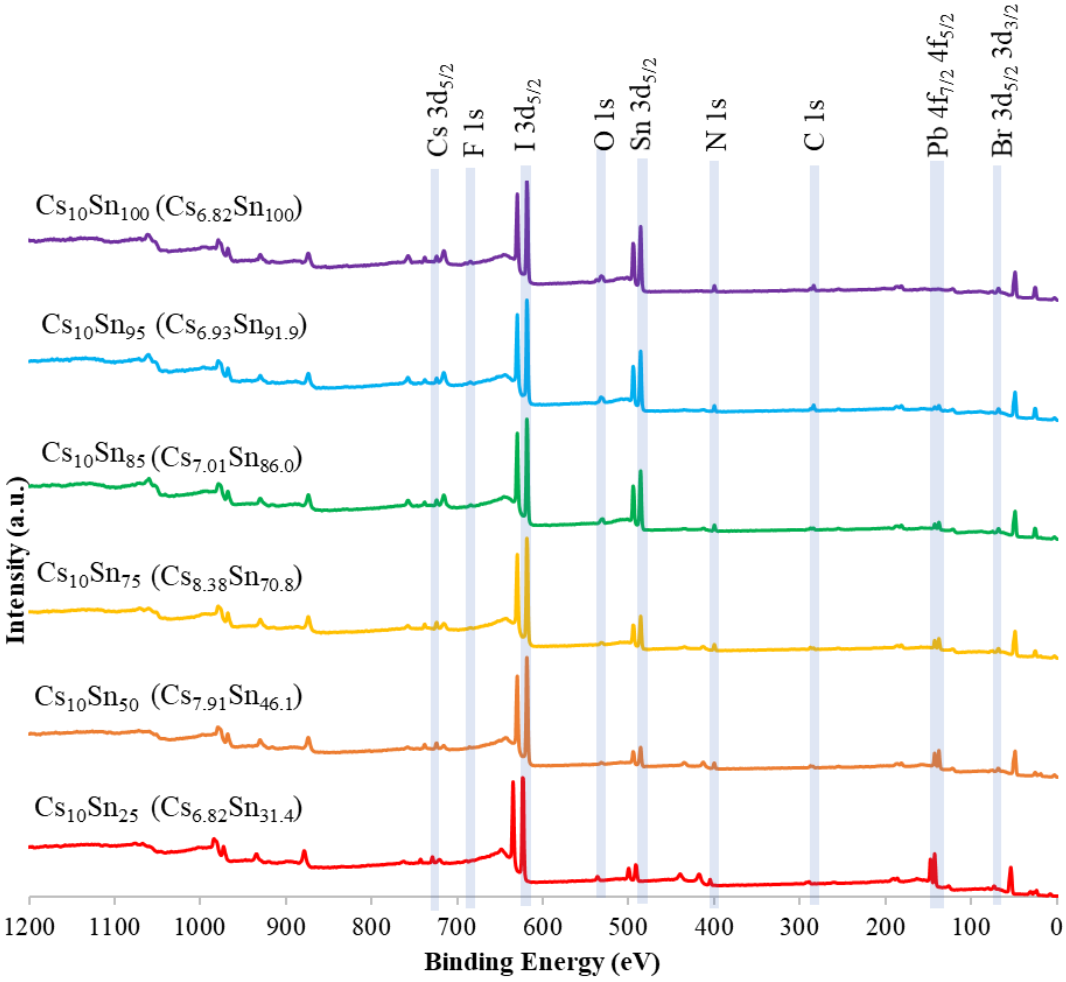

Figure 3-21. XPS survey of $Cs_{10}Sn_{25}$, $Cs_{10}Sn_{50}$, $Cs_{10}Sn_{75}$, $Cs_{10}Sn_{85}$, $Cs_{10}Sn_{95}$, $Cs_{10}Sn_{100}$ with corresponding C 1s, N 1s, O 1s, Cs 3d, Sn 3d, I 3d, Pb 4f, F 1s, and Br 3d peak positions. Compositions in parenthesis shown with true % of Cs and Sn.

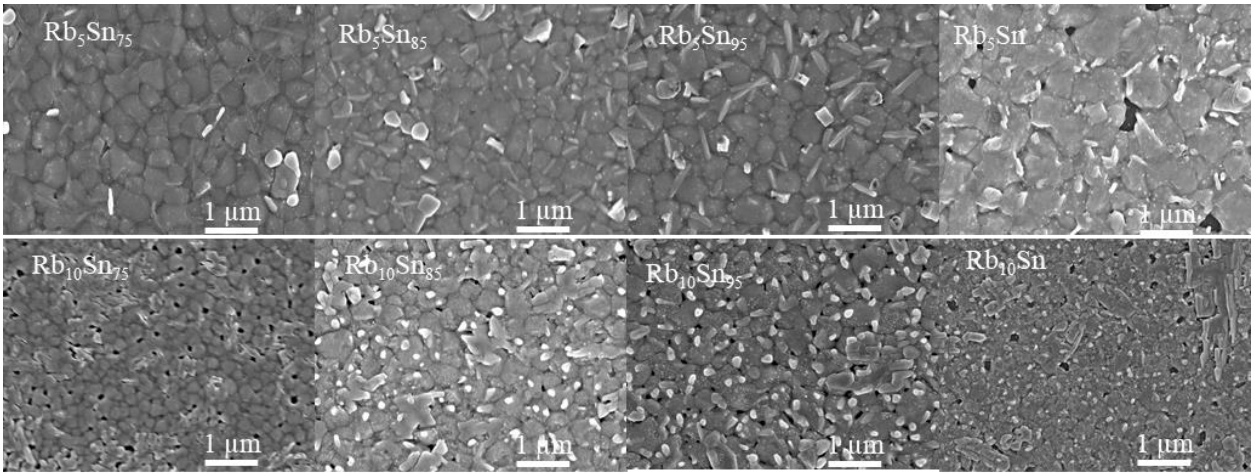

Figure 3-22. SEM images of $Rb_x(MA_{0.17}FA_{0.83})_{1-x}Pb_{1-y}Sn_y(I_{0.83}Br_{0.17})_3$ perovskite thin films with x = 0.05, 0.1 and y = 0.75, 0.85, 0.95, 1 at 20,000 magnification.

percentage and this could be problematic if this oxygen is are oxidizing the Sn from the Sn^{2+} to Sn^{4+} state. It has been previously reported that Sn^{2+} and Sn^{4+} signals appear at 486.25 eV and 486.5 eV, respectively. Our XPS results do not show two separate peaks because our step size was too large at 1 eV. If we want to analyze the oxidation state of Sn, we would need to take high resolution spectra in the future. The Cs 3d peak at 724 eV, I 3d peak at 619 eV, N 1s peak at 400 eV, C1s peak at 284 eV, and Br 3d peak at 68 eV all show minimal changes in peak intensity. Because the Br doublets was unresolved, the Br $3d_{5/2}$ and $3d_{3/2}$ peaks were measured for the composition area, but this doublet measurement was again taken to account when calculating percentage content of each atom. Because the Br and Pb peaks require lower binding energy, these peaks are difficult to resolve without high resolution UPS scanning. Compared with the other films, $Cs_{10}Sn_{25}$ shows a noticeable shift in all XPS peak positions and UPS spectrum to higher binding energies suggesting charging. Charging typically occurs for samples that are insulators and as the film is flooded with excess electrons, we see a shift to higher binding energies. Because our film is conductive, but our substrate is not, this could be due to a simple loose copper contact to our film and so UPS and XPS data for the $Cs_{10}Sn_{25}$ compositions are unreliable. The "true" perovskite composition at the surface for each sample is in parenthesis in Figure 3-21. Although there is excess SnF_2 in each sample,

almost all samples showed a lower "true" Sn %, which is defined in terms of Pb content ($Pb_{100-x}Sn_x$) and not is terms of total atom content, is lower than expected. All samples also saw a lower "true" Cs%, which is defined in terms of organic cation content $Cs_x(M)_{100-x}$ and not is terms of total atom content, compared to the theoretical Cs in the sample.

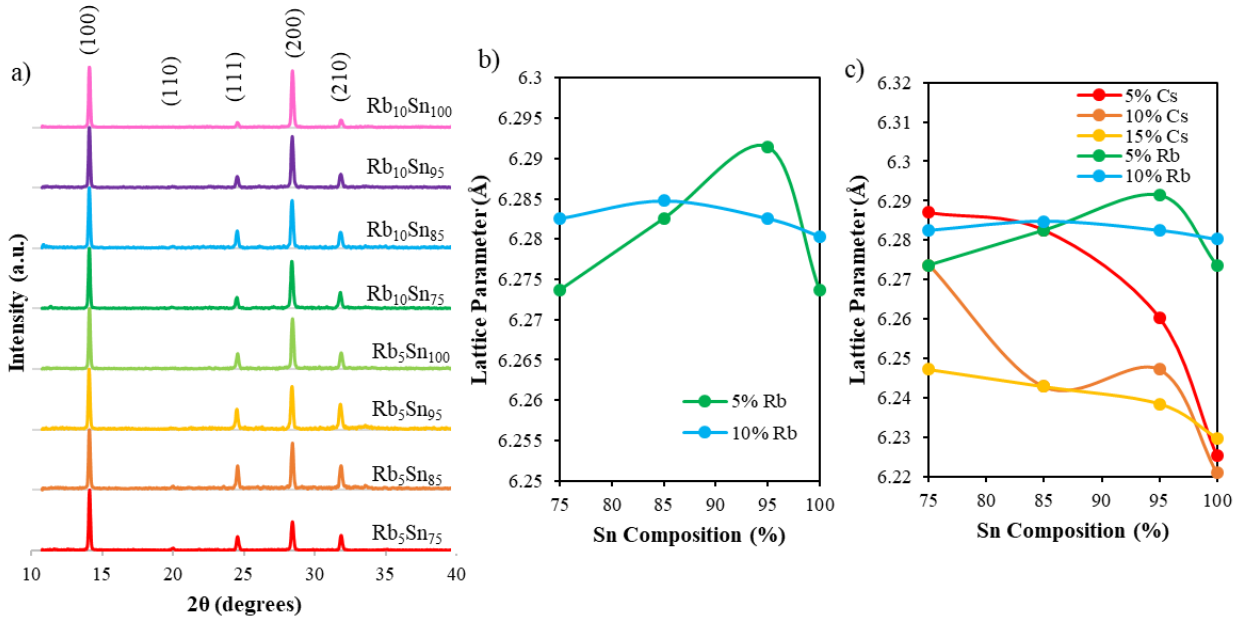

Figure 3-23. (a) XRD patterns of $Rb_x(MA_{0.17}FA_{0.83})_{1-x}Pb_{1-y}Sn_y(I_{0.83}Br_{0.17})_3$ perovskite thin films with x = 0.05, and 0.1and y = 0.75, 0.85, 0.95, and 1.0. (b) The cubic lattice parameters as a function of Sn composition for each Rb composition of all perovskites. (c) The cubic lattice parameters as a function of Sn composition for each Cs and Rb composition of all perovskites with Cs and Rb.

Figure 3-22 shows the SEM images of the perovskite thin films with the compositions of $Rb_x(MA_{0.17}FA_{0.83})_{1-x}Pb_{1-y}Sn_y(I_{0.83}Br_{0.17})_3$, where x = 0.05, and 0.1, and y = 0, 0.25, 0.50, 0.75, and 1.0. Although 5% Rb shows minimized pinholes, there is amorphous phase segregation in all perovskite films. The phase segregation increases with increased amount of Sn, with 75% Sn having the lesser amount and 100% Sn having the greatest amount. The Rb_5Sn_{75}, Rb_5Sn_{85}, and Rb_5Sn_{95} compositions have visible grains with well-defined boundaries visible beneath the segregation on the surface. Rb_5Sn_{100} has poorly formed grains with low boundary definition. The 10% Rb compositions have severe phase separation and pinholes in all films. The 75, 85, and 95%

Sn films again have better defined grains than the 100% Sn composition for 10% Rb.

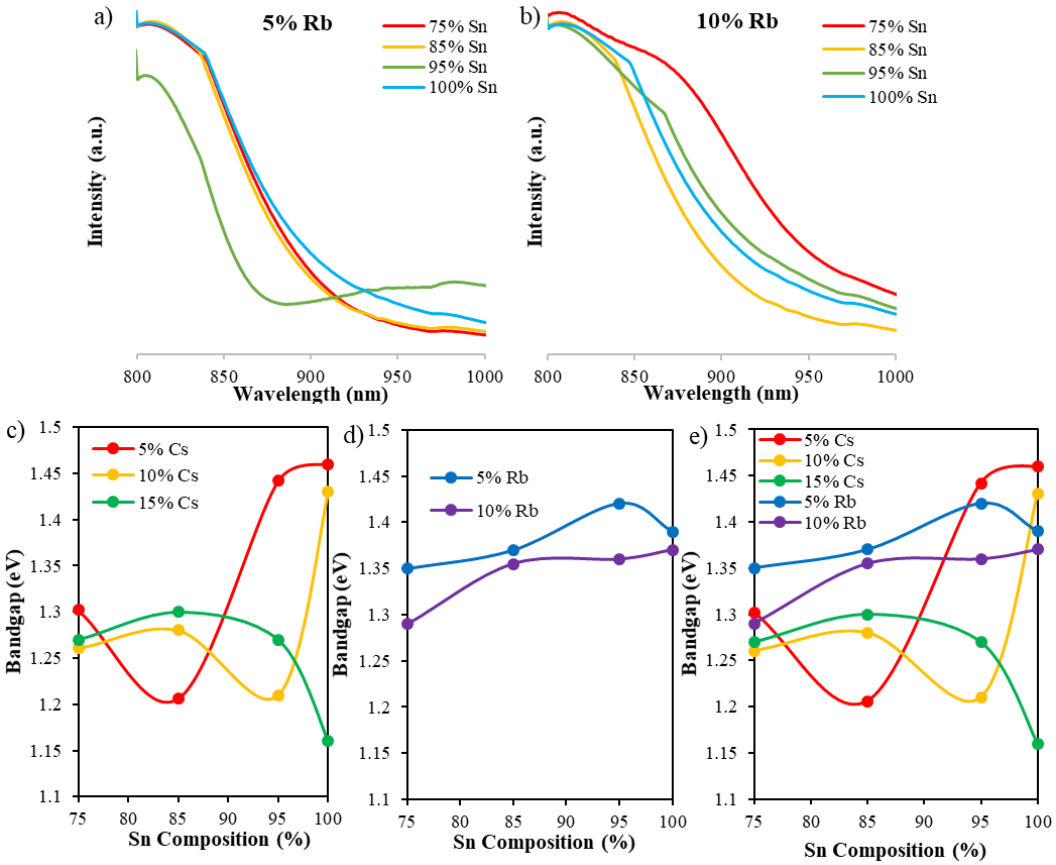

Figure 3-24. UV-vis absorption spectra of $Rb_x(MA_{0.17}FA_{0.83})_{1-x}Pb_{1-y}Sn_y(I_{0.83}Br_{0.17})_3$ perovskite thin films for (a) 5% Rb, (b) 10% Rb with y = 0.75, 0.85, 0.95, 1.0. The optical band gaps derived from the absorption onsets are also shown. (c) The band gap of Cs_xSn_y perovskite thin films as a function of Sn composition for different Cs contents. (d) The band gap of Rb_xSn_y perovskite thin films as a function of Sn composition for different Rb contents (e) The band gap of perovskite thin films as a function of Sn composition for different Rb and Cs contents.

Figure 3-23 shows the corresponding normalized XRD spectra and lattice parameters for the Rb doped perovskites. Figure 3-23a shows that all the Rb perovskite are in the cubic phase. The lack of additional peaks suggests that the phase segregation seen in the SEM images are noncrystalline. The Rb perovskite (110) peak is almost eliminated, sharing the trend with the Cs high Sn perovskites for preferred orientation instead on the (100) and (200) peaks. Figure 3-23b show the lattice parameter trends for 5% and 10% Rb for the Sn compositions tested. There is no overall trend for these lattice parameters. We would expect that the 10% Rb has a smaller lattice

parameter than 5% Rb, because of the smaller ionic radius, but this only occurs at 95% Sn when the lattice parameter for Rb_5Sn_{95} decreases from 6.291 Å to 6.283 Å for $Rb_{10}Sn_{95}$. Unfortunately, because of the corresponding increase in segregation with the 10% Rb, the smaller atom could have precipitated into the amorphous phase in the perovskites for the other Sn percentages, creating an overall increase in lattice parameter in the bulk crystalline perovskite material. Figure 3-23c shows the lattice parameter trends for both Cs and Rb cations. We would expect that the Rb doped perovskites would have a smaller lattice parameter than the Cs doped perovskites but due to the phase segregation, that is not the case. Because the Cs perovskite have no phase segregation except for the 15% Cs compositions, they are observed to have the lower lattice parameter.

Figure 3-24a shows the UV-Vis absorption spectra of $Rb_x(MA_{0.17}FA_{0.83})_{1-x}Pb_{1-y}Sn_y(I_{0.83}Br_{0.17})_3$ perovskite thin films for x = 0.05, and 0.10, with y = 0.75, 0.85, 0.95, 1.0. For both 5% and 10% Rb, the minimum band gap is at 75%. This again goes against observation in literature where the Pb/Sn hybrids should have the minimum band gap because of the minimize lattice distortion increasing M-X orbital overlap. We have previously shown that for Sn concentrations above 50%, increasing perovskite doping with smaller cations decrease the material band gap. Therefore, we expect that Rb would follow the same trend and would lower the band gap when compared with the same amount of Cs dopant. Instead, we find the opposite trend where the Rb perovskites have the largest band gap for almost all Sn composition. This again could be attributed to the phase separation with this Rb dopant. Phase segregated Rb would make the mean radius of the A-site bulk material larger, which explains both the larger lattice parameter for these Rb doped perovskites compared with the Cs doped and the larger band gap. We previously illustrated how at high Sn contents, the addition of the smaller Cs cation, which decreases the average A-site radius, decreased the band gap. Because Rb segregated out, the opposite trend

would be expected resulting in a larger band gap compared to the Cs doped perovskites.

3.2.7 Material Stability and Device Performance of High 75-100% Sn Range

The annealing temperature of the 75%-100% Sn range with only Cs or Rb as the inorganic component was kept at 110°C. This was chosen based on the earlier SEM images showing smoothest densest films for the 100% Sn composition. Figure 3-25 shows the film morphology of Rb_xSn and $Rb_xCs_x(MA_{0.17}FA_{0.83})_{1-x}Sn(I_{0.83}Br_{0.17})_3$ that were instead annealed at 100 °C. There was an improvement in the film morphology at this lower annealing temperature, showing that for Rb films the higher annealing temperature exacerbated the phase segregation process. All films have a decreased concentration of pinholes. The 5% Rb film has no noticeable phase segregation. With increased Rb, there is an increased amount of phase segregation with 20% Rb having the poorly defined grain boundaries and high amounts of phase segregation. Rb_5Cs_5Sn was expected to have minimize phase segregation but instead had more phase segregation than Rb_{10}. The films were then left in ambient conditions for 8 days. All films showed very noticeable phase segregation with large precipitates reaching multiple microns in size. All films also had a decrease in grain

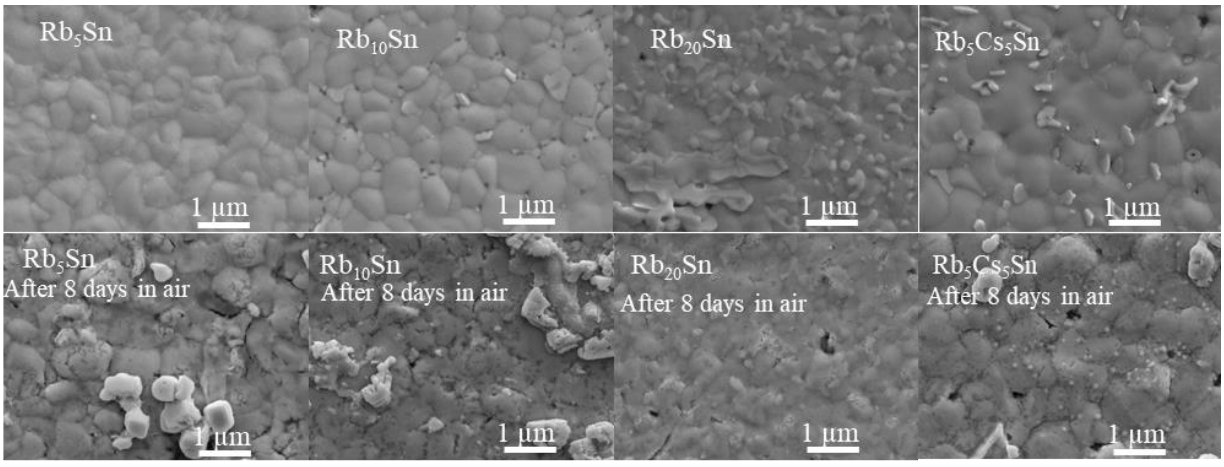

Figure 3-25. SEM images of $Rb_xCs_x(MA_{0.17}FA_{0.83})_{1-x}Sn(I_{0.83}Br_{0.17})_3$ perovskite thin films with x = 0.05, 0.1, and 0.2 at 20,000 magnification before and after 8 days in air exposure. The films were annealed at 100C for 10 min.

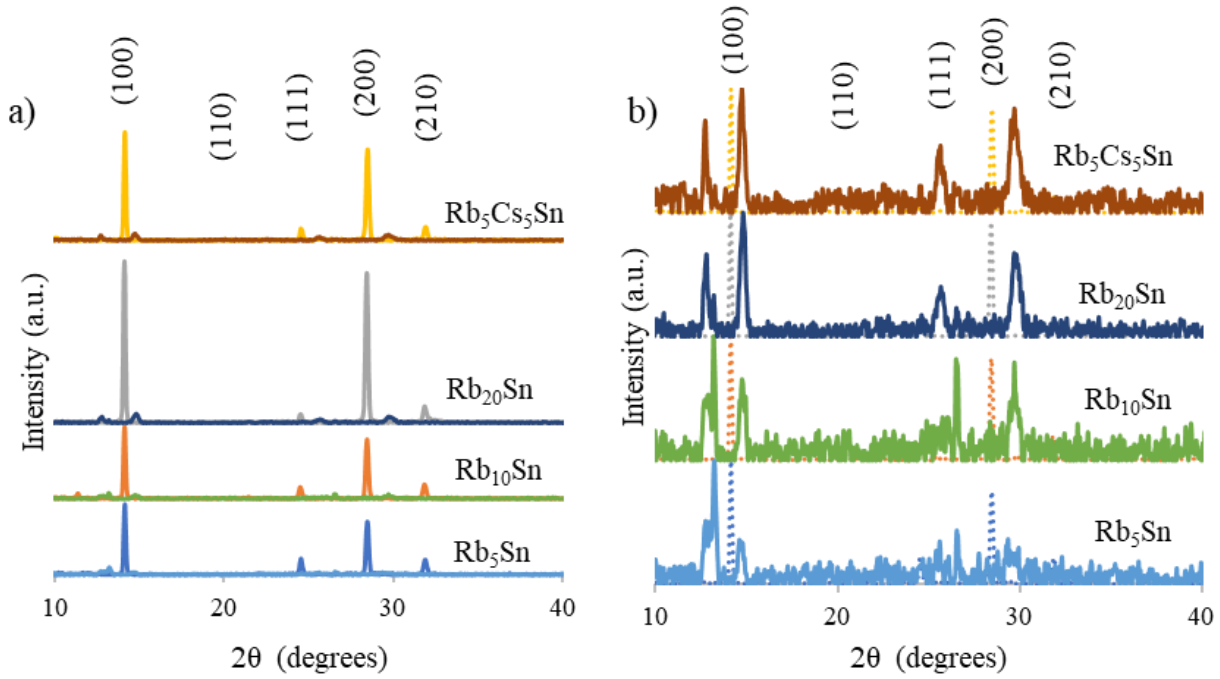

Figure 3-26. (a) XRD patterns of $Rb_xCs_y(MA_{0.17}FA_{0.83})_{1-x-y}Sn(I_{0.83}Br_{0.17})_3$ perovskite thin films with x = 0.05, 0.1, and 0.2, y = 0, 0.05 with fresh films and after 8 days in air. The spectra are not normalized to show decrease in intensity after 8 days in air. (b) XRD patterns of $Rb_xCs_y(MA_{0.17}FA_{0.83})_{1-x-y}Sn(I_{0.83}Br_{0.17})_3$ perovskite thin films with x = 0.05, 0.1, and 0.2, y = 0, 0.05 with fresh films (dotted line) and after 8 days in air (solid line) normalized to show shifts in peaks and appearance in new peaks.

crystallinity and grain boundary definition showing degradation of the perovskite material.

Figure 3-26a shows the XRD spectra of the corresponding before and after air exposure. Although the fresh films show the cubic XRD peaks, after 8 days in air, the intensity of all the peaks is decreased making the peaks illegible without normalization. Figure 3-26b shows the normalized XRD spectra before and after air exposure. The fresh films are the dotted lines while the air exposed films are in solid lines. The cubic peaks are degraded while new phase contamination peaks as well as lead iodide peaks are introduced into the XRD spectra.

To see how viable the current Rb triple cation mixture was in PVSCs, we fabricated PVSCs with the same structure used in the cesium triple cation devices. Figure 3-27 illustrated the current density-voltage (J-V) characteristics of $Rb_xCs_x(MA_{0.17}FA_{0.83})_{1-x}Sn(I_{0.83}Br_{0.17})_3$ PVSCs with x = 0, 0.05, 0.10 along with Table 3-3 showing the corresponding photovoltaic parameters. Cs_0Sn does

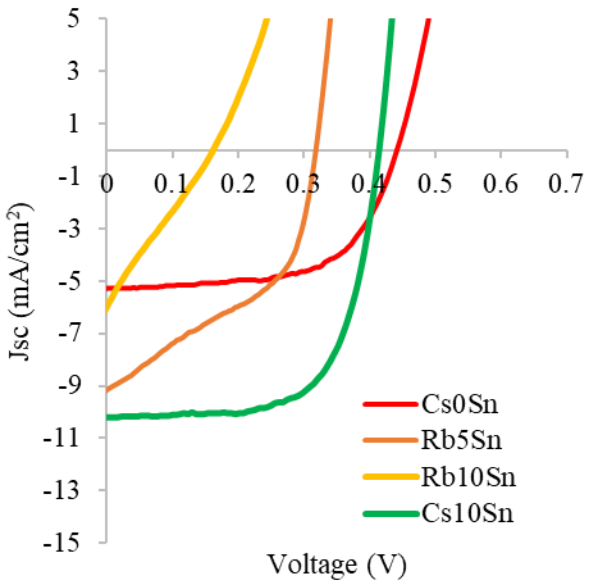

Figure 3-27. The current density-voltage (J-V) characteristics of $Rb_xCs_y(MA_{0.17}FA_{0.83})_{1-x-y}Sn(I_{0.83}Br_{0.17})_3$ PVSCs with x = 0, 0.05, 0.10, y= 0, 0.1under AM 1.5 illumination at a scan rate of 0.01V s^{-1} from 0 to 1.2 V.

Table 3-3. The photovoltaic parameters from $Rb_xCs_y(MA_{0.17}FA_{0.83})_{1-x-y}Sn(I_{0.83}Br_{0.17})_3$ PVSCs with x = 0, 0.05, 0.10, y= 0, 0.1 measured under AM 1.5 illumination from forward J-V scans

Device	V_{oc} (V)	J_{sc} (mA cm^{-2})	FF	PCE (%)	PCE_{max} (%)
Cs_0Sn	0.44 ±0.01	5.03 ±0.47	0.61 ±0.01	1.34 ±0.16	1.44
Rb_5Sn	0.31 ± 0.01	8.43 ± 1.86	0.44 ± 0.04	1.15 ± 0.20	1.28
$Rb_{10}Sn$	0.16 ±0.00	5.64 ±0.38	0.26 ±0.01	0.24 ±0.0	0.24
$Cs_{10}Sn$	0.41 ±0.00	8.98 ±1.39	0.65 ±0.02	2.43 ±0.45	2.81

not have any cation and with the addition of 5% Rb, there is a decrease in fill factor from an average of 0.61 to 0.26. The J_{sc} increases from an average of 8.43 to 5.03 mA/cm^2 but the Rb_5 devices have a much larger standard deviation showing a lessened reproducibility. The V_{oc} also decreased from an average of 0.44 to 0.31. A further addition to Rb_{10} decreases the V_{oc} further to 0.16. This shift suggests a decrease in band energy alignment possibly by the upward shift of both conduction and valence band with the introduction of Rb to the perovskite composition. The current density lowers down to 5.64 mA/cm^2 and the FF also drops to an average of 0.26 with a max PCE of 0.24 for $Rb_{10}Sn$ most likely due to the small phase segregation.

3.2.8 Optimizing Pure Sn Film Morphology Through Varying SnF_2 Conditions

To better compare our device performance to other labs, we want to increase the J_{sc} in our pure Sn devices by further improving the morphology and crystallinity through experimenting with SnF_2 additives and annealling conditions. Xiao et al. has shown how increased amounts of SnF_2 can act as nucleation sites that lead to smooth, pinhole free, dense grain growth of $MASnIBr_2$ thin films. Their optimized SnF_2 content was determined to be 30 mol% excess SnF_2, which resulted in a max PCE of 3.70% and an increased Jsc of 13.71 mA/cm^2.[110] To decrease the amount of pinholes in the pure Sn perovskite films, which would decrease nonradiative recombination and increase the current density of the corresponding devices, we added both 10 mol% and 20 mol% SnF_2 in preparing the $(Cs_{0.05}(MA_{0.17}FA_{0.83})_{0.95}Sn(I_{0.83}Br_{0.17})_3$,

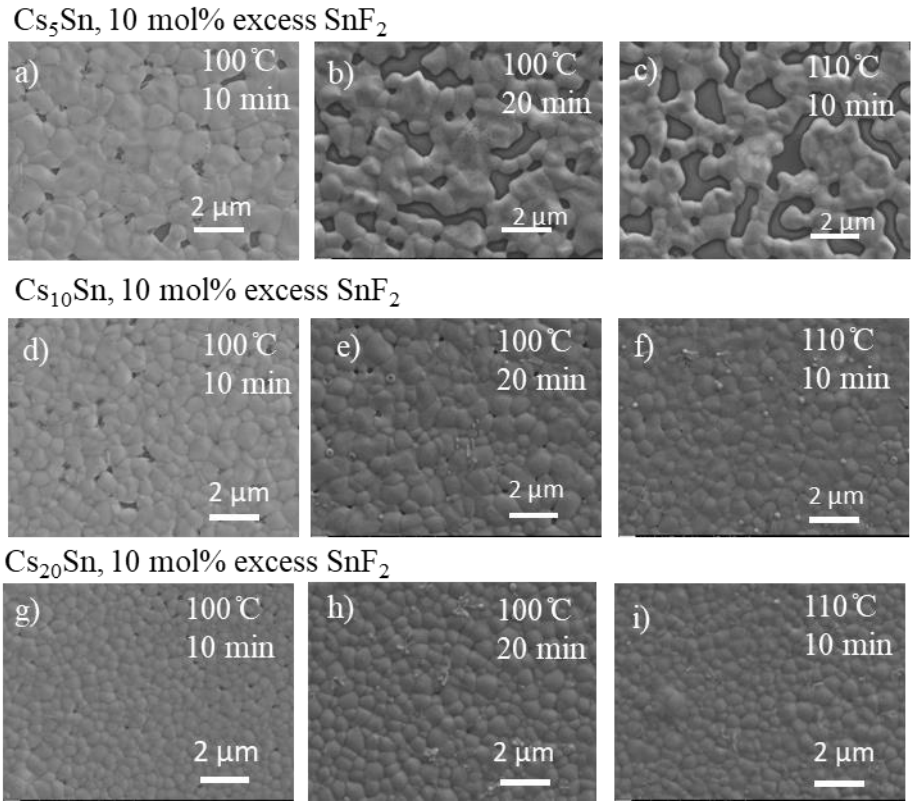

Figure 3-28. SEM images of perovskites with the perovskite composition $Cs_{0.05}(MA_{0.17}FA_{0.83})_{0.95}Sn(I_{0.83}Br_{0.17})_3$ with 10 mol% excess SnF_2 annealed at (a) 100°C for 10 min, (b) 100°C for 20 min, and (c) 110°C for 10 minutes, 10 mol% excess SnF_2 annealed at (d) 70°C, (e) 80°C, and (f) 110°C and 20 mol% excess SnF_2 annealed at (g) 70°C, (h) 80°C, and (i) 110°C.

$(Cs_{0.10}(MA_{0.17}FA_{0.83})_{0.90}Sn(I_{0.83}Br_{0.17})_3$, $(Cs_{0.20}(MA_{0.17}FA_{0.83})_{0.80}Sn(I_{0.83}Br_{0.17})_3$ films. To make description simple, we will use the notation Cs_xSn to represent the thin films. For example, Cs_5Sn represents the thin films with the composition of $Cs_{0.05}(MA_{0.17}FA_{0.83})_{0.95}Sn(I_{0.83}Br_{0.17})_3$. Figure 3-28 shows the SEM images of the Cs_5Sn thin films prepared with the addition of 10 and 20 mol% of SnF_2 and annealed at 70°C, 80°C, and 100°C temperatures. For Cs_5Sn, 3-29 a-c show that higher annealing temperatures result in and longer annealing time produced worse film morphology. For the films in Figure 3.28b-i, lower annealing temperature were explored which would allow more time for the perovskites to grow before removing the DMSO complexed to SnI_2. The higher temperature above 70°C improve the grain boundary definition of the films but small pin holes

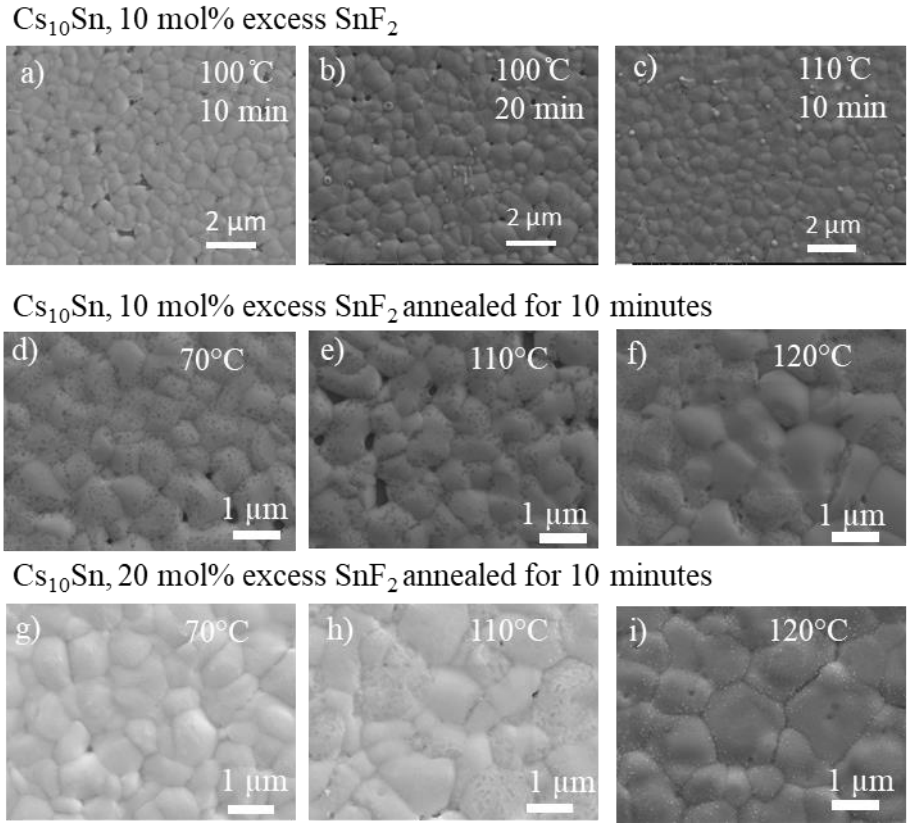

Figure 3-29. SEM images of perovskites with the perovskite composition $Cs_{10}Sn$ $(Cs_{0.10}(MA_{0.17}FA_{0.83})_{0.90}Sn(I_{0.83}Br_{0.17})_3)$ with 10 mol% excess SnF_2 annealed at (a) 100°C for 10 min, (b) 100°C for 20 min, and (c) 110°C for 10 minutes, 10 mol% excess SnF_2 annealed at (d) 70°C, (e) 110°C, and (f) 120°C and 20 mol% excess SnF_2 annealed at (g) 70°C, (h) 110°C, and (i) 120°C.

can still be seen in all films. Unfortunately, for Cs_5Sn perovskite compositions, increasing to 20 mol% SnF_2 also increased phase segregation on the material surface. Figure 3-29 shows the SEM images of the $Cs_{10}Sn$ with varying mol% of SnF_2 and annealing temperatures. Figure 3-29a-c shows that a higher annealing temperature was able to lessen the concentration of pinholes although there is still slight phase segregation in all films. The longer annealing temperature resulted in further phase segregation showing that excess heat could exacerbate the phase segregation mechanism in our triple cation pure Sn films. Comparing Figure 3-29-f and g-i, the addition of 20 mol% excess SnF_2 did improve the smoothness of the films, potentially acting as nucleation sites to lessen pinholes and increase the grain size. For the $Cs_{10}Sn$ films, the higher annealing temperatures also resulted in larger grains with better defined grain boundaries. Figure

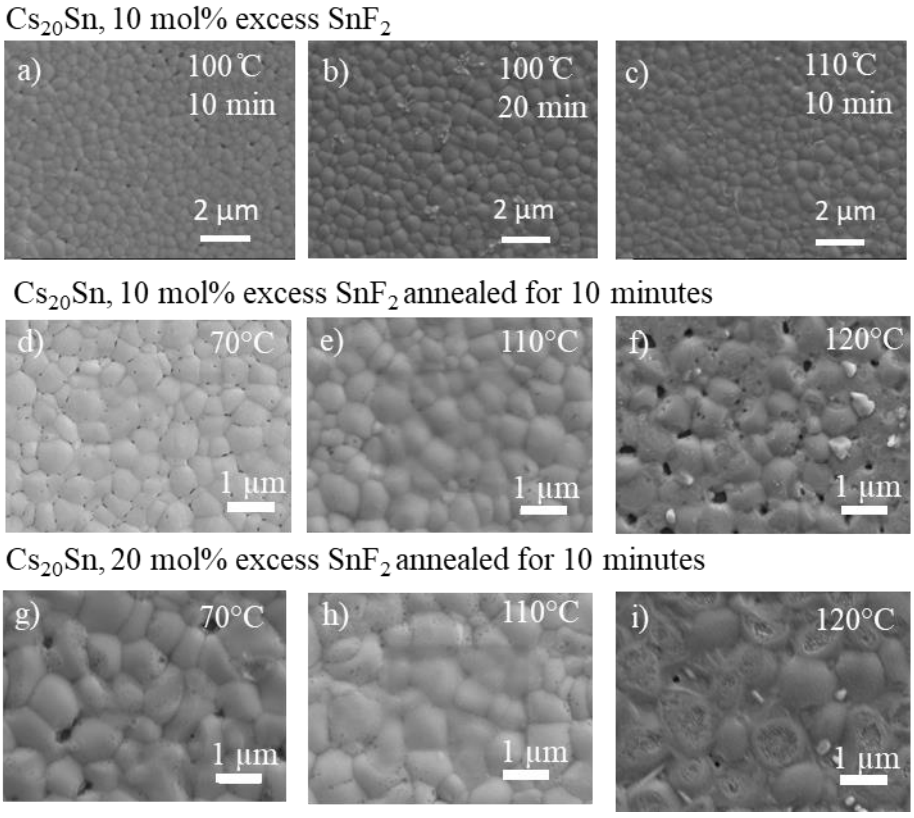

Figure 3-30. SEM images of perovskites with the perovskite composition $Cs_{0.2}(MA_{0.17}FA_{0.83})_{0.8}Sn(I_{0.83}Br_{0.17})_3$ with 10 mol% excess SnF_2 annealed at (a) 100°C for 10 min, (b) 100°C for 20 min, and (c) 110°C for 10 minutes, 10 mol% excess SnF_2 annealed at (d) 70°C, (e) 110°C, and (f) 120°C and 20 mol% excess SnF_2 annealed at (g) 70°C, (h) 110°C, and (i) 120°C.

3-30a-c also shows that for $Cs_{20}Sn$ films, a higher annealing temperature of 110°C compared to 100°C resulted in less pinholes and the lower annealing time of 10 minutes was able to prevent further phase segregation caused by longer annealing time. For the $Cs_{20}Sn$ films in Figure 3-30d-f and g-i, the 120°C annealing temperature resulted in poorly formed perovskite grains with deformities on the surface as well as phase segregation. The lower annealing temperature introduced more pinholes to the film along the grain boundaries. The addition of 20 mol% SnF_2 did increase the grain sizes of the $Cs_{20}Sn$ as well but otherwise there was no significant change in film morphology with 110°C remaining the optimal annealing temperature. Figure 3-31 shows the XRD spectra of the $Cs_{10}Sn$ composition with 10, 20 and 30 mol% SnF_2 excess annealed at 110°C for 10 minutes. All the $Cs_{10}Sn$ perovskite films show the cubic crystal structure peaks with no excess peaks. Even though SnF_2 was added to the precursor solution, there were no shifts in peak position for the films prepared with the addition of different molar percent of SnF_2, suggesting that the SnF_2 was not introduced into the crystal structure itself. Previous research has also shown the lack of peak shifting with SnF_2 introduction and have concluded that the SnF_2 is not integrated into the crystal lattice of the perovskite films.[69,105] There is also a slight increase in peak intensity

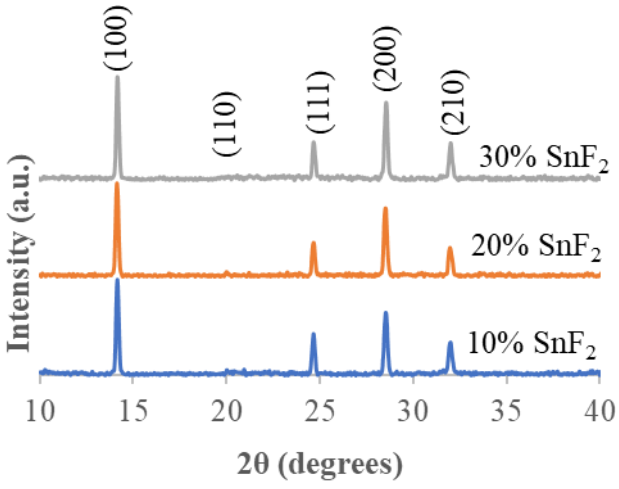

Figure 3-31. XRD spectra of $Cs_{10}Sn$ annealed at 110°C for 10 minutes with 10%, 20%, and 30% SnF_2.

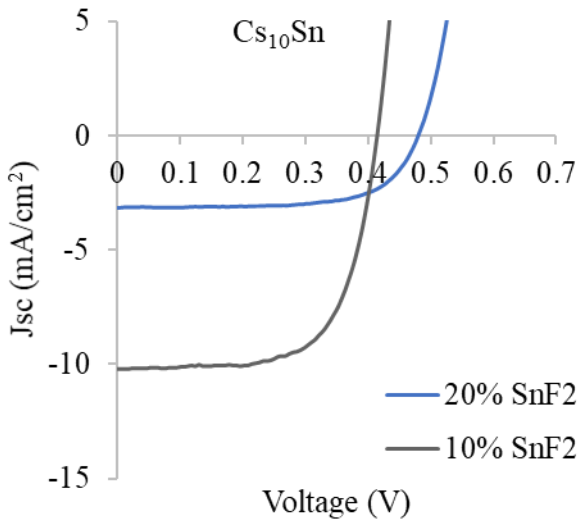

Figure 3-32. J-V curve for the $Cs_{10}Sn$ composition with 10% and 20% molar excess SnF_2 taken under AM 1.5 illumination at a forward scan rate of 0.01V s^{-1} from 0 to 1.2 V.

Table 3-4. Corresponding photovoltaic parameters for the $Cs_{10}Sn$ composition with 10% and 20% molar excess SnF_2.

Device	V_{oc} (V)	J_{sc} (mA cm^{-2})	FF	PCE (%)	PCE_{max} (%)
10% SnF_2	0.41 ±0.00	8.98 ±1.39	0.65 ±0.02	2.43 ±0.45	2.81
20% SnF_2	0.48 ± 0.01	3.23 ± 0.01	0.65 ± 0.03	1.00 ± 0.03	1.02

with increased SnF_2 additive showing an increase in crystallinity. Figure 3-32 shows the J-V curves with the $Cs_{10}Sn$ films with 10 and 20 mol% excess SnF_2 and Table 3-4 shows the corresponding PV parameters. Although the average V_{oc} increases from 0.41V for 10% SnF_2 to 0.48V for 20% SnF_2, the SnF_2 does not integrate into the crystal structure, shown by the lack of shift in lattice parameter in Figure 3-31, so this improvement in V_{oc} could not be due to a downward shift of valence and conduction bands. An alternative explanation could be that the SnF_2 in the grain boundaries and interface facilitate the transport of electron and holes to the corresponding transport layers. The FF remains constant at 0.65 with the extra addition of SnF_2. Although the SEM images in Figure 3-29 showed an increase in grain size with increased SnF_2 and the growth in peak intensity also suggest an increased crystallinity, the average J_{sc} decreased from 8.98 to 3.23 mA/cm^2, which could be evidence that for $Cs_{10}Sn$, 20% excess SnF_2 increases recombination

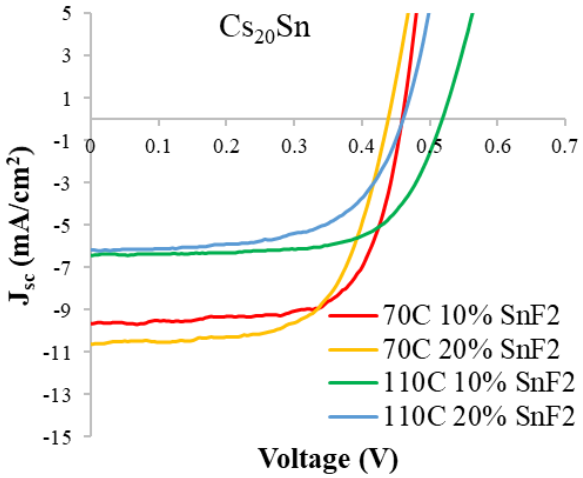

Figure 3-33. J-V curves for the $Cs_{20}Sn$ composition with 10% and 20% molar excess SnF_2 at the annealing temperatures 70°C and 100°C taken under AM 1.5 illumination at a forward scan rate of 0.01V s^{-1} from 0 to 1.2 V.

Table 3-5 Corresponding photovoltaic parameters for the $Cs_{20}Sn$ composition with 10% and 20% molar excess SnF_2 at the annealing temperatures 70°C and 100°C

Device	V_{oc} (V)	J_{sc} (mA cm^{-2})	FF	PCE (%)	PCE_{max} (%)
70C 10% SnF_2	0.46 ±0.00	8.99 ±0.63	0.69 ±0.01	2.83 ±0.22	3.02
70C 20% SnF_2	0.43 ± 0.00	9.82 ± 0.68	0.64 ± 0.02	2.71 ± 0.24	2.99
110C 10% SnF_2	0.50 ±0.02	6.27 ±0.52	0.61 ±0.07	1.92 ±0.36	2.19
110C 20% SnF_2	0.46 ± 0.02	5.85 ± 0.24	0.61 ± 0.04	1.63 ± 0.15	1.71

centers in the perovskite films. This decrease in J_{sc} is the main contributor to the lower PCE of 1.02% for the 20 mol% excess SnF_2 compared to the PCE 2.81% for the 10 mol% excess SnF_2. Figure 3-33 shows the photovoltaic performance of the $Cs_{20}Sn$ composition after being annealed at 70°C and 100°C with 10 and 20 ml% excess SnF_2 with Table 3-5 showing the PV parameters. For both 10 and 20 mol% SnF_2, the 70°C anneal temperature had a higher J_{sc} despite having more pinholes compared to films annealed at 110°C. The FF also decreased at 110°C but the V_{oc} increased. At the anneal temperature 70°C, when increasing SnF_2 to 20 mol% excess, the average V_{oc} decreased from 0.46 to 0.43 V, the average J_{sc} was increased from 8.99 to 9.82 mA/cm^2, and the FF decreased from 0.69 to 0.64. At 110°C, when increasing SnF_2 to 20 mol% excess, the average V_{oc} decreased from 0.50 to 0.46 V, the average J_{sc} was decreased from 6.27 to 5.85

mA/cm^2, and the FF decreased remained constant. The 10 mol% excess SnF_2 consistently had a higher PCE for the $Cs_{20}Sn$ composition with the PCE_{max} at 3.02% when annealed at 70°C.

3.2.9 Optimizing Pure Sn Film Morphology Through Solvent Tuning

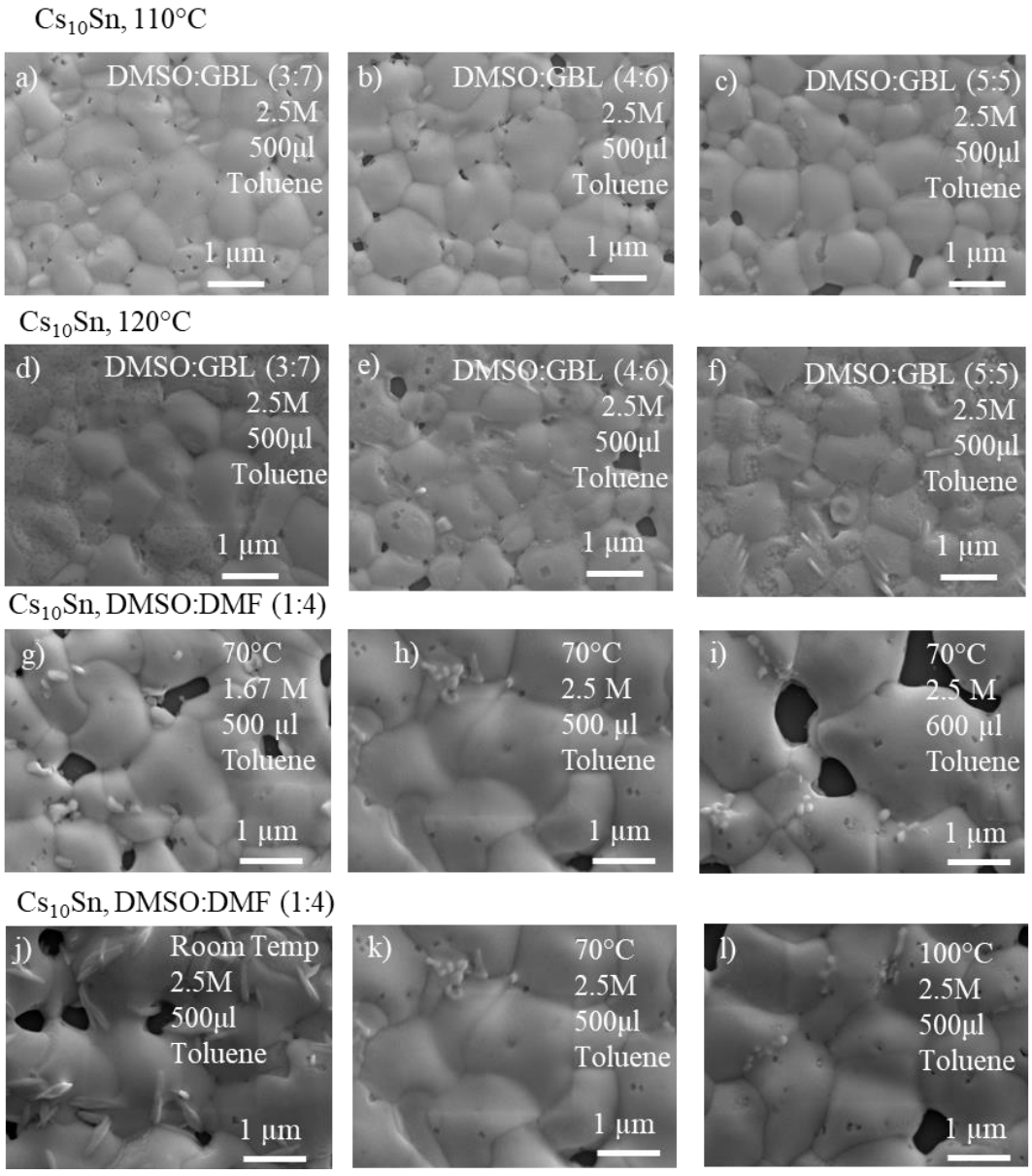

Figure 3-34. SEM images of the $Cs_{10}Sn$ composition at an annealing temperature of 110°C with a DMSO:GBL ratio of (a) 3:7, (b) 4:6, and (c) 5:5, and an annealing temperature of 120°C with a DMSO:GBL ratio of (d) 3:7, (e) 4:6, and (f) 5:5. Solvent use DMSO:DMF (1:4) with 70°C with a concentration of (g)1.67M and a 500 µl antisolvent wash, (h) 2.5M and a 500 µl antisolvent wash and (i) 2.5M and a 600 µl antisolvent wash. DMSO:DMF (1:4) with a concentration of 2.5M and a temperature of (j) room temperature, (k) 70°C and (l) 100°C.

Different solvent mixtures for pure Sn perovskite such as a pure DMSO solvent show a better morphology prompting us to increase the DMSO in our DMSO:GBL solvent mixture as well as study the solvent mixture of at a ratio of 1:4.[110,111] These solvent mixtures affect the rate of DMSO removal upon annealing from the SnI_2 3DMSO complex, directly affecting the film morphology. To allow for more controlled grain growth and a slower removal of DMSO, for the $Cs_{10}Sn$ composition, the solvent mixture was increased from a DMSO:GBL ratio of 3:7, 4:6, and 5:5 at 110 ℃ and 120℃ annealing temperature. For the 110℃ annealing temperature, although there is a slight decrease in pinholes with an increase in DMSO (Figure 3-34b,c), there is also a darker phase that begins around the grain boundaries. Because of the higher annealing temperature of DMSO, we hypothesized the 120℃ yield smoother grains since there larger amount of DMSO would requires a higher temperature to evaporate (Figure 3-34d,e,f). Unfortunately, the higher annealing temperature remove solvent too quickly, not allowing for proper perovskite formation and encouraging deformities that begin in Figure 3-34e and become worse in Figure 3-34f. The increased DMSO ratio to 5:5 increase phase segregation with white thin crystals appearing on the perovskite surface which have been previously attributed in our earlier works to cation iodide crystals such as MAI and FAI.[40] The MAI crystals suggest that there was an incomplete reaction of MAI and SnI_2 at the higher annealing temperature of 120°C, supported by the deformities on the perovskite grains in Figure 3-34l.

Figure 3-34 also shows the SEM images of the implemented DMSO:DMF solvent mixture with varying conditions. Although past literature had a lower concentration for this solvent mixture, the higher concentration of 2.5M decreased the amount of pinholes compared to the 1.67M concentration. Because the higher concentration had a less pinholes but still phase segregation, we tested a larger anti-solvent wash volume (Figure 3-34i). The 600µl toluene anti

solvent addition further increased both pinholes and phase segregation compared with the 500µl addition (Figure 3-34h). Compared with the films synthesized with the DMSO:GBL solvent mixture, the DMSO:DMF solvent symthesized films have less defined grain boundaries. Because of the higher concentration, we also tried a higher annealing temperature (Figure 3-34l) to make certain all DMSO was removed from the complexed SnI_2. The higher annealing temperature of 100°C resulted in an increased concentration of pinholes.

3.3 Conclusion

The optimized triple cation Cs/FA/MA and double halide Br/I compositions were applied to Pb-Sn alloyed perovskites $Cs_x(MA_{0.17}FA_{0.83})_{1-x}Pb_{1-y}Sn_y(I_{0.83}Br_{0.17})_3$. The corresponding devices achieved high efficiency on a PEDOT:PSS inverted architecture with a PCE_{max} of 15.78% for the $Cs_{0.10}(MA_{0.17}FA_{0.83})_{0.90}Pb_{0.75}Sn_{0.25}(I_{0.83}Br_{0.17})_3$ PVSC and a record high PCE_{max} of 11.05% for the high Sn $Cs_{0.05}(MA_{0.17}FA_{0.83})_{0.95}Pb_{0.25}Sn_{0.75}(I_{0.83}Br_{0.17})_3$ PVSC. Adding Cs to the triple cation Cs/MA/FA, mixed halide Br/I Pb-Sn alloyed perovskites suppressed yellow phase and Sn^{4+} impurities, creating highly uniform and crystalline perovskite films that can retain ~80% of their initial PCE for 30 days in the inert condition followed by 5 days in the ambient condition with a relatively humidity of 35 ± 5%. For our unexplored high 75%-95% Sn range, we have illustrated the novel phenomena of Cs and Rb addition being able to shift the band gap minimum towards higher amounts of Sn, which shines a light on interesting interactions between the cation and octahedral tilting of Pb/Sn hybrids. By identifying a more accurate band gap minimum for Pb/Sn perovskite hybrids, we have been able to narrow down the key ideal band gap of 1.3-1.4 eV for these systems, allowing us to be able to tailor high Sn perovskites with a Shockley Queisser limit of 33% in future works. Finally, we have explored optimization of pure Sn perovskites in terms of solvent engineering and morphology optimizations Overall, this study demonstrated the

implementation of the triple cation, double halide as an effective strategy for improving performance and stability of high Sn PVSCs, providing a route towards lead-free devices in the future.

CHAPTER FOUR: TUNING CESIUM-GUANIDINIUM IN FORMAMIDINIUM TIN TRIIODIDE PEROVSKITES WITH ETHYLENEDIAMMONIUM ADDITIVES FOR EFFICIENT AND STABLE LEAD-FREE SOLAR CELLS

4.1 Introduction

Perovskite solar cells (PVSCs) have progressed rapidly in recent years. With the record power conversion efficiency (PCE) reaching 25.2%[9] and the potential for cost effective roll-to-roll printing capabilities, PVSCs are well positioned to encourage a transition into a clean energy economy. However, the toxicity of the lead-based perovskite materials and low stability and poor performance of lead-free perovskite alternatives present a challenge towards commercialization of perovskite technologies. Tin-based perovskites have been investigated as low-toxic alternatives to lead-based perovskites because tin has comparable ionic radius (Sn^{2+}, 1.15 Å and Pb^{2+}, 1.19 Å)[12] and is also a group 14 metal, allowing Sn to maintain the crucial MX_6 octahedron.[60] Tin-based perovskites have certain intrinsic advantages over lead-based perovskites for photovoltaic devices such as a more favorable, comparably smaller band gap resulting in a higher Schockley-Queisser limit, and a more rapid charge carrier mobility.[112,113] Unfortunately, the main drawback of pure Sn perovskites is an oxidation reaction that hinders photovoltaic performance. Tin-containing PVSCs have been shown to degrade from the oxidation of Sn^{2+} to the more thermodynamically favored Sn^{4+}, even in inert atmospheres, due to the small activation energy for the oxidation reaction.[65,68] The high levels of self-p-doping caused by Sn^{4+} create a high defect density, also resulting in low open-circuit voltage, V_{oc}.[114]

One strategy for improving the performance and stability of tin-based PVSCs has been focusing on the A-site cation mixtures. Single A-site cation pure Sn perovskites, such as cesium tin triiodide ($CsSnI_3$), methylammonium tin triiodide ($MASnI_3$), and formamidinium tin triiodide ($FASnI_3$) have been thoroughly explored in previous literature.[83] Although $CsSnI_3$ was the first explored

active layer for pure Sn PVSCs, it has been plagued with low PCE and V_{oc} because of its small tolerance factor, creating an orthorhombic perovskite phase.[104,115] $MASnI_3$ PVSCs demonstrated promising performance with a PCE of 6%. However, the devices were unstable and had poor reproducibility because of poor film morphology and Sn oxidation.[116,31] $FASnI_3$ was hypothesized to be more stable against oxidation because of increased hydrogen bonding and a lesser dipole moment, allowing it to better rotate in the octahedral cage and interact with the halides.[83,94]

Recently, another organic cation has been demonstrated to further protect Sn against oxidation.[117] Guanidinium (GA^+) cations have been used in Sn based PVSCs to improve performance and stability in ambient conditions. Due to the larger ionic radius of GA^+ (r = 2.78 Å) compared with FA^+ (r = 2.53 Å) and MA^+ (r = 1.80 Å), density functional theory (DFT) calculations predict that the cubic-phase $GASnI_3$ tends to have a shorter hydrogen bonding length and stronger interactions with the SnI_6 octahedron.[118] The higher amounts of bonded amines create a symmetrical structure in GA^+ and a zero electric dipole moment, unlike FA^+ and MA^+, allowing for freer rotation of GA^+ in the SnI_6 framework. The high hydrogen bonding capability and free rotation make GA^+ effectively passivate under-coordinated iodide ions resulting in longer carrier lifetimes and increased Voc because of reduced recombination centers.[119]The capability of passivating under-coordinated iodide ions is particular important for pure Sn perovskites because iodide vacancies induce the oxidation of Sn^{2+} to Sn^{4+}.[68] In addition, the incorporation of GA^+ in $FASnI_3$ makes a less tendency of phase segregation because of the multiple hydrogen bonding sites. Therefore, GA^+ is an excellent candidate for stabilizing mixed A-site Sn based perovskites. However, simply incorporating GA^+ into $GA_{0.20}FA_{0.80}SnI_3$ perovskites yielded very low efficient PVSCs with a PCE of 0.5% even though extra SnF_2 was added as a reduce agent.[117] This could be due to the increased local lattice strain created by introducing such a large organic cation. Increased

local lattice strain has been theorized by increasing point defect formations to relieve the strain.[120] The increased point defects could be the sites for oxidation and/or trap centers, affecting the performance of Sn-based PVSCs significantly.

One method that has been shown to "hollow" out three-dimensional (3D) perovskites and reduce lattice strain is by introducing ethylenediammonium diiodide ($EDAI_2$). $EDAI_2$ has been explored as an A-site cation in 3D $FASnI_3$ and $MASnI_3$ perovskites.[121] Shallow trap states are localized in the crystal bulk structure and are located near the conduction or valence band edges. Deep trap states involve grain boundary defects and are located closer to the middle of the band gap.[122,123] The incorporation of such a large divalent cation results in not only the occupation of A-sites, but also the removal of B- and X-sites, reducing both bulk defects and shallow trap states. In addition, the divalent cations terminate crystal surfaces, reducing deep trap states at grain

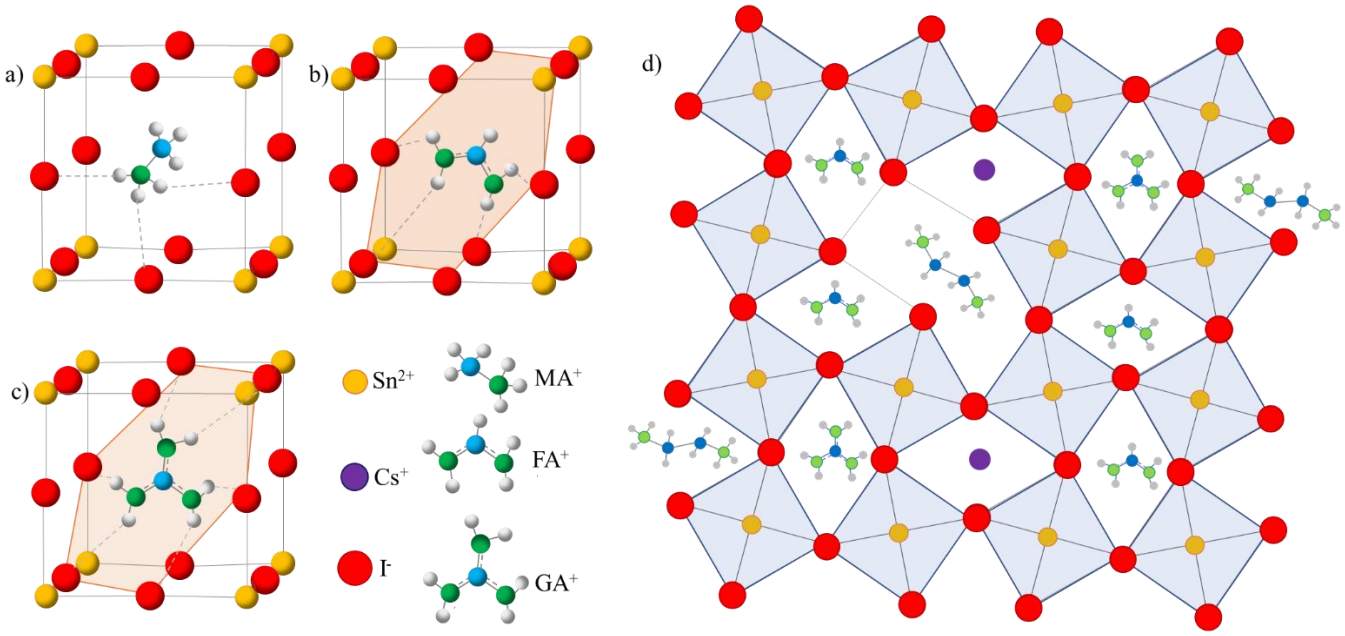

Figure 4-1. SnI_6 inorganic framework highlighting N-H---I hydrogen bonding in (a) $MASnI_3$,(b) $FASnI_3$, and (c) $GASnI_3$. (d) Schematic illustration of the 3D $(CsGA)_xFA_{100-2x}SnI_3$ perovskite with an $EDAI_2$ additive showing EDA^{2+} cations creating potential hollowing inside the crystal as well as passivating defects along the grain boundaries. Yellow, purple, red, grey, blue, and green spheres represent Sn, Cs, I, H, C, and N atoms, respectively and octahedrons are marked by blue squares.

boundaries. The performance of $FASnI_3$ PVSCs improved from a PCE of 1.40% without $EDAI_2$ to 7.14% with 10% $EDAI_2$ and the efficiency was maintained after 1000 h for encapsulated devices.[121] It has been demonstrated that incorporating $EDAI_2$ in $MASnI_3$ lowers the electron trap state density and increases the carrier lifetimes, which leads to the improvement of the device performance from a PCE of 0.17% without $EDAI_2$ to 5.49% with 15% $EDAI_2$.[124] The significant improvement of device performance and stability is attributed the occupation of point defects inside the crystalline grains and passivation of defects at grain boundaries by $EDAI_2$ cations, decreasing both shallow and deep trap states. Adding $EDAI_2$ to $FA_{80}GA_{20}SnI_3$ greatly enhanced the device performance from a PCE 0.5% without $EDAI_2$ to the maximum PCE of 7.4% with 1% $EDAI_2$.[125] More interestingly, the PCE even increased to the maximum 8.9% after the device was stored in a glove box for over 1400 h. The fascinating behavior is due to the slow crystal relaxation and surface passivation induced by $EDAI_2$. Another method of reducing lattice strain caused by a large organic cation is the addition of a smaller counter ion, such as Cs^+. A small cation can fill point defects, reducing shallow trap states, and protecting the sites from oxidation.[120] Using Cs^+ to counterbalance the large GA^+ cation in a $FASnI_3$ perovskite should allow for the retention of the stabilizing effects of GA^+ while reducing local lattice strain, improving the performance of the corresponding devices.

In this study, we implement both GA^+ and Cs^+ cations into the $FASnI_3$ crystal structure to introduce more hydrogen bonding and to reduce local strains, respectively, within the perovskite crystals (Figure4-1a-d). We further incorporate a range of $EDAI_2$ to replace some octahedral sites inside the crystal and to passivate defects at the grain boundaries (Figure4-1d) to relax lattice strains and reduce oxidation and trap states. We successfully synthesize the densely packed, lead-free polycrystalline $(CsGA)_xFA_{100-2x}SnI_3$ with $EDAI_2$ films. The substitution of FA^+ with a pair of

Cs^+ and GA^+ lead to a $(CsGA)_{15}FA_{70}SnI_3$ device with a maximum PCE of 5.01%, much higher than simply incorporation of GA^+ in $GA_{0.20}FA_{0.80}SnI_3$,[117] but the device loses the diode behavior after storage in a nitrogen-filled glove box for 30 days. With the $EDAI_2$ additive, freshly made $(CsGA)_{15}FA_{70}SnI_3$ with 1% $EDAI_2$ devices reach a record maximum PCE of 5.72%. UV-*Vis* absorption and ultraviolet photoelectron spectroscopy (UPS) results show that the addition of $EDAI_2$ reduces the amount of trap states in perovskite thin films, improving the short-circuit current, J_{sc} and open-circuit voltage, V_{oc}. Devices made with $(CsGA)_{15}FA_{70}SnI_3$ and 1% $EDAI_2$ reach a maximum PCE of 5.69% and the maximum PCE increases to 6.39% after storage in a nitrogen-filled glove box for 4 days and retains 70% of the initial PCE for 45 days. Thin film trap state reduction and device stability improvement highlight the importance of $EDAI_2$ as a mitigating agent. Tuning cation sizes and integrating divalent cation create new routes for making efficient and stable pure Sn PVSCs.

4.2 Results and Discussion

4.2.1 Road to Optimizing Pure Sn Perovskites

Introducing guanidinium into the perovskite formula $Cs_x(MA_{0.17}FA_{0.83})_{1-x}Pb_{1-y}Sn_y(I_{0.83}Br_{0.17})_3$, which has been studied in Chapter 3, we begun optimizations of the pure Sn perovskite. Figure 4-2 shows the SEM images and XRD patterns of the perovskite formula $Cs_x(MA_{0.17}FA_{0.83})_{1-x}Pb_{1-y}Sn_y(I_{0.83}Br_{0.17})_3$ with y = 0.75 and 1, and the Cs is replaced with 10% GA, a mix of 5% Cs and 5% GA, and a mix of 5% GA and 5% Rb. The SEM images show that GA is too large of a cation to integrate by itself into the perovskite composition and results in a phase change shown by the tetragonal peaks because of the increased tolerance factor illustrated in Figure 4-3a. With high and pure Sn levels, the tolerance factor increases due to the smaller ionic radius of Sn compared to Pb.

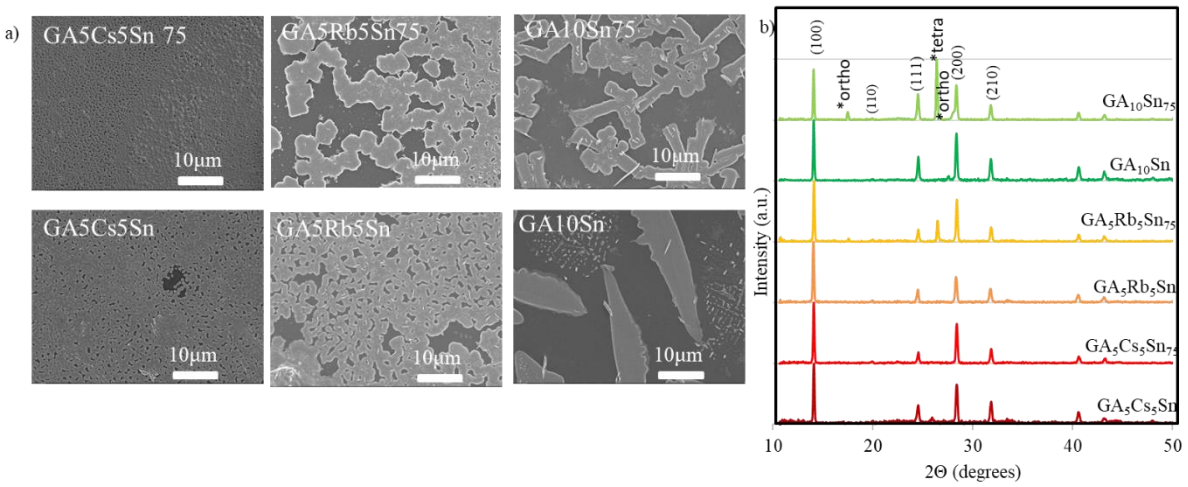

Figure 4-2. (a) SEM images and (b) XRD patterns integrating GA, Cs, and Rb into 75% and 100% Sn perovskites into the perovskite formula $Cs_x(MA_{0.17}FA_{0.83})_{1-x}Pb_{1-y}Sn_y(I_{0.83}Br_{0.17})_3$ The impurity peaks for the orthorhombic and tetragonal phases are marked in the XRD patterns.

This exacerbates the phase change issues when integrating GA into the crystal structure unless it is mitigated by a smaller counter cation as well. Although the SEM images in figure 4-2 show that when Rb was introduced as a potential small counter cation to GA and improved the perovskite morphology compared to the GA perovskite, the Cs counter cation shows much smoother and dense perovskite grains. This could be because Cs and GA have a smaller size difference than Rb and GA. Too large of a size difference would increase the lattice strain making perovskite formation more difficult. The Rb/GA mixtures also have orthorhombic peak that is typical when the tolerance factor is too small, showing that there could be Rb heavy perovskites that are not integrating with GA. At this high and pure Sn amounts, the SEM images still show segregation that we previously demonstrated is due to facilitated segregation from SnF_2 and Br ions separating out into $SnBr_2$. To eliminate this segregation issue, we removed Br ions from the perovskite composition and are focusing on a pure iodide halide perovskite. The tolerance factor chart for this new perovskite formula is shown in Figure 4-3b and with decreasing Br, the tolerance factor is lowered into a more cubic range away from the tetragonal phase change. Because there is no Br/I

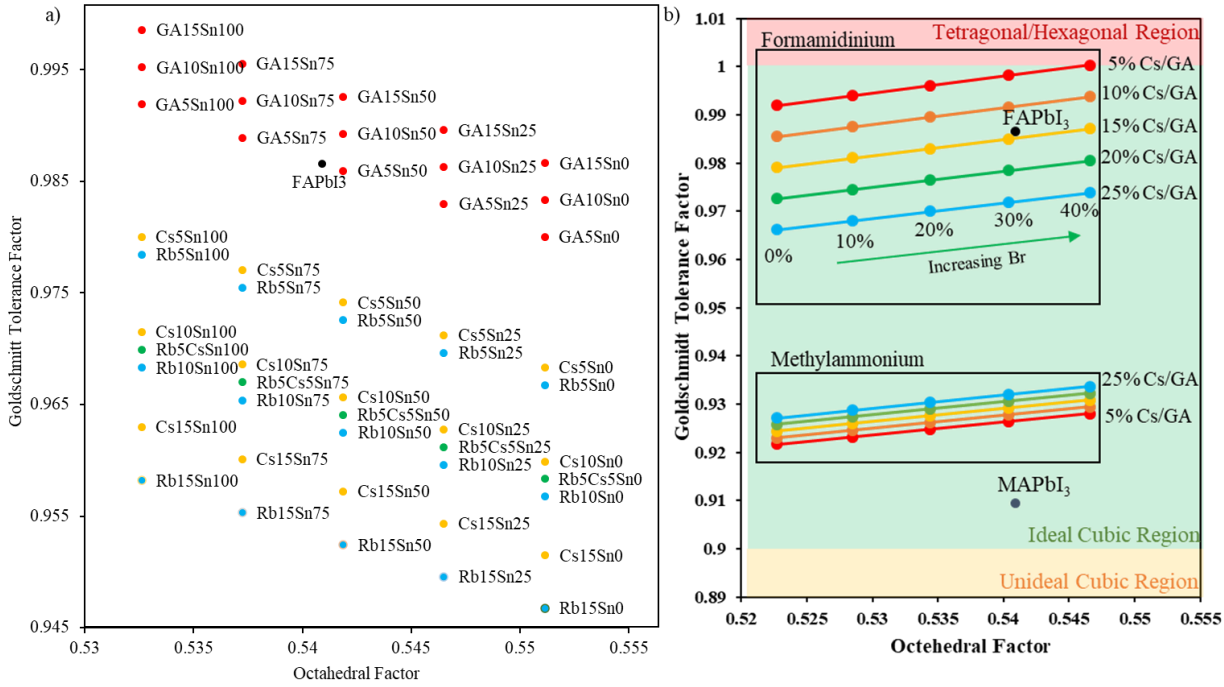

Figure 4-3. Tolerance factor charts using the formula (a) $Cs_x(MA_{0.17}FA_{0.83})_{1-x}Pb_{1-y}Sn_y(I_{0.83}Br_{0.17})_3$ while integrating Cs, GA, and Rb mixtures for x and the formula (b) $(CsGA)_xFA_{100-2x}SnI_3$ and $(CsGA)_xMA_{100-2x}SnI_3$.

mixture, we also explored disconnecting FA and MA to have a new compositional formula of $(CsGA)_xFA_{100-2x}SnI_3$ and $(CsGA)_xMA_{100-2x}SnI_3$. This formula would help better isolates the specific impacts of MA and FA to the perovskite films while both integrating the larger cation GA and stabilizing phase change issues with a smaller cation Cs.

Figure 4-4 shows the SEM images and XRD patterns for $(CsGA)_xFA_{100-2x}SnI_3$ and $(CsGA)_xMA_{100-2x}SnI_3$ with a range of different percentage of Cs/GA annealed at 90, 100, and 110°C. For the formamidinium based perovskites, the $FASnI_3$ film, which was annealed at 100°C, has extensive pin holes and poor coverage. When comparing with the films also annealed at 100°C, this coverage is improved with increased amounts of Cs/GA. 5% Cs/GA has the highest tolerance factor and has large segregates scattered in the film. These segregates disappear at higher levels of

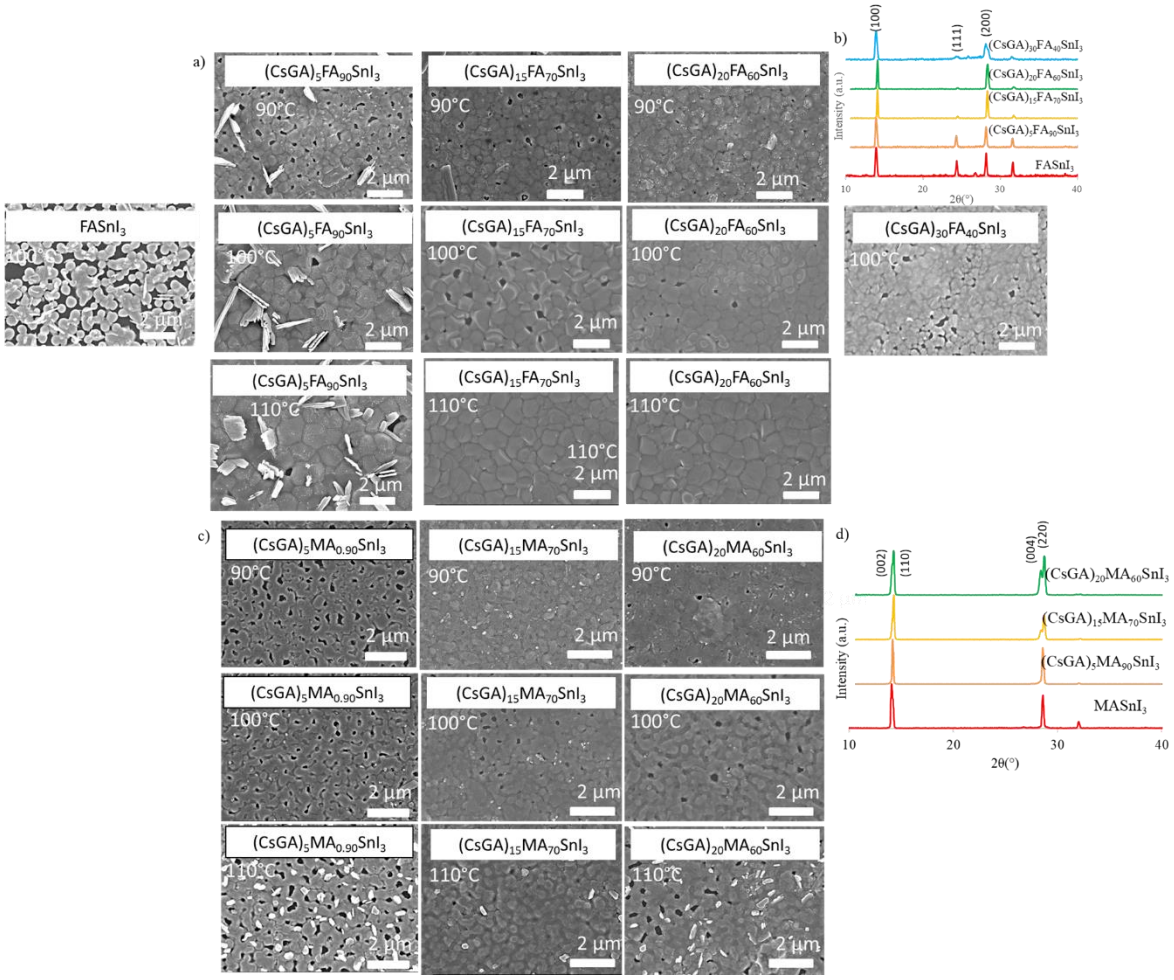

Figure 4-4. (a) SEM images for $FASnI_3$, $(CsGA)_5FA_{90}SnI_3$, $(CsGA)_{15}FA_{70}SnI_3$, $(CsGA)_{20}FA_{60}SnI_3$, and $(CsGA)_{30}FA_{40}SnI_3$ at anneal temperatures 90, 100, and 110°C. (b) XRD patterns for the FA based compositions all annealed at 100°C (c) SEM images for $(CsGA)_5FA_{90}SnI_3$, $(CsGA)_{15}FA_{70}SnI_3$, and $(CsGA)_{20}FA_{60}SnI_3$ at anneal temperatures 90, 100, and 110°C. (d) XRD patterns for MA compositions all annealed at 100°C.

Cs/GA, but the 30% Cs/GA begins to show poorer perovskite formation. Previous literature has shown that above 25% GA, the perovskite begins to break out of a 3D structure because of the larger cation radius of GA. This breaking of the 3D structure could explain the poorer perovskite formation and impure peaks in 30% Cs/GA while the other XRD structures are cubic. For the 15% and 20% Cs/GA, the films are further improved by increasing the anneal temperature from 100 to 110°C, aligning with the observations in Chapter 3. For the methylammonium based perovskites, with increased Cs/GA, the XRD patterns show a change from a cubic structure to a tetragonal

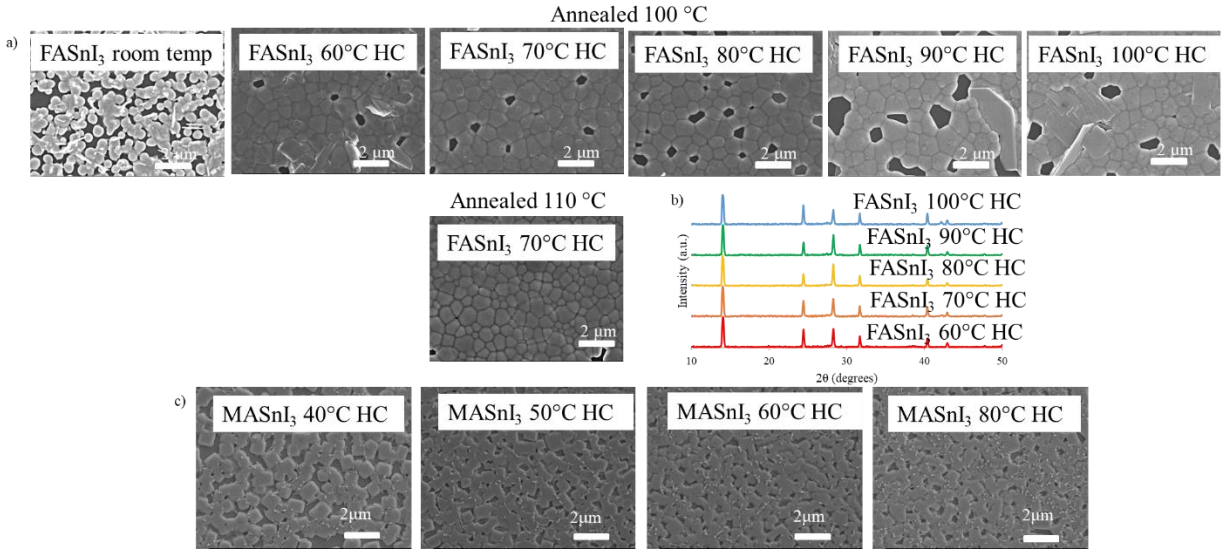

Figure 4-5. (a) $FASnI_3$ without and with hot casting (HC) at 60, 70, 80, 90, and 100°C annealed at 100 and 110°C. (b) Corresponding XRD patterns for the films fabricated with hot casting all annealed at 100°C. (c) $MASnI_3$ with hot casting at 40, 50, 60, and 80°C all annealed at 100°C.

structure signaled by the increased peak splitting. Although there are less pinholes with increase Cs/GA, there are still pinholes covering the surfaces and small light segregates. With increased annealing temperature, the number of segregates also severely increases emphasizing the temperature sensitivity that methylammonium has been shown to possess. Figure 4-5 shows the SEM images and XRD patterns during the application of a hot casting step during thin film synthesis with $FASnI_3$ and $MASnI_3$ to understand if this method can be used on the new Cs/GA compositions to better perovskite morphology. Hot casting involves heating up the precursor solution prior to spin coating, increasing wettability and nucleation. With $FASnI_3$, there is a distinct increase of coverage and decrease of pinholes with the introduction of hot casting. The use of hot casting helps decreases the surface tension and dragging force of the precursor, allowing for better coverage.[71] The hot precursor also allows the antisolvent drop to more effectively remove DMSO from the complexed Sn, allowing for controlled reaction at the proper temperature. 70°C is the optimal temperature with the least number of pinholes and no visible segregates. While keeping

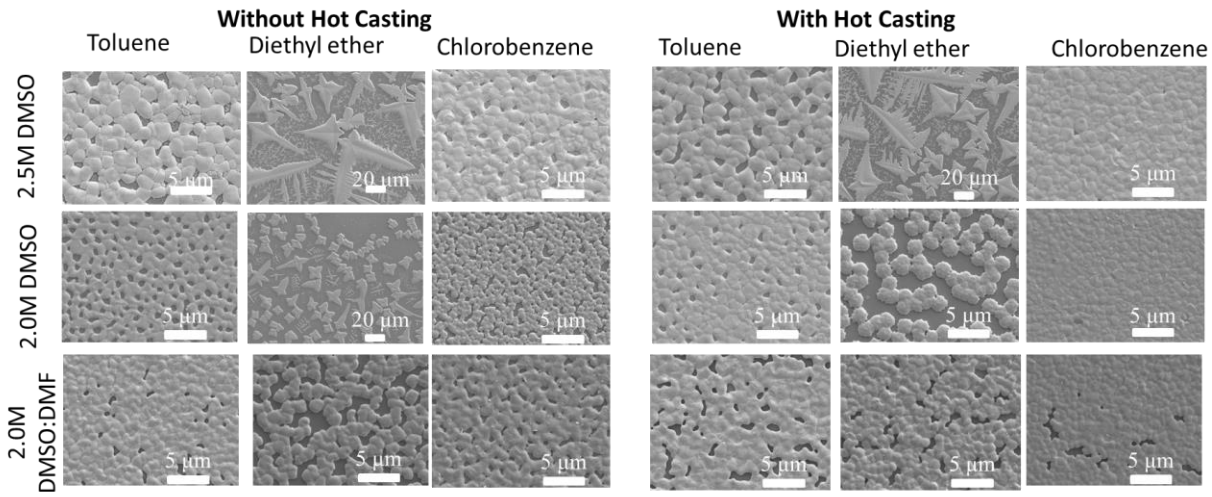

Figure 4-6. SEM images for the $(CsGA)_{15}FA_{70}SnI_3$ perovskite composition with molarities and solvent: 2.0 M and DMSO:DMF at 2:8 volume ratio, 2.0 M and DMSO, and 2.5 M and DMSO with antisolvent toluene, diethyl ether, and chlorobenzene, without and with hot casting at 70°C all annealed at 110°C.

the hot casting temperature at 70°C and increasing the anneal temperature to 110°C, the pinholes are further minimized and show a smooth dense perovskite film. When the hot casting is increased to 90°C, there are huge sheets that protrude from the perovskite grains and larger pinholes possibly because the high temperatures increase the reaction time too quickly when the antisolvent is added. For the $MASnI_3$ perovskite, hot casting was lowered to try to avoid temperature degradation but hot casting still does not improve the number of pinholes, the perovskite coverage, or the segregate amount most likely because of how $MASnI_3$ easily degrades under high temperatures through a deprotonation process. Because $MASnI_3$ is so sensitive to heat treatments and does not seem to improve with Cs/GA introduction, we are moving forward with the formamidinium based perovskite that has showed more thermal resilience and better integration of the Cs/GA additives.

To probe the relationship between the morphology of the pure Sn perovskite and both the precursor molarity and solvent, antisolvent choice, without and with the hot casting treatment at 70°C. Figure 4-6 focuses on only $(CsGA)_{15}FA_{70}SnI_3$, solvent mixtures at 2.5M and DMSO, 2.0M

and DMSO, and 2.0M DMSO:DMF in a 2:8 ratio, and antisolvent diethyl ether, toluene (the one used in Chapter 3), and chlorobenzene. Because of the low boiling point of diethyl ether, it did not have enough time to interact as the antisolvent choice to properly remove the DMSO, resulting in poor perovskite formation. With the higher molarity of 2.5 M in DMSO, this effect is exacerbated because the diethyl ether was even less able to interact with the thicker film, resulting in no observable perovskite grains. Across the board, hot casting improves perovskite coverage because of the increased wettability. Compared to the antisolvent toluene used in Chapter 3, chlorobenzene results in better perovskite coverage and with no observable pinholes when hot casting is applied. Although chlorobenzene is more polar than toluene, this improved perovskite formation and coverage could be because chlorobenzene has a chloride end group instead of the methyl end group, allowing the chloride to interact with the Sn-3DMSO complex and better displace the DMSO.

The old synthesis method (GBL:DMSO solvent mixture, toluene antisolvent, no hot casting) was compared with the optimized synthesis method (DMSO solvent, chlorobenzene antisolvent,

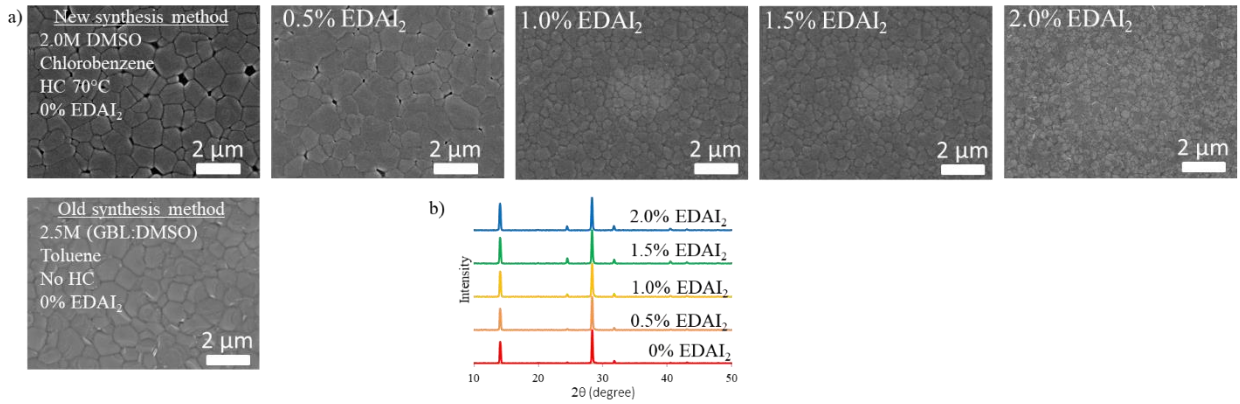

Figure 4-7. (a) SEM images of perovskite composition $(CsGA)_{15}FA_{70}SnI_3$ with the old synthesis method utilizing the precursor with 2.5 M total concentration in GBL:DMSO, a toluene antisolvent, and no hot casting compared with the new synthesis method of the precursor with 2.0 M total concentration in DMSO, a chlorobenzene antisolvent and hot casting at 70°C. The new method then incorporates 0, 0.5, 1.0, 1.5, and 2.0% $EDAI_2$. (b) XRD patterns with the new synthesis method that incorporates 0, 0.5, 1.0, 1.5, and 2.0% $EDAI_2$.

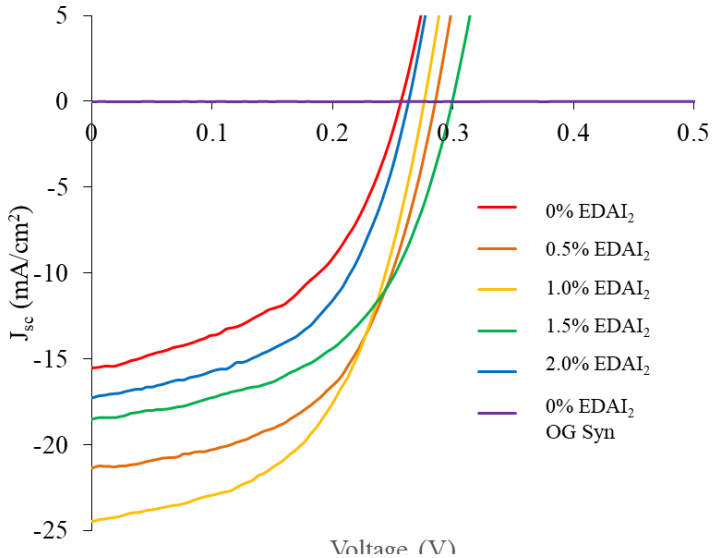

Figure 4-8. J-V curves of $(CsGA)_{15}FA_{70}SnI_3$ composition with the old composition labeled OG syn, and the new synthesis with 0, 0.5, 1.0, 1.5, and 2.0% $EDAI_2$ under AM 1.5G illumination scanned from -0.1 to 0.6 V at a scan rate of 0.01 V s^{-1}.

Table 4-1. Average photovoltaic parameters and the best performance device photovoltaic parameters corresponding to J-V curves from Figure 4-8 measured under AM 1.5G illumination obtained from the forward J-V measurements.

Composition	V_{oc}	J_{sc} (mA/cm$_2$)	Fill Factor	PCE %	Max %
0% $EDAI_2$ OG	0.494	0.013	0.60	0.0038	
0% $EDAI_2$	0.25±0.01	12.57±2.93	0.478±0.03	1.55± 0.36	1.91
0.5% $EDAI_2$	0.285±0.01	17.04±4.26	0.532±0.03	2.48±0.62	3.10
1.0% $EDAI_2$	0.277±0.02	20.14±4.16	0.516±0.02	2.81±0.58	3.39
1.5% $EDAI_2$	0.300±0.01	15.6±2.8	0.52±0.03	2.36±0.42	2.78
2.0% $EDAI_2$	0.263±0.02	13.64±3.56	0.522±0.02	1.88±0.49	2.37

70°C hot casting) with and without the addition of $EDAI_2$ for composition $(CsGA)_{15}FA_{70}SnI_3$ in SEM images and XRD patterns shown in Figure 4-7, and the J-V scans to compare the performance as shown in Figure 4-8 with the solar cell architecture ITO (200 nm)/PEDOT:PSS (50 nm)/perovskite (400 nm)/$PC_{60}BM$/BCP/Ag (100 nm) with table 4-1 showing the PV parameters. With the new synthesis method, even with no $EDAI_2$, the perovskite grains are larger, more defined, contain no segregates and less amorphous. The XRD patterns for the new synthesis

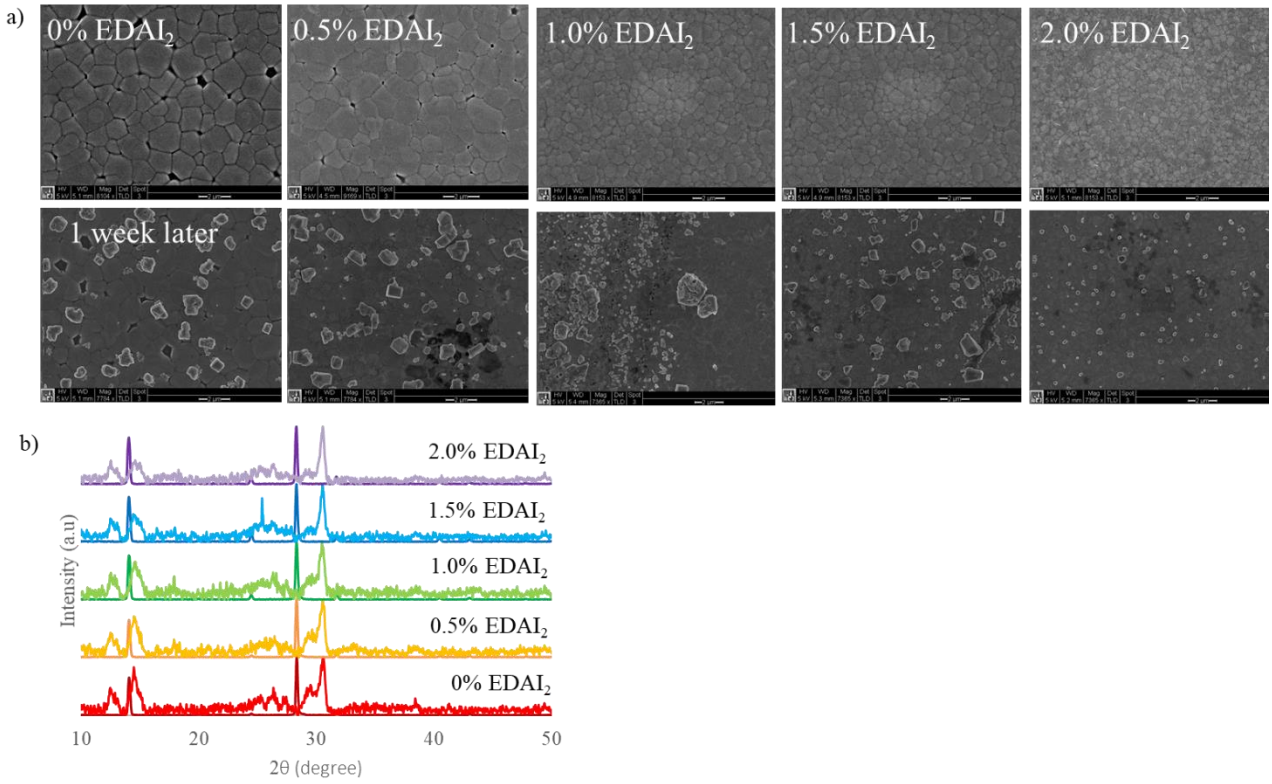

Figure 4-9. (a) SEM images of perovskite film $(CsGA)_{15}FA_{70}SnI_3$ with 0, 0.5, 1.0, 1.5, and 2.0% $EDAI_2$ freshly made and after a week of exposure to the ambient condition. (b) XRD patterns of $(CsGA)_{15}FA_{70}SnI_3$ with 0, 0.5, 1.0, 1.5, and 2.0% $EDAI_2$ freshly made and after a week of exposure to the ambient condition.

method show no impurity peaks and are a crystal structure for all $EDAI_2$ amounts. The new synthesis method has a functional J-V curve with a max PCE of 1.91% for 0% $EDAI_2$ while the old synthesis method has an extremely low J_{sc} of 0.013mA/cm^2 and a PCE of 0.0038%. This could be because the old synthesis method does contain segregates which act as nonradiative trap assisted monomolecular recombination sites, severely impacting the current density. This new synthesis method reduces these recombination sites and segregates, improving the PCE by multiple orders of magnitude. Although the performance is improved with this synthesis method, and there is further improvement with the introduction of $EDAI_2$, the PCE doesn't reach anything higher than 3.39%. To explore whether the new synthesis method and $EDAI_2$ introduction helps stability in ambient conditions, films were left outside the glove box for 7 days (Figure 4-9).The SEM images

after a week show similar segregation issues that has been found with the use of SnF_2. There is also severe degradation of the crystallinity with no perovskite cubic peaks after a week in ambient conditions. To eliminate the phase segregation issues, SnF_2 was replaced with SnI_2, which has been shown to not have similar segregation effects but can fill the same role to minimize oxidation.

4.2.2 Integration of $EDAI_2$ on Morphology, Crystallinity, and Band Gap with Cs/GA

A one-step solution process with chlorobenzene anti-solvent was used to form the pure Sn perovskite films. All precursors (FAI, SnI_2, GAI, CsI, and $EDAI_2$) were dissolved in pure DMSO to a total concentration of 2.0 M and spin coated on ITO/glass substrates. A 10 mol% excess SnI_2 was added to suppress vacancies in the crystal lattice. All films were annealed at 110°C for 10 min. The pure Sn perovskite films have the compositions of $(CsGA)_xFA_{100-2x}SnI_3$+y% $EDAI_2$, where x = 5, 10, 15, and 20, and y = 0, 0.5, 1.0, 1.5, and 2.0. In order to simplify further discussion, we implement a notation of $(CsGA)_x$ to represent the various compositions. For example, $(CsGA)_5$ would correlate to $(CsGA)_5FA_{90}SnI_3$. The anti-solvent wash with the highly non-polar chlorobenzene was performed while spin coating to remove excess DMSO from SnI_2·3DMSO. The removal of excess DMSO results in the formation of A-SnI_2-2DMSO intermediates, allowing for a slower removal of DMSO and a growth of polycrystalline perovskite thin films upon annealing, and thus minimizing pinholes. Although SnF_2 has been used to minimize oxidation of Sn^{2+} to Sn^{4+}, excess SnF_2 have been shown to form separated phases and phase segregation on perovskite film surfaces or grain boundaries over time.[94,105] Excess SnI_2 has been shown to be effective in preventing Sn^{2+} oxidation by both compensating and suppressing Sn^{2+} vacancies without having any adverse side effects on phase stability and phase segregation.[92,126] Previous research has argued that excess SnI_2 may even be more effective than SnF_2 as a reducing agent

since SnF_2 is hard to dissociate in films because of low solubility and stability.[127] To minimize SnF_2 assisted phase segregation, we use excess SnI_2, plus $EDAI_2$ to reduce Sn^{2+} oxidation.

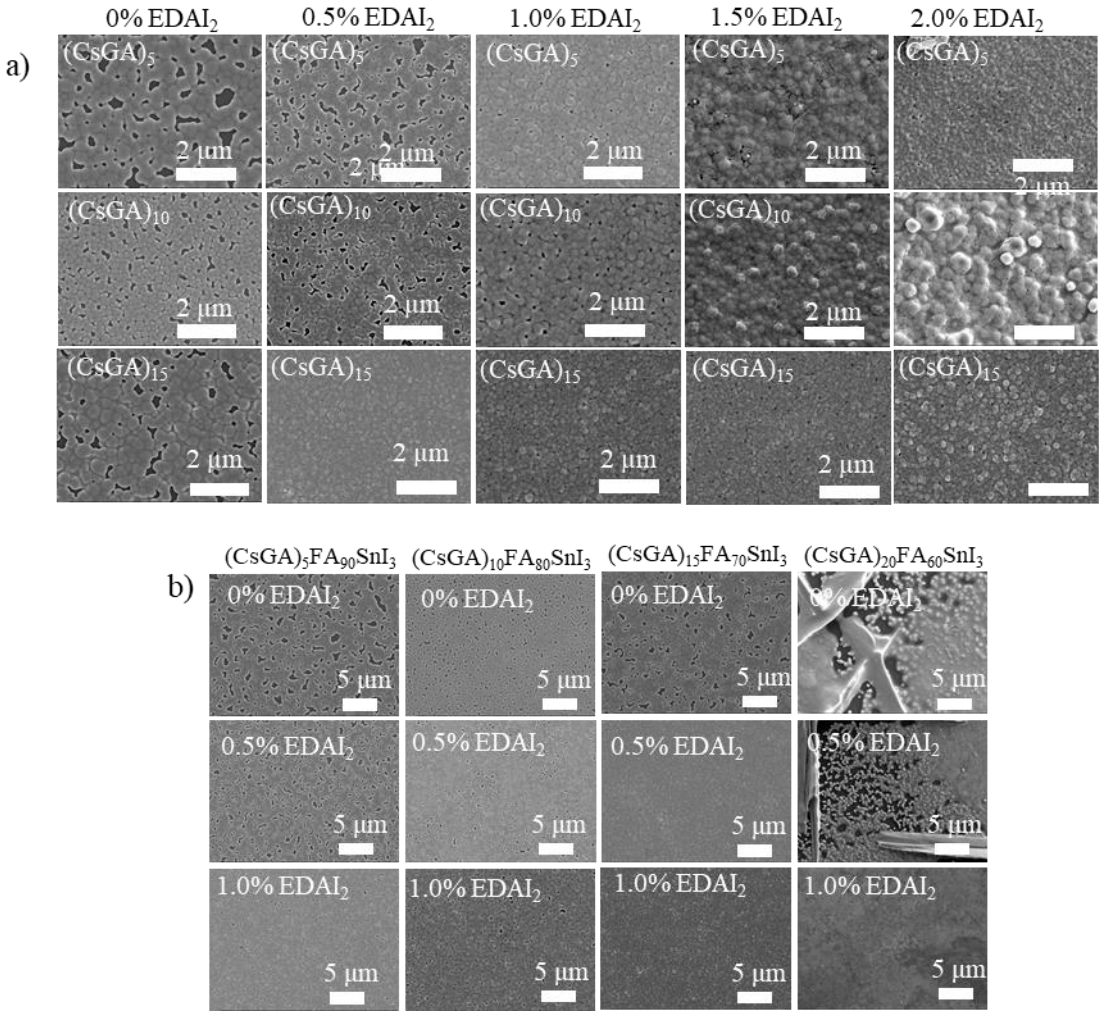

Figure 4-10. (a) High magnification SEM images of $(CsGA)_x$+y% $EDAI_2$ perovskite thin films with x =5, 10, and 15, and y = 0, 0.5, 1.0, 1.5, and 2.0. and (b) Low magnification SEM images of $(CsGA)_x$+y% $EDAI_2$ perovskite thin films with x =5, 10, 15, and 20 and y = 0, 0.5, and 1.0.

Figure 4-10a shows the scanning electron microscopy (SEM) images of the synthesized films with compositions of $(CsGA)_xFA_{100-2x}SnI_3$ + y% $EDAI_2$ where x = 5, 10, and 15 where y = 0, 0.5, 1.0, 1.5, 2.0. $(CsGA)_{15}$+y% $EDAI_2$ perovskite thin films. Without the addition of $EDAI_2$, $(CsGA)_{15}$ films have flat, large grains and pinholes, which may be due to few nuclei and a rapid crystal growth rate.[128] $EDAI_2$ has been previously shown to act as a controlled agent and balance the

kinetic processes between crystal growth and nucleation. The divalent nature of $EDAI_2$ allows for uniform nucleation and, in tandem with slow crystal growth, forms densely packed perovskite films.[125] Because of this increased nucleation, from 0 to 1.0% $EDAI_2$, there is a decrease in grain size and number of pinholes. Dense, small grains are formed for the $(CsGA)_{15}$+1.0% $EDAI_2$ film. The SEM images for $(CsGA)_5$+y% $EDAI_2$ and $(CsGA)_{10}$+y% $EDAI_2$ perovskite thin films illustrate a similar trend in decreasing grain size and pinholes from 0 to 1.0% $EDAI_2$. When increasing $EDAI_2$ to 1.5% and 2%, the perovskite grains jut out from surfaces as shown in $(CsGA)_5$,$(CsGA)_{10}$ and $(CsGA)_{15}$ film. This effect has been observed more drastically with 5% $EDAI_2$ incorporation, coupled with decreased crystal density due to the replacement of B- and X-sites.[129] Figure 4-10b shows the low magnification SEM images of all $(CsGA)_x$+y% $EDAI_2$ films to demonstrate the consistency of film morphologies.

X-ray diffraction (XRD) was used to characterize the phase and crystallinity of the thin films. Figure 4-11a shows the XRD patterns for $(CsGA)_5$, $(CsGA)_{10,}$ $(CsGA)_{15,}$ $(CsGA)_{20}$+0-2.0% $EDAI_2$ thin films with indexed cubic peaks. Previous literature has shown a pseudo cubic orthorhombic phase for $FASnI_3$ with Amm2 space group.[121] We compared the XRD pattern of $(CsGA)_{15}$+1.0% $EDAI_2$ film and the simulated XRD patterns of $FASnI_3$ with the cubic Pm3m and orthorhombic Amm2 space groups in Figure4-12. The XRD pattern of $(CsGA)_{15}$+1.0% $EDAI_2$ film matches very well with the peaks corresponding to the cubic phase and does not show any peak splitting and characteristic peaks that are shown in the orthorhombic phase. Kubicki *et al*. used NMR to demonstrate the direct evidence of GA^+ incorporation into the $MAPbI_3$ and $FAPbI_3$ lattice forming phase-pure materials, dispelling the hypothesis that GA^+ is too large to enter the perovskite crystal structure.[130] We estimated the average A-site cation radii with mixed triple cations and calculated the Goldschmidt tolerance factors of $(CsGA)_xFA_{100-2x}SnI_3$ without $EDAI_2$ based on the average A-

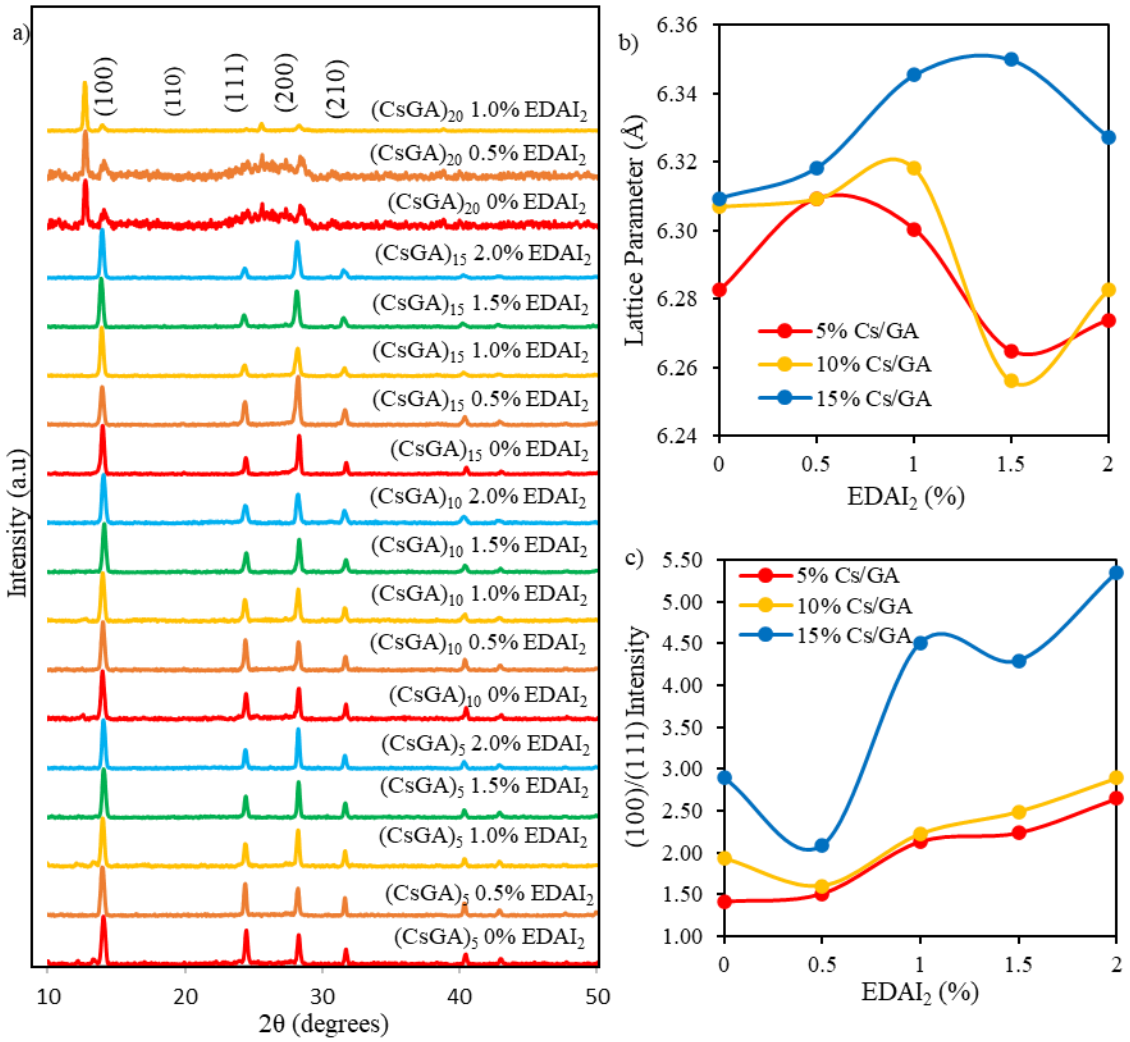

Figure 4-11. (a) XRD patterns of $(CsGA)_x$+y% $EDAI_2$ perovskite thin films with x = 5, 10, 15, and 20 and y = 0, 0.5, 1.0, 1.5, and 2.0. and the corresponding (b) cubic lattice parameter and (c) the (100)/(111) peak intensity ratio as a function of percent $EDAI_2$.

site cation radii (Table 4-2). As the concentration of FA^+ (r = 2.53 Å) decreases and concentrations of both Cs^+ (r = 1.67 Å) and GA^+ (r = 2.78 Å) increase, the average A-site cation radius decreases from 2.50 Å $(CsGA)_5$ to 2.47 Å $(CsGA)_{10}$ to 2.44 Å $(CsGA)_{15}$. This trend is reflected in the decrease in lattice parameter from 6.291 Å to 6.274 Å to 6.269 Å for $(CsGA)_5$, $(CsGA)_{10}$, and $(CsGA)_{15}$, respectively, with 0% $EDAI_2$ (Figure4-11b), indicating the incorporation of CsGA into the perovskite crystal structures. The incorporation of CsGA suppresses the tolerance factor of $FASnI_3$, pushing the tolerance factor into the more ideal cubic region. Without $EDAI_2$, $(CsGA)_5$

Table 4-2. Average A-site cation radius (Ra) and Goldschmidt tolerance factors (GTF) for $(CsGA)_xFA_{100-2x}SnI_3$ with x = 0, 5, 10, 15, 20, and 25. The average A-site cation radius was calculated as $Ra = (x(R_{Cs} + R_{GA}) + (100-2x)R_{FA})/100$, where R_{Cs} is the radius of Cs^+ (1.67 Å), R_{GA} is the radius of GA^+ (2.78 Å), and R_{FA} is the radius of FA^+ (2.53 Å). The $EDAI_2$ effect was not included in the calculations.

Sample	Ra (Å)	GTF
$FASnI_3$	2.53	0.998
$(CsGA)_5FA_{90}SnI_3$	2.50	0.992
$(CsGA)_{10}FA_{80}SnI_3$	2.47	0.986
$(CsGA)_{15}FA_{70}SnI_3$	2.44	0.979
$(CsGA)_{20}FA_{60}SnI_3$	2.41	0.973
$(CsGA)_{25}FA_{50}SnI_3$	2.38	0.966

and $(CsGA)_{10}$ have the tolerance factors of 0.992 and 0.986, respectively, approaching the tetragonal/hexagonal region. Small peaks emerge at 13.28° and in 12.12° in the XRD patterns of $(CsGA)_5$ and $(CsGA)_{10}$ with 0% $EDAI_2$ thin films might be attributed to the orthorhombic impurity phase due to higher tolerance factors. No impurity phase peaks present in the XRD pattern of the $(CsGA)_{15}$ with 0% $EDAI_2$ thin film because the tolerance factor has been pushed far enough into the ideal cubic region (Table 4-2). Although further increasing CsGA content can reduce the average A-site radii and tolerance factors, both XRD patterns and SEM images show the formation of 2D guanidinium based perovskites and diminished 3D perovskites in $(CsGA)_{20}$+0-1.0% $EDAI_2$ thin films. More amorphous perovskites were formed with 0 and 0.5% $EDAI_2$, which is consistent with the previous observations with high GA^+ content in $MAPbI_3$ perovskites. Phase changes from 3D to 1D structures when GA^+ was increased above 25% in $MAPbI_3$ perovskites.[131]

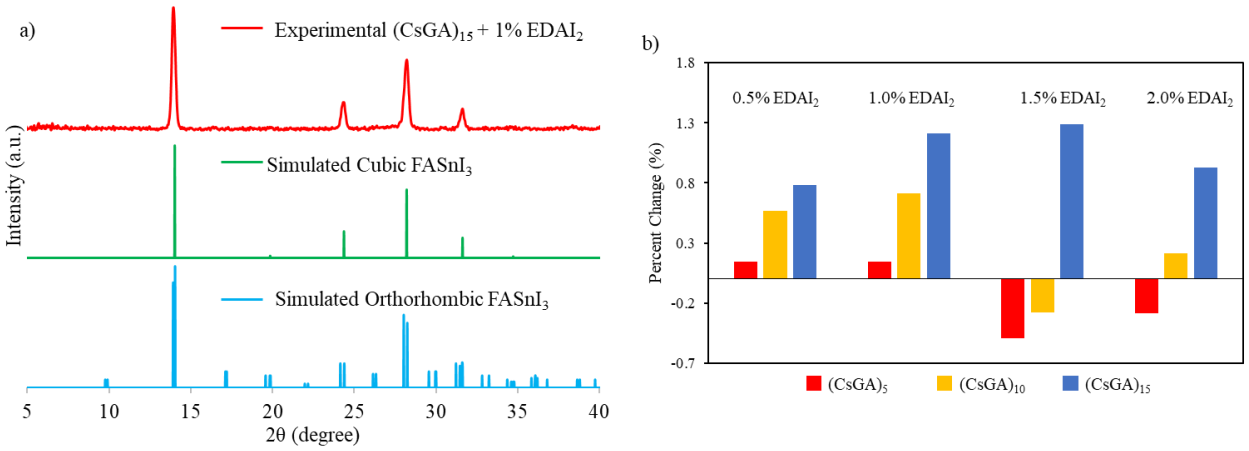

Figure 4-12. (a) XRD pattern of $(CsGA)_{15}$+1.0% $EDAI_2$ thin film along with simulated XRD patterns of cubic and orthorhombic phases of $FASnI_3$. (b) Percent change in lattice parameter of $(CsGA)_5$, $(CsGA)_{10}$, and $(CsGA)_{15}$ thin films comparing the percent lattice parameter change of adding 0.5%, 1.0%, 1.5%, and 2% $EDAI_2$ relative to 0% $EDAI_2$.

The $GA_{0.2}FA_{0.8}SnI_3$ thin films showed a preferred growth direction along the (120) plane without the $EDAI_2$ incorporation, which was altered to the (100) plane when 1% $EDAI_2$ was added.[117] We plotted the (100)/(111) peak intensity ratio as a function of $EDAI_2$ percent for $(CsGA)_5$, $(CsGA)_{10}$ and $(CsGA)_{15}$ (Figure4-11c). Our results show, even without $EDAI_2$, the $(CsGA)_5$, $(CsGA)_{10}$ and $(CsGA)_{15}$ films exhibit a preferred (100) orientation with the (100)/(111) peak intensity ratio increasing from 1.41 for $(CsGA)_5$ to 2.89 for $(CsGA)_{15}$, indicating that the incorporation of Cs^+ can alter the preferred orientation of crystal growth. The increasing of (100) orientation may be due to the increased hydrogen bonding from GA^+ and defect mitigation of Cs^+ allowing orientation to a more stable facet. The (100)/(111) peak intensity ratios increase with the increasing of $EDAI_2$. This trend is particularly prominent for the $(CsGA)_{15}$ thin films because of a large decrease in the (111) peak intensity for the $(CsGA)_{15}$ thin films with 1.0-2.0% $EDAI_2$. The (100) facet, which has a A-X or B-X layer termination, has been found to be most stable with the highest level of BX_6 coordination.[132] The $EDAI_2$ assisted growth of the (100) perovskite facet is

due to hydrogen bonding and interaction with the halide cage. $EDAI_2$ then becomes the terminating end group and passivates defects in the grain boundary, which is illustrated in Figure4-1d.

The effective ionic radius of $EDAI_2$ is estimated to be 3.74 Å.[129] Theoretically, the incorporation of $EDAI_2$ into the 3D structure of the ABX_3 as an A-site replacement would push the tolerance factor above 1, outside the optimum cubic range.[29] Previous XRD results showed an orthorhombic phase $FASnI_3$ perovskite was transformed to a tetragonal phase with 39% $EDAI_2$ incorporation.[21] Because of the larger and divalent nature of $EDAI_2$, the cation not only takes the A-site but also hollows and protrudes into the space of vacant B-site and displaces X-site. This hollowing effect decreased the crystal density while maintaining 3D crystal structures, which was confirmed using H-NMR.[29] We calculated the cubic phase lattice parameters of $(CsGA)_5$, $(CsGA)_{10}$ and $(CsGA)_{15}$ with different amounts of $EDAI_2$ added and plotted them as a function of percent $EDAI_2$ (Figure4-11b). The changes in lattice parameter of $(CsGA)_5$, $(CsGA)_{10}$ and $(CsGA)_{15}$ thin films by adding $EDAI_2$ relative to no $EDAI_2$ are plotted in Figure4-12b. For $(CsGA)_{15}$ films, the lattice parameter increases 1.21% and 1.28% from 6.269 Å without $EDAI_2$ to 6.345 Å with 1% $EDAI_2$ and 6.350 Å with 1.5% $EDAI_2$, respectively. Further increasing $EDAI_2$ to 2%, the lattice parameter decreases to 6.327 Å comparing to the peak value with 1.5% $EDAI_2$ but still has a 0.93% increase comparing to that with 0% $EDAI_2$. The similar trends were shown for $(CsGA)_5$ and $(CsGA)_{10}$ films, except that the lattice parameter decreases with 1.5% $EDAI_2$ and then increase with 2.0% $EDAI_2$ for both $(CsGA)_5$ and $(CsGA)_{10}$ films. It is noted that the negative lattice parameter changes exhibited for $(CsGA)_5$ with 1.5 and 2.0% $EDAI_2$ and $(CsGA)_{10}$ with 1.5% $EDAI_2$. Another interesting trend is that more lattice parameter increases for larger amount CsGA substitution thin films with 0.5 and 1.0% $EDAI_2$ addition. For $(CsGA)_5$ films, the lattice parameter increases the same 0.14% from 6.291 Å without $EDAI_2$ to 6.300 Å with 0.5% and 1% $EDAI_2$, while the corresponding increases

are 0.57% and 0.71% from 6.274 Å without $EDAI_2$ to 6.31 Å with 0.5% $EDAI_2$ and 6.318 Å with 1% $EDAI_2$, respectively, for $(CsGA)_{10}$ films. The results indicate that EDA^{2+} ions are integrated into the crystal lattices, replacing octahedral sites in the perovskites and introducing a small "hollowing" effect as illustrated in Figure4-1d. Stronger "hollowing" effect in the larger CsGA substation films with the same small amount of $EDAI_2$ addition (0.5 and 1.0%) could be because the incorporation of larger amount of small Cs^+ cations makes more A-site spaces to accommodate more EDA^{2+}, creating more hollow centers and expanding the crystal lattice. The decrease of the lattice parameter for both $(CsGA)_5$ and $(CsGA)_{10}$ with 1.5% $EDAI_2$ films could be due to expelling large GA^+ cations from the perovskite lattice and most EDA^{2+} being to passivate or terminate, instead of hollowing, the perovskite crystals. Although the lattice parameter for $(CsGA)_{15}$ with 2.0% $EDAI_2$ film decreases comparing to that of the film with 1.5% $EDAI_2$, the lattice parameter is still larger than that of the film without $EDAI_2$. This suggests that it might be an energy balance between hollowing crystal structures and terminating crystal surfaces with $EDAI_2$. Nonetheless, the results of increased crystal orientation towards the (100) plane and the lattice parameter variations with the addition of $EDAI_2$ reveal that $EDAI_2$ can both create hollow centers inside crystals and passivate grain boundaries.

To investigate the impacts of both CsGA and $EDAI_2$ on optical and electronic properties, we collected UV-Vis absorption and static photoluminescence (PL) spectra of $(CsGA)_5$, $(CsGA)_{10}$ and $(CsGA)_{15}$ thin films. The UV-Vis and PL spectra of $(CsGA)_5$, $(CsGA)_{10}$ and $(CsGA)_{15}$ thin films with 0 and 1% $EDAI_2$ addition are shown in Fig.4-13. The optical band gaps derived from the UV-Vis absorption cutoffs of 0 and 1% $EDAI_2$ are 1.44 and 1.45 eV, respectively, for $(CsGA)_5$, 1.43 and 1.44 eV, respectively, for $(CsGA)_{10}$, and 1.42 and 1.43 eV, respectively, for $(CsGA)_{15}$. Without $EDAI_2$, the band gap decreases slightly from 1.44 to 1.42 eV, when increasing CsGA from 5 to

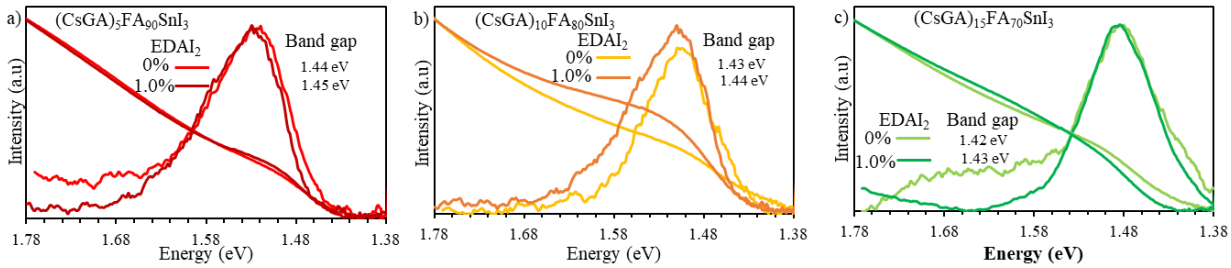

Figure 4-13. PL spectra and normalized UV-Vis absorption spectra of (a) $(CsGA)_5$ (b) $(CsGA)_{10}$ and (c) $(CsGA)_{15}$ thin films with 0 and 1.0% $EDAI_2$. The optical band gaps derived from the UV-Vis absorption cutoffs are displayed inside the plots.

15%. The average cation radius and lattice parameter decrease for these films as discussed above. In Chapter 3, we showed the band gap of $Cs_x(MA_{0.17}FA_{0.83})_{1-x}Sn(I_{0.83}Br_{0.17})_3$ perovskites decrease with a decreasing lattice parameter due to a smaller average cation radius.[133] Both A-site induced BX_6 octahedral tiling and B-X overlap on conduction and valence band edges of perovskites influence these band gap trends.[101] The correlation between the band gap decreasing and the lattice parameter decreasing for $(CsGA)_x$ without $EDAI_2$ reflects that the same mechanism plays the role, where the increased isotropic lattice constrictions and B-X overlap make the valence band maximum shift upwards more than the conduction band minimum.[37] For all $(CsGA)_x$, when 1% $EDAI_2$ is added, there is a 0.01 eV blue shift of band gaps because of decreased isotropic lattice constrictions, decreasing B-X overlap. This blue shift is also due to the larger and divalent nature of EDA^{2+} displacing B-site and X-site atoms, eliminating several B-X connections. These missing B-X connections decreases the orbital overlap of the remaining Sn-I bonds, narrowing the width of the valance band and conduction band.[124,125] In addition, the UV-Vis absorption cutoff edges are sharpener and the PL peaks are narrower and stronger for $(CsGA)_{10}$ and $(CsGA)_{15}$ with 1.0% $EDAI_2$. These phenomena are more obvious with increasing CsGA substitution and diminish for $(CsGA)_5$ films. The opening of band gap, sharpening of UV-Vis absorption cutoff edge, and

narrowing with increased intensity of PL peak further suggest that the addition of $EDAI_2$ can reduce the trap states between band gaps by reducing point defects inside the crystals via the hollowing effect and by reducing surface defects via passivating grain boundaries. Moreover, a greater amount of CsGA substitution is crucial for integrating EDA^{2+} cation and utilizing its effect on decreasing trap states.

4.2.3 Exploring Photovoltaic Performance with Cs/GA Cations and $EDAI_2$

The $(CsGA)_x$+y% $EDAI_2$ films were deployed as active layers in PVSCs with an inverted device structure ITO/PEDOT:PSS/perovskite/ $PC_{60}BM$/BCP/Ag, which is illustrated in the cross-sectional SEM image in Figure4-14a. Solution processed PEDOT:PSS acts as the hole transport layer (HTL) while the spin-coated $PC_{60}BM$ acts as the electron transport layer (ETL) as well as reduces surface roughness and passivates possible traps.[103] Solution processed BCP layer acts as a hole blocking layer (HBL) to increase charge separation and minimize recombination. Unlike Pb-based PVSCs, the record breaking PCE and highest stabilities for pure Sn perovskites have been achieved on inverted (p-i-n) architectures.[134] In general, the exciton generation rate is higher in the active layer closer to the light incident side, or the transparent electrode side, and gradually decreases towards the metal electrode side. For inverted p-i-n devices, the high amount of hole carriers generated at the perovskite/HTL layer can be quickly collected by the HTL, greatly reducing the possibility of Sn^{2+} being oxidized to Sn^{4+} by extra holes. In contrast, the high amount of hole carriers generated at the perovskite/ETL in n-i-p devices must transfer through the active layer to be collected by the HTL on the top of the active layer. This could increase the oxidation of Sn^{2+} to Sn^{4+}.[134] In addition, the commonly used metal oxide ETLs such as TiO_2 and SnO_2 may have oxygen vacancies that accelerate tin oxidation.[135]

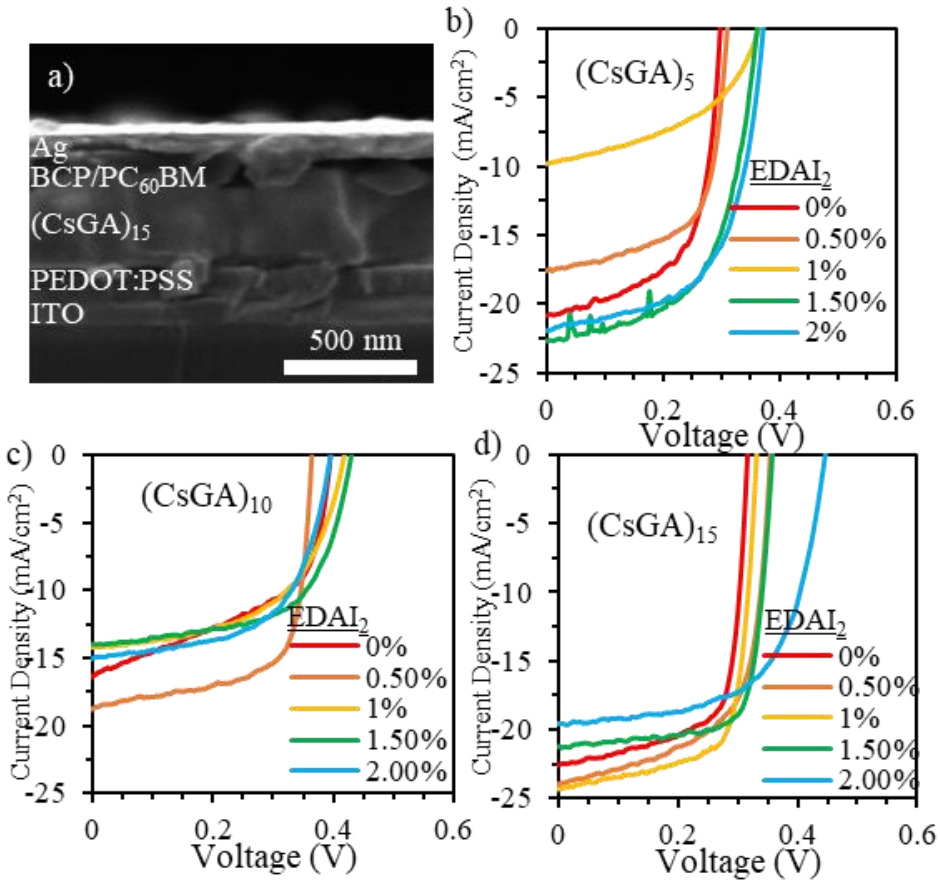

Figure 4-14. (a) Cross-sectional SEM image showing the $(CsGA)_{15}$+1.0% $EDAI_2$ PVSC with the following layers: ITO (200 nm)/PEDOT:PSS (50 nm)/perovskite (400 nm)/$PC_{60}BM$/BCP/Ag (100 nm). The photocurrent density–voltage (J–V) characteristics of the best performance PVSCs with the active layer (b) $(CsGA)_5$+y% $EDAI_2$ (c) $(CsGA)_{10}$+y% $EDAI_2$ (d) $(CsGA)_{15}$+y% $EDAI_2$ thin films with y = 0, 0.5, 1.0, 1.5, and 2.0 under AM 1.5G illumination scanned from -0.1 to 0.6 V at a scan rate of 0.01 V s^{-1}.

Figures 4-14 shows the photocurrent density-voltage (J-V) characteristics of the devices fabricated with $(CsGA)_5$, $(CsGA)_{10}$, and $(CsGA)_{15}$+y% $EDAI_2$ active layers with y = 0, 0.5, 1.0, 1.5 and 2.0. Detailed photovoltaic parameters are summarized in Table 4-3. The trends with average V_{oc}, J_{sc}, FF, and PCE with increasing Cs/GA and varying $EDAI_2$ amounts is illustrated in Figure 4-15. Devices containing the active layers $(CsGA)_{15}$ without $EDAI_2$ exhibit the maximum PCE of 5.01%, with the corresponding V_{oc} of 0.32 V, J_{sc} of 22.61 mA/cm^2, and FF of 0.70. The maximum PCE of our $(CsGA)_{15}$+0% $EDAI_2$ devices is much higher than 0.5% PCE of the devices

Table 4-3. Average photovoltaic parameters and the best performance device photovoltaic parameters in parenthesis along with series resistance, R_s and Shunt resistance, R_{sh} of PVSCs containing $(CsGA)_{15}$+y% $EDAI_2$ with y = 0, 0.5, 1.0, 1.5, and 2.0 measured under AM 1.5G illumination obtained from the forward J-V measurements.

Device	V_{oc} (V)	J_{sc} (mA cm^{-2})	FF	PCE (%)	R_s Ω.cm^2	R_{sh} Ω.cm^2
$(CsGA)_5$ +0%	0.30±0.02 (0.29)	15.75±2.80 (20.71)	0.54±0.05 (0.61)	2.58±0.60 (3.71)	3.51	45.56
$(CsGA)_5$ +0.5%	0.31 ±0.01 (0.31)	13.26±3.44 (17.46)	0.55±0.07 (0.64)	2.29±0.73 (3.40)	4.22	66.59
$(CsGA)_5$ +1.0%	0.32±0.04 (0.36)	12.70±2.79 (9.81)	0.38±0.08 (0.46)	1.50±0.17 (1.61)	16.22	73.08
$(CsGA)_5$ +1.5%	0.36±0.00 (0.32)	22.35±2.35 (22.61)	0.57±0.02 (0.70)	4.61±0.61 (5.14)	5.35	57.19
$(CsGA)_5$ +2.0%	0.36±0.01 (0.37)	21.21±2.03 (21.89)	0.53±0.07 (0.59)	4.01±0.68 (4.78)	5.59	57.95
$(CsGA)_{10}$ +0%	0.36±0.04 (0.39)	14.91±1.18 (16.27)	0.36±0.13 (0.51)	2.01±1.10 (3.26)	7.70	53.40
$(CsGA)_{10}$ +0.5%	0.34±0.02 (0.36)	15.82±2.89 (18.66)	0.63±0.04 (0.68)	3.44±0.94 (4.56)	3.63	84.17
$(CsGA)_{10}$ +1.0%	0.39±0.01 (0.42)	11.90±1.99 (14.19)	0.56±0.03 (0.55)	2.61±0.5 (3.24)	10.19	86.07
$(CsGA)_{10}$ +1.5%	0.42±0.01 (0.43)	11.77±2.53 (13.93)	0.61±0.03 (0.61)	3.05±0.80 (3.66)	8.47	109.60
$(CsGA)_{10}$ +2.0%	0.40±0.01 (0.39)	13.49±4.55 (15.02)	0.57±0.03 (0.59)	3.03±0.90 (3.50)	8.42	93.10
$(CsGA)_{15}$ +0%	0.30±0.02 (0.32)	20.84±3.31 (22.61)	0.71±0.01 (0.70)	4.45±0.87 (5.01)	2.40	64.46
$(CsGA)_{15}$ +0.5%	0.35±0.02 (0.35)	21.43±2.28 (24.03)	0.61±0.04 (0.63)	4.58±0.61(5.39)	4.22	66.59
$(CsGA)_{15}$ +1.0%	0.35±0.02 (0.33)	20.81±1.78 (24.32)	0.63±0.06 (0.71)	4.62±0.63 (5.72)	2.72	78.00
$(CsGA)_{15}$ +1.5%	0.38±0.01 (0.36)	20.23±1.18 (21.16)	0.66±0.06 (0.75)	5.05±0.53 (5.69)	3.05	133.92
$(CsGA)_{15}$ +2.0%	0.43±0.02 (0.45)	15.20±2.50 (19.53)	0.57±0.04 (0.62)	3.74±0.94 (5.40)	6.67	92.14

with $GA_{0.2}FA_{0.8}SnI_3$ without $EDAI_2$, particularly, the maximum V_{oc} of 0.32 V versus the reported V_{oc} of ~0.1 V.[117] Adding Cs^+ to balance the larger cation GA^+ could decrease shallow trap states by Cs^+ filling in defects, which increases V_{oc} and improves J_{sc} and FF, culminating in much better device performance. Adding 0.5 and 1.0% $EDAI_2$ increases the maximum PCE to 5.39% and 5.72% due to both increased V_{oc} of 0.35 and 0.33 V, and J_{sc} of 24.03 and 24.32 mA/cm^2, respectively. Adding 1.5% $EDAI_2$ further increases the V_{oc} to 0.36 V and particularly increases the FF to 0.75, maintaining a high maximum PCE of 5.69%. The high FF may be due to the increasing Shunt resistance, R_{sh}, from 64.46 Ω.cm^2 with 0% $EDAI_2$ to 133.92 Ω.cm^2 with 1.5% $EDAI_2$. When adding 2.0% $EDAI_2$, although the V_{oc} increases to the largest of 0.45 V, the lowest J_{sc} of 19.53 mA/cm^2 and FF of 0.62 decrease the maximum PCE slightly to 5.40%. The lowest J_{sc} may be due to an increase in series resistance, R_s, to the maximum of 6.67 Ω.cm^2 among all

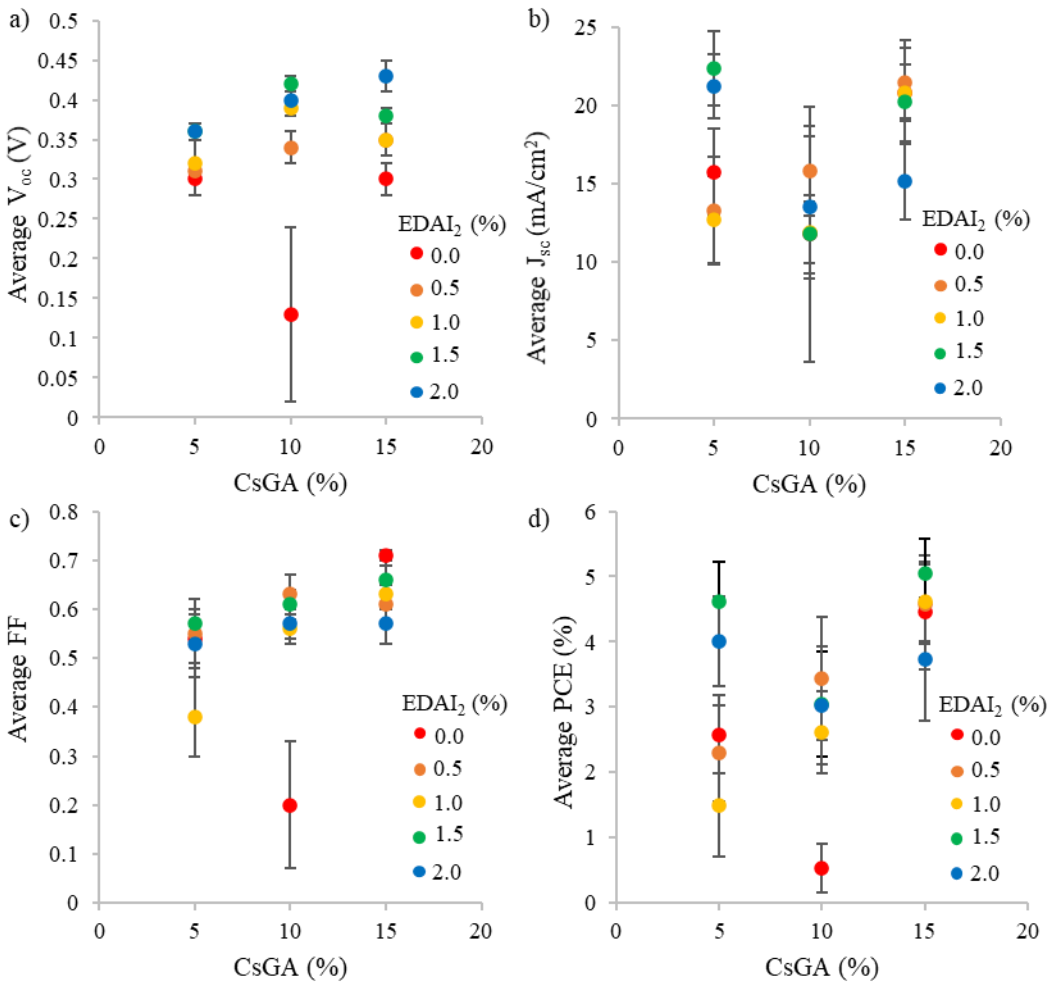

Figure 4-15. The averages of (a) V_{oc}, (b) J_{sc}, (c) FF, and d) PCE of PVSCs as a function of Cs/GA % for different $EDAI_2$ contents with $(CsGA)_xFA_{100-2x}SnI_3$ and y% $EDAI_2$ perovskite thin films as the active layers.

$(CsGA)_{15}$ devices. Figure 4-16 shows that the photocurrent at the maximum power point versus time for the $(CsGA)_{15}$+0-1.5% $EDAI_2$ devices remained stable under illumination in an inert atmosphere for the 10 min test period. The better performance exhibited by $(CsGA)_{15}$ with 0.5-1.5% $EDAI_2$ devices could be the benefits of improved film quality, (100) plane dominated termination, and reduced trap states. A declined performance of $(CsGA)_{15}$ with 2.0% $EDAI_2$ could be due to rough surface, creating more interface trap states. For the 5% Cs/GA perovskite, the 0% $EDAI_2$ addition reaches a PCE_{max} of 3.71% with an average PCE of 2.58%, an average V_{oc} of

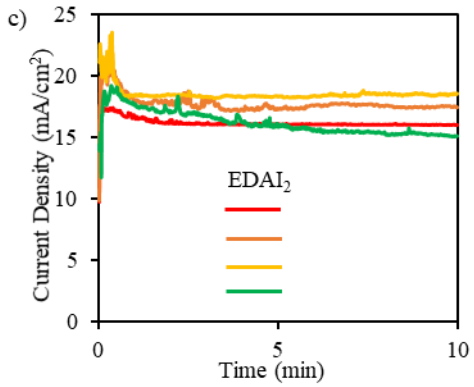

Figure 4-16. Photocurrent density at the maximum power point versus time for the $(CsGA)_{15}$+0-1.5% $EDAI_2$ devices under illumination.

0.30V, J_{sc} of 15.75 mA/cm^2, and FF of 0.54. This performance increases with the1.5% $EDAI_2$ addition which reaches a PCE_{max} of 5.14% with the average V_{oc} increases to 0.36V, J_{sc} increasing to 22.35 mA/cm^2, and FF increasing to 0.57. The 10% Cs/GA without $EDAI_2$ results in a shorted device with an average PCE of 2.01% with a corresponding V_{oc} of 0.36 V, J_{sc} of 14.91 mA/cm^2, and FF of 0.36. The addition of 0.5% $EDAI_2$ increases the performance of the 10% Cs/GA perovskites devices which reaches a PCE_{max} of 5.14% increasing the average V_{oc} of 0.34V, increasing the J_{sc} of 15.82 mA/cm^2, and increasing the FF of 0.63. Overall, figure 4-16 shows that PVSCs based on $(CsGA)_5$ and $(CsGA)_{10}$ with 0-2% of $EDAI_2$ active layers exhibit lower maximum PCEs compared to the counterparts of $(CsGA)_{15}$ mainly because of the lower J_{sc}'s and FF's. This could be attributed to more pinholes and impurity phases in the perovskite films, resulting in higher R_s and lower R_{sh}. This supports the hypothesis that the higher amount of Cs/GA allows for $EDAI_2$ to be better integrated into perovskite structure, improving these pinhole, defect, and phase impurity issues.

Previous study has shown that devices based on $GA_{0.2}FA_{0.8}SnI_3$ with 1% $EDAI_2$ active layers exhibited a V_{oc} of 0.619 V compared to 0.49 V for the devices based on $FASnI_3$ with 1% $EDAI_2$ active layers because of the downshifted valence band maximum to -5.20 eV versus -4.92 eV,

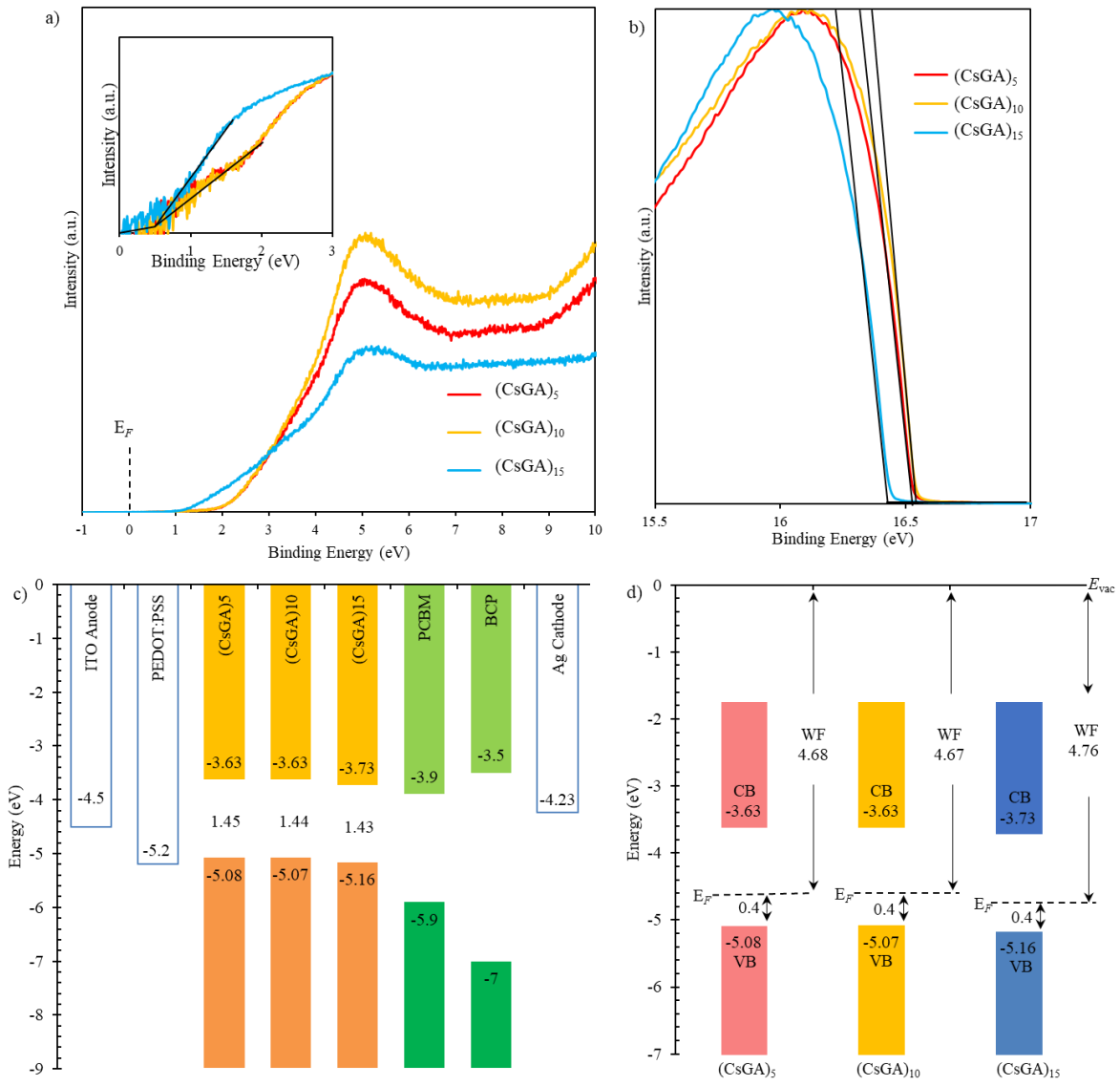

Figure 4-17. UPS spectra for (a) the valence band edge region and the Fermi levels and (b) the secondary electron energy cut off region for $(CsGA)_5$, $(CsGA)_{10}$, and $(CsGA)_{15}$ with 1.5% $EDAI_2$ thin films (c) Band energy diagram of PVSCs with $(CsGA)_x$+1.5% $EDAI_2$ active layers, where x = 5, 10, and 15. (d) Energy level scheme for the $(CsGA)_5$, $(CsGA)_{10}$, and $(CsGA)_{15}$ with 1.5% $EDAI_2$ based on the parameters derived from the UPS spectra.

which aligns better to the work function of PEDOT:PSS (-5.2 eV) as the HTL. The V_{oc}'s of our devices are low compared to the reported V_{oc}'s. To further investigate this, we conducted the ultraviolet photoelectron spectroscopy (UPS) analysis of $(CsGA)_5$, $(CsGA)_{10}$ and $(CsGA)_{15}$ with 1.5% $EDAI_2$ films because the devices based on these films exhibit high performance. Figure 4-

17c shows the energy diagram of the materials involved in the devices. The valence band maxima (VBM) of $(CsGA)_5$, $(CsGA)_{10}$ and $(CsGA)_{15}$ with 1.5% $EDAI_2$ were obtained from their UPS spectra (Figure4-17a,b) and the conduction band minima (CBM) were estimated from the VBM and the optical band gaps determined from the UV-Vis spectra of the $(CsGA)_5$, $(CsGA)_{10}$ and $(CsGA)_{15}$ with 1.0% $EDAI_2$ films. The VBM are determined to be -5.08, -5.07 and -5.16 eV for $(CsGA)_5$, $(CsGA)_{10}$ and $(CsGA)_{15}$ with 1.5% $EDAI_2$, respectively. All of them are unfavorable for hole transport with the PEDOT:PSS HTL,[117] which could lead to low V_{oc}'s. The deepest VBM and the smallest band gap of $(CsGA)_{15}$ make the CBM downshift to -3.73 eV. Both downshifted VBM and CBM of $(CsGA)_{15}$ makes the best energy alignment with the HTL and ETL, respectively, which could explain the best performance of devices based on $(CsGA)_{15}$ films. The $(CsGA)_5$, $(CsGA)_{10}$ and $(CsGA)_{15}$ with 1.5% $EDAI_2$ films have the Fermi level 0.4 eV above the VBM, indicating the p-type doping of all these perovskites (Figure4-17d). Previous studies have shown that guanidinium addition in $MAPbI_3$ transfers the perovskite to a p-type semiconductor with the Fermi level shifting from 1.1 to 0.89 eV above the VBM for $MAPbI_3$ and $GA_{0.25}MA_{0.75}PbI_3$, respectively.[136] X-site anion interstitial (X_i), A-site and B-site vacancy (V_A and V_B), and antisite (A_B, X_A and X_B) point defects typically cause p-type perovskites.[123] Sn-based perovskites tend to be p-type due to self-doping by Sn^{4+}.[134] The p-type nature of $(CsGA)_{15}$ with 1.5% $EDAI_2$ film could be due to $EDAI_2$ having a "hollowing" impact on the perovskite structure, giving the increased lattice parameter. $EDAI_2$ has been shown to favor replacing the octahedral cages with B-site and X-site and these metal and halide defects (vacancies and antisites) contribute to a more p-type perovskite.[121,129,137] Since the lattice parameters of $(CsGA)_5$ and $(CsGA)_{10}$ with 1.5% $EDAI_2$ films are even smaller than those without $EDAI_2$ because of the possibility of

expelling GA^+ cations, A-site vacancies could be formed in these perovskites besides aforementioned point defects, resulting in p-type perovskites.

XPS survey in Figure 4-18b show how incorporating increased amounts of Cs/GA decreases the amount of oxygen adhered to the perovskite surface. After perovskite films were exposed to ambient conditions, oxygen atomic concentration decreased from 23.19% to 17.21%

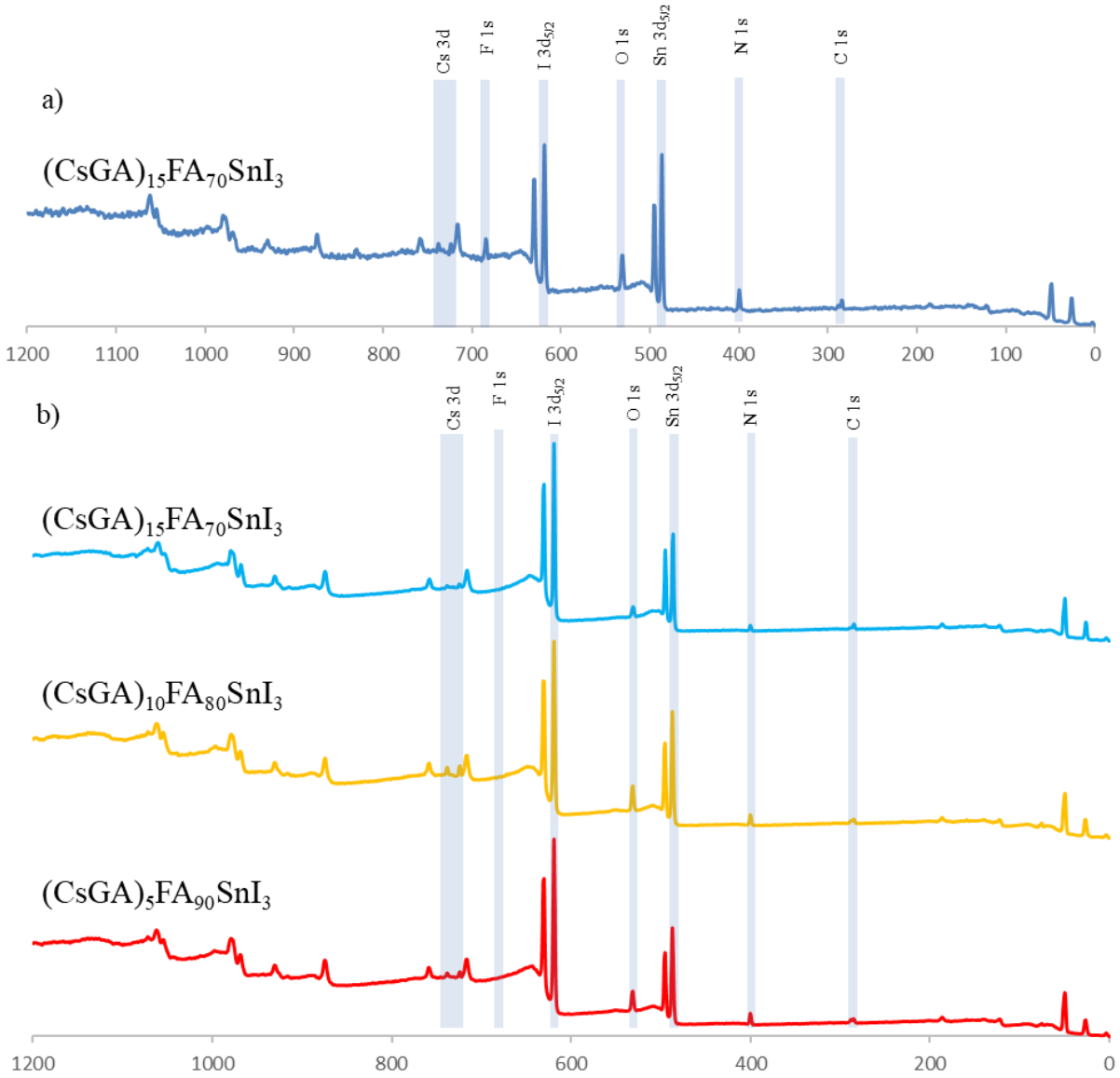

Figure 4-18. (a) XPS survey scan of $(CsGA)_{15}$ perovskite film using SnF_2 as a reducing agent and old synthesis method of GBL:DMSO, a toluene antisolvent, an no hot casting (b) XPS survey scan of $(CsGA)_5$ $(CsGA)_{10}$ $(CsGA)_{15}$ perovskite films using 1.5% $EDAI_2$, excess SnI_2 as an alternative reducing agent, DMSO solvent, and chlorobenzene antisolvent with hot casting at 70°C.

when Cs/GA amounts were increased from 5% to 15%. This supports the hypothesis that integrating smaller cations eliminates potential sites for defects that are prone to attacks by O_2 and H_2O. Interestingly, figure 4-18a, which utilizes the old synthesis method of a GBL:DMSO solvent mixture at 2.5M, a toluene antisolvent, SnF_2 reducing agent, and no hot casting, shows the $(CsGA)_{15}$ perovskite film composition with a much larger O 1s peak compared with figure 4-18b, which utilizes the new synthesis method with a DMSO solvent, 10% excess SnI_2, a chlorobenzene antisolvent, hot casting at 70°C, and 1.5% $EDAI_2$. This shows how the new synthesis method is able to decrease oxygen affinity on the perovskite surface, decrease attack sites for oxygen, and decrease potential overall Sn oxidation.

4.2.4 Improved Integration and Defect Mitigation of $EDAI_2$

The balanced charge generation, recombination and extraction rates are key factors in determining solar cell performance.[138] Charge recombination results in loss of photogenerated charges, lowering J_{sc} and FF. The maximum V_{oc} of a solar cell can be achieved when all photogenerated charges recombine solely radiatively.[86] To understand device performance related to the mitigation of defects by incorporating of $EDAI_2$ in $(CsGA)_{15}$ perovskites, we investigated the evolution of V_{oc}, J_{sc} and FF as a function of light intensity for $(CsGA)_{15}$ with 0-1.5% $EDAI_2$ with the JV curves shown in figure 4-22. The V_{oc} of light intensity is an independent exploration of recombination than that of J_{sc} and FF. The current is zero under open-circuit conditions with all photogenerated carriers recombine within the cell. Recombination studies near open-circuit are, therefore, particularly sensitive to recombination mechanisms and the impact of shallow traps. The open-circuit voltage shows a logarithmic dependence on light intensity with a slope of nk_BT/q, where n represent different recombination mechanisms, k_B is the Boltzmann constant, T is the

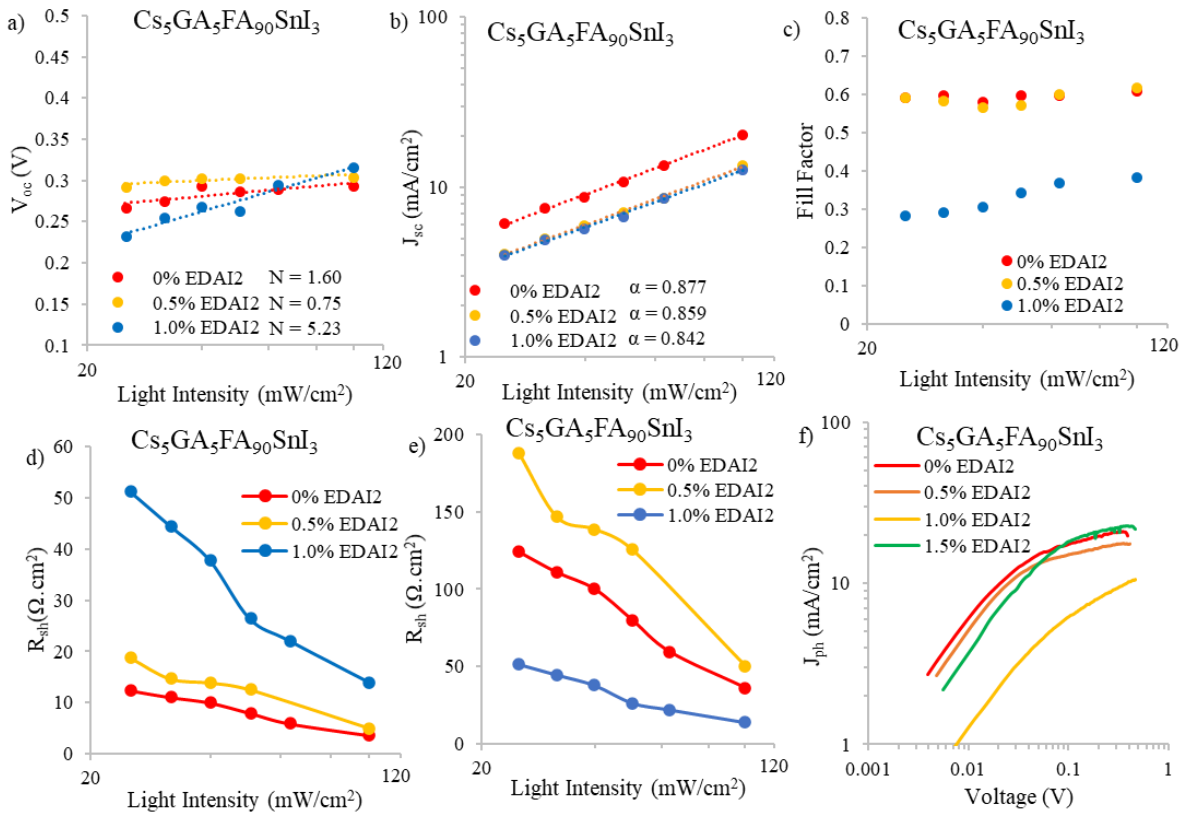

Figure 4-19. (a) V_{oc} as a function of light intensity (b) J_{sc} as a function of light intensity (c) FF as a function of light intensity (d) series resistance as a function of light intensity (e) shunt resistance as a function of light (f) photocurrent density as a result of effective voltage for $(CsGA)_5FA_{90}SnI_3$ with varying $EDAI_2$.

absolute temperature, and q is the elementary charge. When n > 2, monomolecular recombination dominates and trap states play a significant role, while n ~ 1, bimolecular recombination dominates, demonstrating minimal shallow trap states in perovskites.[139] The V_{oc} versus logarithmic scale light intensity plots for $(CsGA)_{15}$ devices show the slope changes from greater than 2 to close to 1 for without $EDAI_2$ addition to 1.0 and 1.5% $EDAI_2$ additions (Figure4-21a), indicating the charge carrier recombination from monomolecular, trap-state assisted recombination to biomolecular recombination. These results are consistent with the trap-state reduction shown by the UV-Vis and PL spectra, which further supports the hypothesis that $EDAI_2$ has a hollowing effect, reducing bulk defects.

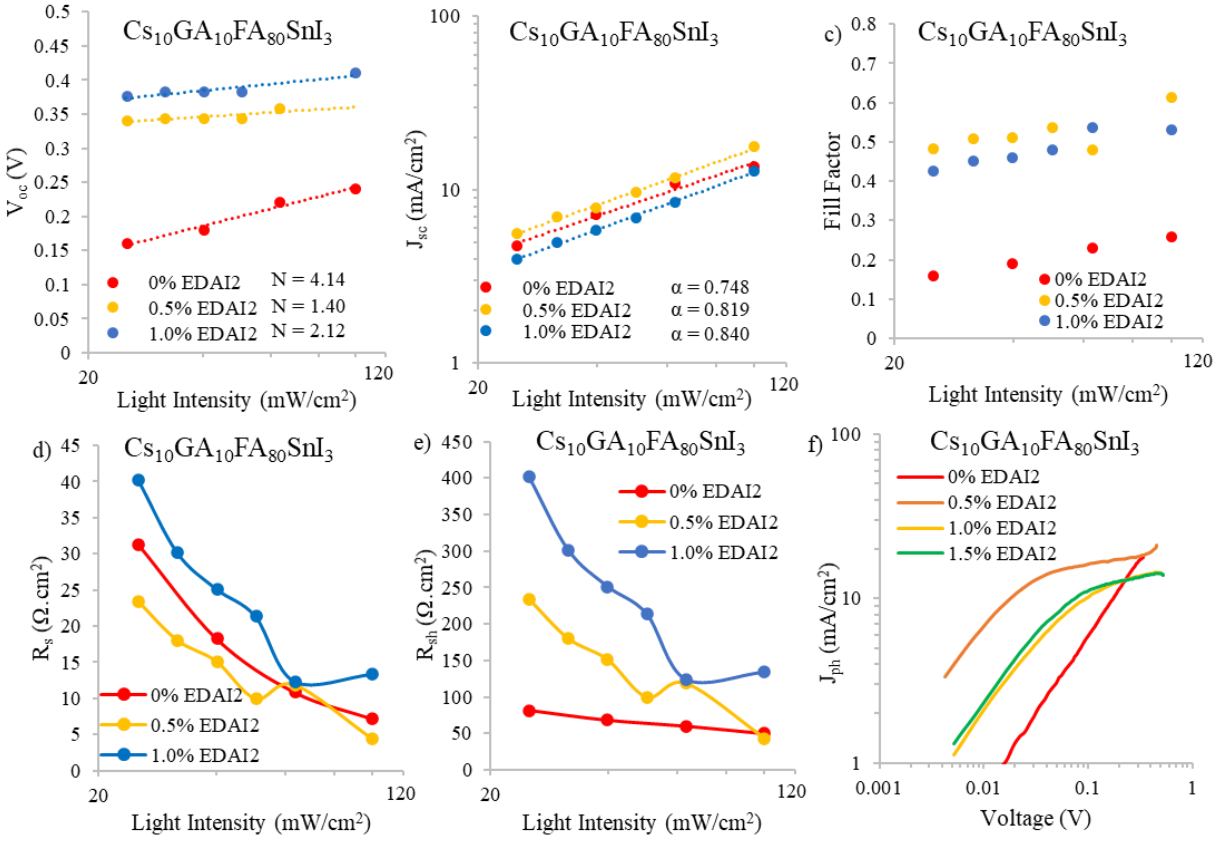

Figure 4-20. (a) V_{oc} as a function of light intensity (b) J_{sc} as a function of light intensity (c) FF as a function of light intensity (d) series resistance as a function of light intensity (e) shunt resistance as a function of light (f) photocurrent density as a result of effective voltage for $(CsGA)_{10}FA_{80}SnI_3$ with varying $EDAI_2$.

Figure 4-21b shows the double logarithmic scale with the relation of J_{sc} versus light intensity. For the power law dependence of J_{sc} on light intensity ($J_{SC} \propto I^{\alpha}$), the deviation from unity of the slope implies bimolecular recombination. When α is less than 1, this could be a result of bimolecular recombination, variations in both carrier mobilities or distribution in the density of states. When α ~ 0.75, spaces charge effects might be induced by the interfacial layers. When α = 1, there are no space charge effects and all carriers are swept out prior to recombination.[139,140] For $EDAI_2$ addition from 0% to 1.5%, α values changes from 1.21 to 1.00. This shows that the addition of $EDAI_2$ reduces the deep trap states by passivating grain boundaries and charge carriers are effectively extracted. We also plotted FF as a function of logarithmic scale light intensity (Figure4-

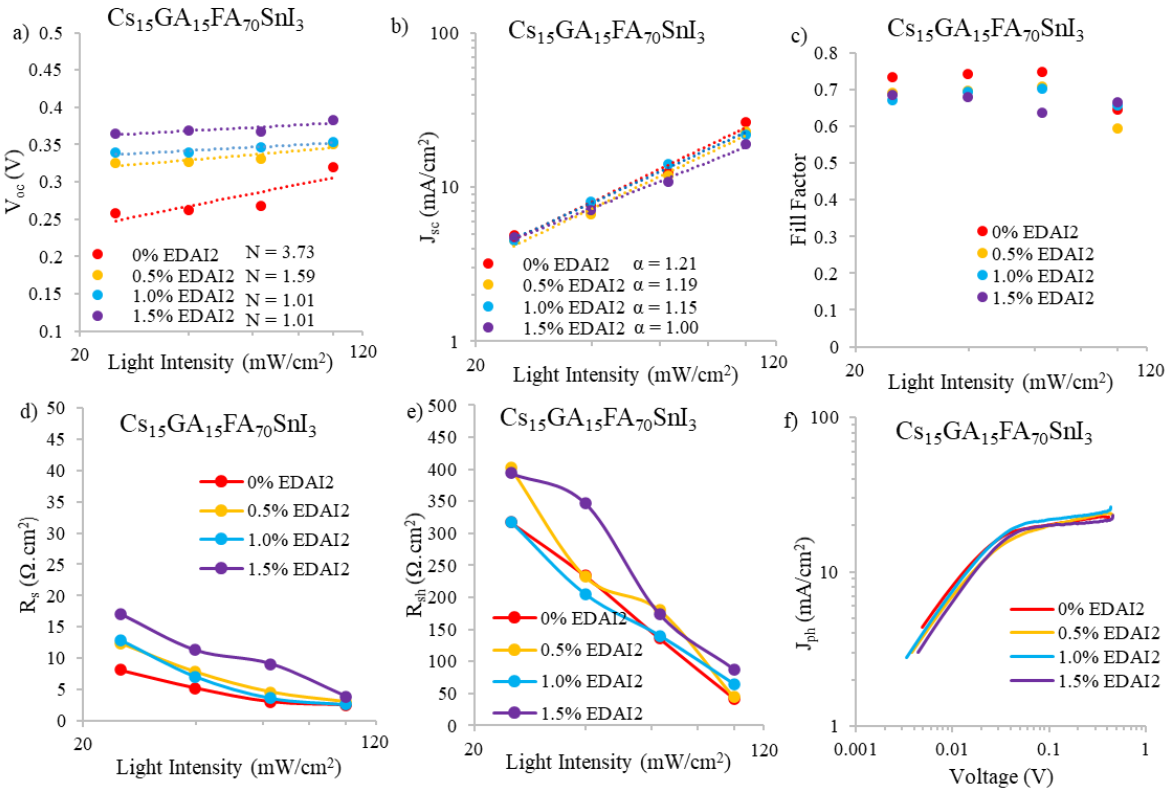

Figure 4-21. (a) V_{oc} as a function of light intensity (b) J_{sc} as a function of light intensity (c) FF as a function of light intensity (d) series resistance as a function of light intensity (e) shunt resistance as a function of light (f) photocurrent density as a result of effective voltage for $(CsGA)_{15}FA_{70}SnI_3$ with varying $EDAI_2$.

21c). These FF trends show the different capabilities of the perovskite materials to support balanced charge carrier generation and extraction over this range of light intensities. At low light intensities, the device of $(CsGA)_{15}$ without $EDAI_2$ show higher FF's than the devices with 0.5-1.5% $EDAI_2$, indicating that despite the trap-states, low density charge carriers in $(CsGA)_{15}$+0% $EDAI_2$ are still able to be extracted due to intrinsic high charge carrier mobility and long diffusion length of perovskites.[141,34,142] When light intensity increases to 1 sun, 100 mW/cm^2, more charge carriers are recombined via trap-states, leading to a significant decrease of FF for $(CsGA)_{15}$ with 0 and 0.5% $EDAI_2$. The device of $(CsGA)_{15}$ with 1.5% $EDAI_2$ retains the same level of FF at 1 sun illumination, demonstrating the reduction of trap-states by adding $EDAI_2$. To elucidate whether the FF reduction under 1 sun for the devices of $(CsGA)_{15}$ without $EDAI_2$ and with 0.5-1%

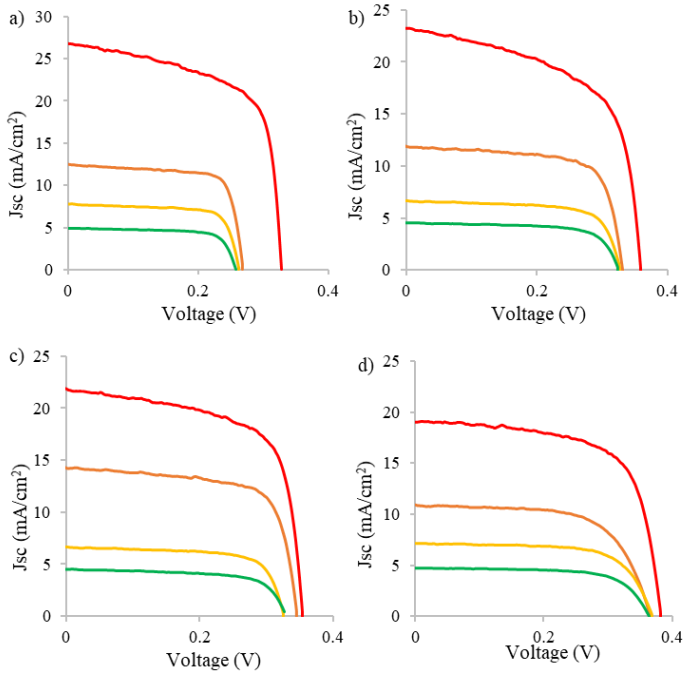

Figure 4-22. J-V characteristics of $(CsGA)_{15}FA_{70}SnI_3$ with (a) 0%, (b) 0.5%, (c) 1.0%, and (d) 1.5% $EDAI_2$ respect to change in light intensity of 100 mW/cm^2 (red line), 63.10 mW/cm^2 (orange line), 39.81 mW/cm^2 (yellow line), and 25.12 mW/cm^2 (green line).

$EDAI_2$ is due to charge extraction limit, we explored the photocurrent density (J_{ph}) as a function of effective voltage (V_{eff}). J_{ph} is defined as $J_{ph} = J_1 - J_d$, where J_1 and J_d represent the current densities in light and dark conditions, respectively. V_{eff} is defined as $V_{eff} = V_0 - V$, where V_0 is the compensation voltage defined as J_{ph} (V_0) = 0, and V is the applied voltage.[138] Figure 4-21f shows for all devices, photocurrent densities under 1 sun reach the saturation at a similar low effective voltage ~0.05 V, suggesting that charge extraction is not a limit factor. The low saturation effective voltage could be linked to the better band alignment of $(CsGA)_{15}$ with the charge selective layers. Figure 4-19 and 4-20 also show V_{oc}, J_{sc}, FF, R_s, and R_{sh} as a function of light intensity for (CsGA) and $(CsGA)_{10}$, respectively. $(CsGA)_5$ shows almost no trend with n or α supporting that the $EDAI_2$ is not well integrated since the smaller amount of Cs/GA doesn't relax the lattice strain enough. With $(CsGA)_{10}$, there is a slight trend of α with it increasing from 0.748 to 0.819 to 0.849 with 0%,

0.5%, and 1% $EDAI_2$, respectively. The $EDAI_2$ also improved the n value of $(CsGA)_{10}$, lowering it from a high value of 4.14 to 1.40 with the addition of 0.5% $EDAI_2$. Although both of these values are improved, they still are in the range of trap assistant mono molecular recombination because the $EDAI_2$ is not as efficiently integrated as with $(CsGA)_{15}$. Figure 4-19 and 4-20 show Both $(CsGA)_5$ and $(CsGA)_{10}$ also show R_s and R_{sh} values with a higher dependence on light intensity compared with $(CsGA)_{15}$, showing comparatively higher leakage due to the poorer perovskite film quality, affecting charge separation and charge collection efficiency.

4.2.5 Stabilizing Potential Through Triple Cation and $EDAI_2$ Routes

To explore hysteresis, forward and backward scans were both taken. Hysteresis is governed by charge accumulation and ion migration. The perovskite soft nature can more easily facilitate ion migration, resulting in hysteresis issues in the perovskite field. With extreme iodide ion migration and a poor selection of transport layer, the oxidation of Ag to AgI (yellow color change) can be seen and leads to performance decrease.[143] Although the choice of transport layers facilitate electronic transport from the perovskite absorber, they also can block ionic transport across the interfaces. This of course prevents defects from poisoning the electrodes and introducing defects in the transport layers. Unfortunately, it also inevitably contributes to ionic accumulation and low frequency capacitance which increases space charge near the interfaces, tunneling ions, and ion-induced electric fields.[144,145] These effects can be exacerbated by the dipole moment of the organic cation. MA^+ has the strongest dipole moment with $MAPbI_3$ suffering from larger amounts of hysteresis compared with $FAPbI_3$ and the lower dipole moment of FA^+. These impacts result in severe hysteresis with distorted J-V curves shapes, a change in photovoltaic performance metrics, and voltage dependent capacitive, caused by electric field ionic redistribution, and non-capacitive

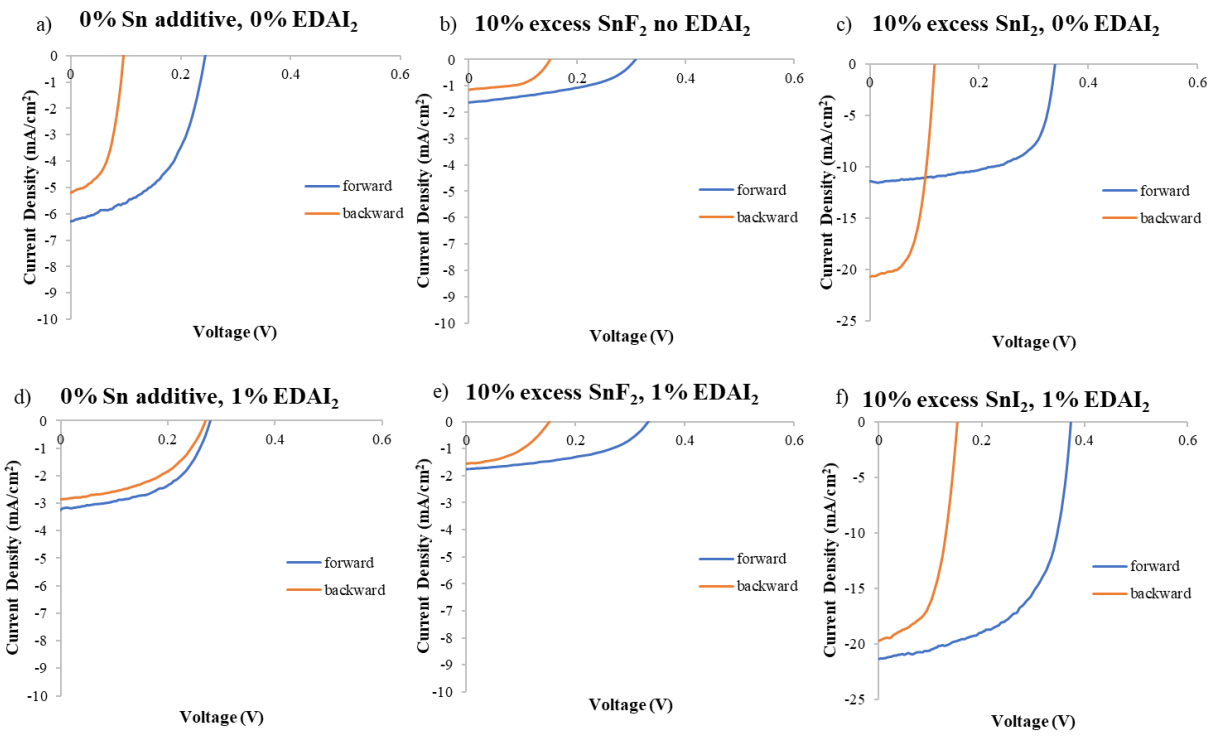

Figure 4-23. Forward and backward scans for $(CsGA)_{15}$ with (a) 0% Sn additive and 0% $EDAI_2$, (b) 10 mol% excess SnF_2 and no $EDAI_2$, (c) 10 mol% excess SnI_2 and 0% $EDAI_2$, (d) 0% Sn additive and 1% $EDAI_2$, (e) 10 mol% excess SnF_2 and 1% $EDAI_2$, (f) 10 mol% excess SnI_2 and 1% $EDAI_2$.

current components.[146] Also, this ionic migration and accumulation makes PVSCs more sensitive to environmental exposure and degradation.[147]

Forward backward scans in Figure 4-23 and Table 4-4 show the hysteresis of the composition $(CsGA)_{15}$ using various types of dopants and reducing agents. Figure 4-23a shows the hysteresis of a $(CsGA)_{15}$ film with 0% Sn additive and 0% $EDAI_2$ and reflects a large difference in V_{oc}. Without any Sn additive or $EDAI_2$, the perovskite has a high level of p-doping, and lacks grain passivation, resulting in uneven transport, large recombination, and high hysteresis. When 1% $EDAI_2$ is added (Figure 4-23d), the hysteresis significantly decreases with a similar J_{sc} and V_{oc} for forward backward scans because of $EDAI_2$ acting to both passivate grain boundaries and stabilize the perovskite structure with increased hydrogen bonding. Unfortunately, the J_{sc} is much

Table 4-4. Forward backward scan photovoltaic parameters of $(CsGA)_{15}FA_{70}SnI_3$ with various Sn additives and with and without 1% $EDAI_2$.

Device	Scan	V_{oc}	J_{sc}	FF
0% Sn additive, 0% $EDAI_2$	F	0.245	6.27	0.596
	B	0.099	5.19	0.510
0% Sn additive, 1% $EDAI_2$	F	0.279	3.22	0.524
	B	0.270	2.85	0.479
10% excess SnF_2, 0% $EDAI_2$	F	0.307	1.63	0.434
	B	0.149	1.146	0.528
10% excess SnF_2, 1% $EDAI_2$	F	0.332	1.74	0.273
	B	0.152	0.488	0.714
10% excess SnI_2 0% $EDAI_2$	F	0.339	11.44	0.642
	B	0.118	20.76	0.562
10% excess SnI_2 1.0% $EDAI_2$	F	0.351	22.15	0.653
	B	0.146	19.49	0.542

smaller than because there is no Sn additive such as excess SnI_2 or SnF_2 to reduce further p-doping throughout the perovskite structure, increasing recombination. The combination of a Sn additive and 1% $EDAI_2$ is critical for higher performance in this system. When Sn additives are added (Figure 4-23b,c,e,f), there is again hysteresis with a significant difference in V_{oc} for forward and backward scans. Although the addition of Cs does decrease potential sites for oxidation by allowing more flexibility with the lattice structure, this flexibility may also assist in movement when there are excess additives such as SnI_2 or SnF_2, especially when paired with a large counter ion such as GA. This movement in Sn additives would result in this larger difference in V_{oc} that is seen in Figure 4-23.

To determine the impact of mixing CsGA with FA in A-site and adding $EDAI_2$ on the stability of pure Sn perovskite solar cells, long-term device stability in the inert environment was evaluated. Figure 4-24 shows the normalized V_{oc}, J_{sc}, FF, and PCE of $(CsGA)_{15}$+0-1.5% $EDAI_2$ devices over

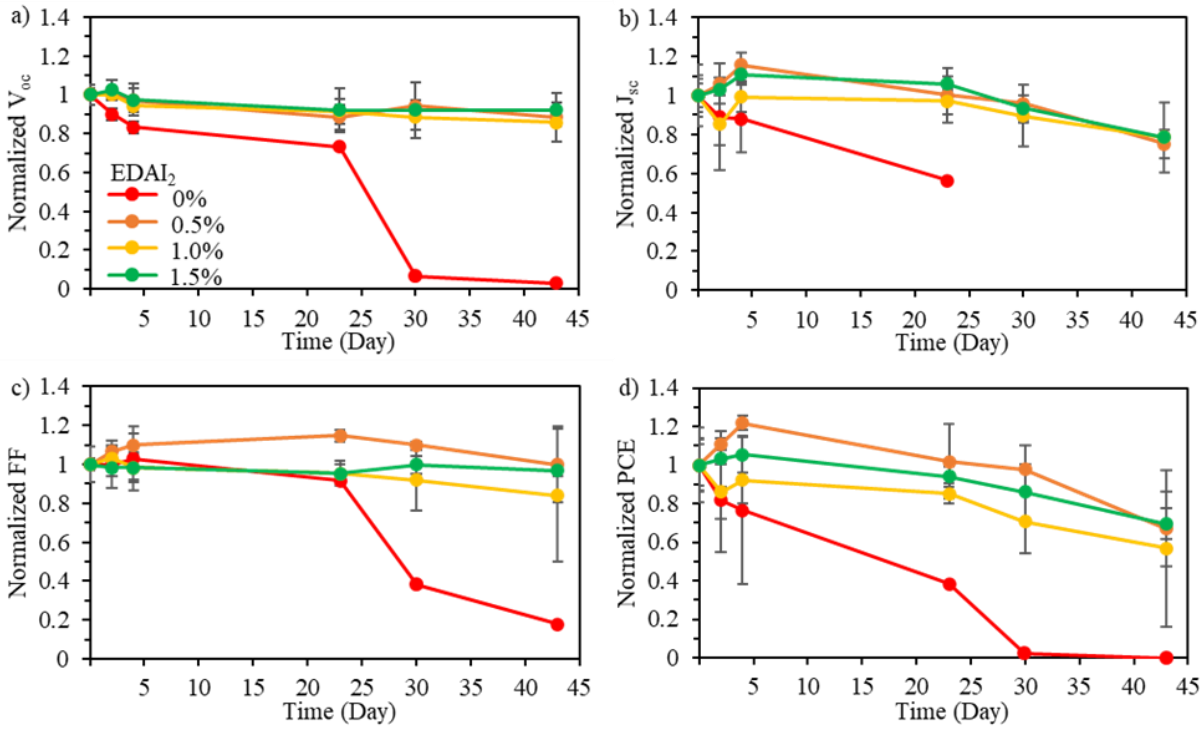

Figure 4-24. Normalized (a) Voc, (b) Jsc, (c) FF, and (d) PCE of the devices containing the active layers of $(CsGA)_{15}FA_{70}SnI_3$ with 0, 0.5, 1.0, and 1.5% $EDAI_2$, respectively, over time in the glovebox. The $(CsGA)_{15}$+0% $EDAI_2$ devices showed a short-circuited behavior after 30 days.

45 days in inert nitrogen atmosphere. The devices with 0% $EDAI_2$ show a decrease of all photovoltaic parameters over time and after 30 days show a short-circuited behavior. This short-circuited behavior is due to highly oxidized $Sn^{4+,}$ which has been shown to create a metal- like conductivity in perovskite solar cells. [148] The addition of $EDAI_2$ greatly increased the device stability, further demonstrating the $EDAI_2$ capabilities of reducing point defects by hollowing crystal structures and passivating grain boundaries. When 0.5-1.5% $EDAI_2$ is added, Figure 4-24 shows that the V_{oc} is very stable while the J_{sc} and FF briefly increases during storage. The performance of the $(CsGA)_{15}FA_{70}SnI_3$ with 1.5% $EDAI_2$ device increases the maximum PCE from 5.69% to 6.39% after 4 days of storage. Previously with $GA_{0.2}FA_{0.8}SnI_3$ perovskite films and 1% $EDAI_2$, the efficiency also increased in storage as well.[117] Since this phenomena only occurs with

$EDAI_2$ addition in our research and mostly impacts J_{sc}, this shows that there is an increased amount of grain passivation over time. The $EDAI_2$ is successfully able to prevent oxidation, maintaining these photovoltaic parameters.

4.3 Conclusion

In summary, pure Sn perovskite devices were optimized with choice of solvent, molarity, antisolvent, and the addition of a hot casting treatment to improve perovskite coverage, minimize pinhole density, and improve crystallinity. The addition of Cs^+ and GA^+ into $FASnI_3$ was implemented to utilize the high hydrogen bonding capability of the GA^+ organic cation while relaxing local lattice strain and filling point defects with a smaller Cs^+ counter cation. The $EDAI_2$ additive not only yielded pinhole-free cubic phase $(CsGA)_xFA_{100-2x}SnI_3$ perovskite films but also decreased both shallow and deep trap states in the perovskite films. With increased CsGA, the relaxed strain allowed for more integration of $EDAI_2$ into the crystal structure, increasing these positive impacts. The devices with $(CsGA)_{15}FA_{70}SnI_3$ and 0-2% $EDAI_2$ all achieved a maximum PCE higher than 5% with the highest of 5.72% for a fresh device with $(CsGA)_{15}FA_{70}SnI_3$ and 1% $EDAI_2$. Although there was hysteresis, it is mitigated by $EDAI_2$ and has been linked specifically to excess SnI_2 and ionic migration and accumulation at the interfaces, allowing for further improvement through interfacial engineering. After storage, the maximum PCE was increased from 5.69% to 6.39% for the $CsGA)_{15}FA_{70}SnI_3$ and 1.5% $EDAI_2$ devices. The devices with $EDAI_2$ additives showed better long-term stability than those without $EDAI_2$. Overall, this study demonstrates cation tuning to integrate stabilizing factors into pure Sn perovskites, creating potential routes for further improving lead-free devices in the future.

CHAPTER FIVE ENGINEER HOLE TRANSPORT LAYER FOR PURE TIN ACTIVE LAYER DEVICES TO ACHIEVE LARGE V_{oc} AND HIGH PHOTOVOLTAIC EFFICIENCY

5.1 Introduction

Tin perovskite solar cells have achieved the highest efficiency of all lead-free perovskites. Although there has been incredible progress in tin PVSC, the efficiencies achieved as still much lower than lead based perovskites. One critical factor hindering pure tin perovskite performance is the extremely low open-circuit voltage. High defect density in tin perovskites due to its soft nature have contributed to lower voltages and our previous work (Chapter 4) has shown reducing this defect density does improve the voltage. Other labs have also attempted to solve this voltage loss issue by adding reducing additives[149] and by manipulating the dimensionality[150] of pure Sn perovskites. Even with these defect improvements, compared to its band gap, tin perovskites have shown a voltage loss of 0.7V, which is much larger than the lead counterparts. Typical low V_{oc} in the range of 0.4-0.7 V with a large V_{oc} loss (0.6 – 0.9V) have plagued pure Sn-based PVSCs, which have limited the achievement of high PCE. Aside from the defect density, the poorer transport alignment with the tin perovskite energy bands could be the limiting factor to the tin perovskite device performance. The lowest unoccupied molecular orbital (LUMO) of the typical electron transport layer (ETL) used for tin perovskites (such as $PC_{60}BM$ and C_{60}) is very low and doesn't align well with the conduction band minimum of the tin perovskite absorber.[151] The PEDOT:PSS hole transport layer (HTL) also has a low highest occupied molecular orbital (HOMO) that is lower than the valence band maximum of the tin perovskite absorber, transforming it into a hole blocking layer. The choice of charge transport material and the corresponding work functions have been shown to significantly affect the V_{oc} of perovskite solar devices.

Conventional n-i-p structures with a $MAPbI_3$ absorber materials have been shown to exhibit a V_{oc} over 1.1 V.[152] The inverted p-i-n devices with a PEDOT:PSS HTL and $PC_{60}BM$ ETL

have been shown to exhibit a comparatively lower V_{oc} less than 1.0 V even for the pure Pb composition. Hole transport layer has been tuned to better align with the energy band of these pure Pb compositions to increase the V_{oc}. Huang and coworkers implemented a poly[bis94-phenyl)(2,4,6-trimethylphenyl)amine] (PTAA) that replaces PEDOT:PSS as the hole transport layer, which improved the V_{oc} from <1.0 to 1.1 V because of the larger work function of PTAA.[153] Park et al. was able to increase the V_{oc} of the $MAPbI_3$ perovskite devices from <1.0 to 1.08 V by implementing an inorganic nanostructured p-type NiO HTL with also a larger work function to better align with the $MAPbI_3$ valence band maximum.[154] Zuo et al. were able to increase the V_{oc} by modifying the work function of the PEDOT:PSS HTL layer itself via the addition of polymer electrolyte PSS-Na, changing the PEDOT to PSS ratio.[155] Lee et al. was able to show that the work function of PEDOT:PSS correlated with amount of PSS allowing work function tuning of PEDOT:PSS by changing the content of PSS, specifically on concentration of PSS on the film's surface.[156] Although there have been many works, including the works above, focused on HTL tuning to lower the work function, better aligning with the energy band of Pb perovskite absorbers and increasing the V_{oc}, there has been only a handful of works focused on increasing work function of PEDOT:PSS to better align with pure Sn perovskite absorbers. Liu et al. changed the work function of the PEDOT:PSS HTL from -5.10 eV to -4.79 eV by introducing 0.2% polyethylene glycol (PEG). This additive to the PEDOT:PSS was able to increase the V_{oc} from 0.29 V to 0.37 V, decrease hysteresis in the $FASnI_3$ PVSCs, and increase the PCE from 2.01% to 5.12%.[151] Their results show that device performance can be improved in pure Sn perovskites by minimizing the interfacial energy band gap mismatch between the absorber layer and the hole transport layer.

Our goal for this work is to further minimize this energy mismatch through engineered HTLs to increase hole injection at the perovskite:HTL interface as well as passivate the pure Sn

perovskite surface to minimize interface combination. In this work, solvent treatments were used to alter the PSS content and morphology of the PEDOT:PSS surface can improve the V_{oc} of pure Sn devices with the optimized composition $(CsGA)_{15}FA_{70}SnI_3$+1.0% $EDAI_2$. Three different methods, a cosolvent method, a solvent wash method, and a solvent immersion method were used to impact PSS segregation and content. Various solvents were tested depending on polarity, dipole moment, and boiling points as well as acids to dissolve PSS. Using XPS and Raman spectroscopy, we studied the impacts of PSS levels with the solvent treatments and potential impacts on film conductivity. Because this was an initial, unoptimized test and a proof of concept, there is plenty of room for improvement. But even so, we increased our record pure Sn performance from 5.72% to 6.29% and 6.16% with a 5% dimethyl sulfoxide (DMSO) cosolvent and methanol solvent wash, respectively. The V_{oc} for the maximum PCE devices was able to increase from 0.33V for the untreated PEDOT:PSS to 0.45V for a 10% DMSO cosolvent, decreasing the energy loss and showing the potential in engineering transport layers specifically for pure Sn perovskite devices.

5.2 Results and Discussion

5.2.1 Implementing Alternative PSS Ratios With PH 1000 and AI 4083 PEDOT:PSS

Initially, the composition from Chapter 3, $Cs_{10}(MA_{0.17}FA_{0.83})_{1-x}Pb_{1-y}Sn_y(I_{0.83}Br_{0.17})_3$, was used to explore whether a better aligned transport layer would severely affect the low performance (~2%) found. To minimize the 0.35 eV energy band mismatch between the pure Sn composition E_{VBM} and that of the PEDOT:PSS HTL, we hypothesized an altered PEDOT:PSS ratio that results in an upshifted work function could better align with the pure Sn perovskite energy band and better facilitate carrier transport. We implemented a Clevios PH 1000 PEDOT:PSS transport layer with a work function of 4.8 eV and studied the impacts of this alternative transport layer on the pure Sn V_{oc} and device performance.

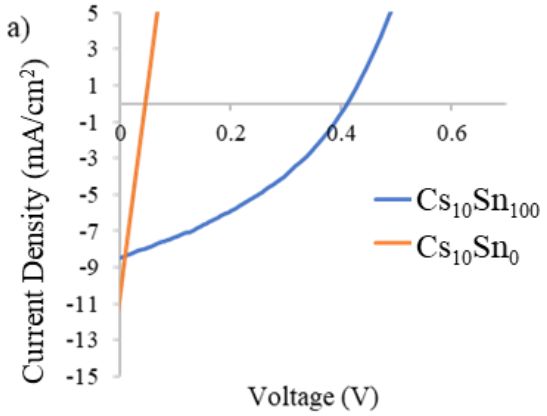

Device	V_{oc} (V)	J_{sc} (mA cm^{-2})	FF	PCE (%)	PCE_{max} (%)
$Cs_{10}Sn_{100}$	0.41 ±0.01	8.02 ±1.01	0.36 ±0.04	1.14 ±0.23	1.25
$Cs_{10}Sn_0$	0.02 ± 0.01	7.42 ± 3.47	0.18 ± 0.04	0.04 ± 0.04	0.11

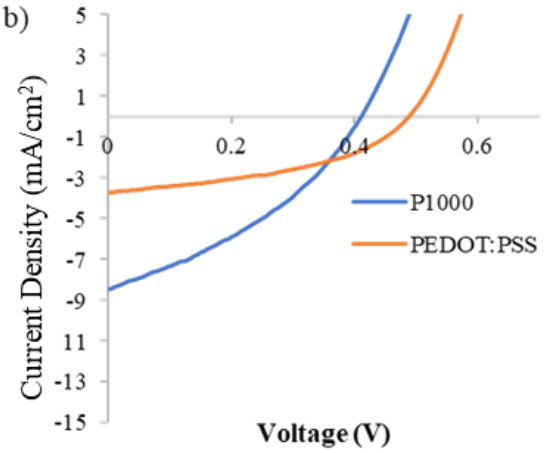

Device	V_{oc} (V)	J_{sc} (mA cm^{-2})	FF	PCE (%)	PCE_{max} (%)
P1000	0.41 ±0.01	8.02 ±1.01	0.36 ±0.04	1.14 ±0.23	1.25
AI-4083	0.48 ± 0.01	3.23 ± 0.01	0.65 ± 0.03	1.00 ± 0.03	1.02

Figure 5-1. J-V curves with corresponding photovoltaic parameters of (a) PH 1000 HTL with $MAPbI_3$ and $Cs_{10}Sn$ active layers. (b) $Cs_{10}Sn$ active layer with PH1000 and AI 4083 PEDOT:PSS HTL.

To decrease the energy band mismatch in our Sn devices, Clevios PH 1000 was tested as a HTL for the pure Sn composition $Cs_{10}(MA_{0.17}FA_{0.83})_{90}Sn(I_{0.83}Br_{0.17})_3$ ($Cs_{10}Sn$) and pure Pb $Cs_{10}(MA_{0.17}FA_{0.83})_{90}Sn_0(I_{0.83}Br_{0.17})_3$ ($Cs_{10}Sn_0$). The typical AI 4083 PEDOT:PSS previously used in Chapter 3 has a PEDOT to PSS weight ratio of 1:6 creating a work function range of -5.0 to -5.2 eV. Tuning the PEDOT to PSS ratio has been shown the change of the work function of the

HTL.[156] The PH 1000 has a PEDOT to PSS weight ratio of 1:2.5, allowing for an upshifted work function range of -4.8to -5.0 eV. We hypothesized this upshift work function would increase the V_{oc} of our $Cs_{10}Sn$ (the same notation used in Chapter 3) device and improve the photovoltaic performance. Figure 5-1a shows that the PH 1000 HTL does increase the V_{oc} from an average of 0.02 to 0.41 V for pure Pb ($Cs_{10}Sn_0$) and pure Sn ($Cs_{10}Sn$), respectively. most likely because of the better band alignment. The J_{sc} increases slightly from an average of 7.42 to 8.02 mA/cm^2 when shifting to pure Sn, but these J_{sc} are similar with the standard deviation for pure Sn being much lower than pure Pb, suggesting far more reproducibility of function solar devices. The shape of the J-V curve for the pure Pb is similar to that of a diode, showing severe leakage that is alleviated with a pure Sn film, which shows a more typically shaped JV curve. Although the PCE increases from 0.04 to 1.14% for pure Sn, the PCE is still lower than literature PCE for pure Sn due to the low FF of the devices and J_{sc}.

Unfortunately, in Figure 5-1b, the pure Sn perovskite devices made with PH 1000 PEDOT:PSS do not have a higher V_{oc} than that of the AI 4083 PEDOT:PSS. Comparatively, the PH 1000 PEDOT:PSS has a lower V_{oc} of 0.41 V compared to 0.48 V and the FF decreases to 0.36 from 0.65. The J_{sc} of the PH 1000 PEDOT:PSS device does have a higher current density of 8.02 compared to 3.23 mA/cm^2 which is due to the higher conductivity of PH 1000 PEDOT:PSS. Although we expect the device with PH 1000 PEDOT:PSS to have a higher V_{oc} because of the theoretical upshifted work function and better energy band alignment, PH 1000 PEDOT:PSS has a much higher viscosity of 50 mPa.s compared with AI 4083 viscosity of 5-12 mPa.s which could have affected the efficiency of annealing and the morphology with the conditions used for films. For this first experiment, both transport layers were dropped on the substrate with a 85 µl volume rather than the usual 70 µl drop. The anneal temperature was also lowered to 120 °C for 25 min

rather than the 150°C for 10 min protocol used in Chapter 3. The degree of surface segregation of PSS and PEDOT, which directly influences the work function, has been shown to depend on the heat treatment protocol.[156] These annealing conditions could have affected the segregation of PSS and PEDOT creating altered ratios with a downshifted work function and decreasing the $V_{oc.}$ Because of the heightened viscosity and altered PSS content, the spin conditions of the PH 1000 PEDOT:PSS layer can be further optimized to truly see the effects of the better aligned work function.

5.2.2 Solvent Treatments to AI 4083 PEDOT:PSS Films and Device Performance

PEDOT:PSS is a polymer electrolyte that consists of a negatively charged insulating PSS and a positively charged conducting conjugated PEDOT. The hydrophilic PSS acts as a dopant while also helping to disperse and stabilize the oxidized hydrophobic PEDOT in polar solvents such as water. To probe multiple avenues of solvent treatments, we focused on 3 solvent treatment methods and solvents. Table 5-1 shows the relative polarity, dipole moment, and boiling point of the solvents used as treatments dimethyl sulfoxide (DMSO) ethylene glycol (EG), methanol (CH_3OH) and water (H_2O) for comparison.[157–159] The cosolvent method involves adding another solvent directly into the PEDOT:PSS solution at a specific volume ratio and spinning overnight. DMSO was utilized as a cosolvent because of the strong dipole moment of 3.96 D allowing for

Table 5-1. Relative polarity, dipole moment, and boiling point for the solvents utilized for treatments DMSO, EG, CH_3OH, and H_2O for comparison.

Solvent	Relative Polarity	Dipole (D)	Boiling Point (°C)
DMSO	0.444	3.96	189
EG	0.79	2.27	198
CH_3OH	0.762	1.69	64.7
H_2O	1	1.85	100

strong dipole-charge interactions to form between PEDOT:PSS and DMSO. DMSO interactions with PEDOT:PSS has previously increased charge carrier mobility through these dipole-charge interactions and increased the work function through enhanced PEDOT and PSS segregation.[160] EG was used as an option with a lower dipole moment of 2.27 D to compare and both solvents have high boiling points to allow for a control annealing process. The cosolvent method will focus on better segregating the PEDOT and PSS, increasing the work function and improving energy alignment and hole transport.[161] The solvent wash method utilizes polar solvents that will remove PSS from the surface of the PEDOT:PSS for improved energy alignment. Because of the high polarity of EG (0.79), it was also explored as a solvent washing agent that would dissolve and remove surface level PSS during spin coating. The other washing agent, CH_3OH, has a similarly high polarity of 0.762 but a lower boiling point to eliminate the need for excess annealing. The solvent immersion utilizes the hydrophilic nature of PSS to dissolve it off the PEDOT:PSS surface for improved energy alignment. Both H_3PO_4 and H_2SO_4 have been shown to dissolve PSS from the PEDOT:PSS surface.[162]

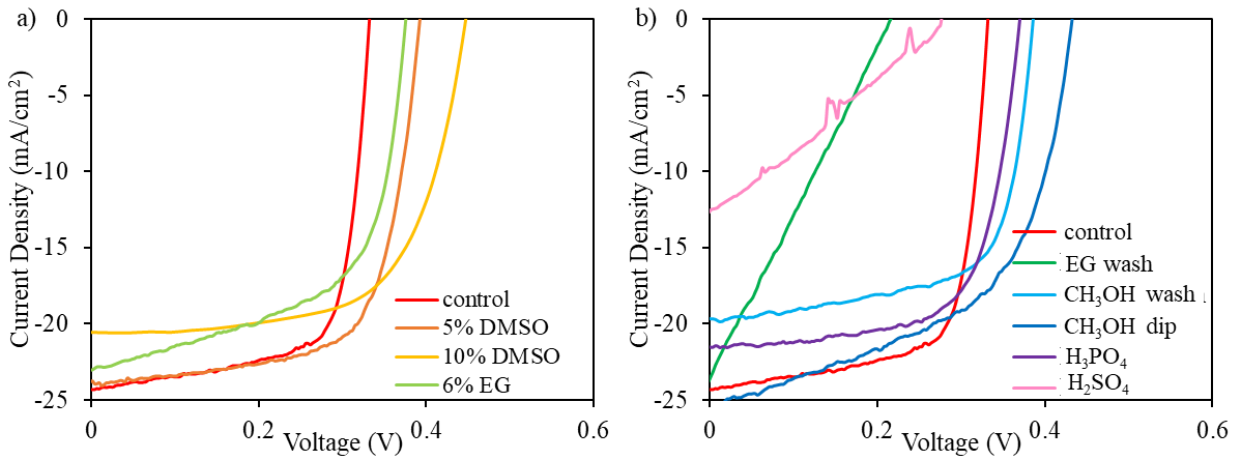

Figure 5-2. J-V curves with the $(CsGA)_{15}$ perovskite solar cells on the normal PEDOT:PSS as control and (a) cosolvent 5 and 10% DMSO and 6% EG and (b) solvent washes with EG and CH_3OH, and solvent and acid immersions in CH_3OH, H_3PO_4, and H_2SO_4.

The perovskite $(CsGA)_{15}FA_{70}SnI_3$+1.0% $EDAI_2$ synthesis method was the same as in Chapter 4 as was the inverted device structure. For the control, Al 4083 PEDOT:PSS was spun at 5000 rpm for 60 s and annealed at 150°C for 10 min. For the solvent treatments that utilized a cosolvent, such as 5 and 10% DMSO, and 6% EG, the cosolvent was mixed with PEDOT:PSS and stirred overnight. The PEDOT:PSS emulsion with cosolvent was spin coated and annealed at the same conditions as the control unless otherwise specified. For solvent washes, such as the EG wash and CH_3OH wash, after annealing the PEDOT:PSS layer as control, an additional 70 µl of solvent was added then spun at 5000 rpm for 60 s followed with annealing at 150 °C for 3 min. For the solvent immersions, such as CH_3OH, H_3PO_4, and H_2SO_4, after annealing the PEDOT:PSS layer as control, the film was immersed in the solvent for 3 min. For CH_3OH solvent, the film was then annealed again briefly at 150 °C for 3 min. For acids, the film was rigorously sprayed with DI water and then annealed at 150 °C for 10 min. These exploring experiments were not optimized specifically for any solvent and used conditions from Chapter 3 and 4.

Figure 5-2 shows the J-V curves with the $(CsGA)_{15}$ and 1.0% $EDAI_2$ perovskite (the perovskites in Chapter 4) on HTLs based a control PEDOT:PSS, and PEDOT:PSS prepared with cosolvent 5 and 10% DMSO and 6% EG, solvent washes with EG and CH_3OH, and solvent immersions in CH_3OH, H_3PO_4, and H_2SO_4. Table 5-2 shows the corresponding PV parameters. EG wash and H_2SO_4 both had a diode J-V curve with a low V_{oc}, FF, and PCE. All others had a max PCE that was higher than the control PEDOT:PSS due to a higher V_{oc}. For the cosolvent mixtures, the V_{oc} incrementally improved from 0.33 V for the control PEDOT:PSS to 0.39 V with 5 %/ DMSO to 0.45 V with 10% DMSO with both DMSO mixtures having max PCE higher than the control's 5.72% at 5.88% and 6.29%. Although with the increase of DMSO mixed into the PEDOT:PSS, there was also a decrease in J_{sc} from 24.32 mA/cm^2 to 23.74 24.32 mA/cm^2 to 20.58

Table 5-2. Corresponding photovoltaic parameters for the $(CsGA)_{15}$ and 1.0% $EDAI_2$ perovskite solar cells with the HTLs of a control PEDOT:PSS, PEDOT:PSS prepared with cosolvent 5 and 10% DMSO and6% EG, solvent washes with EG and CH_3OH, and solvent immersions in CH_3OH, H_3PO_4, and H_2SO_4.

Sample	V_{oc} (V)	J_{sc} (mA/cm^2)	FF	PCE
Control	0.35±0.02 (0.33)	20.81±1.78 (24.32)	0.63±0.06 (0.71)	4.62±0.63 (5.72)
5% DMSO	0.39±0.02 (0.39)	21.80±1.18 (23.74)	0.61±0.08 (0.68)	5.05±0.76 (6.29)
10% DMSO	0.40±0.03 (0.45)	19.56±1.05 (20.58)	0.64±0.06 (0.65)	4.94±0.89 (5.88)
6% EG	0.32±0.09 (0.38)	23.55±1.38 (23.01)	0.37±0.13 (0.59)	2.94±1.54 (5.02)
EG wash	0.08±0.09 (0.22)	26.58±2.24 (23.49)	0.26±0 (0.26)	0.52±0.51 (1.29)
Methanol Wash	0.38±0.01 (0.39)	20.45±2.78 (25.34)	0.66±0.07 (0.63)	5.04±0.75 (6.16)
Methanol Dip	0.37±0.02 (0.39)	18.34±0.76 (19.64)	0.63±0.06 (0.67)	4.30±0.63 (5.03)
H_2SO_4	0.11±0.12 (0.28)	17.24±4.80 (12.56)	0.28±0.03 (0.29)	0.45±0.40 (0.98)
H_3PO_4	0.36±0.04 (0.37)	19.18±1.60 (21.49)	0.57±0.17 (0.67)	3.98±1.46 (5.28)

24.32 mA/cm^2 and a FF decrease from 0.71 to 0.68 to 0.65 for PEDOT:PSS, 5% DMSO, and 10% DMSO, respectively. The V_{oc} increase suggests better alignment with the perovskite absorber valence band and the HTL work function but the lower J_{sc} and FF shows that the morphology of the DMSO and the altered polarity of the mixed PEDOT:PSS may have impacted the wettability for the perovskite layer addition, increasing potential pinholes and recombination sites. In summary, the DMSO addition decreased back charge recombination but may have increased defect recombination in the perovskite layer. The third solvent mixture with 6% EG had a higher V_{oc} as well at 0.38 V, but the FF was much lower at 0.59 and, more importantly, there was a high standard deviation, suggesting the morphology of the PEDOT:PSS was not even. For the solvent washes, the EG wash resulted in a diode J-V curve, but the methanol wash was able to achieve a higher V_{oc} from 0.33 V for PEDOT:PSS to 0.39 V after a methanol wash and a higher PCE growing from 5.72% to 6.16%. The J_{sc} also increases slightly from 24.32 mA/cm^2 before the solvent wash to 25.34 mA/cm^2 after. There was a small decrease in FF suggesting an increase in leakage again suggesting a subpar perovskite layer. For the solvent immersions, there was a V_{oc} increase for the

methanol immersion and phosphoric acid immersion, but also a slight decrease in J_{sc} and FF, limiting the PCE from record levels. Although none of these methods were optimized in terms of volume, anneal conditions, or spin conditions, there was already improvements in the V_{oc} and PCE for the DMSO cosolvent method, and the methanol wash method, suggesting room for further device performance growth.

5.2.3 Characterization of Solvent Treated PEDOT:PSS Films

To understand the device performance with different PEDOT:PSS HTLs, the surface morphology, chemical structure, and chemical composition were investigated using AFM, Raman, and XPS. The cosolvent method with 10% DMSO increased the V_{oc} from 0.33 V to 0.45 V, but because there was a decrease in J_{sc}, potentially due to poorer perovskite morphology, different anneal conditions were explored and the AFM images were acquired. Figure 5-3 shows the AFM images of normal PEDOT:PSS, 10% DMSO cosolvent at the normal spin conditions, a DMSO

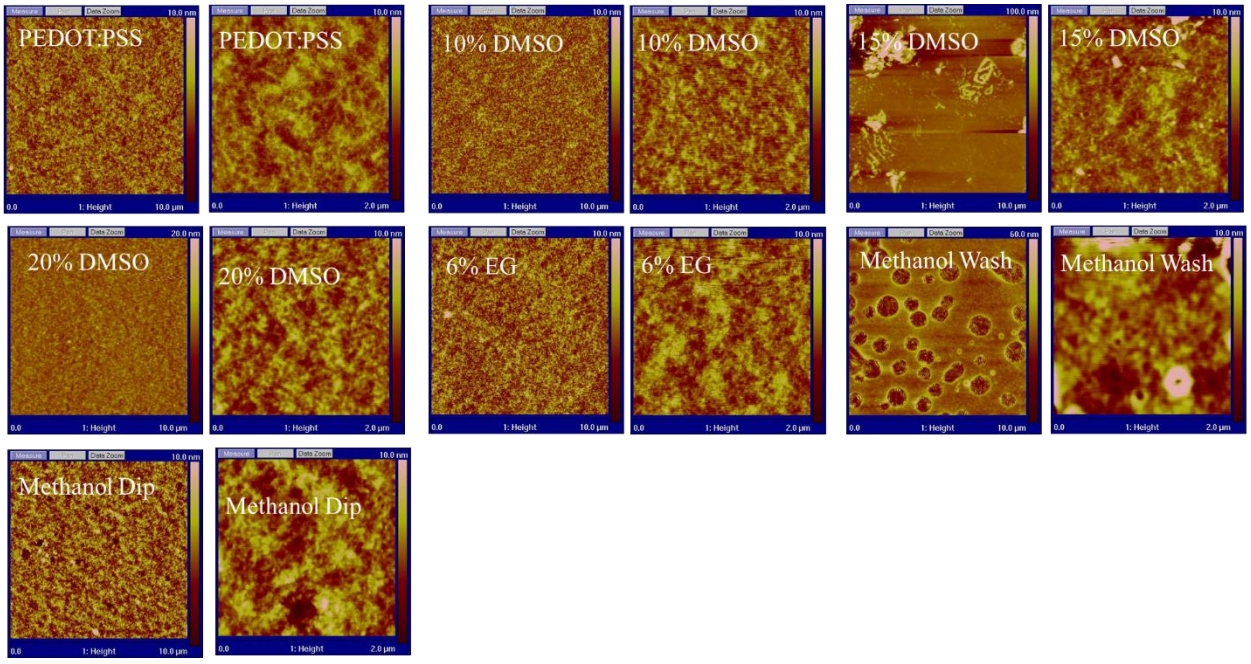

Figure 5-3. AFM topographic images at two different scan sizes (10 um x 10 um and 2 um x 2 um) for untreated PEDOT:PSS, 10% DMSO cosolvent, DMSO wash, and varying anneal conditions for 10% DMSO cosolvent.

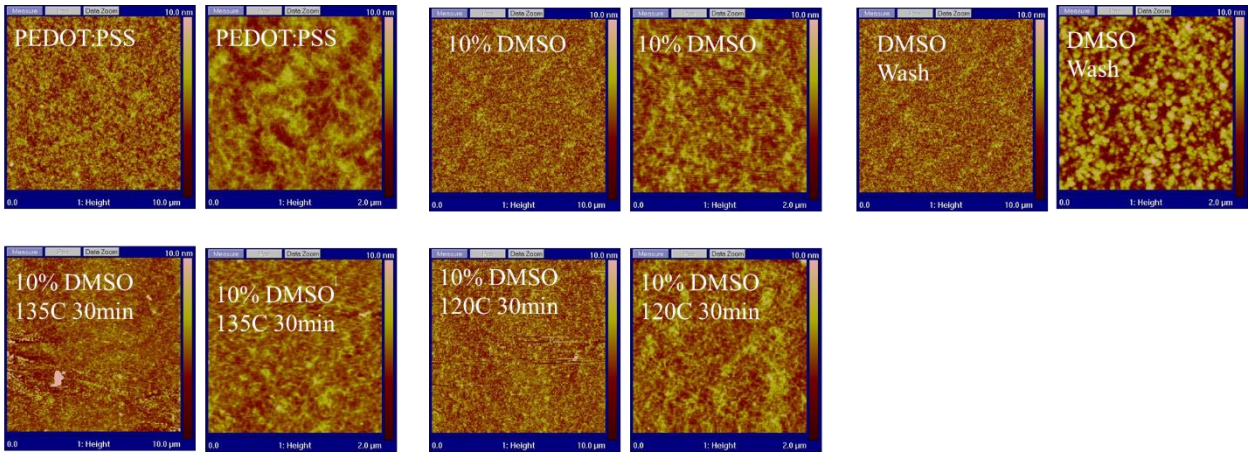

Figure 5-4. AFM topographic images at two scan sizes (10 um x 10 um and 2 um x 2 um) for control PEDOT:PSS, and PEDOT:PSS prepared with 10, 15, and 20% DMSO and 6% EG cosolvent, a methanol wash, and methanol immersion.

wash on a normal PEDOT:PSS film, 10% DMSO cosolvent with a 135°C anneal condition, and 10% DMSO cosolvent with a 120°C anneal condition. Figure 5-4 also has AFM images for cosolvent with 10, 15, and 20% DMSO and 6% EG, a methanol wash, and a methanol immersion. At 15% DMSO, there are large segregates that appear on the film showing an upper limit for a DMSO cosolvent. The 10% DMSO as the varying anneal conditions show smaller a similar decrease of large darker and lighter areas found in the normal PEDOT:PSS film. The AFM image for the DMSO wash shows the most distinct segregation but also seems to increase roughness which may have a negative impact on the perovskite morphology in terms of wettability. For the 6% EG, there are small deposits scattered over the film which may account for the high standard deviation in performance. Surprisingly, even though the methanol wash had a higher V_{oc}, PCE, and a relatively low standard deviation in performance, the AFM images show very large segregates. The methanol dip does not have these same segregates that could be PSS[163] but has an increased roughness that may account for the lower J_{sc}.

XPS measurements were performed to analyze the PEDOT and PSS content. Figure 5.5 shows the high resolution sulfur XPS peak for PEDOT:PSS, cosolvents 5% DMSO, 10% DMSO,

Table 5-3. XPS atomic percentage for PEDOT vs PSS calculated from the S 2p2/3 and 2p ½ , high resolution carbon compositions and a general survey composition for untreated PEDOT:PSS, 5, 10 and 12% DMSO, a methanol dip, and methanol wash.

a)

Treatment	PEDOT %	PSS %
PEDOT:PSS	12.75	87.25
5% DMSO	24.05	75.95
10% DMSO	38.71	61.29
12% DMSO	22.55	77.45
Methanol dip	14.19	85.81
Methanol wash	8.14	91.86

b)

Treatment	C-C %	C-O/C-S %	C=O %
PEDOT:PSS	87.02	9.89	3.09
5% DMSO	79.81	14.96	5.23
10% DMSO	67.47	22.34	10.19
12% DMSO	65.12	26.72	8.16
Methanol dip	87.88	9.25	2.87
Methanol wash	64.04	32.21	3.75

c)

Treatment	C 1s %	Na 1s %	O 1s %	S 2p %	Si 2p %
PEDOT:PSS	65.7	1.77	22.06	10.03	0.44
5% DMSO	61.22	3.27	23.5	9.57	2.44
10% DMSO	10.86	1.89	54.93	0	32.32
12% DMSO	21.71	2.65	46.41	3.53	25.66
Methanol dip	68.39	2.87	19.94	8.8	0
Methanol wash	85.93	1.46	9.66	2.96	0

and 12% DMSO, a methanol immersion, and methanol dip. Both PEDOT and PSS contain one sulfur atom. The PEDOT sulfur atom is within a thiophene ring while the PSS sulfur atom is in a sulfonate, allowing the differences in chemical environments to result in different S(2p) electron binding energies. Because of the three electronegative oxygen atoms withdrawing electron density from the sulfur atoms, the sulfur signal for PSS appears at a higher binding energy (168-169 eV). The PEDOT S(2p) double occurs at 164-165 eV. Table 5-3 shows the XPS atomic percentage for PEDOT vs PSS from the area under the Raman peak as well as high resolution carbon compositions and a general survey composition. For the trends in PSS, the normal, untreated PEDOT:PSS contains 87.25% PSS and this incrementally goes down to 75.95% when the 5% DMSO cosolvent is implemented to 61.29% with the 10% DMSO cosolvent, suggesting there is an increase in the PEDOT:PSS work function with DMSO addition, better aligning with the pure Sn valence band. This increases slightly with 12% DMSO, again suggesting a limit to DMSO that can be added as a cosolvent to maintain the lesser PSS impacts. The methanol wash shows an increase in PSS % to 91.86, suggesting that the performance may be impacted by higher conductivity rather than better alignment since increased PSS allows for a more conductive film.

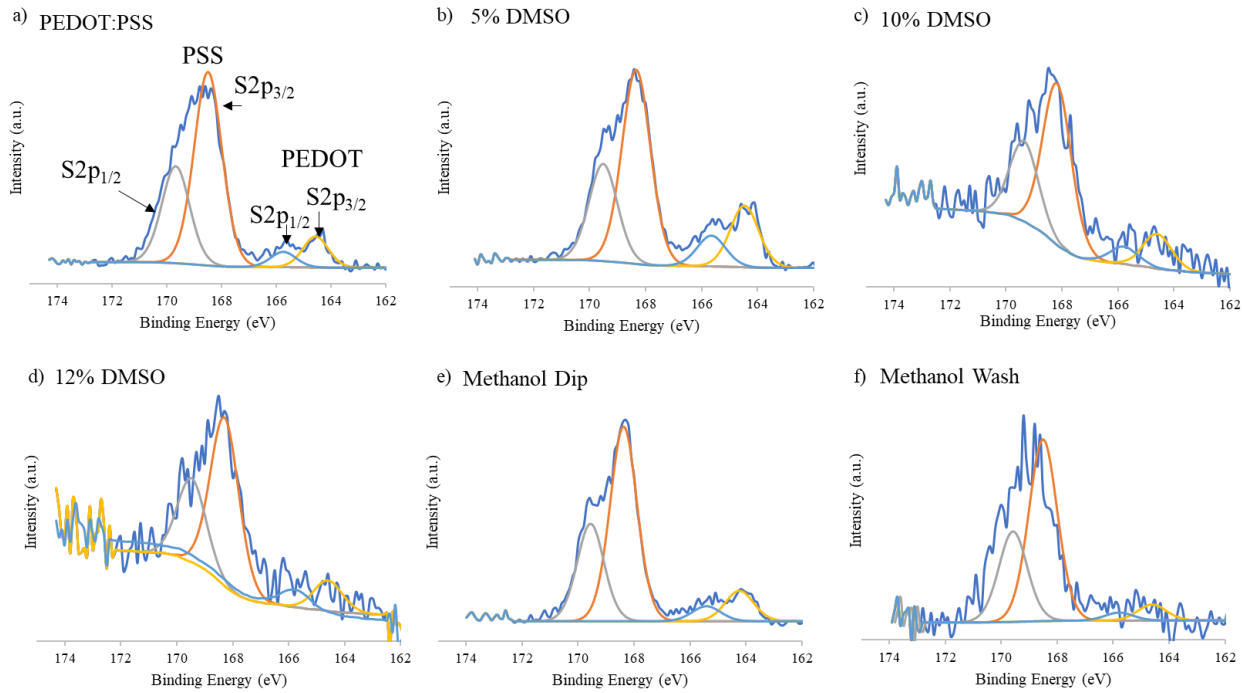

Figure 5-5. XPS high resolution sulfur S2p peak for (a) PEDOT:PSS, (b) 5% DMSO solvent, (c) 10% DMSO cosolvent, (d) 12% DMSO cosolvent, (e) methanol immersion, and (f) methanol wash

This increase in PSS content could be due to the low dipole of CH_3OH (1.69D), which is lower than the dipole of H_2O (1.85D), resulting in less overall segregation and more integration of PSS in the film. The methanol dip shows a comparable amount of PSS (85.81%) compared to the untreated PEDOT:PSS, suggesting these strong segregates may be concentrated deposits of the PSS. For the 10% and 12% DMSO, the survey XPS scan shows high amounts of Si and higher amounts of oxygen which suggests a thin film with exposed glass. The XPS spectra also show more noise and lower intensities also suggesting a thin film, suggesting more DMSO could influence film thickness. This could be better tolerated with optimized spin conditions to thicken the film.

Because the goal of solvent treatments is to affect the levels of PSS, Raman spectra was used to study the PEDOT polymer chemical structure. The max peak is observed at around 1437

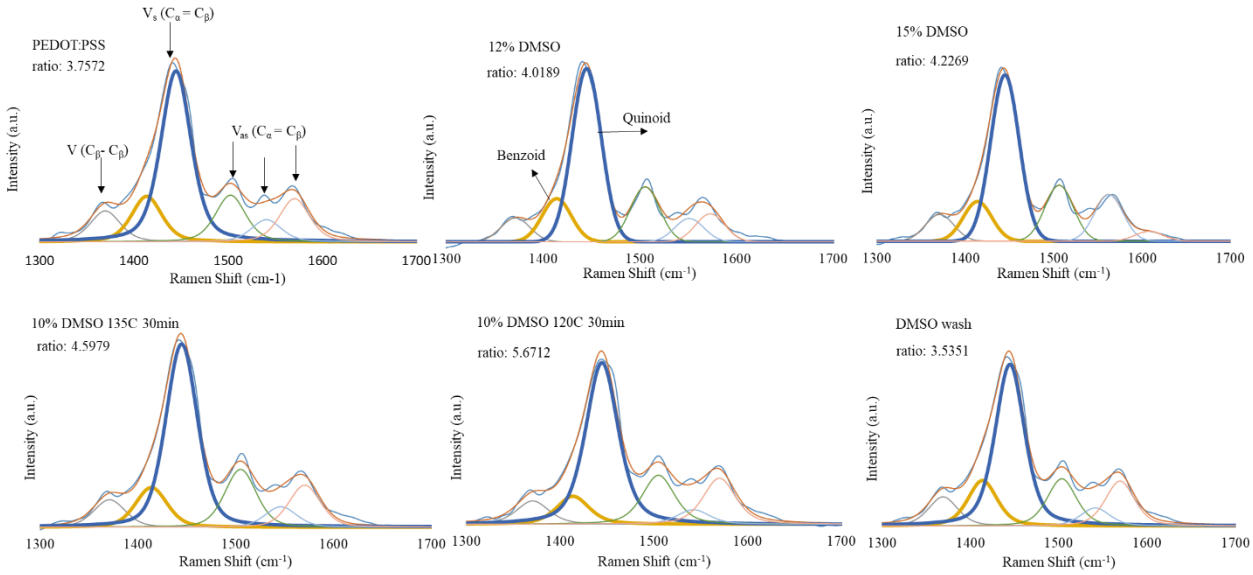

Figure 5-6. Raman spectra for PEDOT:PSS, PEDOT:PSS prepared with 12, 15, and 10% DMSO with varying anneal conditions, and a DMSO wash.

cm^{-1} and is assigned to the $C_\alpha = C_\beta$ symmetric stretching vibrations. The peaks at 1504 cm^{-1} and 1570 cm^{-1} both correspond to $C_\alpha = C_\beta$ asymmetric stretching vibrations.[164] The smaller peak centered at 1534 cm^{-1} is due to splitting of the asymmetric vibrations while the peak centered at 1361cm^{-1} is due to C_β - C_β' vibrations.[165] The most intense peak assumed to $C_\alpha = C_\beta$ symmetric stretching vibrations is a combination of two peaks, the first centered at 1421 cm^{-1} is due to symmetric $C_\alpha = C_\beta$ stretching from benzoid structures in the PEDOT segments, while the second is centered at 1442 cm^{-1} and is due to symmetric $C_\alpha = C_\beta$ stretching from the quinoid structure.[166] The benzoid and quinoid structure of the PEDOT chains correspond to the coiled conformation and expanded-coil, respectively.[167,168] The expanded coil conformation of the quinoid structure allows for two PEDOT chains to exist in the same plane through a inter thiophene double bond rather than a single bond in the benzoid structure.[169] This double bond facilitates π electron delocalization, increasing the conductivity and carrier transport of the PEDOT:PSS films.[170] Figure 5-6 and 5-7 show the Raman spectra for untreated PEDOT:PSS, various treatments of cosolvents with 10% DMSO, 12% DMSO, 15% DMSO, 6% EG cosolvent, washes with DMSO, and

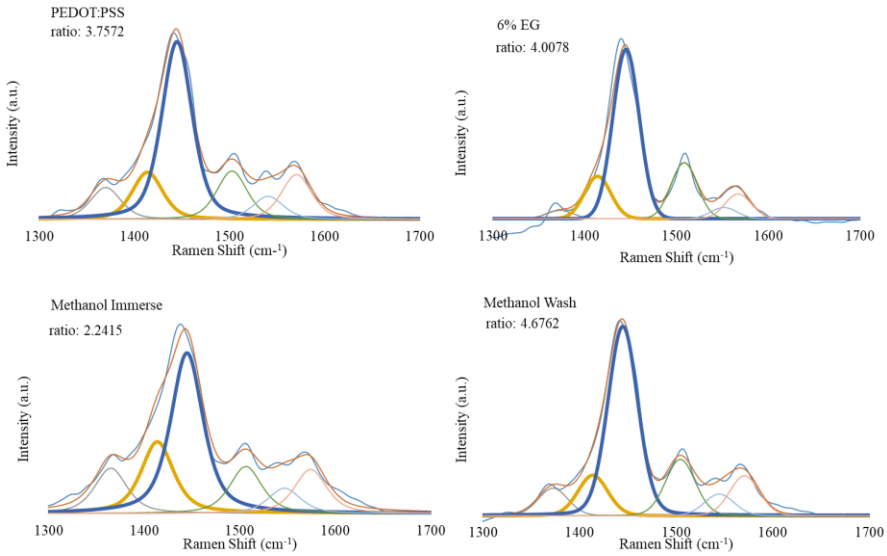

Figure 5-7. Raman spectra for PEDOT:PSS, PEDOT:PSS prepared with 6% EG cosolvent, a methanol immersion, and methanol wash.

Table 5-4. The ratio of quinoid to benzoid structure obtained from the Raman spectra of PEDOT:PSS and PEDOT:PSS prepared with different solvent treatments. The ratios were estimated from the peak area ratios corresponding to the symmetric $C_\alpha = C_\beta$ vibrational mode at 1444 cm^{-1} for quinoid and at 1424 cm^{-1} for benzoid structure.

Treatment	Ratio (Quinoid/Benzoid)
PEDOT:PSS	3.76
12% DMSO	4.02
15% DMSO	4.23
10% DMSO 135C 30min	4.60
10% DMSO 120C 30 min	5.67
DMSO wash	3.53
6% EG	4.01
Methanol Immerse	2.24
Methanol Wash	4.68

methanol, and methanol immersion. The quinoid/benzoid ratio was calculated for each raman spectra using the area around each peak and can be found in Table 5-4. With the DMSO cosolvent addition, the quinoid/benzoid ratio increases from 3.76 for the untreated PEDOT:PSS to 4.02 for 12% DMSO to 4.23 for 15% DMSO, showing that the DMSO addition favors the quinoid structure

and facilitates hole transport. The 10% DMSO with varying treatments also increase the ratio with the 120°C anneal condition reaching 5.67. The methanol immersion also has a high ratio at 4.68, supporting the hypothesis that its high conductivity and transport impacts its performance more than its decreased PSS content. The methanol immersion has a decreased ratio at 2.24 which aligns with its lower device performance because the benzoid confirmation does not facilitate carrier transport.

5.3 Conclusion

In this work, we explored the idea that decreasing the energy mismatch between the PEDOT:PSS and pure Sn perovskite layer would decrease the energy loss, improving the performance of pure Sn devices. Multiple solvent treatment methods were implemented to either segregate PSS or remove it from the PEDOT:PSS surface, increasing the work function. Using a cosolvent method, solvent wash method, and solvent immersion method, we explored how different properties such as dipole moment, polarity, and boiling point could impact the morphology and PSS level of the PEDOT:PSS films. Utilizing the $(CsGA)_{15}FA_{70}SnI_3$+1.0% $EDAI_2$ perovskite film from Chapter 4, we demonstrated a higher performance of 6.29% and 6.16% with a 5% DMSO cosolvent and methanol solvent wash, respectively. The V_{oc} for the maximum PCE devices was also able to increase from 0.33 V for the untreated PEDOT:PSS to 0.45 V for a 10% DMSO cosolvent. This proof of concept shows the value in tailoring transport layers specifically to decrease the energy in pure Sn perovskite to improve the performance of lead-free devices.

CHAPTER SIX: CONCLUSIONS AND OUTLOOK

6.1. Conclusions

Perovskite solar cells are a promising new solar absorber material that combine the benefits of inexpensive printable technology with efficiencies comparable to commercialized silicon solar technology. In less than a decade, the perovskite technologies have been reached a record efficiency of 25.2% and have been applied in the fields of photovoltaic devices, photodetectors, batteries, lasers, light-emitting diodes, and transistors. The toxicity of lead perovskite and the issues with long-term material stability remain roadblocks to commercialization and wider applications. This research is a rounded study focusing on multiple aspects of lead-free films as photovoltaic devices such as studying the impacts of transitioning from a lead perovskite to a tin based perovskite, optimizing the morphology and carrier properties of pure Sn perovskites, reducing energy loses to improve performance, and stabilizing the Sn perovskite against degradation attacks. The conclusions and insights obtained open up new routes for lead-free devices, contributing to this ever-expanding field of emerging perovskite knowledge and applications.

The first portion of my work focused on pushing the efficiency of mixed Pb/Sn halide perovskite to record levels. Figure 6-1 shows a summary content image with the triple cation double halide composition, novel band gap trends, and stability impacts. Lead perovskites had achieved high efficiencies, but once tin was introduced into the composition, efficiencies were lowered, and stability was further hindered. We applied a novel triple cation, double halide composition $Cs_x(MA_{0.17}FA_{0.83})_{1-x}Pb_{1-y}Sn_y(I_{0.83}Br_{0.17})_3$ with x = 0.05, 0.10, and 0.20 and y = 0, 0.25, 0.50, 0.75, and 1.0. For the device architecture, we implemented a simple inverted device structure of indium tin oxide (ITO)/poly (3,4, -ethylenedioxythiphene): polystyrene sulfonate

(PEDOT:PSS)/Perovskite/[6,6]-phenyl-C_{60}-butyric acid methyl ester ($PC_{60}BM$)/fullerene (C_{60})/2,9-dimethyl-7,7-diphenyl-1,10-phenanthroline (BCP)/Ag to eliminate instabilities found in alternative conventional structures. We explored the impacts of cation and halide tuning on the film morphology, and crystallinity, decreasing the pinholes in mixed Pb/Sn devices while maintaining all cubic crystal structures. We explored a novel trend in band gap with increasing Sn and varying cation size, studying the impacts of octahedral tilting and lattice constriction. Our composition and band gap tuning method resulted in an ideal single junction band gap (1.36 eV) for the $Cs_{0.10}(MA_{0.17}FA_{0.83})_{0.9}Pb_{0.75}Sn_{0.25}(I_{0.83}Br_{0.17})_3$, composition, which achieved a maximum PCE of 15.78%. The composition $Cs_{0.05}(MA_{0.17}FA_{0.83})_{0.95}Pb_{0.25}Sn_{0.75}(I_{0.83}Br_{0.17})_3$ (band gap = 1.30 eV), resulting in a record maximum PCE for any 75% Sn device at the time, 11.05%. The triple cation Pb-Sn double halide perovskites not only offer a wide tunability on band gap to achieve

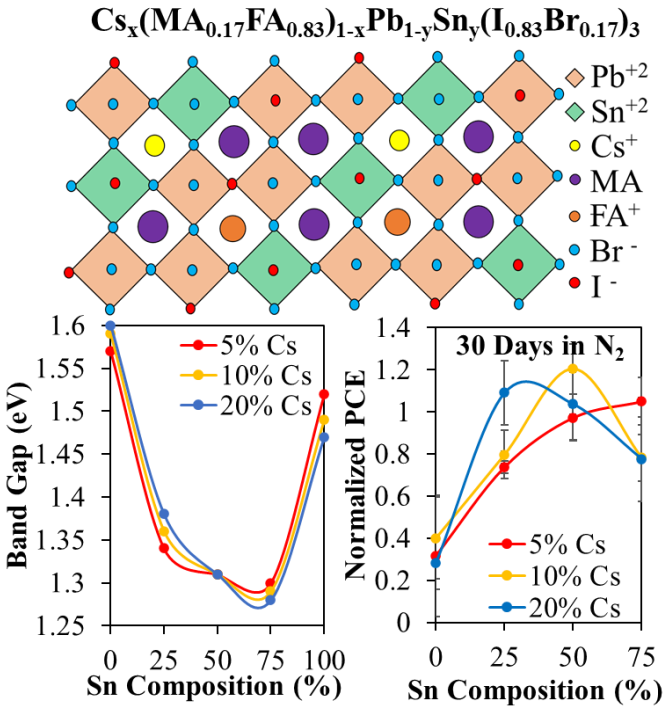

Figure 6-1. Summary content image showing triple halide composition with novel band gap trends and impacts on glovebox stability.

ideal band gaps for single-junction or tandem PVSCs but also greatly improve the performance and stability of high Sn PVSCs, providing our next steps for lead-free devices.

We next focused our efforts on improving the performance and stability of pure Sn devices. Figure 6-2 illustrates the applied cation mixture with Cs and GA and the $EDAI_2$ stabilizing agents with it's impacts on defects and performance. After optimizing the solvent, anneal, antisolvent conditions and implemented a hot casting treatment, we explored a new triple cation mixture $(CsGA)_xFA_{100-2x}SnI_3$. This cation mixture was engineered specifically to combine the benefits of a guanidinium cation, such as increased hydrogen bonding and no dipole moment, with Cs to fix point defects and relax the crystal lattice to better integrate a large stabilizing agent, $EDAI_2$, to passivate defects at grain boundaries and reduce trap states inside the crystal. The $EDAI_2$ additive not only yielded pinhole-free cubic phase $(CsGA)_xFA_{100-2x}SnI_3$ perovskite films but also decreased both shallow and deep trap states in the perovskite films. The devices with $(CsGA)_{15}FA_{70}SnI_3$ and 0-2% $EDAI_2$ all achieved a maximum PCE higher than 5% with the highest of 5.72% for a fresh

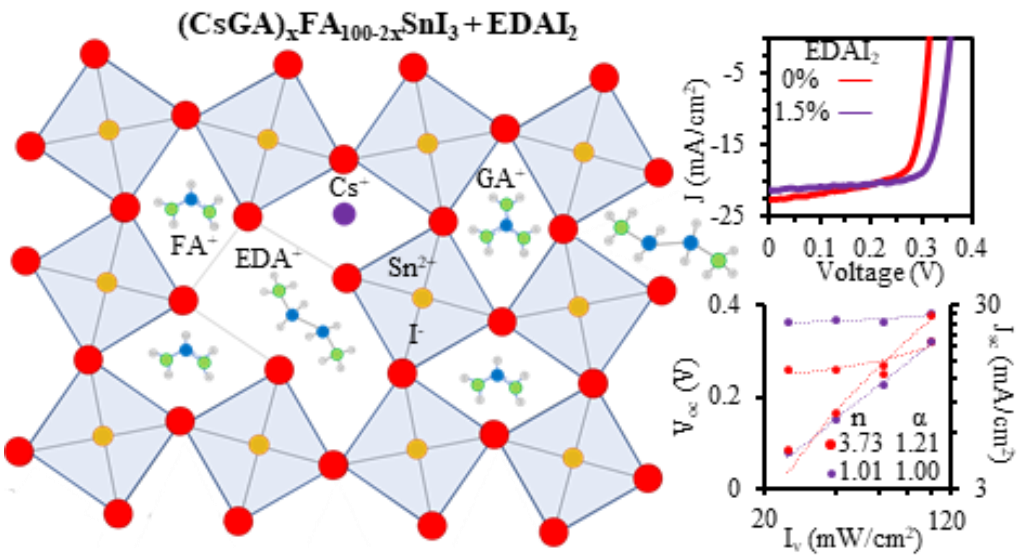

Figure 6-2. Summary content image showing crystal structure of $(CsGA)_xFA_{100-2x}SnI_3$+$EDAI_2$ and impacts on defects and performance.

device with $(CsGA)_{15}FA_{70}SnI_3$ and 1% $EDAI_2$. After storage, the maximum PCE was increased from 5.69% to 6.39% for the $(CsGA)_{15}FA_{70}SnI_3$ and 1.5% $EDAI_2$ devices. The devices with $EDAI_2$ additives showed better long-term stability than those without $EDAI_2$. Here, we have demonstrated an effective route for integrating large stabilizing agents into the crystal structure to that can improve performance and stability.

After focusing on optimizing the pure Sn perovskite layer itself, exploring ways to improve intrinsic properties while also implementing stabilizing components, this final work is dedicated to decreasing the high energy losses (0.6 – 0.9V) that limit the performance of pure Sn devices. To better align the hole transport material PEDOT:PSS work function with the valence band maximum of the perovskite absorber, cosolvent treatments, solvent wash treatments, and solvent immersion treatments were implemented. The solvents utilized have varying dipole moments, polarities, and boiling points, allowing to study the effect of these changes on PEDOT:PSS morphology, conductivity, and PSS content level. Utilizing the $(CsGA)_{15}FA_{70}SnI_3$+1.0% $EDAI_2$ perovskite film, we demonstrated a higher PCE of 6.29% and 6.16% with a 5% DMSO cosolvent and methanol solvent wash, respectively. The V_{oc} for the maximum PCE devices was also able to increase from 0.33 V for the untreated PEDOT:PSS to 0.45 V for a 10% DMSO cosolvent prepared PEDOT:PSS. This proof of concept shows the value in tailoring transport layers specifically to decrease the energy losses in pure Sn perovskite solar cells to improve the performance of lead-free devices.

6.2 Outlook

My work has played a significant role in expanding routes for improving Sn perovskite film morphology, crystallinity, device performance, and stability. Not only have we designed and explored new libraries of Sn compositions, but we have also developed a route for better

integrating crucial stabilizing components into pure Sn films while tackling energy loss issues. This contributes to the advancement of future commercialization of lead-free photovoltaic devices and for use in tandem solar cells with Sn mixed perovskite and utilized because of their favored band gap. This research can also be easily translated to other potential lead-free applications such as photodetectors, batteries, piezoelectrics, lasers, fuel cells, sensors, superconductors, light-emitting diodes, and transistors.

The main performance limiting factor is still the energy loss resulting in a low V_{oc} and PCE. The hole transport layer as well as the electron transport layer need to be better engineered to the perovskite conduction and valence band. Integrating specific derivatives of the HTL with a high work function to help with perovskite nucleation and carrier transport could help minimize this energy loss. Although we focused on upshifting the work function of the HTL to avoid it blocking holes, the LUMO of typical ETL such as $PC_{60}BM$ and C_{60} are very deep. Exploring shallower ETL can help maximize attainable voltages and increase device performances. Alternatively, surface treatment at the interface between the perovskite and transport layer designed to facilitate electron transport could have a similar impact while further prevent ionic migration, accumulation, and electrode poisoning. At this point, the main performance roadblock for pure Sn perovskite devices could be eliminated with interfacial engineering focused on minimizing energy loss and enhancing carrier transport.

With ongoing progress in lab-scale device performance and stability, scaling up perovskite application and device fabrication is the next step. Processing techniques that are being explored to replace spin-coating include spray coating, screen printing, dip coating, inkjet printing, and roll-to-roll coating. Perovskite synthesis can be done at low temperatures and with less energy intensive methods allowing solution processing. Raw materials would therefore be a major fraction of

module costs, resulting in a potentially low levelized cost of energy and short energy payback time for commercialized roll-to-roll perovskite devices. The deployment of large-scale printing approaches are limited by the sensitivity to moisture, requiring re-optimization for roll-to-roll fabrication methods. This makes moisture resistance through additives and precursor engineering key to commercialization. Our tools of utilizing cation tuning to better integrate additives and stabilizing methods can be used in this scaling up field. This could also be combined with use of a reducing atmosphere during device preparation. Making perovskites scalable to the manufacturing level is the next step in the field, making this technology accessible for grid scale energy production.

APPENDIX

Vita

Gabriella Tosado is originally from Miami, Florida and received her B.S in Chemistry, Environmental Science and Policy, and Religious Studies from University of Miami in May 2015. She transitioned to a new field and began her graduate work at the University of Washington in September 2015, joining Professor Qiuming Yu's Research Group and received her Master of Science in Chemical Engineering at the University of Washington in Seattle, WA in 2018. She is expected to receive her Dual Title Doctor of Philosophy in Chemical Engineering and Nanotechnology & Molecular Engineering as well as her Certificate in Nonprofit Management at the University of Washington in Seattle, WA in 2020.

A.1 Publications Completed During Graduate Degree

1) **Tosado, G.A.;** Zheng, E; Yu,Q; Tuning Cesium-Guanidinium in Pure Sn Perovskites with Ethylenediammonium Additives for Lead-Free Perovskite Solar Cells, *Material Advances, submitted*
2) **Tosado, G.A.;** Matos, M; Ahumada, M; Chapko, M; Pozzo, L.D; Evaluation of Solar-Powered Battery Systems for Individuals Using Electricity-Dependent Medical Devices in Puerto Rico Following Hurricane Maria, , *American Journal of Public Health, submitted.*
3) **Tosado, G.A.;** Epstein, E; Nance, E; Introduce a Girl Series as an Educational and Mentorship Tool for Diversity in STEM, *Journal of Science Education and Technology, In preparation.*
4) Zheng, E; Niu, Z; **Tosado, G.A**; Dong, H; Albrikan, Y; Yu, Q.M; Revealing Stability of Inverted Planar MA-Free Perovskite Solar Cells and Electric Field-Induced Phase

Instability, *Journal of Physical Chemistry Letters, submitted.*

5) Niu, Z, Zheng; Dong, H E; Niu, Z; **Tosado, G.A**; Yu, Q.M; Manipulation of PEDOT:PSS with Polar and Non-Polar Solvent Post-Treatment for Efficient Inverted Perovskite Solar Cells, *ACS Applied Materials & Interfaces, submitted.*
6) **Tosado, G.A.;** Lin, Y.Y.; Zheng, E; Yu, Q.M; Impact of cesium on the phase and device stability of triple cation Pb-Sn double halide perovskite films and solar cells, *Journal of Materials Chemistry A,* 2018, DOI: 10.1039/C8TA06391E
7) Zheng, E.J.; Yuh, B; **Tosado, G.A**.; Yu, Q.M., Solution-processed visible-blind UV-A photodetectors based on $CH_3NH_3PbCl_3$ perovskite thin films, *Journal of Materials Chemistry C,* 2017, 5, 3796-3806.

A.2 Presentations Given During Graduate Degree

1) Tosado, G, "The Path of a PhD Student", Invited Speaker, *Provost's Townhall*, Seattle, 2020
2) Tosado, G, Scholastic Research Panel, Invited Speaker, *ARCS Luncheon*, Seattle, 2019
3) Tosado, G; Lin, Y; Zheng, E; Yu, Qiuming, "Impact of Cesium and Tin Doping in Hybrid Organic-Inorganic Perovskite Crystal Solar Cell Performance and Phase Stability". *MRS Conference, Boston, 2018*
4) Tosado, G; Lin, Y; Yu, Qiuming, "Impact of Cesium and Tin Doping in Hybrid Organic Inorganic Perovskite Crystal Solar Cell Performance and Phase Stability". Materials Research Society Conference Poster Session, Boston, November 2017
5) Tosado, G; Yu, Qiuming, "Thin Film Solar Engineering", Expanding Horizons Open Forum Presentation, Ewha University, South Korea, July 2017
6) Tosado, G; Zheng, E; Zhu, L; Yu, Q "Formation of Large Grain Cation Alloyed Iodide

Perovskite Films and Their Deployment in Solar Cells". Expanding Horizons Poster Symposium, EWHA University, South Korea, July 2017

7) Tosado, G; Zheng, E; Zhu, L; Yu, Q "Formation of Large Grain Cation Alloyed Iodide Perovskite Films and Their Deployment in Solar Cells". Graduate Student Symposium, University of Washington, October 2016
8) Tosado, G; Zheng, E; Zhu, L; Yu, Q "Formation of Large Grain Cation Alloyed Iodide Perovskite Films and Their Deployment in Solar Cells". International Conference on Energy Conversion and Storage, Orcas Island, September 2016

A.3 Awards and Fellowships

2019 Board Fellows Program
2018 Research America Civic Engagement Initiative, *Grantee*
2018 Washington State Super STEM Advocate Award
2018 Pacific Science Center Communication Fellowship
2018 Material Research Society Poster Award
2017 National Science Foundation Fellowship
2017 Husky 100 Award
2016 Clean Energy Institute Graduate Fellowship
2016 Clean Energy Institute Education Fellowship
2016 Honorable Mention NSF Fellowship
2015 John Tershin Endowed Chemical Engineering Fellowship
2015 Achievement Rewards for College Scientists (ARCS) Fellowship

Bibliography

(1) Administration, U. S. E. I. International Energy Outlook 2019 with Projections to 2050. *Choice Rev. Online* **2019**, 85. https://doi.org/10.5860/CHOICE.44-3624.

(2) Harringon, R. This incredible fact should get you psyched about solar power https://www.businessinsider.com/this-is-the-potential-of-solar-power-2015-9.

(3) Energy, U. S. D. of. The SunShot Initiative's 2030 Goal: $0.03 per KWh for Solar Electricity https://www.energy.gov/eere/solar/sunshot-2030.

(4) Solanki, C. S. PN Junction Diode an Introduction to Solar Cells. In *Solar Photovoltaics*; 2015; pp 75–84.

(5) Center, F. E. L. Solar Radiation and Photosynthetically Active Radiation https://www.fondriest.com/environmental-measurements/parameters/weather/photosynthetically-active-radiation/.

(6) Rose-Clot, M.; Marco Tina, G. Introduction to PV Plant. *Submerg. Float. Photovolt. Syst.* **2018**.

(7) Kumar, M.; Kumar, A. Performance Assessment and Degradation Analysis of Solar Photovoltaic Technologies: A Review. *Renew. Sustain. Energy Rev.* **2017**, *78* (November 2016), 554–587. https://doi.org/10.1016/j.rser.2017.04.083.

(8) Wang, B.; Xiao, X.; Chen, T. Perovskite Photovoltaics: A High-Efficiency Newcomer to the Solar Cell Family. *Nanoscale* **2014**, *6* (21), 12287–12297. https://doi.org/10.1039/c4nr04144e.

(9) NREL. Best Research-Cell Efficiency Chart https://www.nrel.gov/pv/cell-efficiency.html.

(10) Polman, A.; Knight, M.; Garnett, E. C.; Ehrler, B.; Sinke, W. C. Photovoltaic Materials: Present Efficiencies and Future Challenges. *Science (80-.).* **2016**, *352* (6283). https://doi.org/10.1126/science.aad4424.

(11) Yang, W. F.; Igbari, F.; Lou, Y. H.; Wang, Z. K.; Liao, L. S. Tin Halide Perovskites: Progress and Challenges. *Adv. Energy Mater.* **2019**, *1902584*, 1–30. https://doi.org/10.1002/aenm.201902584.

(12) Chen, Q.; De Marco, N.; Yang, Y.; Song, T. Bin; Chen, C. C.; Zhao, H.; Hong, Z.; Zhou, H.; Yang, Y. Under the Spotlight: The Organic-Inorganic Hybrid Halide Perovskite for Optoelectronic Applications. *Nano Today* **2015**, *10* (3), 355–396. https://doi.org/10.1016/j.nantod.2015.04.009.

(13) Park, N. G. Perovskite Solar Cells: An Emerging Photovoltaic Technology. *Mater. Today* **2015**, *18* (2), 65–72. https://doi.org/10.1016/j.mattod.2014.07.007.

(14) Asif, A. A.; Singh, R.; Alapatt, G. F. Technical and Economic Assessment of Perovskite Solar Cells for Large Scale Manufacturing. *J. Renew. Sustain. Energy* **2015**, *7* (4). https://doi.org/10.1063/1.4927329.

(15) Hu, X.; Huang, Z.; Zhou, X.; Li, P.; Wang, Y.; Huang, Z.; Su, M.; Ren, W.; Li, F.; Li, M.; Chen, Y.; Song, Y. Wearable Large-Scale Perovskite Solar-Power Source via

Nanocellular Scaffold. *Adv. Mater.* **2017**, *29* (42), 1–8. https://doi.org/10.1002/adma.201703236.

(16) Dou, B.; Whitaker, J. B.; Bruening, K.; Moore, D. T.; Wheeler, L. M.; Ryter, J.; Breslin, N. J.; Berry, J. J.; Garner, S. M.; Barnes, F. S.; Shaheen, S. E.; Tassone, C. J.; Zhu, K.; Van Hest, M. F. A. M. Roll-to-Roll Printing of Perovskite Solar Cells. *ACS Energy Lett.* **2018**, *3* (10), 2558–2565. https://doi.org/10.1021/acsenergylett.8b01556.

(17) Song, Z.; McElvany, C. L.; Phillips, A. B.; Celik, I.; Krantz, P. W.; Watthage, S. C.; Liyanage, G. K.; Apul, D.; Heben, M. J. A Technoeconomic Analysis of Perovskite Solar Module Manufacturing with Low-Cost Materials and Techniques. *Energy Environ. Sci.* **2017**, *10* (6), 1297–1305. https://doi.org/10.1039/c7ee00757d.

(18) Haug, F.; Yum, J.; Ballif, C. Organometallic Halide Perovskites: Sharp Optical Absorption Edge and Its Relation to Photovoltaic Performance. **2014**. https://doi.org/10.1021/jz500279b.

(19) Nayak, P. K.; Mahesh, S.; Snaith, H. J.; Cahen, D. Photovoltaic Solar Cell Technologies: Analysing the State of the Art. *Nat. Rev. Mater.* https://doi.org/10.1038/s41578-019-0097-0.

(20) Kaltenbrunner, M.; Adam, G.; Głowacki, E. D.; Drack, M.; Schwödiauer, R.; Leonat, L.; Apaydin, D. H.; Groiss, H.; Scharber, M. C.; White, M. S.; Sariciftci, N. S.; Bauer, S. Improved Stability in Air. **2015**, *14* (August). https://doi.org/10.1038/NMAT4388.

(21) Ibn-mohammed, T.; Koh, S. C. L.; Reaney, I. M.; Acquaye, A.; Schileo, G.; Mustapha, K. B. Perovskite Solar Cells : An Integrated Hybrid Lifecycle Assessment and Review in Comparison with Other Photovoltaic Technologies. *Renew. Sustain. Energy Rev.* **2017**, *80* (March), 1321–1344. https://doi.org/10.1016/j.rser.2017.05.095.

(22) Saliba, M.; Matsui, T.; Seo, J. Y.; Domanski, K.; Correa-Baena, J. P.; Nazeeruddin, M. K.; Zakeeruddin, S. M.; Tress, W.; Abate, A.; Hagfeldt, A.; Grätzel, M. Cesium-Containing Triple Cation Perovskite Solar Cells: Improved Stability, Reproducibility and High Efficiency. *Energy Environ. Sci.* **2016**, *9* (6), 1989–1997. https://doi.org/10.1039/c5ee03874j.

(23) Podolsky, B.; Rosen, N.; Clauser, J. F.; Steinberg, A. M.; Chiao, R. Y.; Vaziri, A.; Weihs, G.; Zeilinger, A.; Bennink, R. S.; Bentley, S. J.; Boyd, R. W.; Ratschbacher, L.; Fedrizzi, A.; Langford, N. K.; Zeilinger, A.; Beijersbergen, M. W.; Spreeuw, R. J. C.; Woerdman, J. P.; Weihs, G.; Zeilinger, A.; Leach, L.; Buller, G. S.; Padgett, M. J.; Andersson, E.; Miatto, F.; Eliel, E. R.; Woerdman, J. P.; Meystre, P.; Schwab, K.; Agarwal, G. S.; Boyd, R. W.; Giovannini, D.; Barnett, S. M.; Padgett, M. J.; Florijn, H. C. B.; Exter, M. P. Van; Pykacz, J.; Nomoto, S. M.; Schubert, W. H.; Novenstern, M. D.; Davis, J. A.; Bandres, M. A.; Broky, J.; Dogariu, A.; Christodoulides, D. N.; Fiorentino, M.; Wong, F. N. C.; Herbst, T.; Poppe, A.; Jennewein, T.; Zeilinger, A.; Hage, B.; Buchler, B.; Lam, P. K.; Maurer, C.; Bernet, S. References and Notes 1. **2012**, *338* (November), 643–648.

(24) Heo, J. H.; Song, D. H.; Im, S. H. Planar CH3NH3PbBr3 Hybrid Solar Cells with 10.4% Power Conversion Efficiency, Fabricated by Controlled Crystallization in the Spin-Coating Process. *Adv. Mater.* **2014**, *26* (48), 8179–8183.

https://doi.org/10.1002/adma.201403140.

(25) Prajongtat, P.; Dittrich, T. Precipitation of CH3NH3PbCl3 in CH3NH3PbI3 and Its Impact on Modulated Charge Separation. *J. Phys. Chem. C* **2015**, *119* (18), 9926–9933. https://doi.org/10.1021/acs.jpcc.5b01667.

(26) Li, Z.; Yang, M.; Park, J. S.; Wei, S. H.; Berry, J. J.; Zhu, K. Stabilizing Perovskite Structures by Tuning Tolerance Factor: Formation of Formamidinium and Cesium Lead Iodide Solid-State Alloys. *Chem. Mater.* **2016**, *28* (1), 284–292. https://doi.org/10.1021/acs.chemmater.5b04107.

(27) Goldschidt, V. M. Die Gesetze Der Krystallochemie. *Naturwissenschaften* **1926**, *14*, 477–485.

(28) Saparov, B.; Mitzi, D. B. Organic-Inorganic Perovskites: Structural Versatility for Functional Materials Design. *Chem. Rev.* **2016**, *116* (7), 4558–4596. https://doi.org/10.1021/acs.chemrev.5b00715.

(29) Liu, W.; Liu, Y.; Wang, J.; Wu, C.; Liu, C.; Xiao, L.; Chen, Z.; Wang, S.; Gong, Q. Twin Domains in Organometallic Halide Perovskite Thin-Films. *Crystals* **2018**, *8* (5). https://doi.org/10.3390/cryst8050216.

(30) Green, M. A.; Ho-Baillie, A.; Snaith, H. J. The Emergence of Perovskite Solar Cells. *Nat. Photonics* **2014**, *8* (7), 506–514. https://doi.org/10.1038/nphoton.2014.134.

(31) Hao, F.; Stoumpos, C. C.; Cao, D. H.; Chang, R. P. H.; Kanatzidis, M. G. Lead-Free Solid-State Organic-Inorganic Halide Perovskite Solar Cells. *Nat. Photonics* **2014**, *8* (6), 489–494. https://doi.org/10.1038/nphoton.2014.82.

(32) Miyata, A.; Mitioglu, A.; Plochocka, P.; Portugall, O.; Tse-wei, J.; Stranks, S. D.; Snaith, H. J.; Nicholas, R. J. <2015 Direct Measurement of the Exciton Binding Energy and Effective.Pdf>. **2015**, 1–22.

(33) Wehrenfennig, C.; Eperon, G. E.; Johnston, M. B.; Snaith, H. J.; Herz, L. M. High Charge Carrier Mobilities and Lifetimes in Organolead Trihalide Perovskites. *Adv. Mater.* **2014**, *26* (10), 1584–1589. https://doi.org/10.1002/adma.201305172.

(34) Stranks, S. D.; Eperon, G. E.; Grancini, G.; Menelaou, C.; Alcocer, M. J. P.; Leijtens, T.; Herz, L. M.; Petrozza, A.; Snaith, H. J. Electron-Hole Diffusion Lengths Exceeding. **2013**, *342* (October), 341–345.

(35) Tanaka, K.; Takahashi, T.; Ban, T.; Kondo, T.; Uchida, K.; Miura, N. Comparative Study on the Excitons in Lead-Halide-Based Perovskite-Type Crystals CH3NH3PbBr3 CH3NH 3PbI3. *Solid State Commun.* **2003**, *127* (9–10), 619–623. https://doi.org/10.1016/S0038-1098(03)00566-0.

(36) Tao, S.; Schmidt, I.; Brocks, G.; Jiang, J.; Tranca, I.; Meerholz, K.; Olthof, S. Absolute Energy Level Positions in Tin- and Lead-Based Halide Perovskites. *Nat. Commun.* **2019**, *10* (1), 1–10. https://doi.org/10.1038/s41467-019-10468-7.

(37) Prasanna, R.; Gold-Parker, A.; Leijtens, T.; Conings, B.; Babayigit, A.; Boyen, H. G.; Toney, M. F.; McGehee, M. D. Band Gap Tuning via Lattice Contraction and Octahedral

Tilting in Perovskite Materials for Photovoltaics. *J. Am. Chem. Soc.* **2017**, *139* (32), 11117–11124. https://doi.org/10.1021/jacs.7b04981.

(38) Zhang, W.; Eperon, G. E.; Snaith, H. J. Metal Halide Perovskites for Energy Applications. *Nat. Energy* **2016**, *1* (6). https://doi.org/10.1038/nenergy.2016.48.

(39) Zhao, Y.; Zhu, K. Organic-Inorganic Hybrid Lead Halide Perovskites for Optoelectronic and Electronic Applications. *Chem. Soc. Rev.* **2016**, *45* (3), 655–689. https://doi.org/10.1039/c4cs00458b.

(40) Zheng, E.; Yuh, B.; Tosado, G. A.; Yu, Q. Solution-Processed Visible-Blind UV-A Photodetectors Based on CH3NH3PbCl3 Perovskite Thin Films. *J. Mater. Chem. C* **2017**, *5* (15), 3796–3806. https://doi.org/10.1039/c7tc00639j.

(41) Du, K. Z.; Tu, Q.; Zhang, X.; Han, Q.; Liu, J.; Zauscher, S.; Mitzi, D. B. Two-Dimensional Lead(II) Halide-Based Hybrid Perovskites Templated by Acene Alkylamines: Crystal Structures, Optical Properties, and Piezoelectricity. *Inorg. Chem.* **2017**, *56* (15), 9291–9302. https://doi.org/10.1021/acs.inorgchem.7b01094.

(42) Kim, Y. H.; Cho, H.; Lee, T. W. Metal Halide Perovskite Light Emitters. *Proc. Natl. Acad. Sci. U. S. A.* **2016**, *113* (42), 11694–11702. https://doi.org/10.1073/pnas.1607471113.

(43) Veldhuis, S. A.; Boix, P. P.; Yantara, N.; Li, M.; Sum, T. C.; Mathews, N.; Mhaisalkar, S. G. Perovskite Materials for Light-Emitting Diodes and Lasers. *Adv. Mater.* **2016**, *28* (32), 6804–6834. https://doi.org/10.1002/adma.201600669.

(44) Manser, J. S.; Saidaminov, M. I.; Christians, J. A.; Bakr, O. M.; Kamat, P. V. Making and Breaking of Lead Halide Perovskites. *Acc. Chem. Res.* **2016**, *49* (2), 330–338. https://doi.org/10.1021/acs.accounts.5b00455.

(45) Kojima, A.; Teshima, K.; Shirai, Y.; Miyasaka, T. Organometal Halide Perovskites as Visible-Light Sensitizers for Photovoltaic Cells. *J. Am. Chem. Soc.* **2009**, *131* (17), 6050–6051. https://doi.org/10.1021/ja809598r.

(46) Kim, H. S.; Lee, C. R.; Im, J. H.; Lee, K. B.; Moehl, T.; Marchioro, A.; Moon, S. J.; Humphry-Baker, R.; Yum, J. H.; Moser, J. E.; Grätzel, M.; Park, N. G. Lead Iodide Perovskite Sensitized All-Solid-State Submicron Thin Film Mesoscopic Solar Cell with Efficiency Exceeding 9%. *Sci. Rep.* **2012**, *2*, 1–7. https://doi.org/10.1038/srep00591.

(47) Focus News. Cosmic Particle Accelerators Identified Newcomer Juices Up the Race to Harness Sunlight. *Science (80-.).* **2013**, *342* (December), 1438–1440.

(48) Christians, J. A.; Miranda Herrera, P. A.; Kamat, P. V. Transformation of the Excited State and Photovoltaic Efficiency of CH3NH3PbI3 Perovskite upon Controlled Exposure to Humidified Air. *J. Am. Chem. Soc.* **2015**, *137* (4), 1530–1538. https://doi.org/10.1021/ja511132a.

(49) Hoye, R. L. Z.; Schulz, P.; Schelhas, L. T.; Holder, A. M.; Stone, K. H.; Perkins, J. D.; Vigil-Fowler, D.; Siol, S.; Scanlon, D. O.; Zakutayev, A.; Walsh, A.; Smith, I. C.; Melot, B. C.; Kurchin, R. C.; Wang, Y.; Shi, J.; Marques, F. C.; Berry, J. J.; Tumas, W.; Lany, S.; Stevanović, V.; Toney, M. F.; Buonassisi, T. Perovskite-Inspired Photovoltaic Materials:

Toward Best Practices in Materials Characterization and Calculations. *Chem. Mater.* **2017**, *29* (5), 1964–1988. https://doi.org/10.1021/acs.chemmater.6b03852.

(50) Frost, J. M.; Butler, K. T.; Brivio, F.; Hendon, C. H.; Van Schilfgaarde, M.; Walsh, A. Atomistic Origins of High-Performance in Hybrid Halide Perovskite Solar Cells. *Nano Lett.* **2014**, *14* (5), 2584–2590. https://doi.org/10.1021/nl500390f.

(51) Berhe, T. A.; Su, W. N.; Chen, C. H.; Pan, C. J.; Cheng, J. H.; Chen, H. M.; Tsai, M. C.; Chen, L. Y.; Dubale, A. A.; Hwang, B. J. Organometal Halide Perovskite Solar Cells: Degradation and Stability. *Energy Environ. Sci.* **2016**, *9* (2), 323–356. https://doi.org/10.1039/c5ee02733k.

(52) Nie, W.; Blancon, J. C.; Neukirch, A. J.; Appavoo, K.; Tsai, H.; Chhowalla, M.; Alam, M. A.; Sfeir, M. Y.; Katan, C.; Even, J.; Tretiak, S.; Crochet, J. J.; Gupta, G.; Mohite, A. D. Light-Activated Photocurrent Degradation and Self-Healing in Perovskite Solar Cells. *Nat. Commun.* **2016**, *7* (May), 1–9. https://doi.org/10.1038/ncomms11574.

(53) Ahn, N.; Kwak, K.; Jang, M. S.; Yoon, H.; Lee, B. Y.; Lee, J. K.; Pikhitsa, P. V.; Byun, J.; Choi, M. Trapped Charge-Driven Degradation of Perovskite Solar Cells. *Nat. Commun.* **2016**, *7* (May), 1–9. https://doi.org/10.1038/ncomms13422.

(54) Heo, J. H.; Han, H. J.; Kim, D.; Ahn, T. K.; Im, S. H. Hysteresis-Less Inverted CH3NH3PbI3 Planar Perovskite Hybrid Solar Cells with 18.1% Power Conversion Efficiency. *Energy Environ. Sci.* **2015**, *8* (5), 1602–1608. https://doi.org/10.1039/c5ee00120j.

(55) Leijtens, T.; Eperon, G. E.; Pathak, S.; Abate, A.; Lee, M. M.; Snaith, H. J. Overcoming Ultraviolet Light Instability of Sensitized TiO2 with Meso-Superstructured Organometal Tri-Halide Perovskite Solar Cells. *Nat. Commun.* **2013**, *4*, 1–8. https://doi.org/10.1038/ncomms3885.

(56) Zhang, P.; Wu, J.; Zhang, T.; Wang, Y.; Liu, D.; Chen, H.; Ji, L.; Liu, C.; Ahmad, W.; Chen, Z. D.; Li, S. Perovskite Solar Cells with ZnO Electron-Transporting Materials. *Adv. Mater.* **2018**, *30* (3), 1–20. https://doi.org/10.1002/adma.201703737.

(57) Xiao, Z.; Bi, C.; Shao, Y.; Dong, Q.; Wang, Q.; Yuan, Y.; Wang, C.; Gao, Y.; Huang, J. Efficient, High Yield Perovskite Photovoltaic Devices Grown by Interdiffusion of Solution-Processed Precursor Stacking Layers. *Energy Environ. Sci.* **2014**, *7* (8), 2619–2623. https://doi.org/10.1039/c4ee01138d.

(58) Sun, K.; Zhang, S.; Li, P. Review on Application of PEDOTs and PEDOT : PSS in Energy Conversion and Storage Devices Review on Application of PEDOTs and PEDOT : PSS in Energy Conversion and Storage Devices. **2015**, No. March. https://doi.org/10.1007/s10854-015-2895-5.

(59) Espinosa, N.; Serrano-luján, L.; Urbina, A.; Krebs, F. C. Solar Energy Materials & Solar Cells Solution and Vapour Deposited Lead Perovskite Solar Cells : Ecotoxicity from a Life Cycle Assessment Perspective. *Sol. Energy Mater. Sol. Cells* **2015**, *137*, 303–310. https://doi.org/10.1016/j.solmat.2015.02.013.

(60) Chatterjee, S.; Pal, A. J. Influence of Metal Substitution on Hybrid Halide Perovskites:

Towards Lead-Free Perovskite Solar Cells. *J. Mater. Chem. A* **2018**, *6* (9), 3793–3823. https://doi.org/10.1039/c7ta09943f.

(61) Liu, X.; Yang, Z.; Chueh, C. C.; Rajagopal, A.; Williams, S. T.; Sun, Y.; Jen, A. K. Y. Improved Efficiency and Stability of Pb-Sn Binary Perovskite Solar Cells by Cs Substitution. *J. Mater. Chem. A* **2016**, *4* (46), 17939–17945. https://doi.org/10.1039/c6ta07712a.

(62) Ogomi, Y.; Morita, A.; Tsukamoto, S.; Saitho, T.; Fujikawa, N.; Shen, Q.; Toyoda, T.; Yoshino, K.; Pandey, S. S.; Ma, T.; Hayase, S. CH3NH3SnxPb(1-x)I3 Perovskite Solar Cells Covering up to 1060 Nm. *J. Phys. Chem. Lett.* **2014**, *5* (6), 1004–1011. https://doi.org/10.1021/jz5002117.

(63) Hao, F.; Stoumpos, C. C.; Chang, R. P. H.; Kanatzidis, M. G. Anomalous Band Gap Behavior in Mixed Sn and Pb Perovskites Enables Broadening of Absorption Spectrum in Solar Cells. *J. Am. Chem. Soc.* **2014**, *136* (22), 8094–8099. https://doi.org/10.1021/ja5033259.

(64) Yang, Z.; Rajagopal, A.; Jen, A. K. Y. Ideal Band gap Organic–Inorganic Hybrid Perovskite Solar Cells. *Adv. Mater.* **2017**, *29* (47), 1–7. https://doi.org/10.1002/adma.201704418.

(65) Liang, K.; Mitzi, D. B.; Prikas, M. T. Synthesis and Characterization of Organic-Inorganic Perovskite Thin Films Prepared Using a Versatile Two-Step Dipping Technique. *Chem. Mater.* **1998**, *10* (1), 403–411. https://doi.org/10.1021/cm970568f.

(66) Hao, F.; Stoumpos, C. C.; Guo, P.; Zhou, N.; Marks, T. J.; Chang, R. P. H.; Kanatzidis, M. G. Solvent-Mediated Crystallization of CH3NH3SnI3 Films for Heterojunction Depleted Perovskite Solar Cells. *J. Am. Chem. Soc.* **2015**, *137* (35), 11445–11452. https://doi.org/10.1021/jacs.5b06658.

(67) Yang, Z.; Rajagopal, A.; Chueh, C. C.; Jo, S. B.; Liu, B.; Zhao, T.; Jen, A. K. Y. Stable Low-Band gap Pb–Sn Binary Perovskites for Tandem Solar Cells. *Adv. Mater.* **2016**, *28* (40), 8990–8997. https://doi.org/10.1002/adma.201602696.

(68) Leijtens, T.; Prasanna, R.; Gold-Parker, A.; Toney, M. F.; McGehee, M. D. Mechanism of Tin Oxidation and Stabilization by Lead Substitution in Tin Halide Perovskites. *ACS Energy Lett.* **2017**, *2* (9), 2159–2165. https://doi.org/10.1021/acsenergylett.7b00636.

(69) Kontos, A. G.; Kaltzoglou, A.; Siranidi, E.; Palles, D.; Angeli, G. K.; Arfanis, M. K.; Psycharis, V.; Raptis, Y. S.; Kamitsos, E. I.; Trikalitis, P. N.; Stoumpos, C. C.; Kanatzidis, M. G.; Falaras, P. Structural Stability, Vibrational Properties, and Photoluminescence in CsSnI3 Perovskite upon the Addition of SnF2. *Inorg. Chem.* **2017**, *56* (1), 84–91. https://doi.org/10.1021/acs.inorgchem.6b02318.

(70) Chung, I.; Lee, B.; He, J.; Chang, R. P. H.; Kanatzidis, M. G. All-Solid-State Dye-Sensitized Solar Cells with High Efficiency. *Nature* **2012**, *485* (7399), 486–489. https://doi.org/10.1038/nature11067.

(71) Bi, C.; Wang, Q.; Shao, Y.; Yuan, Y.; Xiao, Z.; Huang, J. Non-Wetting Surface-Driven High-Aspect-Ratio Crystalline Grain Growth for Efficient Hybrid Perovskite Solar Cells.

Nat. Commun. **2015**, 1–7. https://doi.org/10.1038/ncomms8747.

(72) Erdman, N.; Bell, D. C.; Reichelt, R. *Scanning Ele*; 2019.

(73) Luo, L. Electron Microscope https://www.luolangli.com/microscopy.

(74) Rothmann, M. U.; Li, W.; Etheridge, J.; Cheng, Y. B. Microstructural Characterisations of Perovskite Solar Cells – From Grains to Interfaces: Techniques, Features, and Challenges. *Adv. Energy Mater.* **2017**, *7* (23), 1–17. https://doi.org/10.1002/aenm.201700912.

(75) Leblebici, S. Y.; Leppert, L.; Li, Y.; Reyes-Lillo, S. E.; Wickenburg, S.; Wong, E.; Lee, J.; Melli, M.; Ziegler, D.; Angell, D. K.; Ogletree, D. F.; Ashby, P. D.; Toma, F. M.; Neaton, J. B.; Sharp, I. D.; Weber-Bargioni, A. Facet-Dependent Photovoltaic Efficiency Variations in Single Grains of Hybrid Halide Perovskite. *Nat. Energy* **2016**, *1* (8), 1–7. https://doi.org/10.1038/nenergy.2016.93.

(76) S.T. Misture, R. L. S. X-Ray Diffraction. In *Encyclopedia of Materials: Science and Technology*; 2001.

(77) -Galvan; R., F.; Barranco, V.; Galvan, J. C.; Batlle, Sebastian FeliuFajardo, S.; García. We Are IntechOpen , the World ' s Leading Publisher of Open Access Books Built by Scientists , for Scientists TOP 1 %. *Intech* **2016**, *i* (tourism), 13. https://doi.org/http://dx.doi.org/10.5772/57353.

(78) Liu, Y.; Yang, Z.; Liu, S. F. Recent Progress in Single-Crystalline Perovskite Research Including Crystal Preparation, Property Evaluation, and Applications. *Adv. Sci.* **2018**, *5* (1). https://doi.org/10.1002/advs.201700471.

(79) Analysis Features UV Photoelectron Spectroscopy https://xpssimplified.com/UPS.php.

(80) Hameed, B. S. UV/Vis Absorption Spectrophotometry. In *nanomaterials in chromatography*; 2018.

(81) No Title https://xpssimplified.com/UPS.php.

(82) Tress, W.; Marinova, N.; Inganäs, O.; Nazeeruddin, M. K.; Zakeeruddin, S. M.; Graetzel, M. Predicting the Open-Circuit Voltage of CH3NH3PbI3 Perovskite Solar Cells Using Electroluminescence and Photovoltaic Quantum Efficiency Spectra: The Role of Radiative and Non-Radiative Recombination. *Adv. Energy Mater.* **2015**, *5* (3), 1–6. https://doi.org/10.1002/aenm.201400812.

(83) Stoumpos, C. C.; Malliakas, C. D.; Kanatzidis, M. G. Semiconducting Tin and Lead Iodide Perovskites with Organic Cations: Phase Transitions, High Mobilities, and near-Infrared Photoluminescent Properties. *Inorg. Chem.* **2013**, *52* (15), 9019–9038. https://doi.org/10.1021/ic401215x.

(84) Eperon, G. E.; Paternò, G. M.; Sutton, R. J.; Zampetti, A.; Haghighirad, A. A.; Cacialli, F.; Snaith, H. J. Inorganic Caesium Lead Iodide Perovskite Solar Cells. *J. Mater. Chem. A* **2015**, *3* (39), 19688–19695. https://doi.org/10.1039/c5ta06398a.

(85) McMeekin, D. P.; Sadoughi, G.; Rehman, W.; Eperon, G. E.; Saliba, M.; Hörantner, M. T.; Haghighirad, A.; Sakai, N.; Korte, L.; Rech, B.; Johnston, M. B.; Herz, L. M.; Snaith,

H. J. A Mixed-Cation Lead Mixed-Halide Perovskite Absorber for Tandem Solar Cells. *Science (80-.).* **2016**, *351* (6269), 151–155. https://doi.org/10.1126/science.aad5845.

(86) Shockley, W.; Queisser, H. J. Detailed Balance Limit of Efficiency of P-n Junction Solar Cells. *J. Appl. Phys.* **1961**, *32* (3), 510–519. https://doi.org/10.1063/1.1736034.

(87) Ávila, J.; Momblona, C.; Boix, P. P.; Sessolo, M.; Bolink, H. J. Vapor-Deposited Perovskites: The Route to High-Performance Solar Cell Production? *Joule* **2017**, *1* (3), 431–442. https://doi.org/10.1016/j.joule.2017.07.014.

(88) Rajagopal, A.; Yang, Z.; Jo, S. B.; Braly, I. L.; Liang, P. W.; Hillhouse, H. W.; Jen, A. K. Y. Highly Efficient Perovskite–Perovskite Tandem Solar Cells Reaching 80% of the Theoretical Limit in Photovoltage. *Adv. Mater.* **2017**, *29* (34), 1–10. https://doi.org/10.1002/adma.201702140.

(89) Zhao, Z.; Gu, F.; Li, Y.; Sun, W.; Ye, S.; Rao, H.; Liu, Z.; Bian, Z.; Huang, C. Mixed-Organic-Cation Tin Iodide for Lead-Free Perovskite Solar Cells with an Efficiency of 8.12%. *Adv. Sci.* **2017**, *4* (11). https://doi.org/10.1002/advs.201700204.

(90) Zong, Y.; Wang, N.; Zhang, L.; Ju, M. G.; Zeng, X. C.; Sun, X. W.; Zhou, Y.; Padture, N. P. Homogenous Alloys of Formamidinium Lead Triiodide and Cesium Tin Triiodide for Efficient Ideal-Band gap Perovskite Solar Cells. *Angew. Chemie - Int. Ed.* **2017**, *56* (41), 12658–12662. https://doi.org/10.1002/anie.201705965.

(91) Hu, Y.; Hutter, E. M.; Rieder, P.; Grill, I.; Hanisch, J.; Aygüler, M. F.; Hufnagel, A. G.; Handloser, M.; Bein, T.; Hartschuh, A.; Tvingstedt, K.; Dyakonov, V.; Baumann, A.; Savenije, T. J.; Petrus, M. L.; Docampo, P. Understanding the Role of Cesium and Rubidium Additives in Perovskite Solar Cells: Trap States, Charge Transport, and Recombination. *Adv. Energy Mater.* **2018**, *8* (16). https://doi.org/10.1002/aenm.201703057.

(92) Song, T. Bin; Yokoyama, T.; Aramaki, S.; Kanatzidis, M. G. Performance Enhancement of Lead-Free Tin- Based Perovskite Solar Cells with Reducing Atmosphere-Assisted Dispersible Additive. *ACS Energy Lett.* **2017**, *2* (4), 897–903. https://doi.org/10.1021/acsenergylett.7b00171.

(93) Zhu, L.; Yuh, B.; Schoen, S.; Li, X.; Aldighaithir, M.; Richardson, B. J.; Alamer, A.; Yu, Q. Solvent-Molecule-Mediated Manipulation of Crystalline Grains for Efficient Planar Binary Lead and Tin Triiodide Perovskite Solar Cells. *Nanoscale* **2016**, *8* (14), 7621–7630. https://doi.org/10.1039/c6nr00301j.

(94) Liao, W.; Zhao, D.; Yu, Y.; Grice, C. R.; Wang, C.; Cimaroli, A. J.; Schulz, P.; Meng, W.; Zhu, K.; Xiong, R. G.; Yan, Y. Lead-Free Inverted Planar Formamidinium Tin Triiodide Perovskite Solar Cells Achieving Power Conversion Efficiencies up to 6.22%. *Adv. Mater.* **2016**, *28* (42), 9333–9340. https://doi.org/10.1002/adma.201602992.

(95) Ma, F.; Li, J.; Li, W.; Lin, N.; Wang, L.; Qiao, J. Stable α/δ Phase Junction of Formamidinium Lead Iodide Perovskites for Enhanced near-Infrared Emission. *Chem. Sci.* **2016**, *8* (1), 800–805. https://doi.org/10.1039/c6sc03542f.

(96) Liang, J.; Wang, C.; Zhao, P.; Lu, Z.; Ma, Y.; Xu, Z.; Wang, Y.; Zhu, H.; Hu, Y.; Zhu, G.;

Ma, L.; Chen, T.; Tie, Z.; Liu, J.; Jin, Z. Solution Synthesis and Phase Control of Inorganic Perovskites for High-Performance Optoelectronic Devices. *Nanoscale* **2017**, *9* (33), 11841–11845. https://doi.org/10.1039/c7nr03530f.

(97) Yi, C.; Luo, J.; Meloni, S.; Boziki, A.; Ashari-Astani, N.; Grätzel, C.; Zakeeruddin, S. M.; Röthlisberger, U.; Grätzel, M. Entropic Stabilization of Mixed A-Cation ABX3 Metal Halide Perovskites for High Performance Perovskite Solar Cells. *Energy Environ. Sci.* **2016**, *9* (2), 656–662. https://doi.org/10.1039/c5ee03255e.

(98) Deepa, M.; Salado, M.; Calio, L.; Kazim, S.; Shivaprasad, S. M.; Ahmad, S. Cesium Power: Low Cs+ Levels Impart Stability to Perovskite Solar Cells. *Phys. Chem. Chem. Phys.* **2017**, *19* (5), 4069–4077. https://doi.org/10.1039/c6cp08022g.

(99) Kieslich, G.; Sun, S.; Cheetham, A. K. An Extended Tolerance Factor Approach for Organic-Inorganic Perovskites. *Chem. Sci.* **2015**, *6* (6), 3430–3433. https://doi.org/10.1039/c5sc00961h.

(100) Travis, W.; Glover, E. N. K.; Bronstein, H.; Scanlon, D. O.; Palgrave, R. G. On the Application of the Tolerance Factor to Inorganic and Hybrid Halide Perovskites: A Revised System. *Chem. Sci.* **2016**, *7* (7), 4548–4556. https://doi.org/10.1039/c5sc04845a.

(101) Lee, J. H.; Bristowe, N. C.; Lee, J. H.; Lee, S. H.; Bristowe, P. D.; Cheetham, A. K.; Jang, H. M. Resolving the Physical Origin of Octahedral Tilting in Halide Perovskites. *Chem. Mater.* **2016**, *28* (12), 4259–4266. https://doi.org/10.1021/acs.chemmater.6b00968.

(102) Ferrara, C.; Patrini, M.; Pisanu, A.; Quadrelli, P.; Milanese, C.; Tealdi, C.; Malavasi, L. Wide Band-Gap Tuning in Sn-Based Hybrid Perovskites through Cation Replacement: The FA1-:XMAxSnBr3 Mixed System. *J. Mater. Chem. A* **2017**, *5* (19), 9391–9395. https://doi.org/10.1039/c7ta01668a.

(103) Shao, Y.; Xiao, Z.; Bi, C.; Yuan, Y.; Huang, J. Origin and Elimination of Photocurrent Hysteresis by Fullerene Passivation in CH3NH3PbI3 Planar Heterojunction Solar Cells. *Nat. Commun.* **2014**, *5*, 1–7. https://doi.org/10.1038/ncomms6784.

(104) Konstantakou, M.; Stergiopoulos, T. A Critical Review on Tin Halide Perovskite Solar Cells. *J. Mater. Chem. A* **2017**, *5* (23), 11518–11549. https://doi.org/10.1039/c7ta00929a.

(105) Lee, S. J.; Shin, S. S.; Kim, Y. C.; Kim, D.; Ahn, T. K.; Noh, J. H.; Seo, J.; Seok, S. Il. Fabrication of Efficient Formamidinium Tin Iodide Perovskite Solar Cells through SnF2-Pyrazine Complex. *J. Am. Chem. Soc.* **2016**, *138* (12), 3974–3977. https://doi.org/10.1021/jacs.6b00142.

(106) Snaith, H. J.; Abate, A.; Ball, J. M.; Eperon, G. E.; Leijtens, T.; Noel, N. K.; Stranks, S. D.; Wang, J. T. W.; Wojciechowski, K.; Zhang, W. Anomalous Hysteresis in Perovskite Solar Cells. *J. Phys. Chem. Lett.* **2014**, *5* (9), 1511–1515. https://doi.org/10.1021/jz500113x.

(107) Unger, E. L.; Hoke, E. T.; Bailie, C. D.; Nguyen, W. H.; Bowring, A. R.; Heumüller, T.; Christoforo, M. G.; McGehee, M. D. Hysteresis and Transient Behavior in Current-Voltage Measurements of Hybrid-Perovskite Absorber Solar Cells. *Energy Environ. Sci.* **2014**, *7* (11), 3690–3698. https://doi.org/10.1039/c4ee02465f.

(108) Tang, X.; Van Den Berg, M.; Gu, E.; Horneber, A.; Matt, G. J.; Osvet, A.; Meixner, A. J.; Zhang, D.; Brabec, C. J. Local Observation of Phase Segregation in Mixed-Halide Perovskite. *Nano Lett.* **2018**, *18* (3), 2172–2178. https://doi.org/10.1021/acs.nanolett.8b00505.

(109) Braly, I. L.; Stoddard, R. J.; Rajagopal, A.; Uhl, A. R.; Katahara, J. K.; Jen, A. K. Y.; Hillhouse, H. W. Current-Induced Phase Segregation in Mixed Halide Hybrid Perovskites and Its Impact on Two-Terminal Tandem Solar Cell Design. *ACS Energy Lett.* **2017**, *2* (8), 1841–1847. https://doi.org/10.1021/acsenergylett.7b00525.

(110) Xiao, M.; Gu, S.; Zhu, P.; Tang, M.; Zhu, W.; Lin, R.; Chen, C.; Xu, W.; Yu, T.; Zhu, J. Tin-Based Perovskite with Improved Coverage and Crystallinity through Tin-Fluoride-Assisted Heterogeneous Nucleation. *Adv. Opt. Mater.* **2018**, *6* (1), 1–7. https://doi.org/10.1002/adom.201700615.

(111) Ozaki, M.; Katsuki, Y.; Liu, J.; Handa, T.; Nishikubo, R.; Yakumaru, S.; Hashikawa, Y.; Murata, Y.; Saito, T.; Shimakawa, Y.; Kanemitsu, Y.; Saeki, A.; Wakamiya, A. Solvent-Coordinated Tin Halide Complexes as Purified Precursors for Tin-Based Perovskites. *ACS Omega* **2017**, *2* (10), 7016–7021. https://doi.org/10.1021/acsomega.7b01292.

(112) Nasti, G.; Abate, A. Tin Halide Perovskite (ASnX3) Solar Cells: A Comprehensive Guide toward the Highest Power Conversion Efficiency. *Adv. Energy Mater.* **2019**, *1902467*, 1–16. https://doi.org/10.1002/aenm.201902467.

(113) Yao, H.; Zhou, F.; Li, Z.; Ci, Z.; Ding, L.; Jin, Z. Strategies for Improving the Stability of Tin-Based Perovskite (ASnX3) Solar Cells. *Adv. Sci.* **2020**, *1903540*. https://doi.org/10.1002/advs.201903540.

(114) Ke, W.; Kanatzidis, M. G. Prospects for Low-Toxicity Lead-Free Perovskite Solar Cells. *Nat. Commun.* **2019**, *10* (1), 1–4. https://doi.org/10.1038/s41467-019-08918-3.

(115) Chen, Z.; Yu, C.; Shum, K.; Wang, J. J.; Pfenninger, W.; Vockic, N.; Midgley, J.; Kenney, J. T. Photoluminescence Study of Polycrystalline CsSnI3 Thin Films: Determination of Exciton Binding Energy. *J. Lumin.* **2012**, *132* (2), 345–349. https://doi.org/10.1016/j.jlumin.2011.09.006.

(116) Noel, N. K.; Stranks, S. D.; Abate, A.; Wehrenfennig, C.; Guarnera, S.; Haghighirad, A. A.; Sadhanala, A.; Eperon, G. E.; Pathak, S. K.; Johnston, M. B.; Petrozza, A.; Herz, L. M.; Snaith, H. J. Lead-Free Organic-Inorganic Tin Halide Perovskites for Photovoltaic Applications. *Energy Environ. Sci.* **2014**, *7* (9), 3061–3068. https://doi.org/10.1039/c4ee01076k.

(117) Jokar, E.; Chien, C. H.; Tsai, C. M.; Fathi, A.; Diau, E. W. G. Robust Tin-Based Perovskite Solar Cells with Hybrid Organic Cations to Attain Efficiency Approaching 10%. *Adv. Mater.* **2019**, *31* (2), 1–7. https://doi.org/10.1002/adma.201804835.

(118) Kanno, S.; Imamura, Y.; Hada, M. First-Principles Calculations of the Rotational Motion and Hydrogen Bond Capability of Large Organic Cations in Hybrid Perovskites. *J. Phys. Chem. C* **2018**, *122* (28), 15966–15972. https://doi.org/10.1021/acs.jpcc.8b05570.

(119) Marco, N. De; Zhou, H.; Chen, Q.; Sun, P.; Liu, Z.; Meng, L.; Yao, E. P.; Liu, Y.;

Schiffer, A.; Yang, Y. Guanidinium: A Route to Enhanced Carrier Lifetime and Open-Circuit Voltage in Hybrid Perovskite Solar Cells. *Nano Lett.* **2016**, *16* (2), 1009–1016. https://doi.org/10.1021/acs.nanolett.5b04060.

(120) Saidaminov, M. I.; Kim, J.; Jain, A.; Quintero-Bermudez, R.; Tan, H.; Long, G.; Tan, F.; Johnston, A.; Zhao, Y.; Voznyy, O.; Sargent, E. H. Suppression of Atomic Vacancies via Incorporation of Isovalent Small Ions to Increase the Stability of Halide Perovskite Solar Cells in Ambient Air. *Nat. Energy* **2018**, *3* (8), 648–654. https://doi.org/10.1038/s41560-018-0192-2.

(121) Ke, W.; Stoumpos, C. C.; Zhu, M.; Mao, L.; Spanopoulos, I.; Liu, J.; Kontsevoi, O. Y.; Chen, M.; Sarma, D.; Zhang, Y.; Wasielewski, M. R.; Kanatzidis, M. G. Enhanced Photovoltaic Performance and Stability with a New Type of Hollow 3D Perovskite {en}FASnI3. *Sci. Adv.* **2017**, *3* (8), 1–10. https://doi.org/10.1126/sciadv.1701293.

(122) Ni, Z.; Bao, C.; Liu, Y.; Jiang, Q.; Wu, W. Q.; Chen, S.; Dai, X.; Chen, B.; Hartweg, B.; Yu, Z.; Holman, Z.; Huang, J. Resolving Spatial and Energetic Distributions of Trap States in Metal Halide Perovskite Solar Cells. *Science (80-.).* **2020**, *367* (6484), 1352–1358. https://doi.org/10.1126/science.aba0893.

(123) Jin, H.; Debroye, E.; Keshavarz, M.; Scheblykin, I. G.; Roeffaers, M. B. J.; Hofkens, J.; Steele, J. A. It's a Trap! On the Nature of Localised States and Charge Trapping in Lead Halide Perovskites. *Mater. Horizons* **2020**, *7* (2), 397–410. https://doi.org/10.1039/c9mh00500e.

(124) Spanopoulos, I.; Ke, W.; Stoumpos, C. C.; Schueller, E. C.; Kontsevoi, O. Y.; Seshadri, R.; Kanatzidis, M. G. Unraveling the Chemical Nature of the 3D "Hollow" Hybrid Halide Perovskites. *J. Am. Chem. Soc.* **2018**, *140* (17), 5728–5742. https://doi.org/10.1021/jacs.8b01034.

(125) Jokar, E.; Chien, C. H.; Fathi, A.; Rameez, M.; Chang, Y. H.; Diau, E. W. G. Slow Surface Passivation and Crystal Relaxation with Additives to Improve Device Performance and Durability for Tin-Based Perovskite Solar Cells. *Energy Environ. Sci.* **2018**, *11* (9), 2353–2362. https://doi.org/10.1039/c8ee00956b.

(126) Wang, T.; Yan, F. Reducing Agents for Improving the Stability of Sn-Based Perovskite Solar Cells. *Chem. - An Asian J.* **2020**. https://doi.org/10.1002/asia.202000160.

(127) Zhu, Z.; Chueh, C. C.; Li, N.; Mao, C.; Jen, A. K. Y. Realizing Efficient Lead-Free Formamidinium Tin Triiodide Perovskite Solar Cells via a Sequential Deposition Route. *Adv. Mater.* **2018**, *30* (6), 1–9. https://doi.org/10.1002/adma.201703800.

(128) Ge, Q. Q.; Ding, J.; Liu, J.; Ma, J. Y.; Chen, Y. X.; Gao, X. X.; Wan, L. J.; Hu, J. S. Promoting Crystalline Grain Growth and Healing Pinholes by Water Vapor Modulated Post-Annealing for Enhancing the Efficiency of Planar Perovskite Solar Cells. *J. Mater. Chem. A* **2016**, *4* (35), 13458–13467. https://doi.org/10.1039/c6ta05288f.

(129) Ke, W.; Spanopoulos, I.; Tu, Q.; Hadar, I.; Li, X.; Shekhawat, G. S.; Dravid, V. P.; Kanatzidis, M. G. Ethylenediammonium-Based "Hollow" Pb/Sn Perovskites with Ideal Band Gap Yield Solar Cells with Higher Efficiency and Stability. *J. Am. Chem. Soc.* **2019**, *141* (21), 8627–8637. https://doi.org/10.1021/jacs.9b03662.

(130) Kubicki, D. J.; Prochowicz, D.; Hofstetter, A.; Saski, M.; Yadav, P.; Bi, D.; Pellet, N.; Lewiński, J.; Zakeeruddin, S. M.; Grätzel, M.; Emsley, L. Formation of Stable Mixed Guanidinium-Methylammonium Phases with Exceptionally Long Carrier Lifetimes for High-Efficiency Lead Iodide-Based Perovskite Photovoltaics. *J. Am. Chem. Soc.* **2018**, *140* (9), 3345–3351. https://doi.org/10.1021/jacs.7b12860.

(131) Jodlowski, A. D.; Roldán-Carmona, C.; Grancini, G.; Salado, M.; Ralaiarisoa, M.; Ahmad, S.; Koch, N.; Camacho, L.; De Miguel, G.; Nazeeruddin, M. K. Large Guanidinium Cation Mixed with Methylammonium in Lead Iodide Perovskites for 19% Efficient Solar Cells. *Nat. Energy* **2017**, *2* (12), 972–979. https://doi.org/10.1038/s41560-017-0054-3.

(132) Huang, K.; Yuan, L.; Feng, S. Crystal Facet Tailoring Arts in Perovskite Oxides. *Inorg. Chem. Front.* **2015**, *2* (11), 965–981. https://doi.org/10.1039/c5qi00168d.

(133) Tosado, G. A.; Lin, Y. Y.; Zheng, E.; Yu, Q. Impact of Cesium on the Phase and Device Stability of Triple Cation Pb-Sn Double Halide Perovskite Films and Solar Cells. *J. Mater. Chem. A* **2018**, *6* (36), 17426–17436. https://doi.org/10.1039/c8ta06391e.

(134) Diau, E. W. G.; Jokar, E.; Rameez, M. Strategies to Improve Performance and Stability for Tin-Based Perovskite Solar Cells. *ACS Energy Lett.* **2019**, *4*, 1930–1937. https://doi.org/10.1021/acsenergylett.9b01179.

(135) Lee, S. J.; Shin, S. S.; Im, J.; Ahn, T. K.; Noh, J. H.; Jeon, N. J.; Seok, S. Il; Seo, J. Reducing Carrier Density in Formamidinium Tin Perovskites and Its Beneficial Effects on Stability and Efficiency of Perovskite Solar Cells. *ACS Energy Lett.* **2018**, *3* (1), 46–53. https://doi.org/10.1021/acsenergylett.7b00976.

(136) Prochowicz, D.; Tavakoli, M. M.; Alanazi, A. Q.; Trivedi, S.; Tavakoli Dastjerdi, H.; Zakeeruddin, S. M.; Grätzel, M.; Yadav, P. Charge Accumulation, Recombination, and Their Associated Time Scale in Efficient (GUA) x(MA)1-XPbI3-Based Perovskite Solar Cells. *ACS Omega* **2019**, *4* (16), 16840–16846. https://doi.org/10.1021/acsomega.9b01701.

(137) Ke, W.; Stoumpos, C. C.; Spanopoulos, I.; Mao, L.; Chen, M.; Wasielewski, M. R.; Kanatzidis, M. G. Efficient Lead-Free Solar Cells Based on Hollow {en}MASnI3 Perovskites. *J. Am. Chem. Soc.* **2017**, *139* (41), 14800–14806. https://doi.org/10.1021/jacs.7b09018.

(138) Troughton, J.; Gasparini, N.; Baran, D. Cs0.15FA0.85PbI3 Perovskite Solar Cells for Concentrator Photovoltaic Applications. *J. Mater. Chem. A* **2018**, *6* (44), 21913–21917. https://doi.org/10.1039/c8ta05639k.

(139) Cowan, S. R.; Roy, A.; Heeger, A. J. Recombination in Polymer-Fullerene Bulk Heterojunction Solar Cells. *Phys. Rev. B - Condens. Matter Mater. Phys.* **2010**, *82* (24), 1–10. https://doi.org/10.1103/PhysRevB.82.245207.

(140) Shao, S.; Chen, Z.; Fang, H. H.; Ten Brink, G. H.; Bartesaghi, D.; Adjokatse, S.; Koster, L. J. A.; Kooi, B. J.; Facchetti, A.; Loi, M. A. N-Type Polymers as Electron Extraction Layers in Hybrid Perovskite Solar Cells with Improved Ambient Stability. *J. Mater. Chem. A* **2016**, *4* (7), 2419–2426. https://doi.org/10.1039/c5ta10696f.

(141) Herz, L. M. Charge-Carrier Mobilities in Metal Halide Perovskites: Fundamental Mechanisms and Limits. *ACS Energy Lett.* **2017**, *2* (7), 1539–1548. https://doi.org/10.1021/acsenergylett.7b00276.

(142) Xing, G.; Mathews, N.; Lim, S. S.; Lam, Y. M.; Mhaisalkar, S.; Sum, T. C. Long-Range Balanced Electron- and Hole-Transport Lengths in Organic-Inorganic CH 3 NH 3 PbI 3. **2013**, *6960* (October), 498–500.

(143) Back, H.; Kim, G.; Kim, J.; Kong, J.; Kim, T. K.; Kang, H.; Kim, H.; Lee, J.; Lee, S.; Lee, K. Achieving Long-Term Stable Perovskite Solar Cells: Via Ion Neutralization. *Energy Environ. Sci.* **2016**, *9* (4), 1258–1263. https://doi.org/10.1039/c6ee00612d.

(144) Xiao, Z.; Yuan, Y.; Shao, Y.; Wang, Q.; Dong, Q.; Bi, C.; Sharma, P.; Gruverman, A.; Huang, J. Giant Switchable Photovoltaic Effect in Organometal Trihalide Perovskite Devices. *Nat. Mater.* **2015**, *14* (2), 193–197. https://doi.org/10.1038/nmat4150.

(145) Tress, W.; Marinova, N.; Moehl, T.; Zakeeruddin, S. M.; Nazeeruddin, M. K.; Grätzel, M. Understanding the Rate-Dependent J-V Hysteresis, Slow Time Component, and Aging in CH3NH3PbI3 Perovskite Solar Cells: The Role of a Compensated Electric Field. *Energy Environ. Sci.* **2015**, *8* (3), 995–1004. https://doi.org/10.1039/c4ee03664f.

(146) Chen, B.; Yang, M.; Priya, S.; Zhu, K. Origin of J-V Hysteresis in Perovskite Solar Cells. *J. Phys. Chem. Lett.* **2016**, *7* (5), 905–917. https://doi.org/10.1021/acs.jpclett.6b00215.

(147) Domanski, K.; Roose, B.; Matsui, T.; Saliba, M.; Turren-Cruz, S. H.; Correa-Baena, J. P.; Carmona, C. R.; Richardson, G.; Foster, J. M.; De Angelis, F.; Ball, J. M.; Petrozza, A.; Mine, N.; Nazeeruddin, M. K.; Tress, W.; Grätzel, M.; Steiner, U.; Hagfeldt, A.; Abate, A. Migration of Cations Induces Reversible Performance Losses over Day/Night Cycling in Perovskite Solar Cells. *Energy Environ. Sci.* **2017**, *10* (2), 604–613. https://doi.org/10.1039/c6ee03352k.

(148) Chung, I.; Song, J. H.; Im, J.; Androulakis, J.; Malliakas, C. D.; Li, H.; Freeman, A. J.; Kenney, J. T.; Kanatzidis, M. G. CsSnI 3: Semiconductor or Metal? High Electrical Conductivity and Strong near-Infrared Photoluminescence from a Single Material. High Hole Mobility and Phase-Transitions. *J. Am. Chem. Soc.* **2012**, *134* (20), 8579–8587. https://doi.org/10.1021/ja301539s.

(149) Marshall, K. P.; Walker, M.; Walton, R. I.; Hatton, R. A. Enhanced Stability and Efficiency in Hole-Transport-Layer-Free CsSnI 3 Perovskite Photovoltaics. *Nat. Energy* **2016**, *1* (12), 1–9. https://doi.org/10.1038/nenergy.2016.178.

(150) Qiu, J.; Xia, Y.; Chen, Y.; Huang, W. Management of Crystallization Kinetics for Efficient and Stable Low-Dimensional Ruddlesden–Popper (LDRP) Lead-Free Perovskite Solar Cells. *Adv. Sci.* **2019**, *6* (1), 1–7. https://doi.org/10.1002/advs.201800793.

(151) Liu, X.; Wang, Y.; Xie, F.; Yang, X.; Han, L. Improving the Performance of Inverted Formamidinium Tin Iodide Perovskite Solar Cells by Reducing the Energy-Level Mismatch. *ACS Energy Lett.* **2018**, *3* (5), 1116–1121. https://doi.org/10.1021/acsenergylett.8b00383.

(152) Mahmood, K.; Sarwar, S.; Mehran, M. T. Current Status of Electron Transport Layers in

Perovskite Solar Cells: Materials and Properties. *RSC Adv.* **2017**, *7* (28), 17044–17062. https://doi.org/10.1039/c7ra00002b.

(153) Dong, Q.; Yuan, Y.; Shao, Y.; Fang, Y.; Wang, Q.; Huang, J. Abnormal Crystal Growth in CH3NH3PbI3-XClx Using a Multi-Cycle Solution Coating Process. *Energy Environ. Sci.* **2015**, *8* (8), 2464–2470. https://doi.org/10.1039/c5ee01179e.

(154) Park, J. H.; Seo, J.; Park, S.; Shin, S. S.; Kim, Y. C.; Jeon, N. J.; Shin, H. W.; Ahn, T. K.; Noh, J. H.; Yoon, S. C.; Hwang, C. S.; Seok, S. Il. Efficient CH3NH3PbI3 Perovskite Solar Cells Employing Nanostructured P-Type NiO Electrode Formed by a Pulsed Laser Deposition. *Adv. Mater.* **2015**, *27* (27), 4013–4019. https://doi.org/10.1002/adma.201500523.

(155) Zuo, C.; Ding, L. Modified PEDOT Layer Makes a 1.52 V Voc for Perovskite/PCBM Solar Cells. *Adv. Energy Mater.* **2017**, *7* (2), 4–9. https://doi.org/10.1002/aenm.201601193.

(156) Lee, T. W.; Chung, Y. Control of the Surface Composition of a Conducting-Polymer Complex Film to Tune the Work Function. *Adv. Funct. Mater.* **2008**, *18* (15), 2246–2252. https://doi.org/10.1002/adfm.200700766.

(157) Macgregor, W. S.; Corporation, C. Z. T H E Chemical and Physical Properties of Dmso. **1962**.

(158) Yue, H.; Zhao, Y.; Ma, X.; Gong, J. Ethylene Glycol: Properties, Synthesis, and Applications. *Chem. Soc. Rev.* **2012**, *41* (11), 4218–4244. https://doi.org/10.1039/c2cs15359a.

(159) Denney, D. J.; Cole, R. H. Dielectric Properties of Methanol and Methanol-1-Propanol Solutions. *J. Chem. Phys.* **1955**, *23* (10), 1767–1772. https://doi.org/10.1063/1.1740577.

(160) Hu, Z.; Zhang, J.; Zhu, Y. Effects of Solvent-Treated PEDOT: PSS on Organic Photovoltaic Devices. *Renew. Energy* **2014**, *62*, 100–105. https://doi.org/10.1016/j.renene.2013.06.042.

(161) Xia, Y.; Ouyang, J. PEDOT:PSS Films with Significantly Enhanced Conductivities Induced by Preferential Solvation with Cosolvents and Their Application in Polymer Photovoltaic Cells. *J. Mater. Chem.* **2011**, *21* (13), 4927–4936. https://doi.org/10.1039/c0jm04177g.

(162) Meng, W.; Ge, R.; Li, Z.; Tong, J.; Liu, T.; Zhao, Q.; Xiong, S.; Jiang, F.; Mao, L.; Zhou, Y. Conductivity Enhancement of PEDOT:PSS Films via Phosphoric Acid Treatment for Flexible All-Plastic Solar Cells. *ACS Appl. Mater. Interfaces* **2015**, *7* (25), 14089–14094. https://doi.org/10.1021/acsami.5b03309.

(163) Bai, Y.; Meng, X.; Yang, S. Interface Engineering for Highly Efficient and Stable Planar P-i-n Perovskite Solar Cells. *Adv. Energy Mater.* **2018**, *8* (5), 1–14. https://doi.org/10.1002/aenm.201701883.

(164) Singh, V.; Arora, S.; Arora, M.; Sharma, V.; Tandon, R. P. Characterization of Doped PEDOT: PSS and Its Influence on the Performance and Degradation of Organic Solar Cells. *Semicond. Sci. Technol.* **2014**, *29* (4). https://doi.org/10.1088/0268-

1242/29/4/045020.

(165) Xiong, S.; Fu, J.; Li, Z.; Shi, Y.; Wang, X.; Chu, J. Modulating the Electrochromic Performances of Transmissive and Reflective Devices Using N,N-Dimethyl Formamide Modified Poly(3,4-Ethylenedioxythiophene)/Poly(Styrene Sulfonate) Blend as Active Layers. *J. Macromol. Sci. Phys.* **2015**, *54* (7), 799–810.

(166) Chiu, W. W.; Travaš-Sejdić, J.; Cooney, R. P.; Bowmaker, G. A. Spectroscopic and Conductivity Studies of Doping in Chemically Synthesized Poly(3,4-Ethylenedioxythiophene). *Synth. Met.* **2005**, *155* (1), 80–88. https://doi.org/10.1016/j.synthmet.2005.06.012.

(167) Ouyang, J.; Xu, Q.; Chu, C. W.; Yang, Y.; Li, G.; Shinar, J. On the Mechanism of Conductivity Enhancement in Poly(3,4- Ethylenedioxythiophene):Poly(Styrene Sulfonate) Film through Solvent Treatment. *Polymer (Guildf).* **2004**, *45* (25), 8443–8450. https://doi.org/10.1016/j.polymer.2004.10.001.

(168) Park, H. S.; Ko, S. J.; Park, J. S.; Kim, J. Y.; Song, H. K. Redox-Active Charge Carriers of Conducting Polymers as a Tuner of Conductivity and Its Potential Window. *Sci. Rep.* **2013**, *3*, 1–6. https://doi.org/10.1038/srep02454.

(169) Kang, T. G.; Park, J. K.; Yun, G. H.; Choi, H. H.; Lee, H. J.; Yook, J. G. A Real-Time Humidity Sensor Based on a Microwave Oscillator with Conducting Polymer PEDOT:PSS Film. *Sensors Actuators, B Chem.* **2019**, *282* (September 2018), 145–151. https://doi.org/10.1016/j.snb.2018.09.080.

(170) Farah, A. A.; Rutledge, S. A.; Schaarschmidt, A.; Lai, R.; Freedman, J. P.; Helmy, A. S. Conductivity Enhancement of Poly(3,4-Ethylenedioxythiophene)- Poly(Styrenesulfonate) Films Post-Spincasting. *J. Appl. Phys.* **2012**, *112* (11). https://doi.org/10.1063/1.4768265.